CHARACTERISATION OF AN EXOGAM CLOVER

GERMANIUM DETECTOR

Thesis submitted in accordance with the requirements
of the University of Liverpool for the degree of
Doctor in Philosophy

by

Sébastien Alexandre Adrien Gros

Oliver Lodge Laboratory

April 2005

ACKNOWLEDGEMENTS

The possibility to do research through a Ph.D. in the Nuclear Physics Group at the University of Liverpool was an invaluable enriching experience, and I would like to thank primarily Professor Nolan for giving me this opportunity. I could not thank enough my supervisor, Dr. Andrew Boston, not only for his guidance and his help during these 3 years, but especially for his support in the last months of my course. I also want to thank him for having been such a friend, from the first day I arrived in Liverpool. I take the opportunity to acknowledge John Cresswell and Terry Burns, because most of the work would have taken for ever to complete without their help. In the same manner, I am particularly grateful to Cayetano Santos and Patrice Medina from Strasbourg. for their work in providing and improving their simulation.

When I arrived in Liverpool, Nuclear Physics was a complete new field for me and I would not have gone far into this field without the help and advice that the Nuclear Physics Group gave me at various times during these 3 years, Marielle Chartier, Eddie Paul, and Rodi Herzberg, Graham Jones, and Robert Page. I cannot acknowledge the Group without especially thanking Aled and Carlos for the conversations we had during our lunch at the Guild and during our afternoon coffee breaks; and to Jenny for the mutual support during these 4 years. Thanks to all the Ph.D. students and post docs from the second floor, you all contributed to make these three years and eight months in Liverpool full of great souvenirs!

Finally I would like to thank my family, who supported me from France, and Celia who had to deal with my everyday good and bad moods, and was of great support.

ABSTRACT

EXOGAM is a high efficiency gamma spectrometer dedicated to gamma-ray spectroscopy with radioactive ion beams at GANIL (Grand Accélerateur National d'Ions Lourds, Caen, France). It consists of an array of up to 16 escape suppressed spectrometers (ESS) composed of segmented composite High Purity Germanium (HPGe) CLOVER detectors.

The CLOVER detector is composed of four HPGe crystals housed in the same cryostat. An improvement of the performances of EXOGAM is conditioned to an increase in granularity of the CLOVER detectors. The use of digital Pulse Shape Analysis allows the determination of the position of interaction within a segment. However the complex geometry of the Clover detector requires a thorough characterisation of the detector crystals. This work presents the characterisation of an EXOGAM Clover detector, performed in order to evaluate the detector design for the determination of the position of a gamma-ray interaction with pulse shape analysis.

The approach described in this work consisted in:

1. The simulation of the electrostatic properties of a CLOVER crystal;

2. Experimental measurements consisting of two scans of the front face of a CLOVER detector with two collimated ^{137}Cs and ^{57}Co sources and a third single performed along a crystal segment.

The analysis of the partial rise time distributions of the detector charge pulses, obtained from each position of the scan measurements, allowed the characterisation of the response of the crystal and the determination of active germanium regions offering by poor charge drift properties. The study of the radial variation of the partial T30 and T90 rise time distributions enabled the division of a segment into a maximum of four radial ranges. Finally, the comparison of experimental results with simulated data showed qualitative and reasonable quantitative agreement.

CONTENTS

LIST OF FIGURES

Chapter I

INTRODUCTION

Gamma spectroscopy arrays

The first chapter opens by introducing gamma spectroscopy detector arrays. Important parameters describing the performances of such arrays are presented. The EXOGAM spectrometer is then presented in the second part of the chapter, before closing on the plan followed in the dissertation.

1 Gamma detector arrays for nuclear spectroscopy

1.1 Nuclear gamma spectroscopy arrays parameters

The development of escape suppressed spectrometers (ESS) has revolutionised the field of γ-rays spectroscopy over the past 15 years [Nol94, Bea96]. The performance of an array is given by several parameters:

The resolving power *R* is given by

$$R = \frac{SE_\gamma}{\Delta E_\gamma} PT \tag{I.1}$$

where SE_γ is the average energy separation of consecutive γ-ray transitions belonging to a typical energy spectrum, ΔE_γ is the full width at half maximum (FWHM) energy resolution of the γ-rays peak obtained in the spectrum [Bea96], and *PT* is the peak to total ratio.

The average separation energy in the γ-rays transition depends on the specific experiment carried out, therefore, the limiting parameters to the resolving power are the energy resolution ΔE_γ and *PT*. The energy resolution depends on several factors:

1. The intrinsic resolution of the detector ΔE_i. The intrinsic energy resolution is typically 2 keV at 1.3 MeV.

2. The Doppler broadening ΔE_{iD} resulting from the opening angle of the detector.

3. The Doppler broadening induced by the angular spread of recoil ΔE_{iR}.

4. The Doppler broadening from the velocity spread of the recoil ΔE_{iV}.

The energy resolution is then given by

$$\Delta E_\gamma = \left(\Delta E_i + \Delta E_D + \Delta E_V + \Delta E_R\right)^{1/2} \tag{I.2}$$

A higher peak to total can be achieved by improving the photopeak efficiency ε, which is defined as the ratio of number of γ-rays detected over the number of γ-rays emitted. The total photopeak efficiency ε_T of an array depends generally on the detecting volume surrounding the

target. For an array consisting of N detectors with identical intrinsic efficiency ε_i, the total photopeak efficiency is given by

$$\varepsilon_T = \frac{1}{4\pi}\sum_N \Omega\varepsilon_i \tag{I.3}$$

where Ω is the solid angle covered by an individual detector from the source. The use of Bismuth Germanate Oxide (BGO) instead of large NaI scintillators as Compton suppressors improved the compactness of ESS and allowed more detectors to be placed around the target thus providing larger photopeak efficiency values. Latest arrays maximise the photopeak efficiency by covering the maximum solid angle around the target. For example, GAMMASPHERE [Lee90] utilises then a maximum of 110 Compton suppressed germanium detectors to cover a solid angle of 46% of 4π for the complete array.

2 The EXOGAM array

2.1 Presentation of EXOGAM, design specifications

As for the development of radioactive beams (RIB) accelerators, recent developments in γ-ray spectroscopy detectors and arrays are motivated by the desire to study new physics, and reach unexplored regions of the nuclear chart. Nuclei far from stability are and will be accessible with cross sections large enough to enable the investigation of their properties. However to be able to detect the products from reactions with RIBs, new arrays, with improved performances need to be designed to accommodate for the lower rate of production of exotic nuclei.

At the *Grand Accelarateur National d'Ions Lourds* (GANIL) the SPIRAL facility [Vil01] has been delivering RIBs since 2001. EXOGAM [Sim00] is a European collaboration to build an array of High Purity Germanium detectors (HPGe) dedicated to the spectroscopy of nuclei produced from SPIRAL radioactive beams. In total, EXOGAM comprises 16 escape suppressed segmented Clover [Duc99] detectors (Figure I.1). EXOGAM has been designed in order to accommodate for the specific requirement of experiments with RIBs:

- The lower intensity delivered by RIBs demands the largest possible photo peak efficiency. This is achieved by the use of 16 large volume HPGe detectors in closed packed configuration.

- The study of rare events produced with low cross sections requires a high peak to background ratio and the best energy resolution possible, which are obtained by the use of composite, escape suppressed HPGe spectrometers. The segmentation of each composite detector increases the granularity of the array, thus improving further the peak to background ratio. Figure I.2 presents calculated energy resolutions for the comparison of the performances of the EXOGAM Clover detectors versus single crystal and composite Clover detectors[1]. It clearly demonstrates the advantage of segmented Clover detectors over non segmented composite and single crystal HPGe detectors.

- The modularity of the EXOGAM array allows the configuration of its detector components to accommodate for the specificities of different experimental conditions: various γ-ray energy ranges and multiplicity, different recoils velocity, and particular kinematics of the reactions mechanisms. In this respect, EXOGAM can be combined with ancillary detectors in order to detect light and heavy charged particle or neutrons emitted during a particular reaction.

2.2 Configurations of EXOGAM

EXOGAM can be used with different detector arrangements. When fully assembled, the array comprises 16 Clover detectors. It consists of a ring of 8 detectors at 90°, 4 detectors forward at 45° and 4 detectors backward at 135°, as illustrated in Figure I.3 and Figure I.4, showing respectively a 3D view and a cross section through the detectors arrangement (picture of the EXOGAM array with 16 elements). The detectors can be positioned at different distances from the target:

- In the closed packed configuration, the front face of the clover detectors is located at a 114 mm distance from the target. The suppression shield (see Figure 3.3) consists only of the side elements (configuration A).

- In the pulled back configuration, the detectors are at the furthest from the target (147 mm), and allows for the use of the full suppression shield (configuration B).

[1] Composite Clover and EXOGAM Clover detectors are described in Chapter III.

Furthermore, the distance to the target can be reduced by using the Clover detectors in cube configuration: The closed pack configuration (A) reduces the distance to the target down to 50 mm. In the pulled back configuration (B), the front face of the detectors is at 68 mm from the target. Table I.1 [Sim00] summarised the calculated performances of the EXOGAM array in the different configurations.

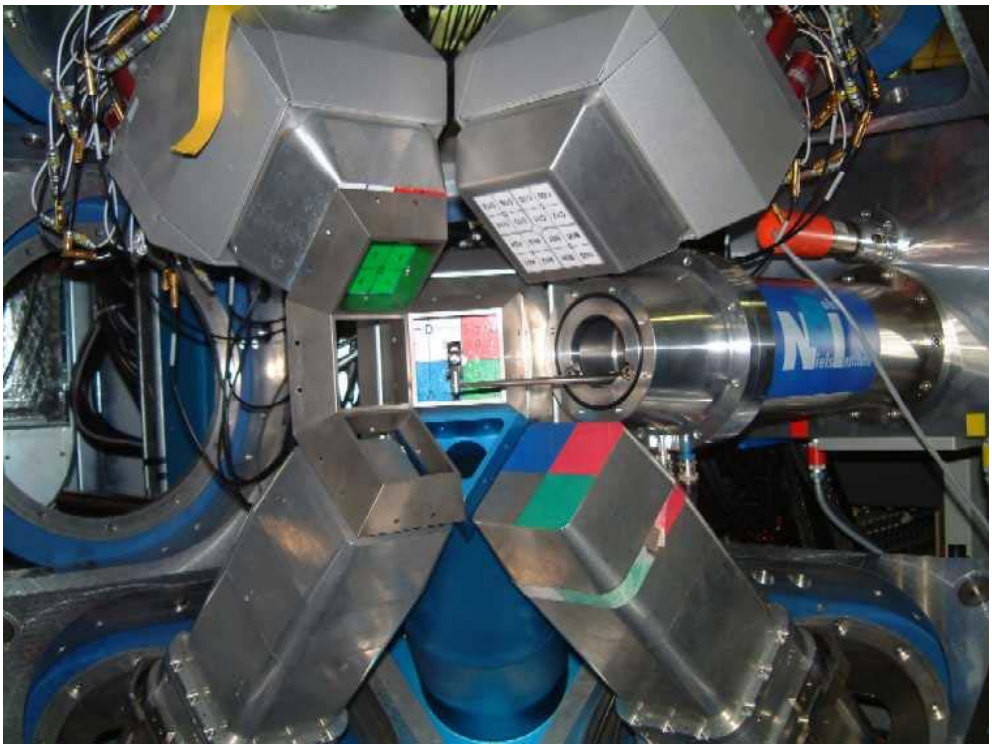

Figure I.1: picture of EXOGAM during the positioning of the detectors prior to an experiment. The two detectors at the top are EXOGAM Clovers equipped with the rear side elements of the escape suppression shield. The two small size detectors at the bottom are prototype segmented Clover detectors.

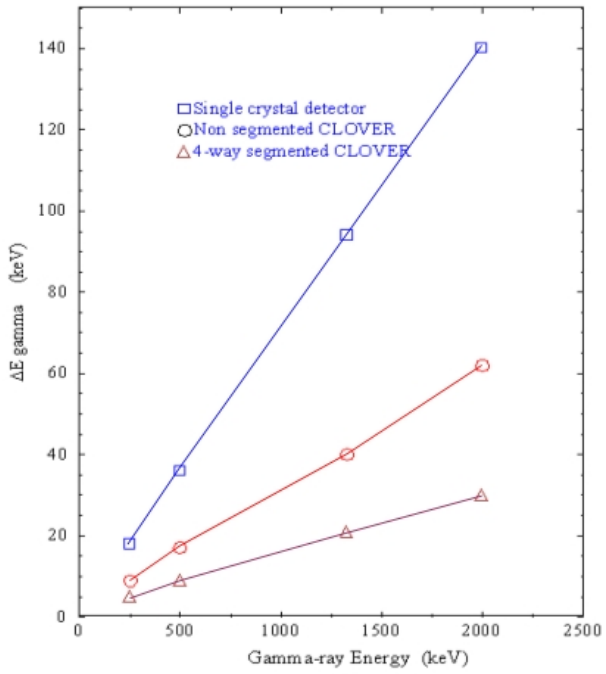

Figure I.2: Calculated energy resolutions ΔE as a function of γ-rays energy for a single crystal detector, a segmented and a non segmented Clover. The detectors are placed at 90° and 6 cm from a source moving with a velocity of v/c =7.5% (From [Sim00]).

Detector Configuration	**Photopeak efficiency (%)**		**PT (%)**	
	662 keV	**1.3 MeV**	**662 keV**	**1.3 MeV**
(a) EXOGAM (A)	28	20	57	47
(b) EXOGAM (B)	17	12	72	60
(c) Gamma-Cube	15	10	72	60

Table I.1: Calculated Photopeak efficiency and P/T for the EXOGAM array, taken from ref. [Sim00]. (a) For the closed packed configuration A, with 16 Clovers at 114 mm; (b) for the full shield configuration B, with 16 Clovers at 147 mm; (c) with the cube configuration in configuration A (full suppression shield) at 68 mm.

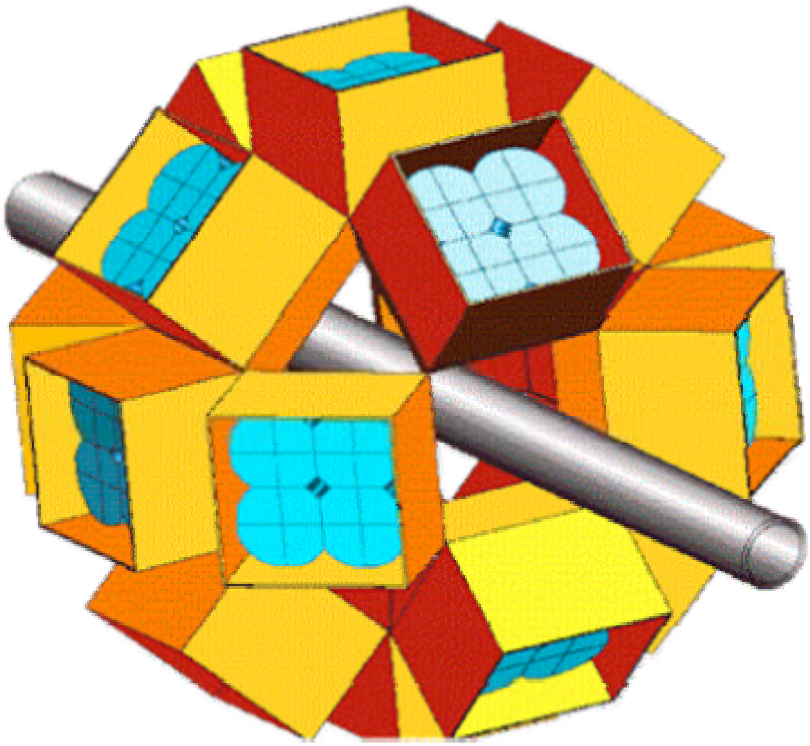

Figure I.3: EXOGAM spectrometer with 16 Clover detectors.

The reader should refer to [Sim00] for further simulated values of the EXOGAM performances.

2.3 Electronics

The electronics used for EXOGAM is based on VME and VXI (VME eXtension for Instrumentation) electronics. The data acquisition is based on several VXI modules to operate with the 16 Clover detectors:

- 8 EXOGAM Centre Contact (ECC) cards digitises the detectors core signals, and measures the energy in both 6 MeV and 20 MeV ranges with 14 bits ADCs;

- 16 VXI card (GOCCE) process the detectors segment signals and measure the energy in both 6 MeV and 20 MeV ranges;

- 4 Escape Suppression Shield (ESS) cards acquire the signals from the BGO shields. The signals from the ESS cards consist of the sum energy from the different shields elements[2].

EXOGAM has been design to enable the use of ancillary detectors, in order to select particular reaction channels. In September 2004, EXOGAM (11 HPGe detectors) was used in combination with the VAMOS spectrometer [VAM] and the CsI charged particle array DIAMANT.

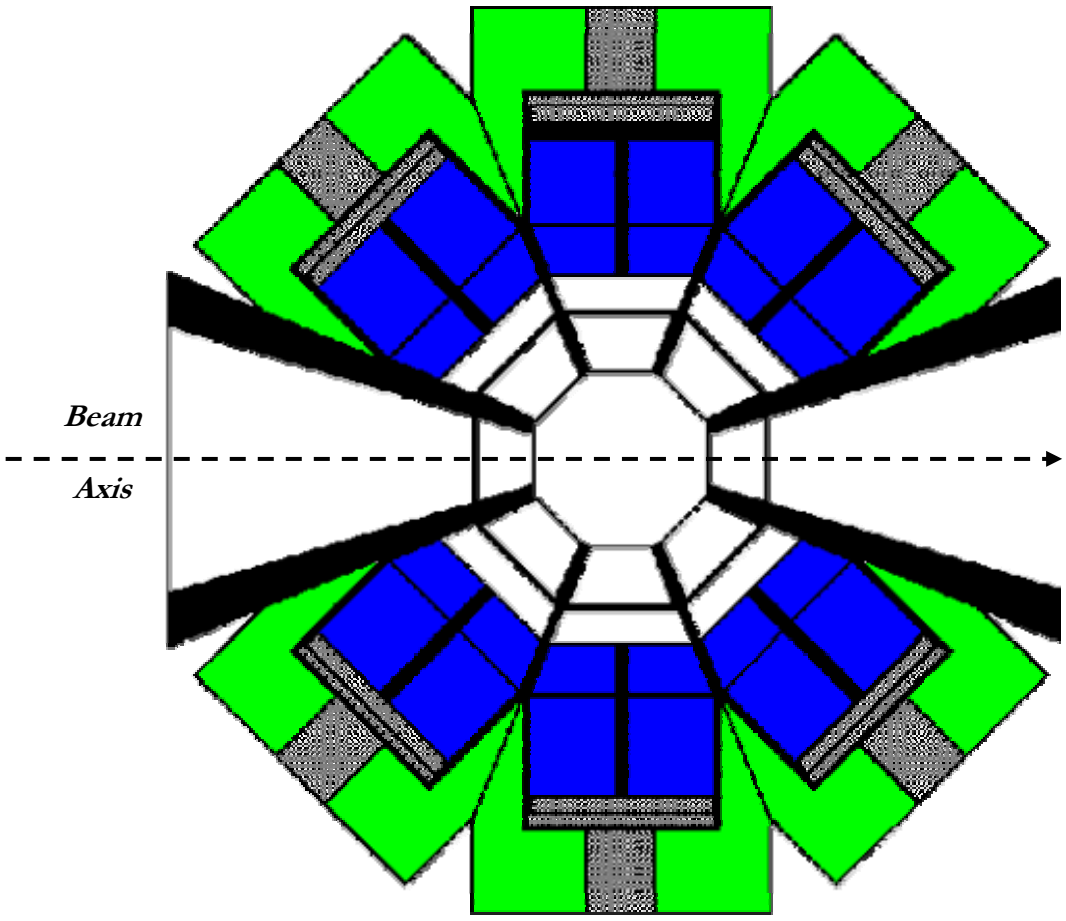

Figure I.4: Cross section through the EXOGAM array.

[2] The operation of the EXOGAM ESS shield is detailed in Chapter III.

Finally, EXOGAM is one of the first gamma spectrometer for which the Pulse Shape Analysis technique will be used with segmented HPGe detectors in order to improve the determination of the impact position of a γ-ray. The feasibility of such PSA techniques to improve the position resolution of segmented germanium detectors has been proved in earlier work [Des02]. However, the Clover detector was not designed for such application. The detailed characterisation of the detector volume and a thorough study of the detector response are necessary to understand the influence of the detector geometry on the signal characteristics, as well as the investigation of the response to different γ-ray energies; before trying to perform Pulse shape analysis.

3 Overview of the thesis

The present dissertation describes the characterisation of an EXOGAM Clover detector manufactured by ORTEC. Following the introduction, the basic principles and operation of HPGe detectors are presented in Chapter II. The EXOGAM clover detector is described in Chapter III. The general design and specifications are introduced; and the basic detector performances are presented. The characterisation methods, consisting of the Pulse Shape Analysis techniques and electric field simulation of HPGe detectors are discussed in Chapter IV.

The detailed description of the experimental work is given in Chapter V: the characterisation measurements and their implications on the analysis are presented along with general results. Chapter VI covers the analysis of the results from the characterisation measurements, and the comparison of the results with simulated data from the simulation developed at Institute of Subatomic Research (I.Re.S.) in Strasbourg. The last chapter concludes with a summary of important results from the characterisation of the Clover.

Chapter II

GAMMA SPECTROSCOPY WITH HPGE DETECTORS

Physical and electrical properties of Germanium

Radiation detection with **H**igh **P**urity **Ge**rmanium (HPGe) detectors

The following chapter summarises important concepts of the operation of HPGe detectors, and the physical processes leading to the generation of a measurable signal from the detectors.

1 Basic Semiconductors physics: Properties of Germanium

Germanium (Ge) crystals have been used for the past 30 years as gamma radiation detectors. The choice of this material for such application is due to its excellent energy resolution, relatively high Z compared to Silicon and the possibility to grow and operate crystals of large volume. Advances in technology allow the production of high granularity, large volume Ge detectors of complex geometries, with the possibility to build a complete Ge arrays around the reaction chambers such as the AGATA shell [Baz04].

1.1 Semiconductor materials

1.1.1 Crystallographic properties of Germanium

Germanium is a semiconductor element found in the Column IV of the Periodic Table. It crystallises as a diamond lattice structure. Such structure has a **F**ace **C**entred **C**ubic (FCC) based lattice with an extra atom added at (¼, ¼, ¼) of each base atom as illustrated in Figure II.1 (a). The properties of the crystal are dependent on the atomic arrangement in the different lattice planes. In order to relate the properties and phenomenon studied in this work, the crystallographic structure is defined using Miller indices [Sze02]. Figure II.1 (b) illustrates different planes and the value of their respective Miller indices.

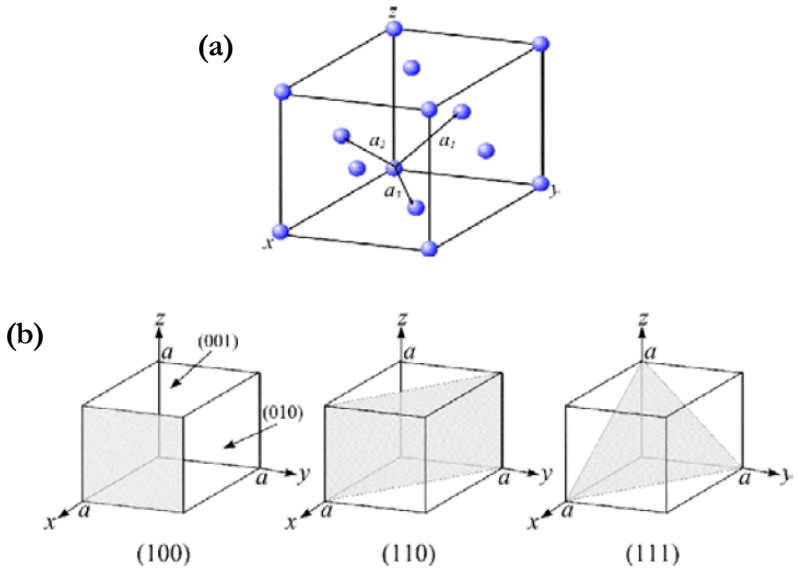

Figure II.1: (a) Crystal structure of Germanium. (b) The lattice planes are indicated by Miller indices.

1.1.2 Elements of band theory for electrical conduction in semiconductors

Solid materials can be classified according to their electrical properties. Insulators have a large resistivity (or small conductivity), while electric conductors have a small resistivity (and a high conductivity); semiconductor materials possess intermediate values of resistivity. When atoms are brought together to form a solid, the allowed energy states for atomic electrons becomes a succession of energy bands of allowed energy, where the electrons are accommodated in.

The *valence band* refers to the lowest energy range allowed below the Fermi energy. For semiconductors the valence band is full; therefore no electric current can be carried by valence electrons when an electric field is applied to a crystal. The *conduction band* is the first partially filled band, where empty energy states are available for electrons to carry an additional momentum in the direction of the field and take part in the electric current within the crystal.

The difference between insulators, metals and semiconductors is described in Figure II.2. The typical band structure of an insulator is represented in Figure II.2 (a): the uppermost filled (valence) band has a large energy separation from the empty conduction band (energy band gap ~ 4 eV) and cannot be overcome by thermal excitation of the electrons. The band configuration of intrinsic semiconductors[3] is shown in Figure II.2 (b). At low temperature, semiconductors behave like insulators; however the energy band gap is smaller: 1.12 eV for Si and 0.67 eV in Ge. As the temperature rises, electrons can be thermally excited from the valence band to the conduction band and can then respond to an applied field. Each time an electron transfers to the conduction band, it leaves an empty space in the valence band, referred to as a *hole*, which can also take part in the conduction. The case for metals is shown in Figure II.2 (c). The uppermost occupied band is partly filled, or alternatively the valence and conduction band overlap, allowing many electrons to respond to the external field.

The concentration of electrons n in the conduction band can be determined as the product of the density of states function $g(E)$ with the electron energy distribution (Fermi distribution) $f(E)$, respectively given in equation II.1 and II.2. The function $g(E)$ is given by

$$g(E) = \frac{4\pi}{h^3}\left(2m_e^*\right)^{\frac{3}{2}}\left(E - E_c\right)^{\frac{1}{2}} \qquad \text{(II.1)}$$

[3] intrinsic, as opposed to extrinsic or doped semiconductors, presented in section 1.1.3.

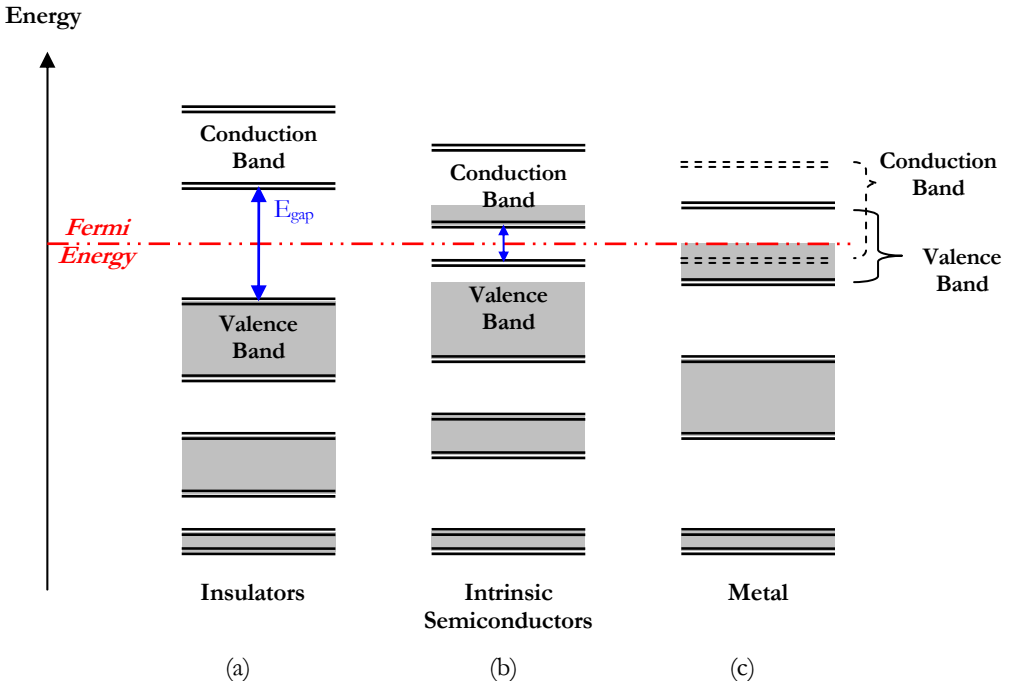

Figure II.2: Schematic description of the energy band classification of solids: (a) insulators, (b) semiconductors, (c) conductors or metals.

Where E_c is the bottom energy of the conduction band, h is Plank's constant and m_e^* is the effective mass of the electron in Germanium. The Fermi distribution $f(E)$ may be written as

$$f(E) = \frac{1}{\exp\left(\frac{E - E_F}{kT}\right) + 1} \tag{II.2}$$

where E_F is the Fermi energy, k is Boltzmann's constant and T is the absolute temperature.

Finally, the electron concentration per unit energy dE is given in equation (II.3)

$$n = \frac{4\pi}{h^3}\left(2m_e^*\right)^{\frac{3}{2}} \int_{E_{band}} \frac{\left(E - E_c\right)^{\frac{1}{2}}}{\exp\left(\frac{E - E_F}{kT}\right) + 1} dE \tag{II.3}$$

The electron concentration is then

$$n \approx 2\left(\frac{2\pi m_e^* kT}{h^2}\right)^{\frac{3}{2}} \exp\left[\frac{-E_C - E_F}{kT}\right] \tag{II.4}$$

Following the same reasoning, the hole concentration, p, in the valence band is given by

$$p \approx 2\left(\frac{2\pi m_h^* kT}{h^2}\right)^{\frac{3}{2}} \exp\left[\frac{E_V - E_F}{kT}\right] \tag{II.5}$$

where E_V is the top energy of the valence band and m_h^* is the effective mass of a hole in Germanium.

1.1.3 Doping of semiconductors

In intrinsic semiconductors, the law of mass action gives

$$np = n_i^2 \tag{II.6}$$

where n_i is the intrinsic electron concentration. This leads to the determination of the Fermi energy,

$$E_F = \frac{E_G}{2} + \frac{3kT}{4}\ln\left(\frac{m_h^*}{m_e^*}\right) \tag{II.7}$$

where, $E_G = E_C - E_V$ is the energy band gap. In Germanium, $E_G = 0.67$ eV, $m_h^* = 0.56m_e$ and $m_e^* = 1.1m_e$, for $T = 75$K, one calculates $E_F \approx 0.328$ eV, which is very close to ½ E_G.

Extrinsic or doped semiconductors are produced by the introduction of foreign atoms as substitution impurities in the crystal lattice. The semiconductor is said to be of n-type when the electronic configuration of the impurity atoms has one or more extra valence electron (donor impurities), e.g. the introduction of Group V atoms such as Phosphorous. In this case four electrons form covalent bounds with neighbouring atoms while the extra electron is weakly bound to the parent impurity atom. The electron sits in an energy level just below the conduction band, and a small amount of thermal energy is required to produce additional negative charge carriers.

In the same way, p-type semiconductors are created by the insertion of Group III atoms (for example Lithium and Boron) in the lattice. Only three electrons form a covalent bond with neighbouring atoms (acceptor impurities), and impurity atoms may capture an electron from a nearby Germanium atom thus creating a hole. In this case, available energy levels lie in the gap just above the valence band. Holes are created when electrons jump into these empty levels. The band structure for doped semiconductors is illustrated in Figure II.3.

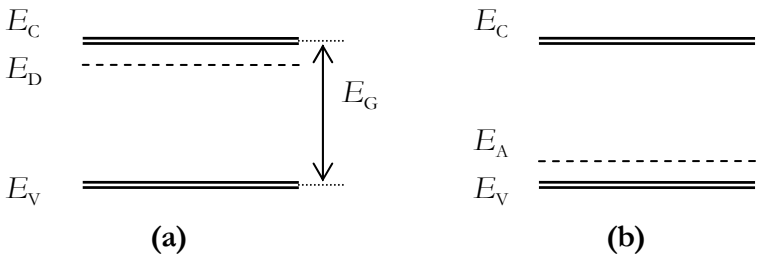

Figure II.3: schematic illustration of band structure for doped semiconductors: (a) n-type, (b) p-type.

1.2 Semiconductor Junction

Four factors govern the distribution and flow of charge in a semiconductor:

Generation. Following the interaction of a γ-ray in the Ge diode, electrons in the valence band receive sufficient energy to be promoted to the conduction band. Electron-hole pairs are created.

Recombination. Germanium is an indirect semiconductor: recombination relies on energy levels lying in the forbidden energy gap. This process occurs at recombination centres arising from the presence defects in the crystallographic structure or impurity atoms. Typically, a recombination centre traps a hole from the valence band, an electron in the conduction band can then fall into the trapped hole and recombination takes place. Such a process results in a loss of electron-hole pairs.

Diffusion. A gradient in the charge carrier concentration induces the diffusion of the species towards regions of lower concentration. The diffusion current density *J* is given by Fick's law. In one dimension:

$$J_{e,h} = -D_{e,h} \frac{\partial(n, p)}{\partial x} \tag{II.8}$$

where $D_{e,h}$ is the diffusion constant for electrons/holes and $\partial(n, p)/\partial x$. is the carrier concentration gradient.

Drift: In presence of an electric field, the drift current density is given by

$$J = e\left(n\mu_n + p\mu_p\right)E \tag{II.9}$$

where n and p are the concentration of electrons in the conduction band and holes in the valence band, with μ_n and μ_p their respective mobility.

1.2.1 The semiconductor junction

For a semiconductor material doped with different type of impurities to produce n-type and p-type regions, with concentrations of donor N_D and acceptors N_A, the concentration gradient results in the diffusion of the charge species towards regions of lower concentrations. The holes diffuse from the p-type region to the n-type region, and electrons diffuse from the n-type region to the p-type region of the material creating a p-n junction. The diffusion results in negatively charged acceptors in the p-type region and positively charged donors in the n-type region, giving rise to an electric field acting from the n-type to p-type regions. A dynamic equilibrium is established between the diffusion current and the drift current, preventing the flow of charge carriers between the two doped regions. The electric field in the transition region creates a space charge region depleted of charge carriers. Figure II.4 describes the operation of a p-n junction.

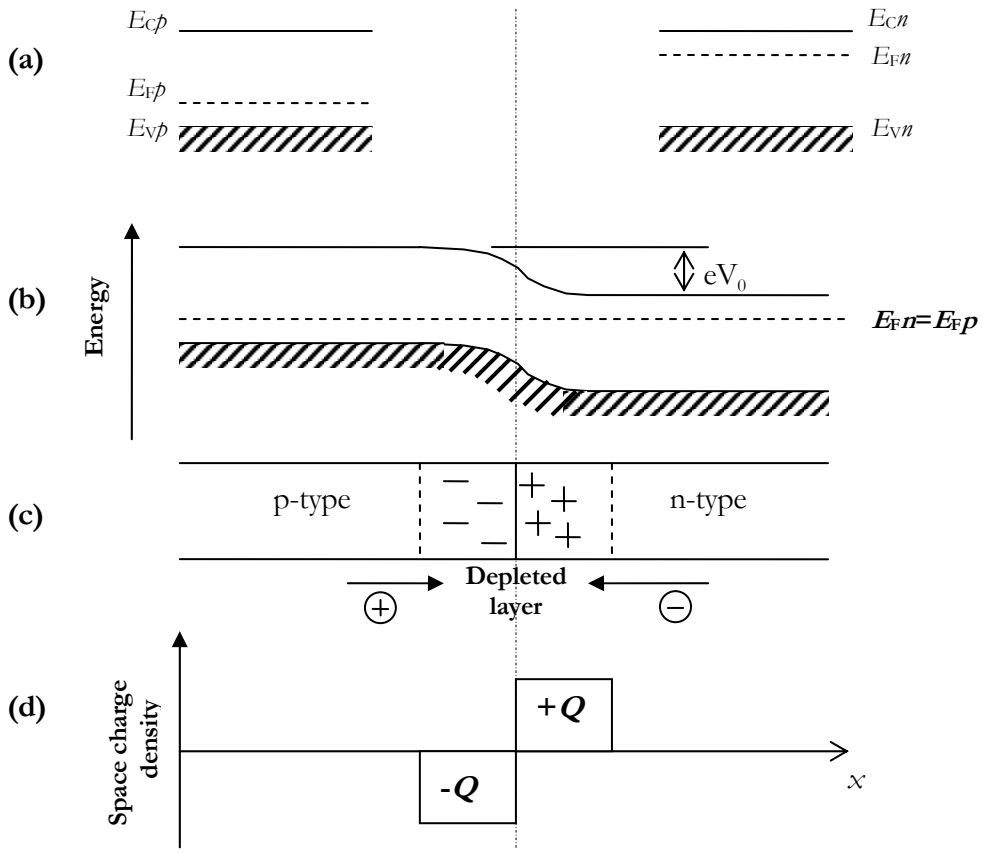

Figure II.4: Schematic description of an abrupt (ideal) p-n junction in equilibrium. (a) represents the band structure of p-type and n-type doped semiconductors, E_F is the Fermi level, E_C is the bottom of the conduction band and E_V is the top of the valence band; (b) junction in equilibrium: a potential gradient is induced in the depleted region, V_0 is the contact potential; (c) schematic of the p-n junction illustrating the diffusion direction of the charge carriers in the junction; (d) space charge density in the depleted region.

1.2.2 The diode

The passage of ionising radiation through a semiconductor material generates electron/hole pairs. However, the electric field across the depleted region is too weak to separate both charges and they quickly recombine. In order to use semiconductors as radiation detectors, a reverse bias must be applied to the material in order to increase the width of the depleted region, and separate the charge carriers before recombination occurs. Typically, values of a few thousands of volts are required to fully deplete a coaxial HPGe crystal of 6 cm diameter by 9 cm length. The differences in applied bias voltage depend on the impurity concentration of the crystals.

The width of the depleted region is given as a function of the applied bias potential V [SB00]

$$W = \left[\frac{2\varepsilon(V_0 - V)}{q} \left(\frac{N_A + N_D}{N_A N_D} \right) \right]^{1/2} \tag{II.10}$$

The electric potential $\varphi(\vec{r})$ in the depleted region is calculated by solving Poisson equation

$$\nabla^2 \varphi(\vec{r}) = -\frac{\rho(\vec{r})}{\varepsilon} \tag{II.11}$$

where ρ is the density of charge within the junction and $\varepsilon=\varepsilon_0\varepsilon_r$; ε_r being the dielectric constant of germanium (ε_r = 16). The space charge density is given by the impurity concentration in the depleted region $\rho = e(N_D - N_A)$.

The electric field in the depleted region can then be calculated from the potential

$$E = -\frac{d\varphi}{dr} \tag{II.12}$$

For a simple coaxial geometry, the electric field can be calculated using the cylindrical capacitor formula [Kno00]

$$E(r) = -\frac{\rho}{2\varepsilon} + \frac{V + \left(\frac{\rho}{4\varepsilon} \left(r_2^{\,2} - r_1^{\,2} \right) \right)}{r \ln \frac{r_2}{r_1}} \tag{II.13}$$

where $\rho(r)$ is the space charge density in the depleted volume, V is the applied reverse bias, and r_1 and r_2 are the respective internal and external radii of the cylinder. For complex detector geometries, analytic formulae are not valid and the use of finite difference methods is required to solve Equations II.11 and II.12.

2 Radiation detection with HPGe Detectors

2.1 Interaction of gamma-rays in Germanium

2.1.1 Main interaction processes

In Germanium, γ-rays interact primarily by three processes:

- Photoelectric absorption. The incident photon of energy E_γ is absorbed by an atomic electron. The photoelectron is ionised, and its kinetic energy is given by

$$E = E_\gamma - E_B \tag{II.14}$$

where E_B is the binding energy of the electron.

- Compton scattering. The incident photon is scattered by an atomic electron, which receives part of the photon energy during the interaction. The relationship between the incident photon energy E_γ and the scattered photon energy $E_{\gamma'}$ is given by the Compton scattering formula:

$$E_{\gamma'} = \frac{E_\gamma}{1 - \frac{E_\gamma}{m_0 c^2}(1 - \cos\theta)} \tag{II.15}$$

where θ is the scattering angle between the incident and scattered photon directions. The energy transferred to the electron during the scattering process is given by

$$E = E_\gamma - E_{\gamma'} - E_B\,. \tag{II.16}$$

In general, $E_B << E$ and is therefore neglected in the calculation of the energy transferred to the electron.

The angular distribution of scattered γ-rays is given by the Klein-Nishina formula [Kno00]:

$$\frac{d\sigma}{d\Omega} = Z{r_0}^2 \left(\frac{1}{1+\alpha(1-\cos\theta)}\right)^2 \left(\frac{1+\cos^2\theta}{2}\right)\left(1 + \frac{\alpha^2(1-\cos\theta)^2}{(1+\cos^2\theta)[1+\alpha(1-\cos\theta)]}\right) \tag{II.17}$$

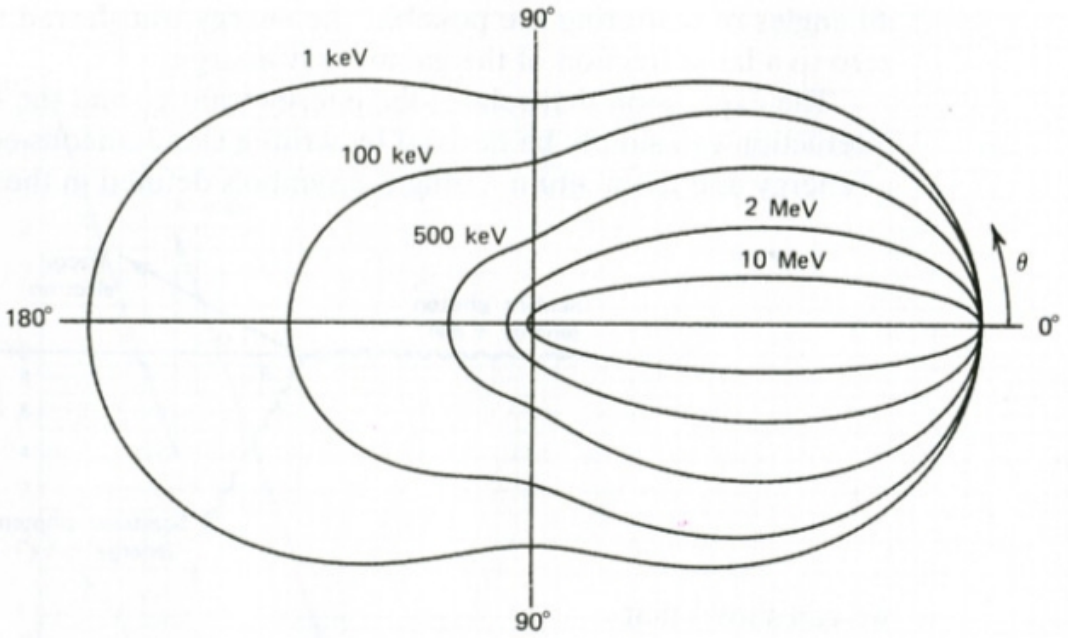

Figure II.5: Polar plot showing the intensity profile of scattering for γ-rays of different energies, incident from the left (from [Kno00]).

where $\alpha = E_\gamma / m_0 c^2$ and r_0 is the classical electron radius (2.817×10^{-13}cm). Figure II.5 shows the angular distribution of Compton scattered γ-rays with incidence from the left. Forward scattering probability increases with γ-rays energies.

- Pair production. If the energy of the γ-ray exceeds twice the rest mass of the electron (1.02 MeV), the photon can be transformed into an electron-positron pair in the Coulomb field of the nucleus. The pair production cross section is however very low for energies up to a few MeV.

2.1.2 Charge carrier generation in Germanium

Following an interaction in the detector, the photoelectron loses energy in the material by impact ionisation and emission of radiation (Bremsstrahlung) from scattering in the field of the nucleus:

$$\left(\frac{dE}{dx}\right)_{tot} = \left(\frac{dE}{dx}\right)_{coll} + \left(\frac{dE}{dx}\right)_{rad} \qquad \text{(II.18)}$$

The energy loss by impact ionisation is given by [Leo94a]

$$-\left(\frac{dE}{dx}\right)_{coll} = 2\pi N_a r_0^{\,2} m_e c^2 \rho \frac{Z}{A}\frac{1}{\beta^2}\left[\ln\frac{\tau^2(\tau+2)}{2\left(I/m_e c^2\right)^2} + P(\tau) - \delta - 2\frac{C}{Z}\right] \tag{II.19}$$

where N_a is Avogadro's number (6.022mol^{-1}), r_0 the classical electron radius, ρ, Z, and A are the respective density, atomic number and atomic weight of the absorbing material; β is the v/c of the incident electron, and τ is the kinetic energy of the incident electron in $m_e c^2$. δ and C are factors accounting for the density and shell correction. $P(\tau)$ is a function of the energy of the incident electron:

$$P(\tau) = 1 - \beta^2 + \frac{\frac{\tau^2}{8} - (2\tau+1)\ln 2}{(\tau+1)^2} \tag{II.20}$$

Ionisation is the main energy loss process at low energies. At high energies the energy loss by Bremsstrahlung becomes comparable to the collision-ionisation process. The contribution of Bremsstrahlung [Leo94] to the energy loss is given by

$$-\left(\frac{dE}{dx}\right)_{rad} = NE_0 4Z^2 r_e^{\,2}\alpha\left(\ln\frac{2E_0}{m_e c^2} - \frac{1}{3} - f(Z)\right) \tag{II.21}$$

where α = 1/137, E_0 is the initial energy of the electron and $f(Z)$ is a correction factor accounting for the Coulomb interaction of the electron in the field of the nucleus.

The photoelectron of energy E, loses its energy in the material by the generation of N electron/hole pairs, given by

$$N = \frac{E}{I} \tag{II.22}$$

where I is the average ionisation energy needed to free an electron, it accounts for the transfer of energy to the material by heat (lattice vibrations). Therefore, I is a statistical value and is larger than the energy band gap. The process of charge carrier generation is not independent in

semiconductors. A correction parameter is therefore introduced in order to account for the statistical variance:

$$\Delta N = \sqrt{FN} \tag{II.23}$$

where F is the Fano factor [Kno00]. F tends to 1 when the charge carriers generation follows Poisson statistics; F ≈ 0.06 for Germanium at 77 K. Therefore, the variance in the electron/hole pair creation is given by

$$\Delta N = \sqrt{F\frac{E}{I}}\,. \tag{II.24}$$

2.2 Signals generation

2.2.1 Generation of induced current

The strong electric field in the depleted region separates the charge clouds before they recombine. The drift of the charges towards their collecting contact induce a current flow through the contacts. The value of the induced current can be calculated with Ramo's theorem [Ram39] for a planar electrode configuration

$$i(t) = q\frac{\varepsilon(x,t)v_d(x,t)}{\psi} \tag{II.25}$$

where q is the charge of the carrier, ε is the intensity of the electric field at the position x and time t, v_d is the drift velocity of the charge and ψ is the electric potential at the electrode.

As introduced by [Gatt82] and described in [Rad88], an extension to Ramo's theorem is the Green's *reciprocity theorem* which allows to determine the induced charge on electrodes from a multi electrode device. Following a γ-ray interaction generating Q_0 charges between the electrodes of a Ge detector, the current induced on the contacts by the moving charges is given by

$$i(t) = Q_0 \cdot v(\vec{r}(t)) \cdot E_w(\vec{r}(t)) \tag{II.26}$$

Where v is the drift velocity of the charges, and E_w is the weighting field. E_w is a parameter which measures the capacitive coupling between the moving charge Q and the sensing

electrode, and depends uniquely on the detector geometry. The weighting field derives from the weighting potential *u*, determined by solving Laplace's equation for a charge density $\rho = 0$:

$$\nabla^2 u = 0 \tag{II.27}$$

and applying a potential of 1V to the electrode of interest and 0V to any other electrodes.

2.2.2 Anisotropic drift velocity in Germanium

The drift velocity of the charges is proportional to the magnitude of the electric field as

$$\vec{v}_{e,h}(r) = \mu_{e,h}\vec{E}(r) \tag{II.28}$$

where $\mu_{e,h}$ is the mobility of the electrons and holes as used in Equation II.4.

The mobility of the charge carriers depends on the direction of the electric field relative to the crystallographic directions. It is a direct effect of the band structure of germanium, presented in Figure II.6: the conduction band possesses several minima at different crystallographic directions. The band structure of germanium and the anisotropic effect have been studied theoretically [Rei62, Sas58] and experimentally [Nat63, Ott75, Reg77]. The minimum of the conduction band lie along the <111> crystallographic direction, while the maximum of the valence band is along the <100> direction. The minimum energy in the conduction band is given by

$$E(\vec{k}) = \frac{\hbar}{2}\left(\frac{k_x^{\,2} + k_y^{\,2}}{m_{\parallel}} + \frac{k_z^{\,2}}{m_{\perp}}\right) \tag{II.29}$$

where k_x, k_y and k_z are the *x*, *y*, *z* components of the wave vector *k*; $m_{||}$ and $m_{\perp}$ are the longitudinal and transversal effective masses. The minimum energy surfaces have therefore an ellipsoidal shape along the <111> and <100> equivalent directions.

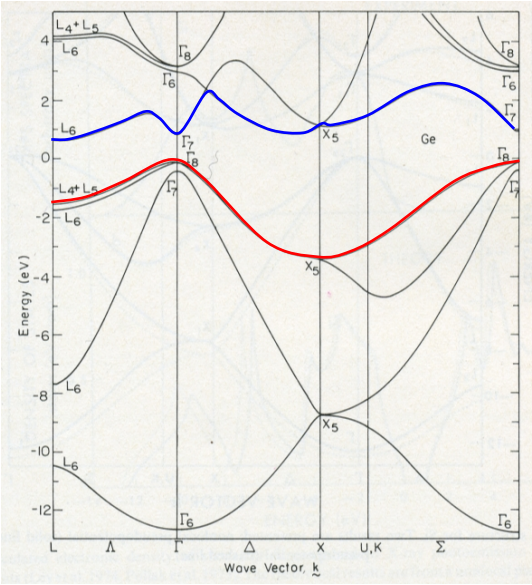

Figure II.6: Energy band structure of germanium in k space. The minimum energy of the conduction band is highlighted in blue; the maximum of the valence band (in red) is taken as the zero reference. The directions L, Γ, and X represent the <111>, <110> and <100> directions respectively. The absolute minimum of the conduction band lies along the L direction (from [Mos82a]).

The difference in energy minima is responsible for the anisotropic mobility in germanium. Figure II.7 and Figure II.8 present calculated drift velocities as a function of the electric field magnitude and the longitudinal anisotropy angle between the drift velocity and the electric field direction, as a function of the electric field orientation for electrons, as given by [Mih00].

At relatively high electric field, the anisotropic behaviour is observed: Figure II.7 shows that the drift velocity is maximum along the <100> directions, and minimum along the <111> direction and reaches a saturation value for $E \sim 10^3$ V/cm. On Figure II.8, the deviation between the electric field and the drift direction of the electrons is maximum at 42° and 66°.

It is clear that the anisotropy is an important parameter to be taken into careful consideration in the design of segmented detectors. Figure II.7 shows that the magnitude of the drift velocity varies with field strength for $E < 10^3$ V/cm. For such field intensities, the collection time will depend on the position of interaction, in the case of detectors with non homogeneous field configurations. From Figure II.8, it is clear that a bad segmentation of the detector could lead to an incorrect determination of the position of interaction.

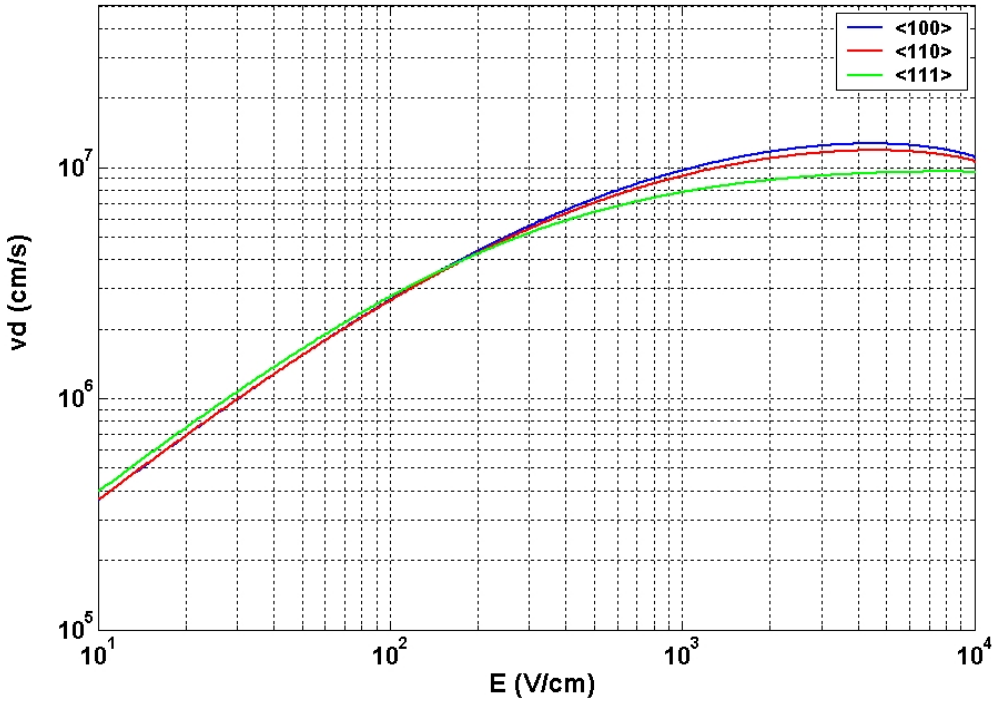

Figure II.7: Calculated dependence between the drift velocity and the electric field in Germanium along the three main <111>, <100> and <110> directions.

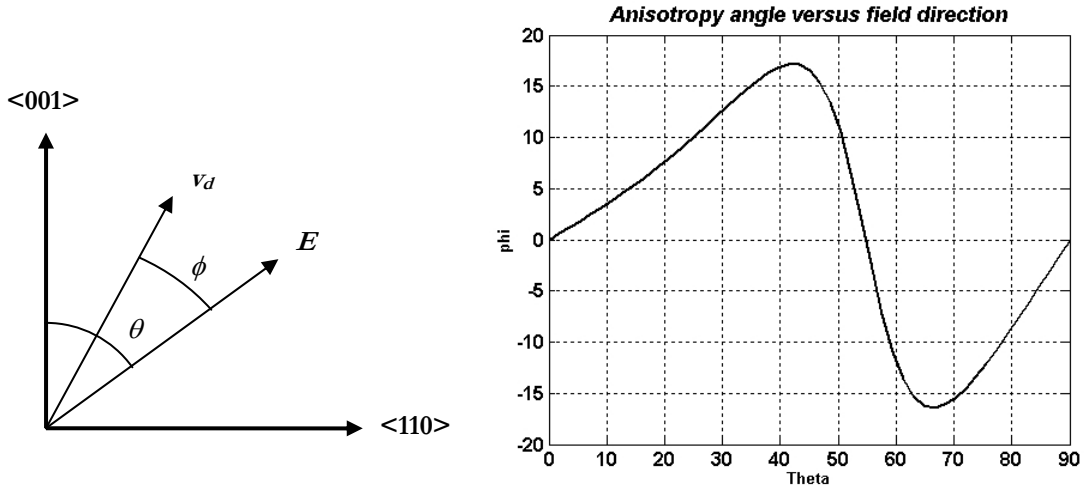

Figure II.8: Calculated longitudinal anisotropy angle ϕ versus electric field direction relative to the crystallographic directions.

2.3 Energy resolution of HPGe

2.3.1 Intrinsic energy resolution

The energy resolution of a detector is defined as the full width at half maximum of the spectral peak (FWHM), assuming that the peak has a Gaussian shape and no background or continuum contribution is superimposed on the peak. The intrinsic energy resolution of a Germanium detector is determined by the contribution of three factors:

$$(\Delta E_i)^2 = (\Delta E_D)^2 + (\Delta E_X)^2 + (\Delta E_E)^2 \quad \text{(II.30)}$$

- ΔE_D is the inherent statistical fluctuation in the number of charge carriers created. This is given by

$$\Delta E_i = 2.35\, I\, \Delta N \quad \text{(II.31)}$$

where I is the average ionisation energy are required to create an electron/hole pair, and ΔN is the variance for electron/hole generation process, given in Equation II.24.

- ΔE_X is due to incomplete charge collection. This effect is important in large volume detectors and is discussed in Chapter V.

- ΔE_E is the electronic noise, inherent to all the electronic components in the acquisition chain after the detector.

Typically, the intrinsic energy resolution of HPGe detectors is ~2 keV at 1MeV.

2.3.2 Doppler broadening

For a nucleus travelling at $\beta = v/c$, the observed energy E_γ, in the laboratory reference system of a γ-ray emitted by a nucleus, is subject to a Doppler shift according to

$$E_\gamma = E_{\gamma 0} \frac{\sqrt{1-\beta^2}}{1-\beta\cos\theta\gamma} \quad \text{(II.32)}$$

where $E_{\gamma 0}$ is the energy of the gamma ray in the rest reference system of the nucleus and θ_γ is the emission angle relative to the trajectory of the nucleus in the laboratory reference system.

Thus, for a given opening angle $\Delta\theta_\gamma$, the observed gamma energy shows an energy broadening ΔE_γ according to

$$\frac{\Delta E_\gamma}{E_\gamma} = \frac{\beta \sin\theta\gamma}{1-\beta\cos\theta\gamma}\Delta\theta\gamma \tag{II.33}$$

The Doppler broadening is maximum for $\theta_\gamma = 90°$.

The overall energy resolution of germanium detectors is then given by the sum of the four contributions mentioned above

$$(\Delta E)^2 = (\Delta E_D)^2 + (\Delta E_X)^2 + (\Delta E_E)^2 + (\Delta E_\gamma)^2 \tag{II.34}$$

2.4 Signal amplification

The signals from germanium detectors are typically processed by charge sensitive preamplifiers. A simplified schematic of a resistive feedback preamplifier is presented in Figure II.9. The amplification stage is based on the use of a Field Effect Transistor (FET). The detector input current $i(t)$ is integrated through a capacitor C_f. This produces a charge pulse $Q(t)$ whose rising time depends on the collection time of the charges in the detector, and whose magnitude is proportional to the detected energy. The capacitor is then discharged through the feedback resistance R_f., the charge pulse decays then exponentially at a rate given by the time constant $\tau = R_f C_f$.

In a reverse biased germanium junction, the random generation of electron/hole pairs due to thermal excitation in the lattice induce a leakage current flowing across the depleted region. An important source of noise is the fluctuation of the leakage. For this reason, HPGe detectors must be operated at cryogenic temperatures, typically of liquid Nitrogen (77 K).

Electronic components in the preamplifier are sources of electronic noise. The main contributor is the FET: random fluctuations in the Gate – Source current and thermal noise in the FET are sources of parallel and serial electronic noise.

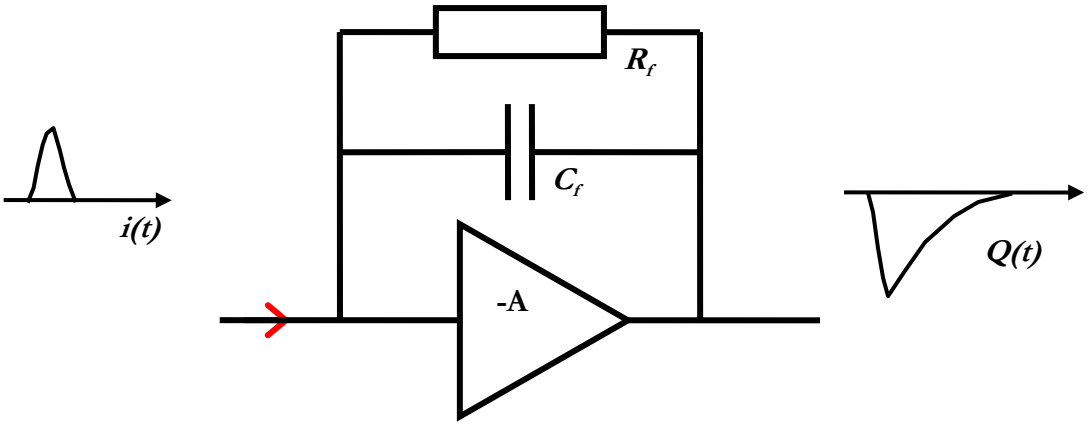

Figure II.9: Simplified schematic illustration of the feedback resistive preamplifier. The input current i(t) is integrated through the feedback capacitor C_f. The capacitor discharges via the feedback resistance R_f.

Chapter III

THE EXOGAM CLOVER HPGE DETECTOR

Recent detectors developments

EXOGAM Clover specifications

After the introduction of The EXOGAM array and the basic principles of γ radiation detection with semiconductor detectors, the following chapter presents some important recent developments in **H**igh **P**urity **Ge**rmanium (HPGe) detectors which led to the design of the composite EXOGAM **E**scape **S**uppressed **S**pectrometer (ESS). Relevant aspects of the design and specifications of the EXOGAM Clover detector are described along with the performance of the Clover 06 module manufactured by ORTEC.

1 Recent HPGe developments

1.1 Composite HPGe detectors

Composite detectors, consisting of several Ge crystals assembled in a single cryostat, were introduced to overcome the Doppler broadening obtained in large single crystal detectors. The result is a large volume detector with a higher granularity. The advantages offered by composite detectors compared to previous single crystal detectors are:

- **Improved efficiency.** The increase in efficiency comes from the extra volume available for the detection of gamma-rays, as well as from the larger solid angle coverage due to the close packing of the crystals.

- **Improved granularity.** Another advantage of composite detectors is the further enhancement of the peak to total ratio (PT). The presence of **E**scape **S**uppressed **S**pectrometer (ESS) shields initially improved considerably the quality of energy spectra. With the use of composite detectors the spectrum quality is raised to a higher level. The increased granularity provides a more precise knowledge of the photon interaction position, thus leading to a better correction of Doppler broadening. It also enables the possibility of adding the energy of multiple scatters, shared between different crystals, and hence the recovery of **F**ull **E**nergy **E**vents (FEE). The improved granularity also facilitates Compton polarisation measurements [Jon95].

Composite detectors can then be operated in two different modes:

- **Direct mode.** When the detector is operated in direct mode, the individual modules of the detector are read out independently from each other. Events coming from the scattering of an initial gamma-ray detected in different crystals are considered as separate events; therefore they are lost in the Compton background.

- **Total or "Add-Back" mode.** The energy of the initial gamma-ray is recovered by the correlation of scattering events occurring in temporal coincidence. The partial energies are summed, and the total energy then contributes to the intensity of the Full Energy Peak (FEP). This Add-back of energies provides a significant improvement of PT and efficiency [Sim00].

Two different designs of composite HPGe detectors have been developed. The Clover detector, developed for the EUROGAM phase II array [Beck92] is composed of four close-ended coaxial HPGe crystals housed in the same cryostat. Each crystal consists of a n-type Germanium diode of 70 mm long by 50 mm diameter. Additionally, each crystal is tapered along 2 adjacent faces at an angle of 7.1 degrees starting from the middle of the face, resulting in an almost square front face; the shape of a EUROGAM Clover crystal is presented in Figure III.1. Results from the investigation and simulation of the main characteristics of the EUROGAM Clover detector are presented in [Duc99].

The composite Cluster detector [Ebe96, Wil96], which was first used in the phase III of EUROBALL, consists of a close packed arrangement of 7 individual aluminium capsules, each containing a coaxial HPGe crystal with ~ 60% relative efficiency. The encapsulation of the germanium crystal in a separate environment was thought of, in order to facilitate the maintenance of the detector in case of failure.

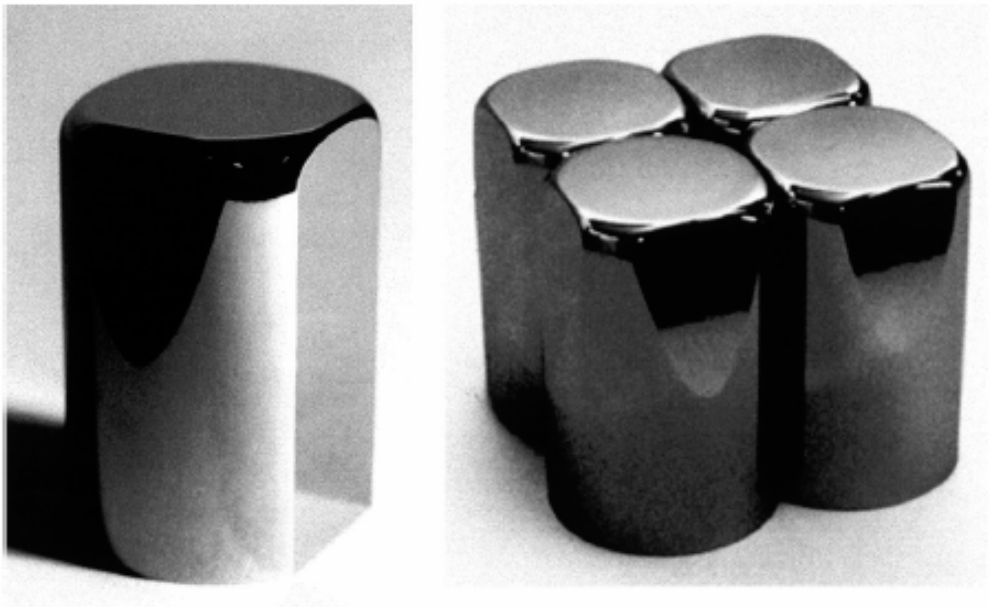

Figure III.1: Crystals from the EUROGAM Clover detector. Single Germanium Crystal (left), and four crystals positioned in the Clover-like configuration (right). Note the square front face of each individual crystal (Pictures taken from [Duc99]).

1.2 Segmented Clover detectors

1.2.1 Detector segmentation

From the beginning of the 1990s, technological advancement allowed the manufacture of reverse bias *n*-type detectors with segmented contacts [San99, San03], and made the concept of **G**amma-**R**ay **T**racking (GRT) a reality, not only for nuclear physics experiments [Lee04, Baz04] but also for astrophysics, medical imaging and national security applications. The processing of the outer contact by ion implantation allows very sharp doping profiles to be obtained and reduces the thickness of dead material at the cathode to a typical thickness less than 0.6μm. The segmentation of the cathode is obtained by photolithographic methods, resulting in a segment separation of the order of 150μm. The anode is doped *n*+ by atomic diffusion of Lithium impurities, resulting in a contact thickness of ~700 μm. Several highly segmented HPGe detectors have now been produced. The first coaxial segmented detector was designed for the GAMMASPHERE [Lee90] array. It consists of an electrical two fold D-shaped segmentation of its Boron implanted outer electrode [Shm98].

Further technological advances followed:

- The PT6X2 prototype [San99, San03] was the first HPGe module with two types of segmentation: photolithographic processing of the Boron outer contact and a physical cut of the inner Lithium diffused contact.

- The first encapsulated segmented HPGe detector was produced for the MINIBALL [Ebe01, Rei02] array, and consisted of a semi hexagonal tapered crystal with a 6 fold segmentation of the Boron outer contact.

- The **G**amma-**R**ay **E**nergy **T**racking **A**rray (GRETA) prototype [Vet00] was the first high fold segmented HPGe detector (with 36 segments) to be tested and calibrated for position with digital PSA methods.

The 24 fold segmented TIGRE detector [Des02] (manufactured by ORTEC) and the 6X6 (CANBERRA EURYSIS), a 36 fold segmented HPGe detector [Pea02, Dob03], were the first prototypes to be available for tests and characterisation at the University of Liverpool. The TIGRE and 6X6 prototypes were developed for the purpose of the **UK G**amma-**R**ay **T**racking with Pulse Shape Analysis project (UK-GRT) [Laz04]. This project was a collaboration between the University of Liverpool, the University of Surrey and CCLRC

Daresbury Laboratory. The aim was to prove the feasibility of gamma-ray tracking: this required the enhanced position determination provided by Pulse Shape Analysis (PSA) with highly segmented HPGe detectors. The project yielded advances in PSA and GRT algorithms, along with the development of a dedicated scanning detector system and a new type of acquisition electronics; both will be presented in detail in Chapter V.

The next modules to be characterised with the Liverpool system were a hexagonal large volume 36-fold segmented tapered canister, with a geometry very similar to the AGATA segmented HPGe crystal (the analysis is currently being done at the University of Manchester); and finally the prototype AGATA/GRETINA capsule. The measurements and analysis of the results from the AGATA prototype is currently ongoing [Nel05].

1.2.2 Composite segmented detectors

The first segmented composite detectors were the MINIBALL Cluster [Ebe01] and the EUROBALL segmented Clover. In order to cover a maximum solid angle of 4π, the MINIBALL array consists of a spherical arrangement of detectors containing 3 capsules, each of which encloses a semi hexagonal tapered crystal with a 6-fold radial segmentation of its outer contact [Gun00]. A prototype of segmented Clover detector was then built in order to test the performance of the future constituent of the EXOGAM array. The segmentation pattern of the Clover divided each crystal in quadrants of equal volume, resulting in a 16 fold segmented composite detector. However, the outputs of adjacent contacts were connected together, which provided 9 output signals. The performance of a segmented EUROBALL Clover is reported in [The98], and results of the first investigations are presented in [She99].

2 The EXOGAM CLOVER detector

2.1 Array performance and gamma-ray detector design considerations

The EXOGAM spectrometer consists of up to 16 Compton suppressed Clover detectors placed around the target chamber. The initial Clover design required several modifications in order to accommodate the flexible configuration of the array. The high efficiency required for EXOGAM could only be achieved by the use of detectors with large volume HPGe crystals. Composite Clover detectors provide large detection volume, combined with the excellent intrinsic energy resolution of Germanium. The segmentation of the crystals was then indispensable to obtain the high granularity that would maintain the good energy resolution and correct the γ-ray peaks for Doppler broadening. The PT had to be improved by the use of

Compton suppressors and the systematic operation of the composite detectors in total mode. Finally, the segmentation was also introduced to further improve the Doppler correction by using digital pulse processing techniques in order to find the location of a γ-ray interaction.

2.2 The EXOGAM Escape Suppressed Spectrometer (ESS) shield

The modularity of EXOGAM imposed a multi-element design on the ESS shield, as shown in Figure III.2 (a) and Figure III.2 (b). The shield consists of three different modules:

- a rear side shield, made of several **B**ismuth **G**ermanate **O**xide crystals (BGO);
- a side shield, made of BGO;
- a back catcher, made of Cesium Iodide CsI(Tl) crystals.

The use of CsI as a back catcher material element was motivated by the possibility to place a material less dense than BGO that would occupy a larger volume, keeping the same performance, and reducing the overall cost of each ESS. The front collimator is used in order to remove false veto events that contribute from direct radiation hitting the ESS shield, as well as to minimise cross scattering between detectors within the array.

The shield can be operated in two configurations: using the back catcher and the rear side modules enables the close packing of the detectors close to the target[4], or by adding the side BGO elements[5] [Sim00]. In EXOGAM, the output of the photomultipliers tubes of the ESS shields are coupled in quadrants as shown in Figure III.3. In this way, events in coincidence between a shield quadrant and its crystal are vetoed, leaving the possibility to record unsuppressed events occurring in other crystals from the same detector.

[4] Configuration A described in Chapter I

[5] Configuration B described in Chapter I.

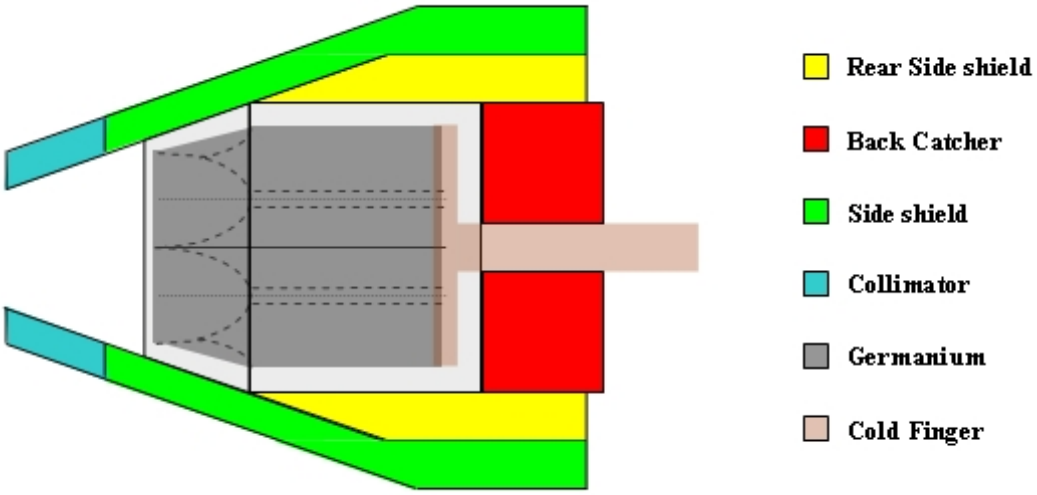

Figure III.2: (a) Schematic illustration of the EXOGAM Escape Suppressed Spectrometer (ESS). The Compton suppression shield is composed of three elements: the *rear side* shields and *back catchers* are used in the closed packed configuration of EXOGAM. The *side* shield is added when the detectors are pushed away from the target. The *collimator* improves the performances by reducing cross scattering between detectors and preventing the radiation from directly hitting the BGO elements.

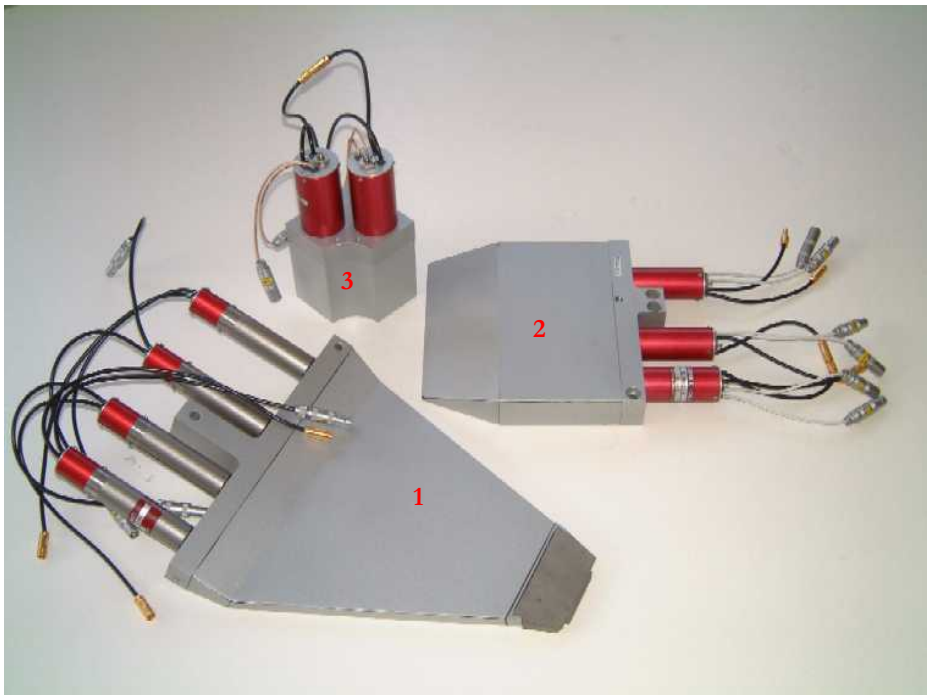

Figure III.2: (b) Individual elements of the ESS shield: (1) BGO side shield with collimator; (2) BGO rear side shield; (3) CsI back catcher.

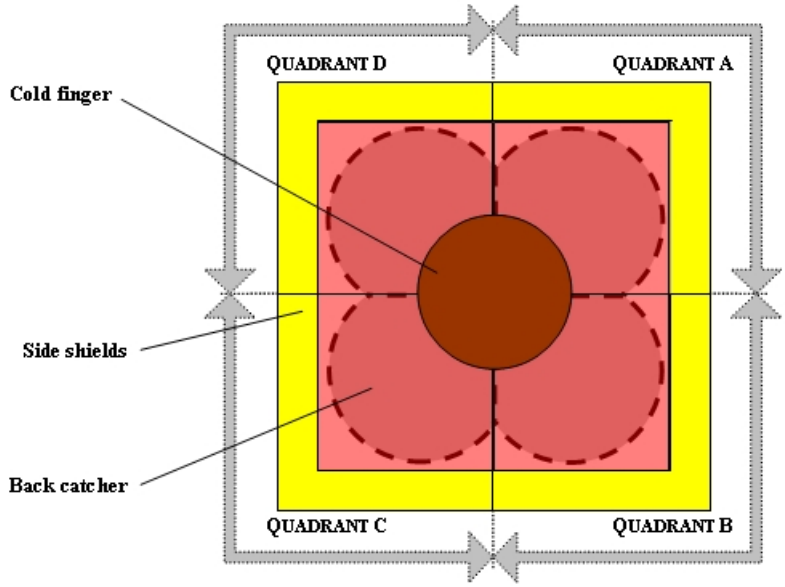

Figure III.3: Back view of the EXOGAM ESS. The dotted line indicates the position of the Germanium crystals relative to the shield. The suppression shield is operated in quadrants, where events resulting in a coincidence between a crystal and its respective quadrant are systematically suppressed. Such a mode of operation has the advantage of allowing the collection of data from the other crystals.

2.3 Detector design and specifications

2.3.1 Detector Geometry

The EXOGAM Clover detector is presented in Figure III.4. It consists of four n-type HPGe crystals mounted inside the same cryostat; the arrangement is shown in Figure III.5. Each crystal is processed from an initial 60 mm diameter by 90 mm long cylinder (minimum specified dimensions). The front of the crystal is tapered for 30 mm with an angle of 22.5 degrees on two adjacent faces, while the opposite sides are cut parallel to the direction of the cylinder, as explained in Figure III.6. The total tapering angle of 45 degrees obtained for the composite detector enables close packing of the EXOGAM detectors in the array. Each crystal is held by clamps at the back, in order to minimise the amount of dead material and reduce the back scattering into the Ge crystals. The separation between the crystals is less than 0.5 mm and the protective end cap is made of aluminium of 1 mm thickness. ORTEC and CANBERRA EURYSIS were the two manufacturers selected to assemble the Germanium crystals, electronics and Dewars, into EXOGAM Clover detectors. Both types of detector have been characterised, and some differences appeared between both products.

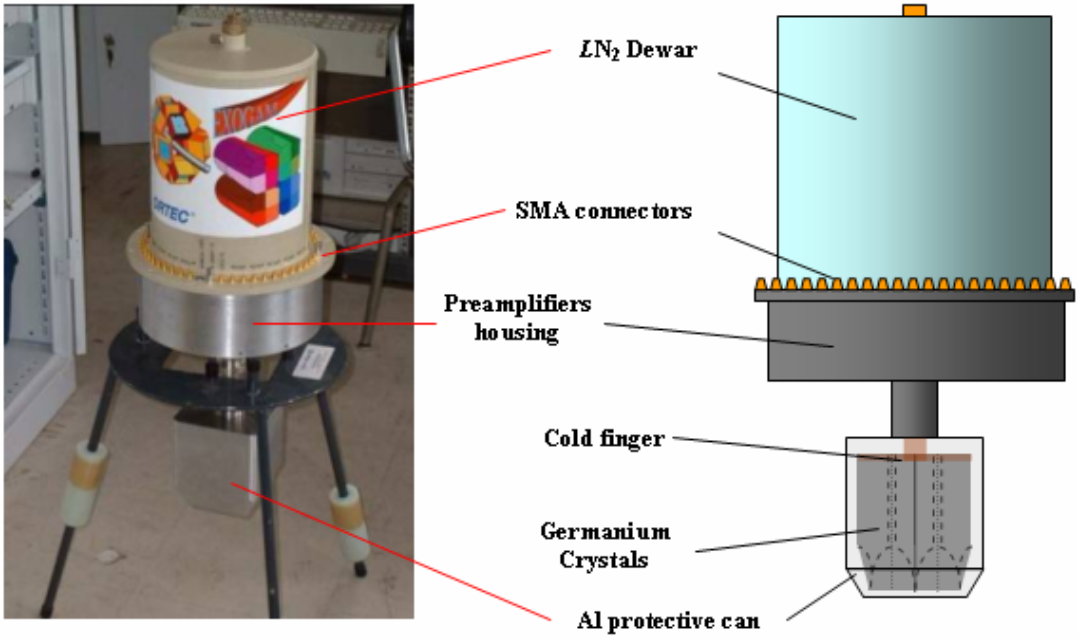

Figure III.4: The EXOGAM Clover detector. The left picture shows the Clover module 06 (ORTEC) on a stand. On the right, a schematic representation of the detector allows one to identify the different components of the module.

The distance between the core electrode and the front face of the crystal was not specified, which resulted in two different designs. ORTEC provided detector crystals with the core electrode starting at an average distance of 8 mm from the front face of the crystal, while the same parameter is 15 mm for CANBERRA EURYSIS detectors. This can result in important differences for the properties of charge transport in the closed ended volume of the crystal. The comparison of both designs is important for the understanding of the properties of HPGe detectors in the particular close ended volume.

2.3.2 Physical and electrical Characteristics

The segmentation pattern of the Germanium crystal is presented in Figure III.6. Each crystal has a 4-fold longitudinally segmented Boron outer contact. The shape of the crystal results in an asymmetric segmentation with a slight difference between the segment volumes. Such segmentation was chosen to obtain a square front face and define an identical opening angle for all segments[6]. A separate reverse bias is applied to each of the core electrodes, ensuring the

[6] With such a configuration, the same opening angle is presented to low energy gamma-rays only.

full depletion of each individual crystal with an operating voltage of at least 200 V in excess of the depletion voltage. The 16 outer electrodes are connected to a common ground.

Additionally, the crystals are grown along the <100> crystallographic direction, and the crystals are shaped so that the flat edges are parallel to the [010] and [001] planes. Considering the anisotropic drift velocity of the charge carriers under high fields [Mih00 and references therein], such a configuration aligns the fast drift directions with the short axes, and the slow directions with the long axes, or cylindrical part of the crystal. This design was chosen to maximise the rise time differences, providing faster pulses for interactions occurring along the short axes relative to the longer axes (Figure III.6).

2.3.3 Front-end electronics

The electrical contacts of the crystals are equipped with AC (anode) and DC (cathode) coupled resistive feedback preamplifiers, based on an initial design by the University of Köln and MPI-K Heidelberg [Ebe00]. Such preamplifiers provide 125 MHz bandwidth, sufficient to conserve the features of the detector output signals. For EXOGAM Clovers, the sensitivity has been specified to be 200 mV/MeV with a decay time constant of 50μs (with 5% tolerance), and the step function response was required to be less than 30 ns rise time. The FET stage was specified to operate at LN_2 temperature. This solution favours the signal to noise ratio, as the use of cold FET minimises the contribution of thermal noise inside the FET and optimise the energy resolution[7]. To provide for easy maintenance, the preamplifiers are mounted on small PCB boards in front of the Dewar (see Figure III.4) and are easily replaceable. Each of the preamplifiers provide two signal outputs (one for timing and one for energy) and is equipped with a "test-pulser" input. The test inputs of the four centre contact preamplifiers are available on the SMA connectors located at the side of the Dewar as illustrated in Figure III.4.

[7] There are still discussions within the community whether HPGe detectors should be used with warm or cold FETs. For the AGATA array, the encapsulation of the Germanium crystals enables the use of cold FETs with the possibility to perform maintenance relatively easily.

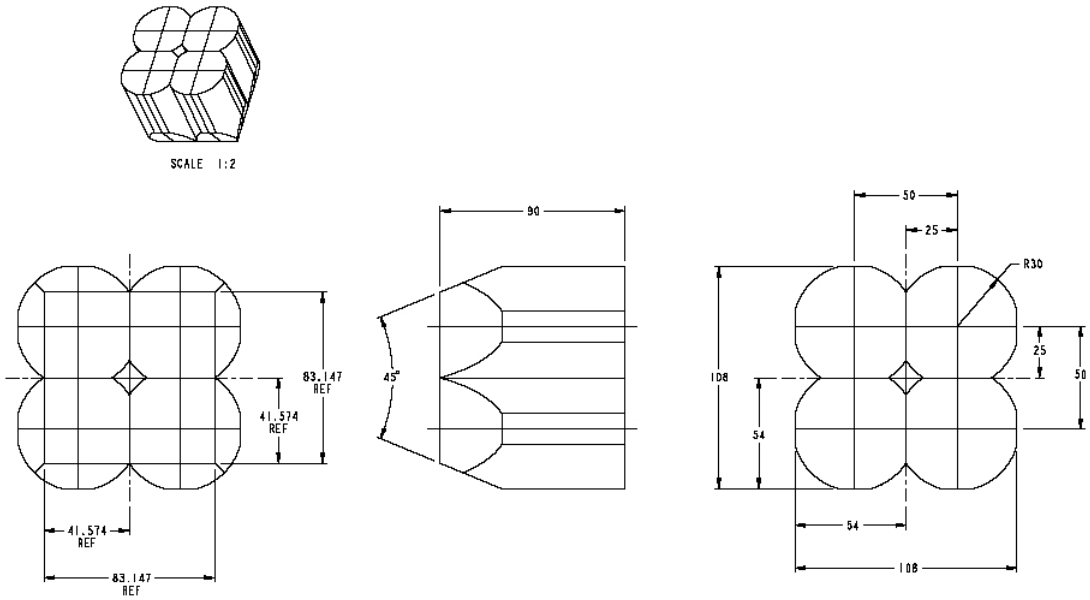

Figure III.5: Drawing explaining the arrangement of the four Germanium crystals in the EXOGAM Clover detector. The crystals are close packed together in the same cryostat, resulting in a total tapering angle of 45°.

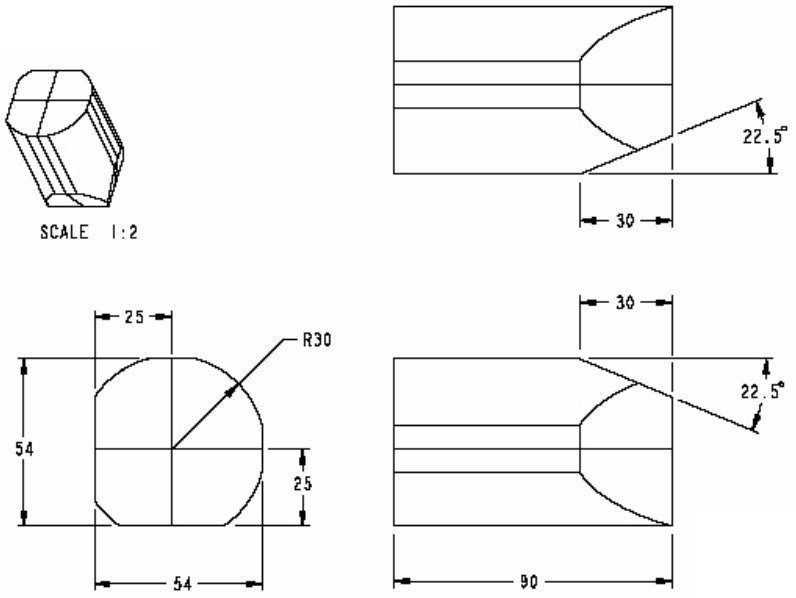

Figure III.6: Technical drawing illustrating the crystal segmentation of the EXOGAM Clover. The initial Germanium cylinder is cut along two adjacent faces, resulting in a long (round sides) and short (flat edges) axes configuration. The front of the crystal is tapered to a distance of 30 mm from the front face. The maximum radius is 30 mm whereas the long and sort axes have respective radii of 25 mm and 29 mm.

2.4 Specifications of the detector performance

2.4.1 Energy resolution and relative efficiency

For each Clover detector, the mean energy resolution of the centre contacts should be less than 2.35 keV at 1332 keV and 1.25 keV at 122 keV. The outer contacts should provide a mean energy resolution less than 2.8 keV at 1332 keV. The relative efficiency of each crystal was required to be above 40%. The photo peak efficiency must be larger than 1.89×10^{-3} for each diode at 1332 keV.

2.5 The EXOGAM Clover 06 Detector performance

In this work, the characteristics of an EXOGAM Clover detector are investigated. The majority of the results presented in this thesis have been obtained from the investigation of the module EXOGAM Clover 06, manufactured by ORTEC. The detector was received at the University of Liverpool in October 2002. Tests were carried out between May and August 2003. The detector was then sent to GANIL in September 2003 and is now part of the EXOGAM array.

The manufacturers were required to perform a set of measurements on each Clover in order to indicate the detector performance and other important parameters needed for the analysis, such as the impurity concentration and the real dimensions of each crystal. The results of these measurements are reported in the **Q**uality **A**ssurance **D**ata **S**heet (QADS) that was delivered with the operation manual of each detector. The QADS for the Clover 06 is presented in Appendix A.

2.5.1 Preamplifiers

The rise time[8] performance of the centre contact preamplifiers was measured with a pulse generator, delivering square signals with a fast rising edge (5ns rise time) into the four TEST inputs available. For each centre contact, 12 pulses were recorded from which an average rise time value was calculated. The values obtained from the measurements are collated in Table III.1. The rise time values range from 25.07 ns to 29.45 ns, showing a good performance for fast pulse responses. The decay time constant was measured from several pulses, giving an average decay constant of ~42 μs (±1.3%).

[8] The rise time of a system (here the preamplifier) is a measure of the system response. It is conventionally taken as the time difference between 10% and 90% of the final state of the system (maximum charge value), evaluated during the transient regime.

2.5.2 Detector efficiency

The relative efficiency of each crystal measured by ORTEC are given in Appendix A. The total relative efficiency of the detector in direct mode is given to be 162.6 % (sum of the individual crystal efficiencies, see Equation I.3).

2.5.3 Energy resolution of the electrodes

The initial energy resolution values of each of the contacts were provided in the QADS. However, the energy resolution was checked for each contact in order to verify that the detector met the specified requirements. Each of the contacts was tested with an ORTEC 671 shaping amplifier with 6μs shaping time and auto base line restore. The four crystals were biased through a common high voltage power supply at +2500V. This is below the recommended operation voltage for crystals B and C, but 200 V above depletion voltage for both crystals[9]. A ^{60}Co source was placed at 25 cm from the front of the detector providing a count rate ≤ 1kHz, and energy spectra were acquired with a TRUMP 8K PCI ADC card [Trum] operated with the ORTEC MAESTRO software. The energy resolution values at 1332 keV measured in Liverpool are shown in Table III.2; the initial numbers provided by ORTEC are added for comparison purposes. The energy resolution measured in Liverpool was in general 0.3 keV worse than the values quoted by the manufacturer. The small differences are probably due to the different measuring environments: the manufacturer has the possibility to make these measurements in a virtually noise free environment, which is difficult to obtain in our laboratory. However, most of the measured values were ≤ 3 keV, and the detector was accepted.

[9] Only one high voltage power supply was available at the time the energy resolution values were checked. At such operating voltages, the entire volume of crystals B and C should be depleted, but there was no way to ensure this at the time of the measurements. Ideally, each crystal must be bias at 500 V above the depletion voltage in order to ensure good drift properties of the charge carriers, while keeping the leakage current to a reasonable level. However, with the particular geometry of the Clover, it is impossible to obtain uniform drift properties over the whole volume of the crystal. This point is discussed in Chapter IV.

Contact	A	B	C	D
Rise time (ns)	26.32	28.45	25.07	29.45
$\sigma_{(\text{rise time})}$ (ns)	0.86	1.85	1.18	1.51

Table III.1: Rise time of the four central contact preamplifiers. The results have been obtained by taking an average of 12 measurements. The systematic 5 ns rise time value of the square signal has been subtracted to each average value. The uncertainty is typically ~4%.

Contact	Measured FWHM (keV)	ORTEC FWHM (keV)	Contact	Measured FWHM (keV)	ORTEC FWHM (keV)
A	2.3	2.3	**C**	2.2	2.3
A1	3.0	2.5	**C1**	2.7	2.5
A2	3.0	2.5	**C2**	3.2	2.5
A3	2.8	2.6	**C3**	2.9	2.7
A4	3.0	2.4	**C4**	2.3	2.4
B	2.3	2.3	**D**	2.2	2.2
B1	3.1	2.4	**D1**	2.8	2.6
B2	2.8	2.5	**D2**	2.8	2.6
B3	2.4	2.5	**D3**	2.4	2.6
B4	3.1	2.6	**D4**	3.1	2.5
Average Segment A	2.95	2.50	**Average Segment C**	2.78	2.51
Average Segment B	2.85	2.49	**Average Segment D**	2.78	2.58

Table III.2: A summary of the energy resolutions measured and provided for ORTEC Clover 06 at 1332 keV. Contacts A, B, C and D represent the central anodes. The average value for the segments is also indicated at the bottom for each crystal.

Chapter IV

CHARACTERISATION METHODS

Pulse Shape Analysis

Simulation of the detector's electrical properties

The following chapter is intended to give the reader a description of the Pulse Shape Analysis (PSA) techniques used to investigate the characteristics of the detector crystal. Experimental methods for evaluating pulse shapes are discussed. A new simulation of germanium crystals: geometry, physical and electrostatic properties – used for the characterisation - will be presented in the second part of the chapter, where detailed results from the electric field simulation of the EXOGAM Clover detector are discussed.

1 Pulse Shape Analysis (PSA)

1.1 Introduction

The use of analogue PSA techniques to extract precise values of energy and time from high purity germanium detectors (HPGe) has proved to be very efficient. However, with the need to improve the location of γ-ray interactions in segmented HPGe detectors, the limits of analogue techniques was reached. Technological advances in the field of digital acquisition[10] and signal processing electronics[11] made possible the development of efficient and accurate digital PSA techniques for the measurement of energy, time and the position of γ-ray interactions.

Digital PSA techniques utilise the shape of the detector current or charge pulse. In order to work effectively, these PSA algorithms are implemented in small ICs such as DSPs or FPGAs, allowing PSA to perform at realistic detector count rates while minimising the amount of data collected. With the segmentation of HPGe detectors, the development of PSA is the next step towards the development of a **G**amma **R**ay **T**racking (GRT) array. Figure IV.1 illustrates the successive steps and information flow in the data processing chain from the Ge detector to GRT.

Figure IV.2 shows typical responses collected from the Clover 06 detector using charge sensitive preamplifiers. The diversity of signal shapes encountered in coaxial HPGe detectors require the use of advanced PSA algorithms, not only able to discriminate real charges from image charge signals (on outer cathodes), but also to identify Compton scatter events (CSE) within a segment and provide accurate position information to the final GRT stage. The use of FPGA is the way forward, as they provide a flexible way for the development of PSA algorithms. Recently, a PSA method providing the measurement of energy, with FWHM values down to the level of analogue electronics, has been implemented in digital electronic modules equipped with FPGAs [Lau04].

The next section describes the PSA methods chosen to characterise the detector response, before presenting simulation of the properties of the Clover crystal.

---

[10] Constant improvement of analogue to digital converters (ADCs): increased resolution and sampling frequency, with a reduction of the price of the components.

[11] Development of dedicated ICs: Digital Signal Processors (DSP), Field Programmable Gate Arrays (FPGA) and Application Specific Integrated Circuits (ASIC)

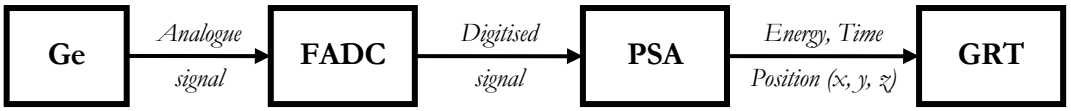

Figure IV.1: Data analysis chain from, the Ge detector signal to the GRT algorithms. The PSA procedure can by done *online* by implementing the algorithms into DSPs or FPGAs or *offline* using a PC. Currently, the use of FPGAs is the way forward.

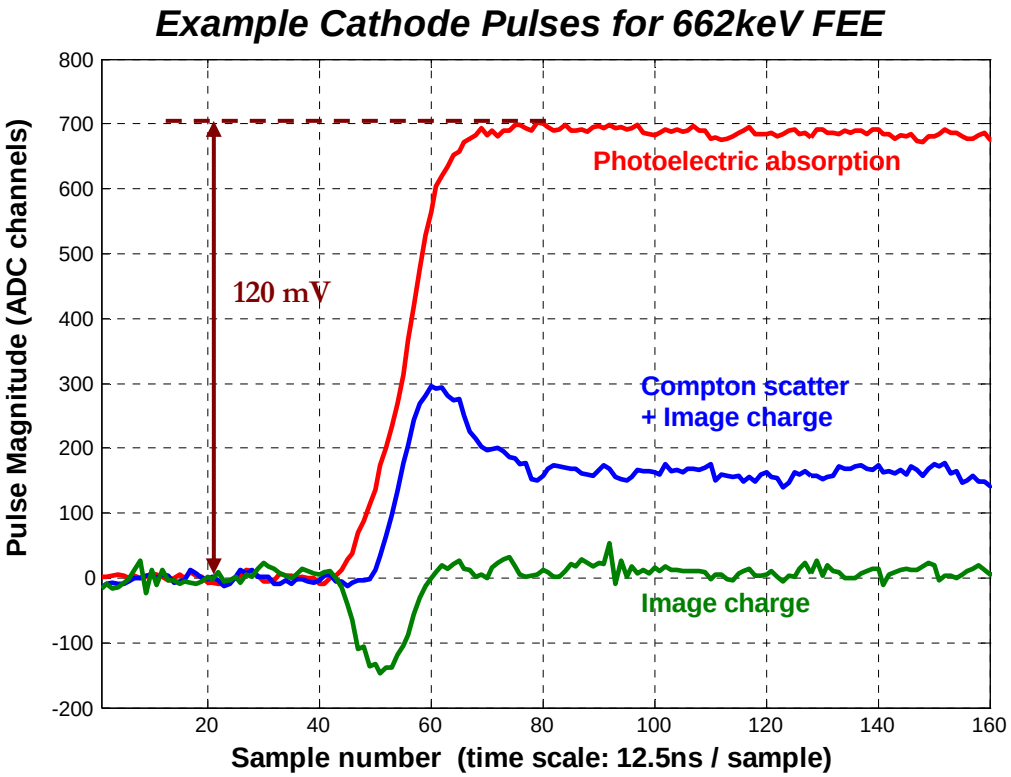

Figure IV.2: Examples of cathode pulses observed for full energy events (FEE). The photoelectric absorption pulse and the image charge pulse (described in section 2.2) are from the same event. The net charge signal results from the collection of the holes by the segment, while a transient charge is induced on the neighbouring segments by the drift of electron/hole clouds. In events where a γ-ray deposited its full energy in two adjacent segments, complex pulse shapes – composed of both net and transient charge signals - arise, as shown by the "Compton scatter + Image charge" pulse.

1.2 Position determination

The drift of the charge carriers within the Ge diode induces a current on each electrode of the crystal (Chapter II, section 2.2). The total current measured at an electrode is the sum of the individual currents induced by the electrons and holes;

$$i_{tot}(t) = i_e(t) + i_h(t) \tag{IV.1}$$

The current signal exhibits a particular shape which depends on the type of carrier in motion, and on the characteristics of this motion relative to the electrodes. The current pulses can be obtained directly with the use of a current preamplifier [Kno00], or from the differentiation of the charge pulse delivered by a charge preamplifier. Depending on the position of interaction within the detector, one type of charge carrier will dominate the current pulse. Figure IV.3 presents ideal current pulses that would be obtained in three different cases for the n-type detector described in this work.

- Figure IV.3 (a) presents the current pulses resulting from an interaction where the electron/hole pairs are created near the anode. There will be a short, large magnitude current induced by the drift of the electrons. The pulse will then describe the drift of holes, until they are collected at the cathode.

- Figure IV.3 (b) presents the pulses for an interaction occurring at the point where the drift time of both charge clouds is identical. The current signal is the shortest.

- Figure IV.3 (c) presents the current pulses for an interaction occurring close to the anode. The holes will be collected shortly after they are generated, and the remaining of the current signal will be induced by the drift of electrons.

1.3 Methods based on current pulse shape analysis

As illustrated by Figure IV.3, the contribution of the charge carrier to the total current signal varies with the position of interaction. This leads to the observation of strongly varying pulse shapes. This fact has been exploited by [Pal97] in his Ph.D. thesis work for the development of the *Steepest Slope Algorithm*, which aims to improve the position resolution of the MINIBALL detectors. This algorithm measures the majority carrier drift time (which is also the time to maximum of the current pulse in n-type detectors). Other current PSA algorithms have been developed previously; they are described and referenced in [Pal97].

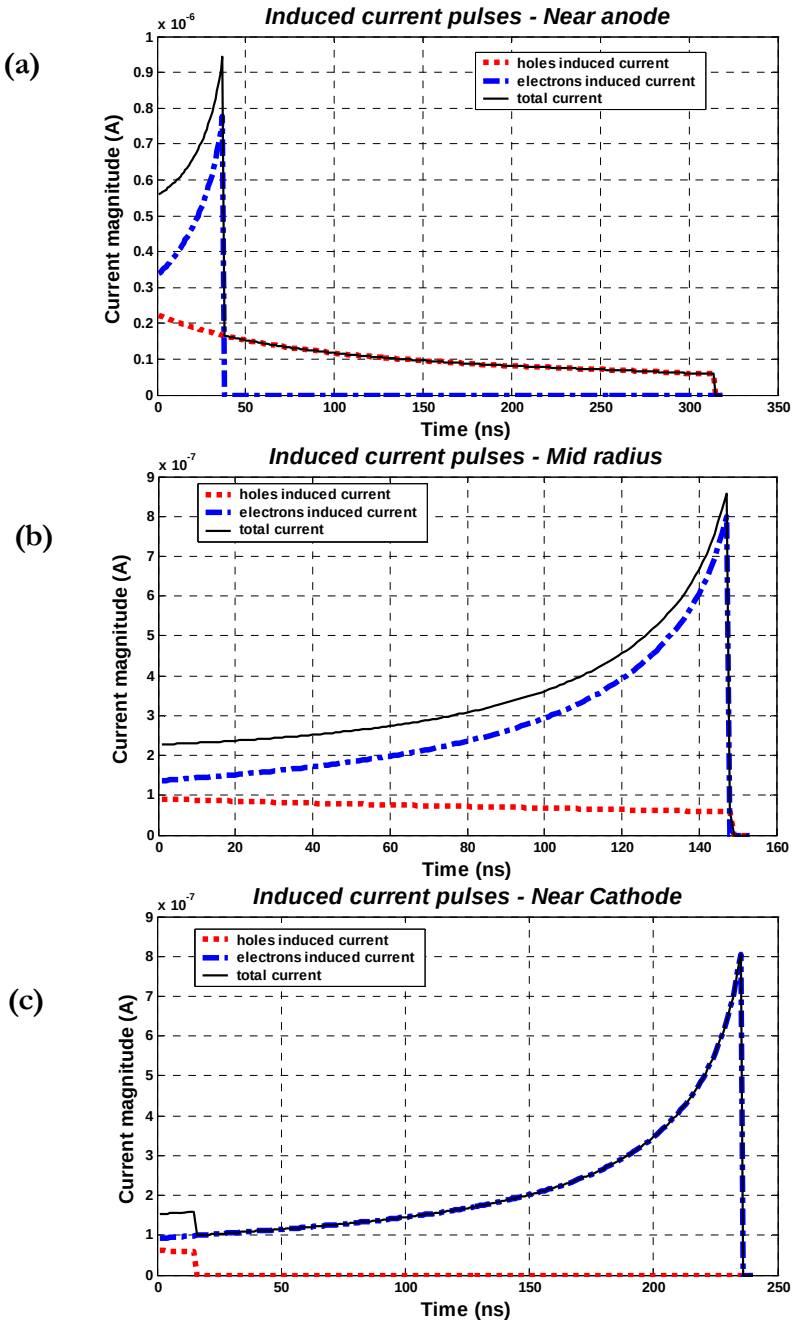

Figure IV.3: Development of the current pulse induced at the anode for an EXOGAM Clover crystal. The detector current pulse (plain black lines) consists of the sum of the electrons (blue dash-dotted lines) and holes (red dotted lines) individual currents. Near the anode (a), the detector pulse consists of a contribution from the drift of the holes, whereas the electrons are the main contributors for interaction near the cathode (c). At the point of equal drift time (b), holes and electrons contribute equally to the development of the pulse. The reader should notice the variation of the time to maximum of current pulse t_{Imax} with radial distance; several analogue and digital PSA techniques are based on the calibration of the radial position of interaction with the time to maximum current pulse. In the present example, t_{Imax} increases from 37 ns to 235 ns. The pulses have been generated by MGS (see section 2 of this chapter) from the simulation of the Clover detector for R = 8 mm, 18 mm and 26 mm respectively along the <011> axis, at a depth of 50 mm from the crystal front face (coaxial region).

1.4 Methods based on charge pulse shape analysis

The charge signal is the integral of the current signal and is induced by the drift of both electron and hole clouds within the active Ge volume,

$$Q_{tot}(t) = \int i_{tot}(t)dt = \int i_e(t)dt + \int i_h(t)dt \,. \qquad \text{(IV.2)}$$

The analysis of the charge signal involves the identification of the contributions from both types of carriers to the growth of the charge pulse. As for the current pulse, when one type of carrier has been collected, the charge pulse results from the drift of a single charge species.

While the collection process results in the growth of a net charge signal on the collecting contact, image charges are induced on adjacent electrodes. The magnitudes of both net and image charge signals are proportional to:

- the charge generated during the interaction, i.e. to the energy of the photon;
- the spatial and temporal variation of the carriers drift velocity[12];
- the spatial magnitude of the weighting field[13].

In addition, the magnitude and polarity of the transient charge signals depend on the position of interaction relative to the adjacent electrodes: the closer to an electrode the interaction occurs, the larger the induced charge signal.

1.4.1 Charge pulse rise time analysis

The shape of the leading edge of the charge pulse exhibits a strong dependence on the position of interaction in between the anode and the cathode. It reflects the contribution of the charge carriers to the development of the pulse discussed in the previous section. This dependence can be studied by a simple analytical model for a true coaxial detector [Kno99a], and it has been shown experimentally [Des02, Ebe01, Kro95 and Kro01] that such an effect can be used to calibrate coaxial HPGe crystals for radial positions of interaction.

---

[12] The drift velocity of the electrons and holes depends on their path relative to the crystallographic structure, and to the direction and magnitude of the electric field (see Chapter II, section 2.2.2).

[13] The concept of weighting field is described in Chapter II section 2.2.2, and is referred to in section 3 of the present chapter.

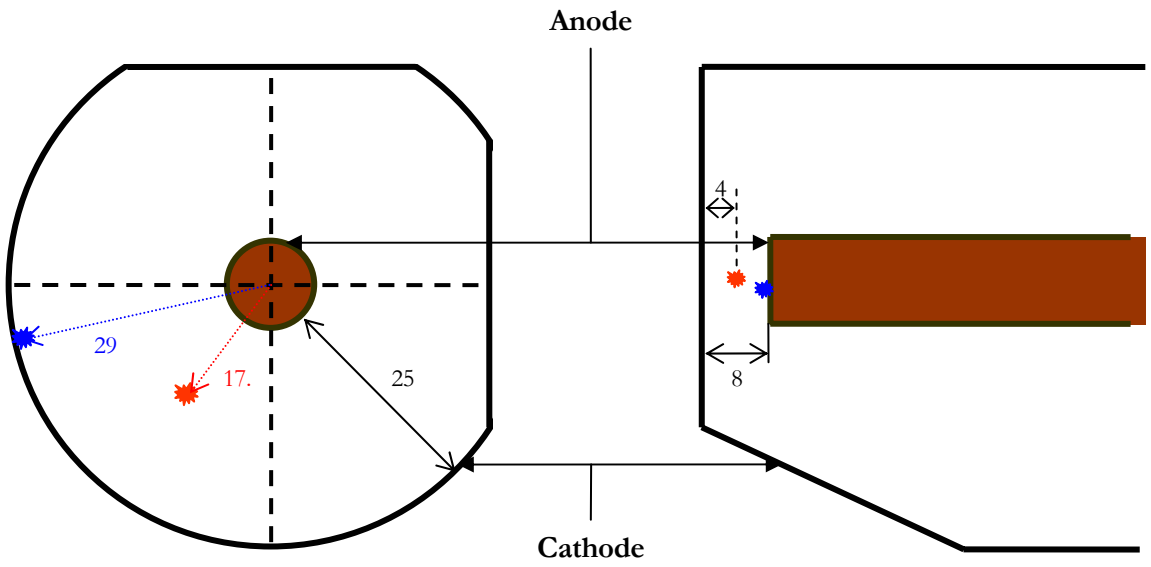

Figure IV.4: Illustration of interaction position for minimum (red) and maximum (blue) charge collection (or pulse rise) time. In the coaxial region (left), the maximum drift time occurs for interactions located at the anode or at the cathode, resulting in a maximum drift distance of 25 mm. The rise time is expected to be faster at mid distance between the anode and the cathode (R ~17.5 mm). At the front (right), the maximum drift distance is 8 mm. Intermediate values of collection times are expected along the taper. The distances indicated in the diagram are in mm.

Given that a typical maximum radius for an interaction in the EXOGAM Clover is 29 mm, and considering a core radius of 5 mm, the charge carriers have a maximum drift distance of 24 mm. The saturated drift velocity along the FCC <110> axis is 10^7 cm/s (see figure II.7); the maximum collection time is expected to be ~240 ns in the coaxial region. The minimum expected collection time is ~125 ns, assuming that the point where positive and negative charge carriers have the same drift time is located at mid distance between the two electrodes. At the front, where the anode-cathode distance is 8 mm, one expects to measure a maximum collection time of ~80 ns and a minimum collection time of ~40 ns at mid distance. Figure IV.4 shows the radii for interaction positions where the extreme rise time values are expected.

1.4.2 The T90-T30 Method

The T90-T30 method was first used with HPGe detector by [Kro96], in order to study the variation of charge pulse shape and can be used to calibrate EXOGAM Clover crystals. Figure IV.5 presents three typical anode signals corresponding to photoelectric absorption of 662 keV γ-rays, measured for different radial positions[14]. The time scale has been reduced in order to

[14] The pulses are actually taken from the scan measurement described in Chapter 5, Section 3.1.3.

consider only the leading edge of the pulses. The rise time T90 is defined as the time measured from 10% to 90% of the total charge magnitude ($t_{90} - t_{10}$).

- **Mid radius.** For the central position of the source, electrons and holes have a similar drift time. This maximises their joined contribution to the growth of the charge pulse (pulse B). As a consequence, the collection time of the charges is minimum and the final pulse magnitude is attained very quickly, resulting in the fastest measured rise time (~130 ns). This result is close to the minimum expected rise time value of 125 ns calculated above. The corresponding current pulses are similar to the signals shown in Figure IV.5 (b).

- **Inner radius.** Close to the anode, the electrons are collected at the beginning of the pulse rise (pulse A). The remaining part of the signal arises from the drift of the holes, and has then a slower rise time (~200 ns), but faster than the expected maximum value of 240 ns. The rate of growth of the pulse reduces until the maximum charge magnitude is reached.

- **Outer position.** Near the cathode, the holes are collected quickly: then the growth of the pulse (C) contributes only from the electrons cloud drifting towards the anode. This again causes a slower charge collection time: the rise time is ~ 205 ns, and is also smaller than the maximum expected value of 240 ns.

The difference between the expected rise time and measured rise time values is explained by the uncertainty in the interaction position due to the divergence of the γ-ray beam from the collimated source. This matter is discussed in appendix B. As illustrated by the examples presented in Figure IV.5, it is therefore possible - in a coaxial detector – to obtain information on the radial position of interaction by looking at the variations of these pulse shapes. This information can be extracted by measuring different partial rising times of the charge pulse.

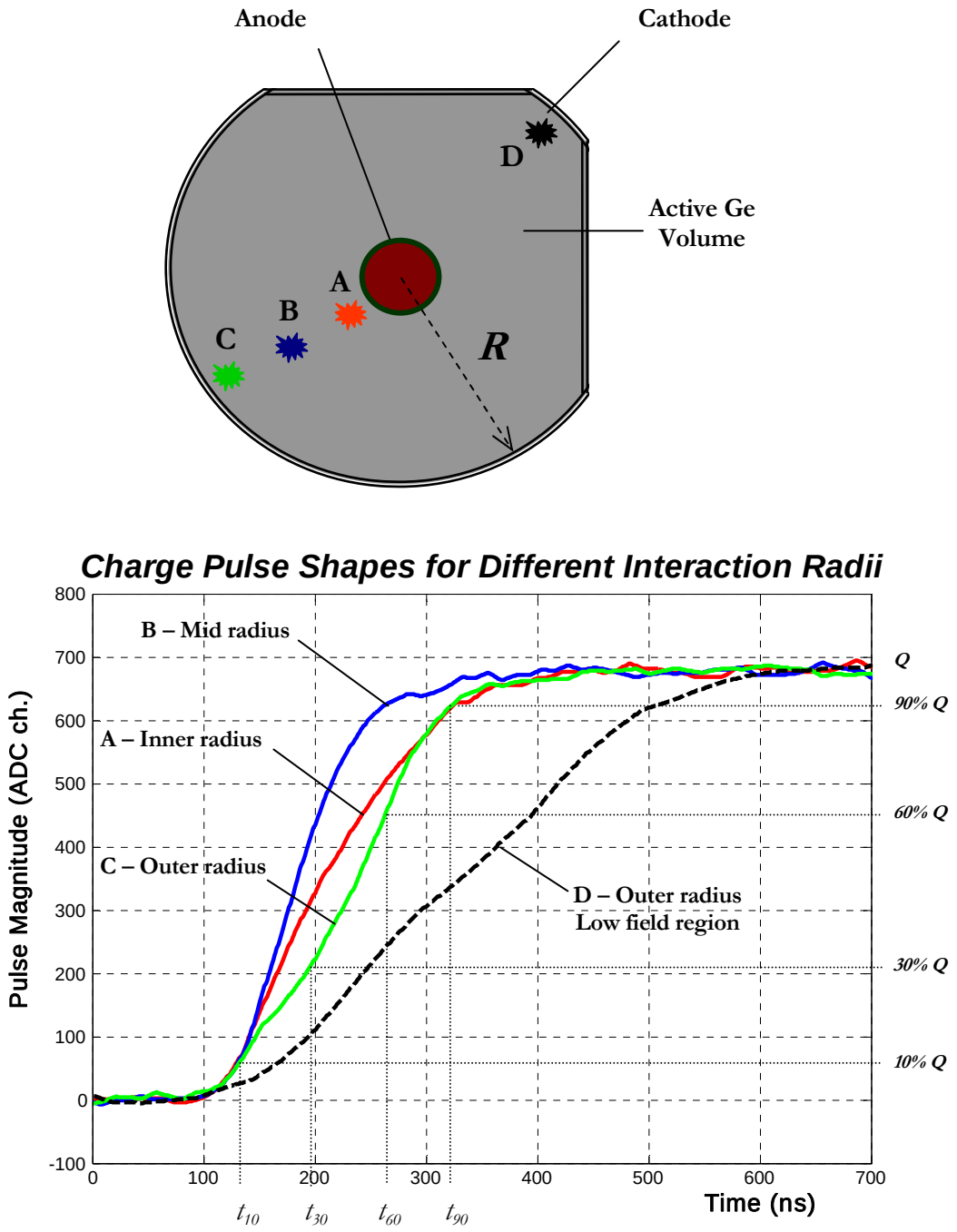

Figure IV.5: Example anode pulses illustrating the use of the T90-T30 PSA method. Pulses resulting from 662 keV photoelectric events have been recorded from the 3 different radial positions shown in the top diagram. *Q* represents the maximum amplitude of the charge pulses. The different time values involved in the measurement of T30, T60 and T90 are indicated on the plot. T90 is long for small and large interaction radii (pulses A and C) while T30 is fast at small radius (A) and long at large radius (C).At mid radius, T90 and T30 are both fast. T60 varies from fast at mid radius (B), to long at large radius (C); an intermediate value is observed for the pulse at small radius (A). A pulse resulting from an interaction in a low field region has been added for comparison purposes. In this case T30, T60 and T90 are much longer than the rise time values expected for photoelectric events.

A) Properties of T90

The previous example shows that pulses arising from an interaction close to the electrodes have a longer rise times than interactions at mid radius. This yields an ambiguity in T90 for interactions occurring in the vicinity of the detector's electrodes, giving identical T90 results for radii close to the opposing contacts. This ambiguity can be relieved by studying the variation of partial rise time values, defined as the time difference between t_{10} (the time from 10% of the total charge magnitude[15]) and t_n as illustrated in Figure IV.5. The T30 pulse rise time is introduced, which is the time from 10% to 30% of the total charge magnitude.

B) Properties of T30

For anode signals, T30 increases slowly as a function of the distance from the anode to the central point, up to a maximum value at the cathode. T30 is measured at the very beginning of the drift process, and can provide information on the electrostatic properties of the crystal near the location of interaction. For interactions close to the anode, the strength of the electric field is maximum, yielding the fastest (and hence saturated) drifting velocities for the charge carriers. The charge pulse will then have an initial fast rising growth rate. On the contrary, close to the cathode, the strength of the electric field is minimum. In the worst cases, the geometry of the crystal can even result in regions where the charge carrier drift velocity is unsaturated. The initial pulse rise may then be slower for interactions located near the cathode. This property of T30 can be used to detect regions of lower field intensity, where the drift velocities are not in a saturated regime. This is more likely to be geometrically situated near the cathode and at the internal corner between two adjacent sides in the EXOGAM Clover detector crystal.

1.4.3 Filtering Compton Scattered Events (CSE)

In segmented detectors, those events that Compton scatter between segments and deposit all of their energy are easily identified from the fold or number of segments which contain energy. In the case of Fold 1 FEE, the use of T90 allows one to separate CSE occurring within the same segment from single site interactions. Such events will result in a Fold 1 in the detector,

[15] The pulses presented in Figure 4.5 have been aligned in order to show the difference in T90. In reality, there is a time jitter due to the noise that introduces a large uncertainty in the determination of the beginning of the pulse rise. The use of t_{10} as a reference for the start of the pulse reduces the uncertainty considerably.

while the number of interactions (Multiplicity)[16] of the event (for 662 keV γ -rays) is more likely to be 2 or 3.

Figure IV.6 illustrates the following discussion. When the charge pulse results from the drift of carriers generated at *N* interaction sites, there will be 2×*N* particular collection times resulting from the electron and holes collection. For instance, in the case of a 2 Compton scatter sequence, 2 absorption sites generate 2 electron and 2 hole drifting clouds. It is theoretically possible to differentiate such a pulse form a single photoelectric absorption signal:

- The contribution of charge carriers generated at the main interaction[17] site will dominate the growth of the pulse;

- A series of discontinuities, each corresponding to collection of a charge cloud, should be observed in the rising edge of the pulse.

T90 should then be longer for CSE than for single photoelectric events. This is only true for cases where the interaction sites are radially separated, i.e. when both electron clouds – and both hole clouds – have different collection times.

1.4.4 Measurement of the radial position of interaction

In the coaxial region of the crystal, investigating the variation of T30 and T90 with the radial position of the interaction can be used to calibrate a crystal for position sensitivity (see Chapter VI). However, the properties of each partial rise time value are perturbed by the anisotropic drift velocity of the charge carriers [Mih00]. Thus for a same radius, T30 and T90 will be faster along the <011> directions relative to the <100> directions.

[16] The multiplicity of an event is defined as the real number of interactions occurring in the detector.

[17] Interaction that deposits the largest amount of energy

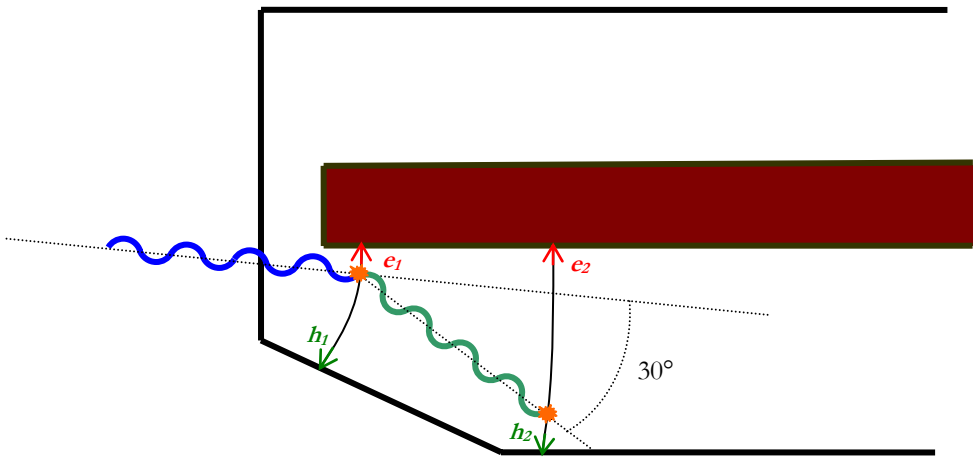

Figure IV.6: The diagram illustrates a two site CSE with a 30° scattering angle. The Compton scattering formula allows one to calculate the energies resulting from a CSE. The first interaction deposits E_1 = 102 keV in the tapered region and generates two charge clouds of e_1 electrons and h_1 holes. The scattered γ ray is absorbed in the second (main) interaction, transferring its energy E_2 = 560 keV to the Germanium and creating e_2 and h_2 charge clouds. There will be 4 collection times, e_1, h_2, h_1 then e_2.

1.4.5 Image charge analysis

It is also possible to calibrate the crystal for azimuthal position. However, the analysis of image charge signals is an inherently complex procedure, requiring reference to the real charge pulse rise time in order to resolve ambiguities on the image charge magnitude. Two possible methods have been used previously [Des02, Lau04] with 6 fold azimuthally segmented coaxial HPGe crystals. The first method measures the absolute magnitude of the transient signals on the direct adjacent electrodes (*m* and *n*) and derives the corresponding image charge asymmetry:

$$A_{m,n} = \frac{Q_m - Q_n}{Q_m + Q_n} \tag{IV.3}$$

The second method calculates the value:

$$L_{m,n} = \mathrm{Log}\left(\frac{Q_m}{Q_n}\right) \tag{IV.4}$$

where $Q_{m,n} = \left|Q_{\max}\right|_{m,n}$.

Figure IV.7 shows results taken from the measurement described in the next chapter. The pulses were obtained from two FEE events occurring at opposite azimuthal locations inside the largest segment (A1) of a Clover crystal: the first interaction site was near the boundary with segment A4 and near the cathode (event 1 (*E1*), in blue); while the second interaction occurred close to the anode, at the boundary with segment A2 (event 2 (*E2*), in red). The corresponding pulses recorded on each outer contact of the crystal are presented on the corresponding plot:

- **A1** shows two net positive charge pulses. Both pulses rise until the maximum charge value is attained. E1 present a longer collection time compared to E2: the holes are the main drifting species for interactions occurring at large radius, whereas electrons are the main pulse contributor at small radius. The holes have a smaller ohmic mobility than electrons at low temperature in germanium [Kno00]. Therefore, it is expected to observe longer rise time at large radius compared to small radius, as observed in pulses from segment A1.

- **A4** (left) displays a positive transient charge signal for *E1* of magnitude ~95 channels (ch), while *E2* probably shows a very small magnitude transient signal of ~15 ch. It is important to highlight that the polarity of the image charge signal depends on the polarity of the drifting charge: in this case the drift of the holes induce a positive magnitude image charge.

- **A2** (right) shows a large magnitude transient signal for *E2* (~ 200 ch). The level of the noise amplitude makes difficult the detection of the transient signal for *E1*. However, image charges appear on adjacent electrodes only during the charge collection process; for the purpose of demonstrating the use of image charge in PSA, the slightly positive bump observed in *E1* signal is considered as a transient charge of magnitude ~ 20 ch.

- In **A3**, the level of the transient signal is too low to be observed, and is below the noise amplitude for both events.

The values of $A_{left,\ right}$ and $L_{left,\ right}$ are shown in Table IV.1. Both parameters vary from a negative value near A4 to a positive value near A2.

Event	Q_{left} (ADC units)	Q_{right} (ADC units)	$A_{left,right}$	$L_{left,right}$
E1, near A4	20	-200	-0.818	-1
E2, near A2	95	15	0.727	0.8

Table IV.1: Magnitudes of image charge signals shown in Figure IV. with corresponding *A* and *L* values. Both parameters are negative for the event 1, and positive for the event 2.

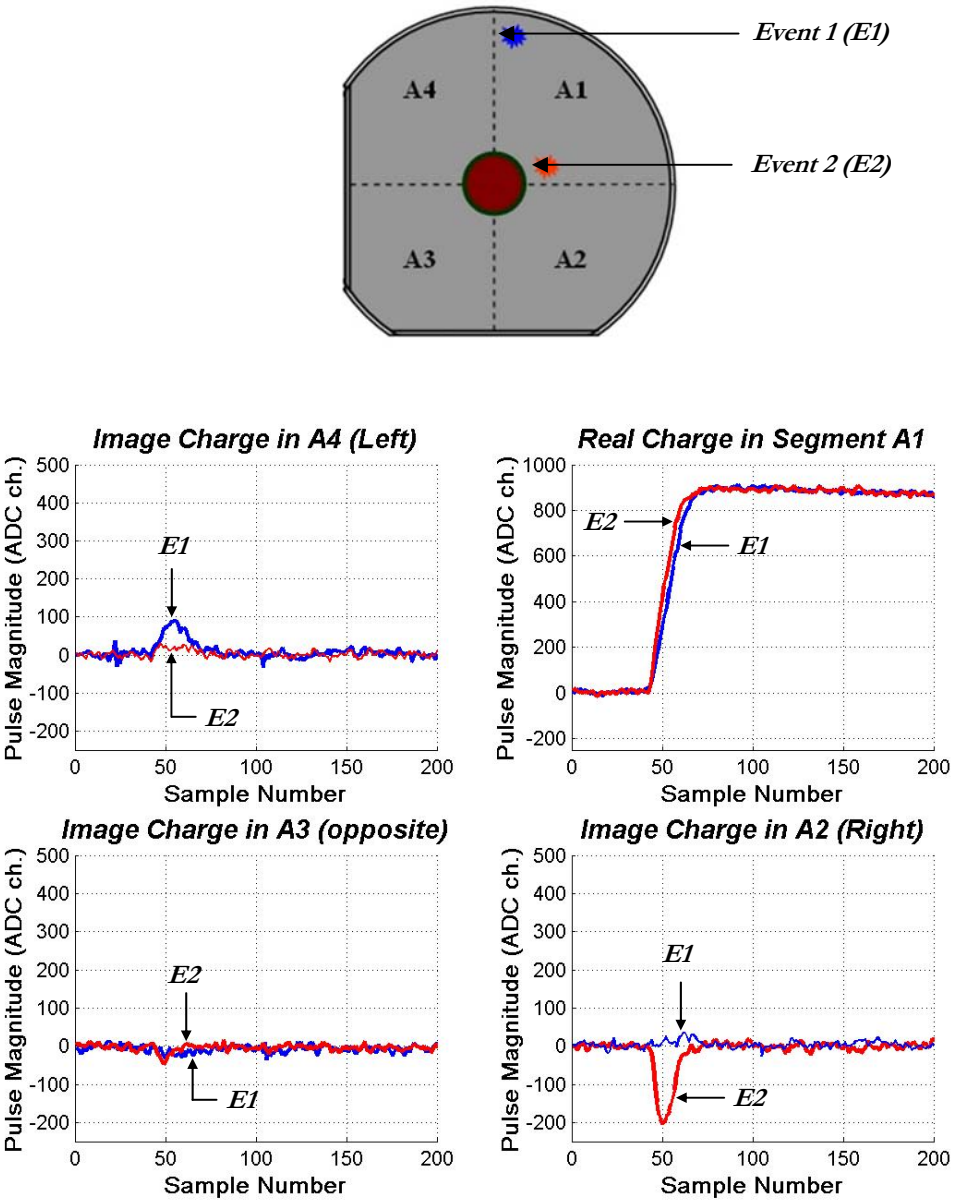

Figure IV.7: Cathode signals for FEE within segment A1. A4 and A2 display large image charge signals, respectively for events occurring in their vicinity. The polarity of the transient signal depends on the polarity of the drifting charge. *E*1 is located near the cathode, the positive magnitude is due to the drift of holes, while the negative pulse observed for *E*2 in A2 results from the drift of electrons.

2 Detector Simulation

The study of the rise time and image charge properties is not possible for the infinite number of interaction positions possible within the crystal. A first approach is to perform a scan of the germanium crystal with a collimated γ-rays source. The realisation of the experimental set-up is described in the next chapter. Such approach provides pulse shape information for a particular set of points, but requires a large amount of time and data storage resources. The second approach is the simulation of the germanium crystal properties. Precise pulse shape information can then be accessed for any given interaction position. Several simulations were performed in the past in order to study the properties of different HPGe detector properties [Kro01] and evaluate the performances of a particular crystal segmentation design [Gör03]. Until now, most of the solutions available were either expensive commercial products, which did not include the specificities inherent to semi-conducting material, or non commercial simulation codes hardly transportable to different detector geometries.

A simulation package [Med04, San04] has been developed at the Institut de Recherche Subatomique (IReS) in Strasbourg (France), in order to simulate the full operation of single segmented HPGe crystal. The package utilises the MATLAB software [MAT], and can be run with Windows and Linux operation systems. Such an approach has the advantage that complex crystal geometries can be handled, while additional complexity can easily be modelled. The anisotropy of charge carrier drift velocities, the influence of temperature on the charge carriers mobility and the influence of neutron damage are some examples of the simulation features.

2.1 Description of the Multi Geometry Simulation (MGS) package

The simulation software is composed of several independent routines designed to model the operation of any Ge crystal geometry. The results are stored in the form of several 3D matrices. A summary of the steps necessary to create a full simulation with MGS operations is illustrated in Figure IV.8. The simulation starts from the definition of the crystal geometry. The electric field inside the crystal is then calculated with Poisson equation,

$$\nabla^2 \varphi = -\frac{\rho}{\varepsilon} \tag{IV.5}$$

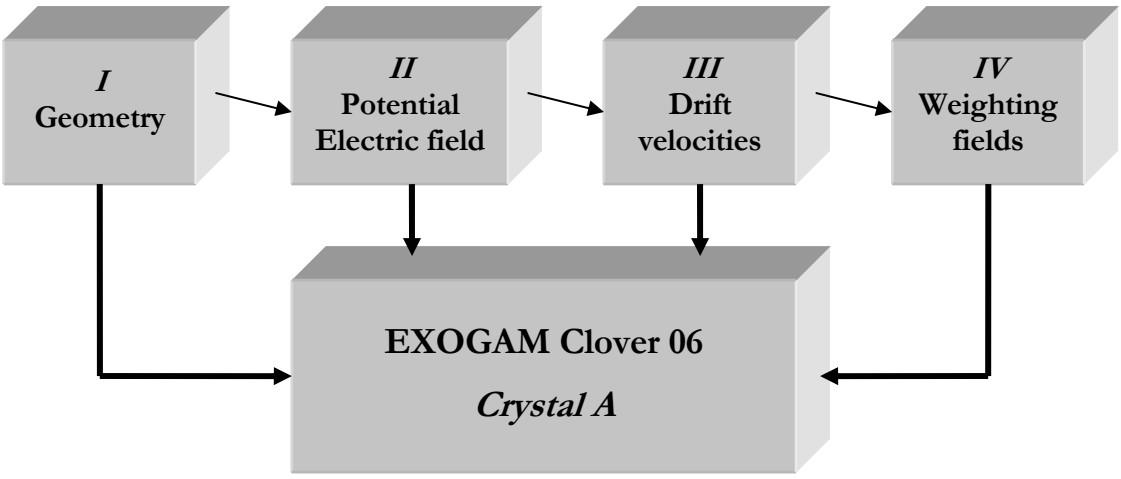

Figure IV.8: The steps necessary to construct a full simulation of the Clover. (I)The dimensions of the crystal are stored in the geometry file. (II) The potential and electric field matrices are built from the initial detector geometry matrices. (III) The drift velocity matrices are calculated from the electric field matrix. (IV) The weighting field matrices are calculated from the information stored in the geometry matrices. Once the four initial blocks have been created, one can start to generate pulses from the detector.

The drift velocities of charge carriers are derived from the work described in [Mih00]. Finally, a set of weighting field matrices are generated as they are required for the application of Equation II.26 in the calculation of the detector signals.

2.2 Features of simulation

MGS offers the possibility to obtain the current and charge signals from an interaction occurring at any point in the crystal volume. It also offers the possibility to scan the crystal by defining a range of either Cartesian or cylindrical coordinates, with any step sizes, for the purpose of detector characterisation.

At this stage, it is important to note that the following assumptions have been made for the simulation of the detector:

1. [Mih00] only reports on the charge transport of electrons. It has been assumed that a ratio of 0.66 exists between the drift velocities of electrons and holes; corresponding to the ratio of electron to hole effective masses at 77 K. However, in [Kno99], the ratio of hole to electron mobilities at 77 K is given to be 0.857. The consequences of this assumption will be discussed later.

2. The second assumption relates to the determination of the electron drift velocity matrix. This quantity is calculated by an empirical formula (Equation IV.9), where the parameters have been defined from fits to experimental data points [Ott75]. These parameters were obtained from germanium samples with different impurity concentrations. Therefore the parameters may need to be adjusted.

3. The response of the preamplifier is not included in the simulation.

This work intends to compare the information provided by the simulation with experimental data and understand the origin of the differences observed. Parameters in the simulation will then be adjusted in order to obtain an agreement between experimental and simulated values.

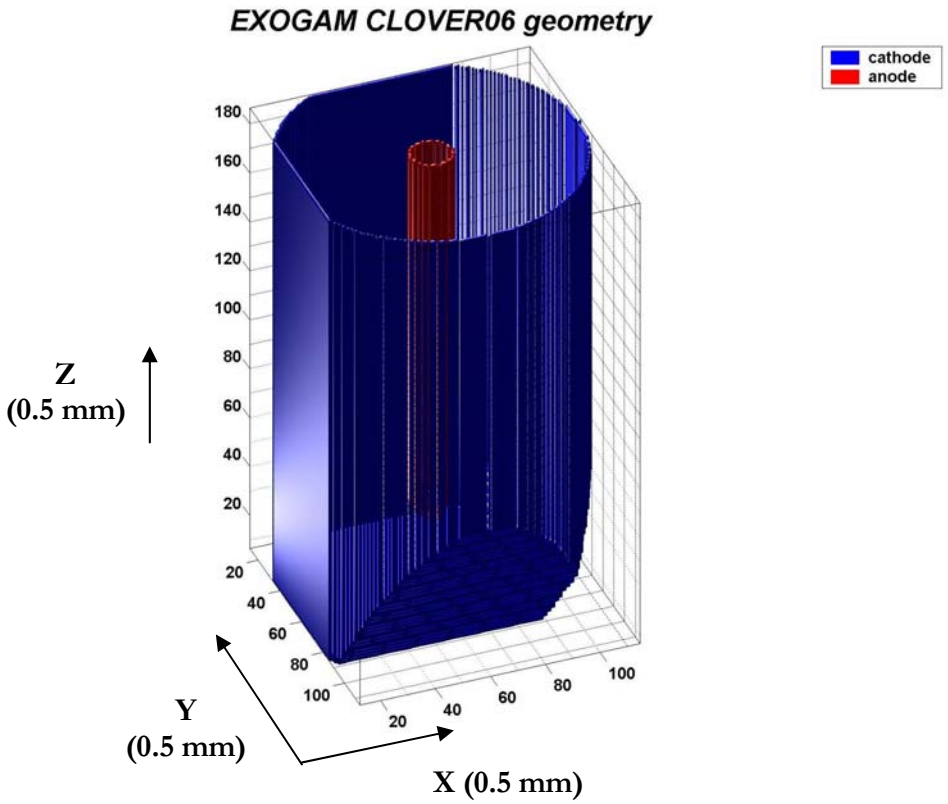

Figure IV.9: Geometry of the simulated EXOGAM Clover crystal, showing the position of the core and outer electrodes. The dimensions indicated are in *grid step size* (½ mm).

2.3 Simulation of the EXOGAM Clover crystal

The properties of Crystal A are being simulated[18]. The values of the parameters provided to MGS in order to generate the detector matrices are summarised in Table IV.2.

2.3.1 Geometry

The basic information used to generate the segmented crystal is stored in a library. The geometry of the simulated crystal is then generated from data provided by the user (see Table IV.2). The initial dimensions of the cylinder from which the crystal was cut were 60 mm diameter by 90 mm long; the crystal was then shaped following the indications given in Figure IV.6. The distance between the anode and the front face was set to 8 mm, with a 5 mm inner radius. Figure IV.9 shows the resulting crystal geometry with outer electrodes.

Geometry	
Grid step (size of the matrix)	0.5 mm
Crystal length (X dimension of the cut crystal)	54 mm
Crystal height (Y dimension of the cut crystal)	54 mm
Crystal depth (Z dimension of the crystal)	90 mm
Angle (taper)	22.5°
Cut depth (tapering depth)	30 mm
Forward space (distance between the Al housing and the front face of the crystal)	3 mm
Back space (distance between the Al housing and the back of the crystal)	10 mm
Lateral space (minimum distance between the housing and the crystal along depth)	3 mm
Distance to cathode (for anode at the front)	8 mm
Radius (anode)	5 mm
Physical and Electrical properties	
Inner contact bias	0V
Outer contact bias	-2500 V
Minimum impurity concentration (back face)	5×10^{9} cm^{3}
Maximum impurity concentration (front face)	1.2×10^{10} cm^{3}
Isolant (include the passivated surface at the back of the crystal, estimated value)	1×10^{10} cm^{3}
Ge permittivity (dielectric permittivity)	16
Temperature (crystal)	95 K

Table IV.2: Parameters required and provided to MGS for the simulation of the EXOGAM Clover Crystal A.

[18] See appendix A for the values of relevant parameters.

In a first attempt, the size of the matrix grid was chosen to be 1 mm, but the precision needed for a full understanding of the detector response function required the reduction of the grid size from 1 mm to 0.5 mm[19]. The operating temperature of the crystal is chosen to be 95 K.

Electric Potential and Electric Field

The space charge density ρ is calculated from the impurity concentration values (*n*-type doped crystal) provided by the manufacturer (Appendix A). These values are given for the front and back surfaces of the crystal, therefore, a linear gradient is estimated over the whole length of the crystal[20]. The solution of Poisson equation,

$$\frac{\partial^2 \varphi}{\partial x^2} + \frac{\partial^2 \varphi}{\partial y^2} + \frac{\partial^2 \varphi}{\partial z^2} = -\frac{\rho(x,y,z)}{\varepsilon} \qquad \text{(IV.6)}$$

gives the potential $\varphi(x, y, z)$ at each point within the matrix defining the detector, where x, y and z are the Cartesian coordinates in the matrix referential, $\rho(x,y,z)$ is the volumetric space charge density, and ε the dielectric permittivity of Germanium. The complex geometry of the EXOGAM Clover crystal makes the solution of Poisson equation impractical. The solution of Equation IV.6 was calculated using two relaxation methods ("Simultaneous Over-Relaxation" (SOR) and "Relaxation"), with boundary conditions defined as $\varphi(x, y, z)_{\text{anode}} = 0$ V and $\varphi(x, y, z)_{\text{cathode}} = -2500$V [21]. Relaxations methods replace partial differential equations by approximate finite difference equations [Pre90].

The estimation of the potential is an iterative process. The relaxation methods determine the solution by starting with a "guess", which is improved at each iteration. The difference between the initial solution and the updated solution is evaluated by a correction (or error) parameter: convergence is reached when the value of the correction becomes constant over iteration. Along with the choice of the solving method, a maximum number of iterations and the minimum value of error are provided to the program. The iterative process either stops

[19] Initially, it was planned to reduce the grid size to 0.1 mm, but the necessary computer resources (storage and computing power) were not available.

[20] It is difficult to measure impurity concentrations less than 1×10^9cm^{-3}, therefore the value measured on the open-ended side of the crystal is approximated.

[21] In reality, the anode is biased at +2500V and the cathode is grounded. However the set of boundary conditions used by the simulation has no impact on the values of the electric field inside the crystal.

when the number of maximum loops is reached or when the required minimum error value is attained.

The SOR method has the advantage of being fast, but converges before an acceptable precision is reached; this algorithm was then used to convergence down to an intermediate value of error. The relaxation method is slower but converges at a much higher precision, refining the previous solutions to a more accurate value of the electric potential within the crystal volume. The evolution of the error parameter is presented in Figure IV.10. The SOR method converged after ~750 loops. Further calculations with the relaxation method improved the error value and converged after ~4000 iterations. The electric potential in the X-Z plane, along Y = 60 (through the centre of the anode) is shown in Figure IV.11. The electric field is then calculated with equation IV.7

$$\vec{E} = -\vec{\nabla}\varphi(x, y, z) \tag{IV.7}$$

using the boundary conditions defined above. The electric field magnitude in the X-Z plane isEshown in Figure IV.12. The colour scheme represents the magnitude of the electric field vector.

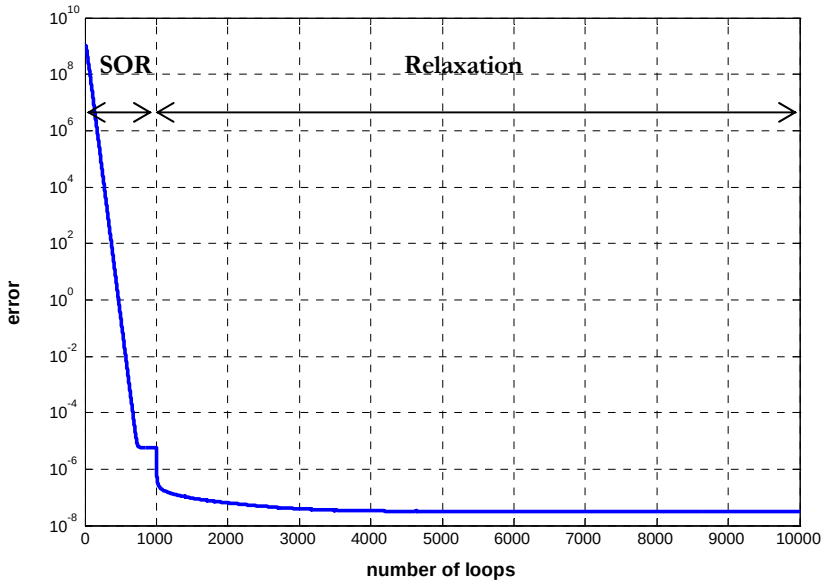

Figure IV.10: Evolution of error during the calculation of the electric potential. The SOR method converged after ~700 iterations at an error of ~8×10^{-6}. The relaxation method required ~4000 iterations before convergence to an error value of ~5×10^{-7}

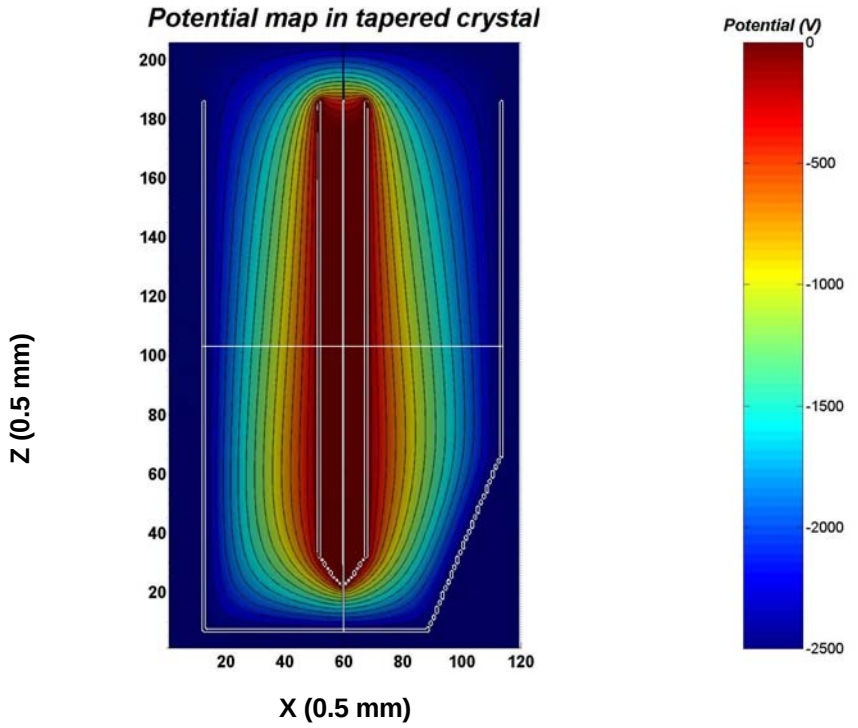

Figure IV.11: Electric potential values along the crystal length, in the X-Z plane at Y = 30 mm (centre of the crystal). The results show regions of low potential at the corner between the front face and the crystal edges. The closing of the equipotential lines at the back of the crystal is an artificial feature of the simulation due to the imposed 0 V potential to edges of the matrix.

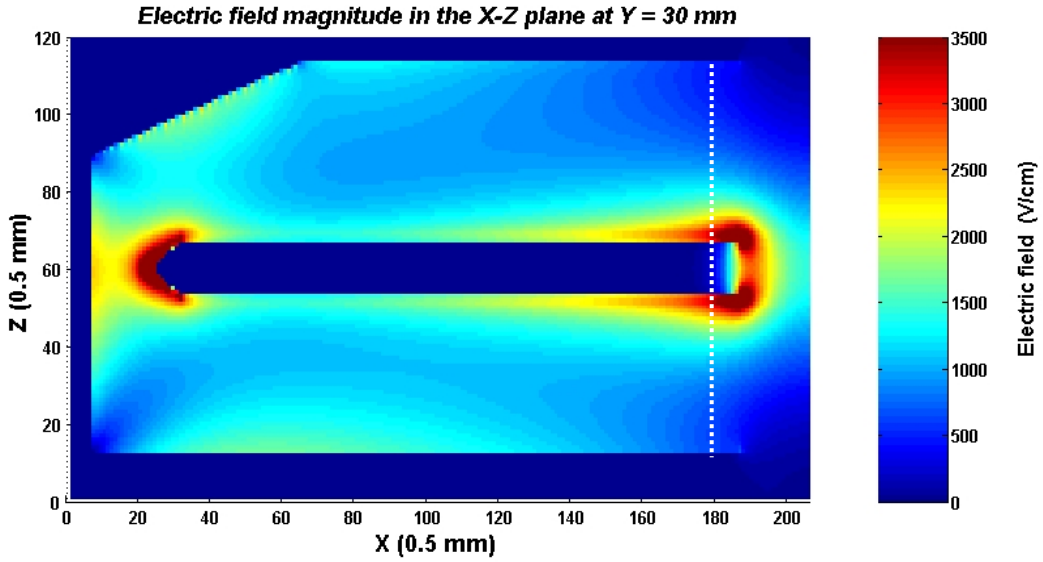

Figure IV.12: Electric field magnitude in the X-Z plane, for Y = 60. The limit between the actual crystal and void space at the back is indicated by the white dotted line. The field is particularly weak at the show front inner corners of the crystal. The back of the crystal presents some weak field regions near the cathode.

Figure IV. presents the electric field magnitude in the X-Y plane at six different depths. In the frontal region of the crystal, the field is stronger (2000-2500 V/cm) where the distance between the electrodes is the smallest. However, the magnitude decreases to values below 500 V/cm at the corners between the flat edges and the front faces. For the taper, the field is stronger along directions normal to the flat edges of the crystal compared to the rounded corners. As the depth increases, the magnitude of the field decreases in the central region. The configuration of the field is more homogenous in the coaxial region, while the magnitude is stronger along the flat edges of the cathode. At the back, the magnitude of the field reduces to typical values < 500 V/cm as one approaches the dead Ge layer.

The low field regions calculated for the front corners and at the back of the crystal indicate that these regions offer poor drift conditions which results in trapping and recombination of charge carriers, and lead to the observation of long collection times and probably charge losses, as discussed in Chapters V and VI.

2.3.2 Charge Carriers Drift Velocities

The drift velocities $\vec{v}_d$ are estimated from the information provided in [Mih00], using the following expression

$$\vec{v}_d = A(\|E\|)\sum_j \frac{n_j}{n} \frac{\gamma_j * \vec{E}_0}{\left(\vec{E}_0 * \gamma_j * \vec{E}_0\right)^{1/2}} \tag{IV.8}$$

where, A is a function which depends on the electric field magnitude E, $\vec{E}_0$ is the normalised electric field vector, and γ_j is the electron effective mass tensor for the j^{th} valley. The values of A and n_j/n were determined for different field magnitudes and orientations from the estimation of the drift velocity v_d in the $\langle 100 \rangle$ and $\langle 111 \rangle$ directions. Both v_d values were derived from fits to experimental data using the empirical formula [Mih00, Oma87]

$$v_{\exp} = \frac{\mu_0 E}{\left(1 + \left(E / E_0\right)^{\beta}\right)^{1/\beta}} - \mu_n E \,. \tag{IV.9}$$

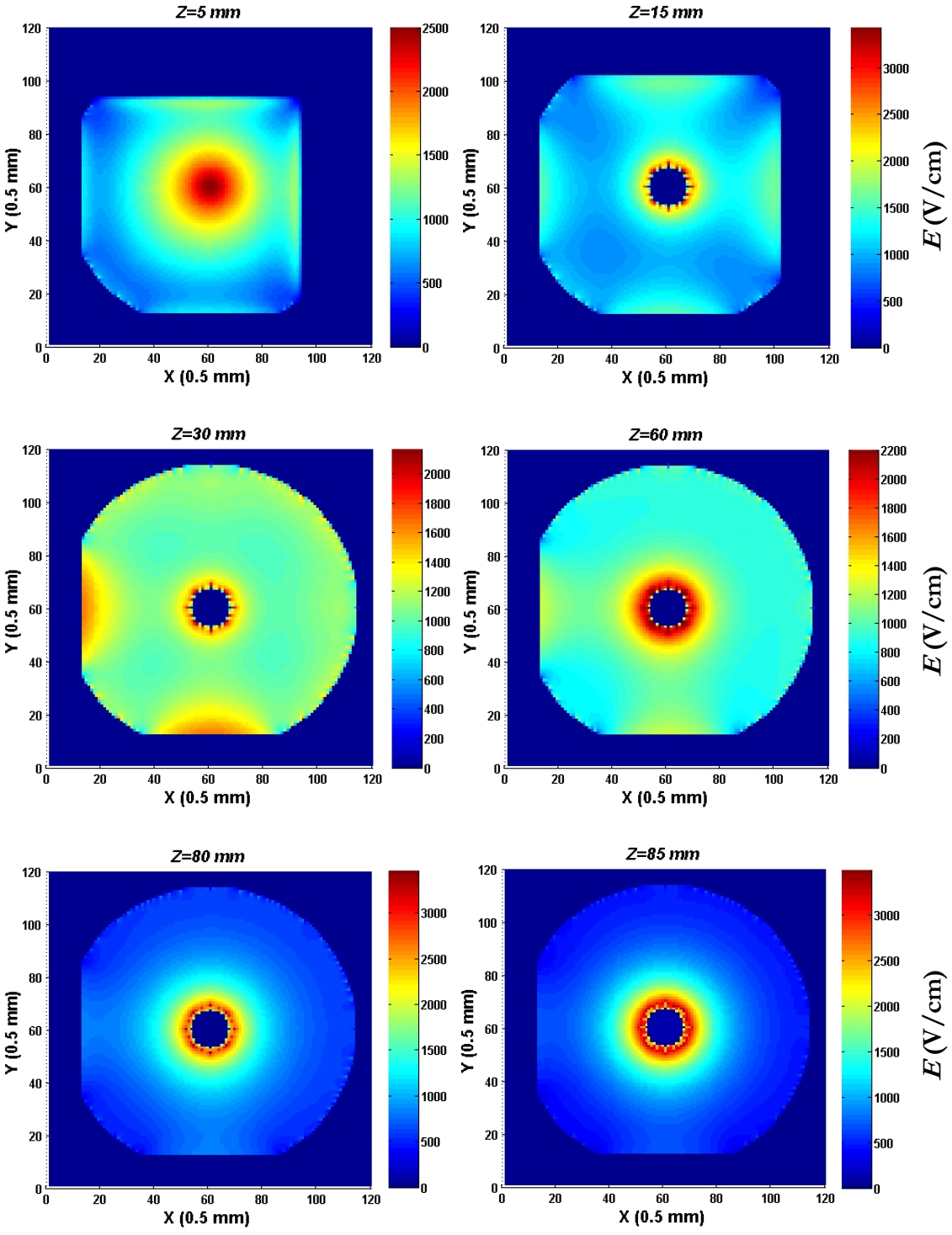

Figure IV.13: Electric field magnitude in the X-Y plane at different depths Z, starting from the front face of the crystal. The colour scale represents the values of electric field magnitude in V/cm. The field is stronger in the frontal region of the crystal, where the distance between the electrodes is the smallest. Along the taper, the field is stronger along directions normal to the flat edges of the crystal. As the depth increases, the magnitude of the field decreases in the central region. At the back, the magnitude of the field reduces as one approach the dead Ge layer.

The initial values of the parameters[22], are given in Table IV.3 below.

Direction	$\mu_0\left[\frac{\text{cm}^2}{\text{V.s}}\right]$	$E_0\left[\frac{\text{V}}{\text{cm}}\right]$	β	$\mu_n\left[\frac{\text{cm}^2}{\text{V.s}}\right]$
$\langle 100 \rangle$	40180	493	0.72	589
$\langle 111 \rangle$	42420	251	0.87	62

Table IV.3: parameters used to model the variation of the electron drift velocity with electric field.

In addition to the anisotropy of the drift velocity, the angle between the velocity and the electric field vectors is taken into account. However, in the case of the EXOGAM Clover, the hole collection is not affected by this effect: the segmentation of the cathode relative to the crystallographic axes has been designed so that a particular segment collects the holes generated inside its volume.

Figure IV.14 presents the drift velocities of electrons calculated by MGS from Equation IV.9 along three major crystallographic axes. The saturation regime is reached for fields greater than 3000 V/cm for the <100> and <110> directions, and ~4000 V/cm for the <111> direction. Figure IV.15 shows the calculated electrons drift velocity in the X-Z plane, along the $\langle 100 \rangle$ direction. The drift velocity appears to be unsaturated in a large region of the crystal volume: particularly at the front corners, and at the back of the crystal. At Z=60 mm, a reduction of ~3×10^6cm/s is predicted for the electrons drifting from the cathode (~800 V/cm) to the anode (~2000V/cm) along the <100> direction. Additionally, the back of the crystal seem to lose holes on the dead layer. The effect is even more pronounced along the <110> direction, as shown by Figure IV.16. The z component of the hole drift velocity is represented in Figure IV.17.

[22]This formula is based on the square-root model [Oma87], which represents the variation of the carrier drift velocity V with electric field E:

$$V = V_s \frac{\mu_0 E}{\left[1 + E/E_C\right]^{1/2}}$$

where V_S is the saturated drift velocity, μ_0 is the ohmic mobility and $E_C = V_S/\mu_0$ is the critical field. The parameter β has been adjusted to account for the term fitting the negative differential mobility of electrons at high fields.

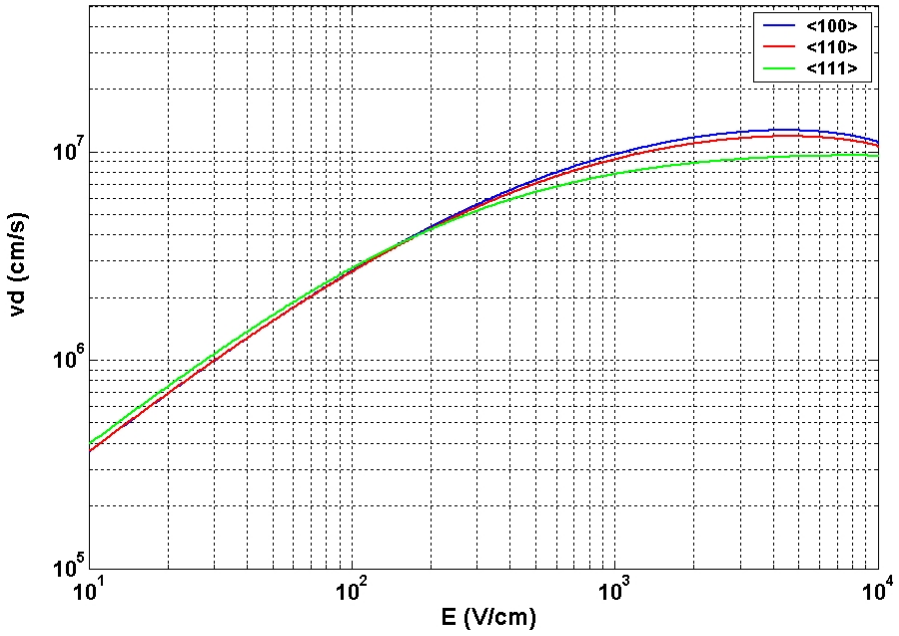

Figure IV.14: Calculated drift velocities of electrons in Ge along the $\langle 100 \rangle$, $\langle 110 \rangle$ and $\langle 111 \rangle$ directions. The saturation regime is attained for E > 3000 V/cm for the $\langle 100 \rangle$ and the $\langle 110 \rangle$ directions. Stronger fields are required to saturate the electron drift velocity along the $\langle 111 \rangle$ direction.

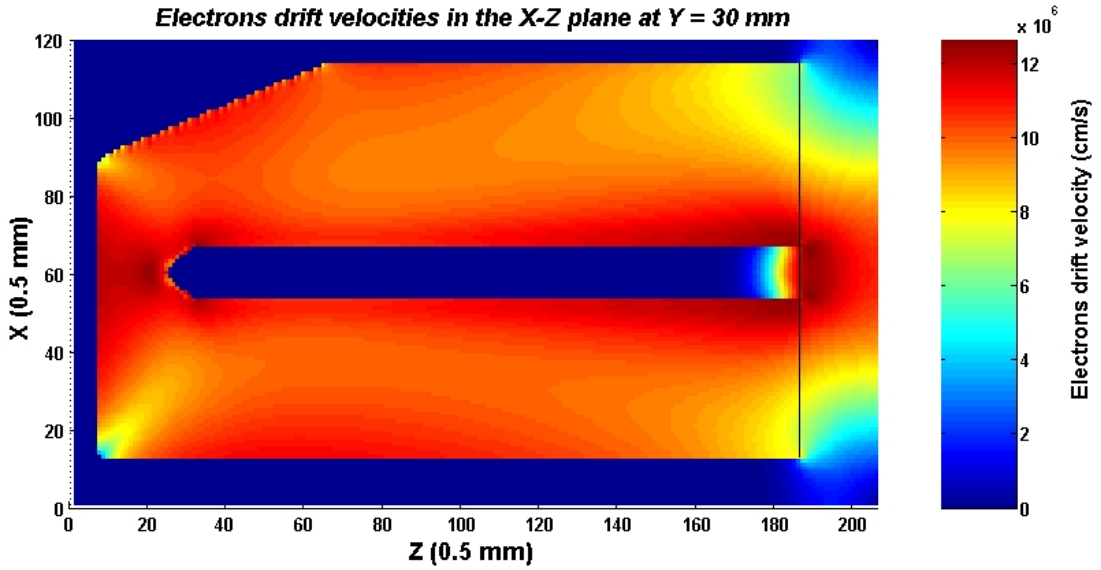

Figure IV.15: Electron drift velocities in the X-Z plane. Non saturated regions (values < 10^7 cm/s) are apparent at the inner corners at the front of the crystal, in the middle of the coaxial region and at the back of the crystal.

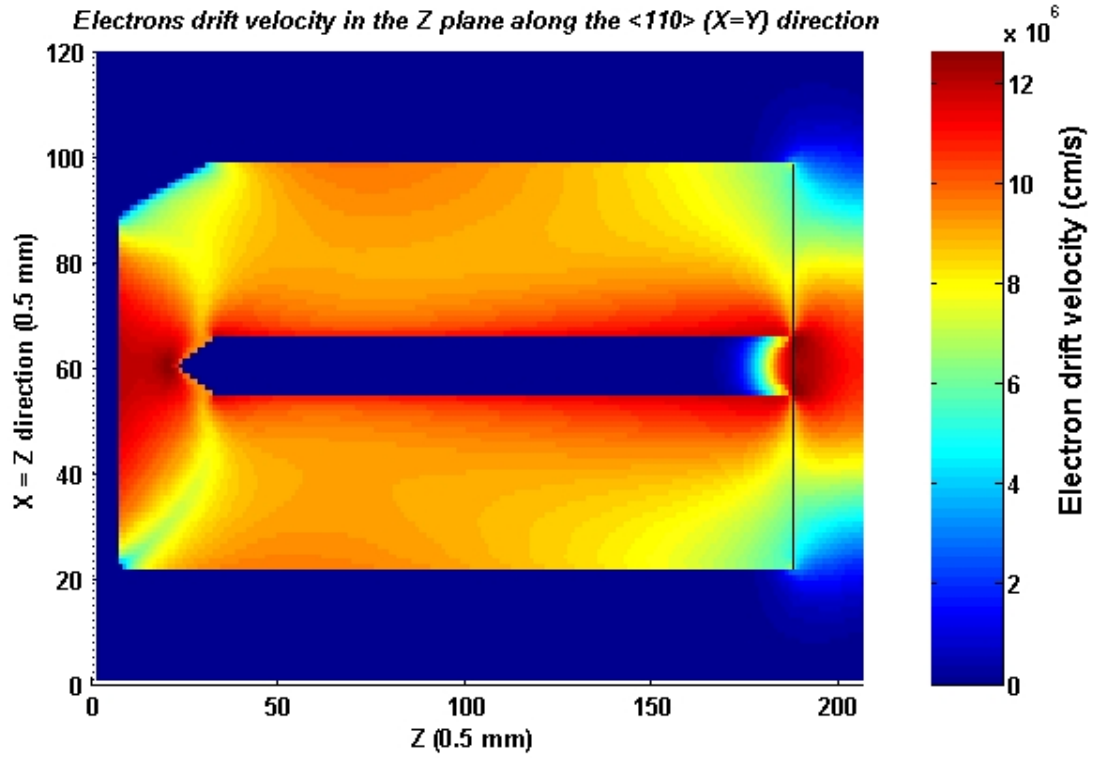

Figure IV.16: Electron drift velocity along the <011> direction.

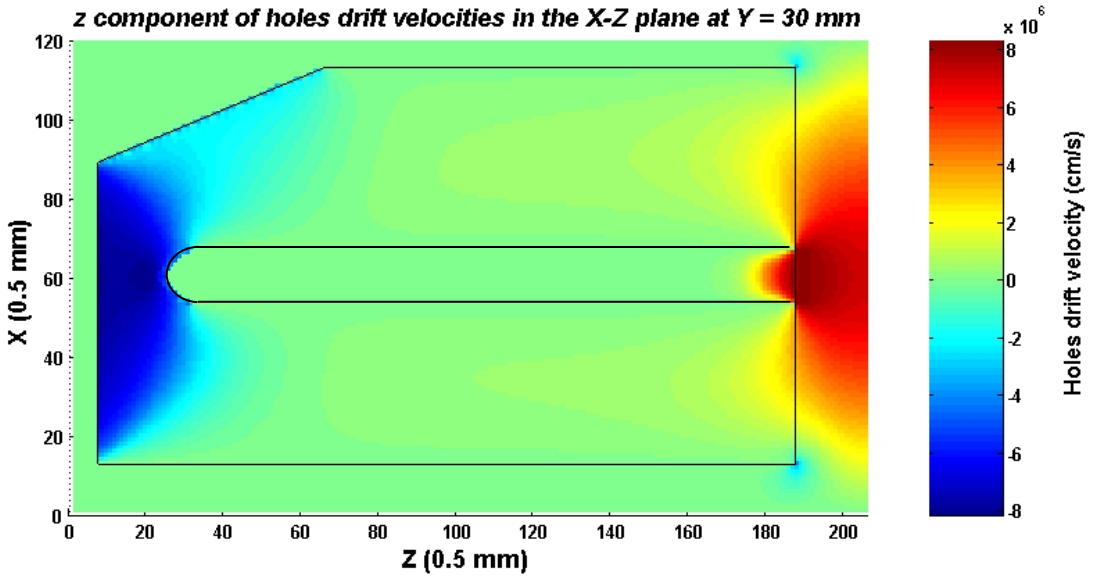

Figure IV.17: Z component of the hole drift velocity in the X-Z plane. The limits of the crystal are indicated by the black lines. An angle shift is present between $v_h(z)$ and the <100> direction, as indicated by the positive value of $v_h(z)$ in the coaxial region, from z = 70 ~ 80. However this is not related to the effect described in [Mih00], it is rather an effect of the electric field configuration within the crystal. The closer to the back of the crystal, the larger $v_h(z)$. One expects the holes to be collected and recombine on the dead layer for interactions occurring in the back volume of the crystal.

2.3.3 Weighting field matrices

The weighting field for the anode and the corresponding outer cathodes are then calculated. The weighting potential is solved in the same manner as the electric potential inside the crystal (convergence of SOR before refining the solution by relaxation method); with a null space charge density and special set of boundary conditions[23]. The weighting field for electrode A1 is shown in Figure IV.18.

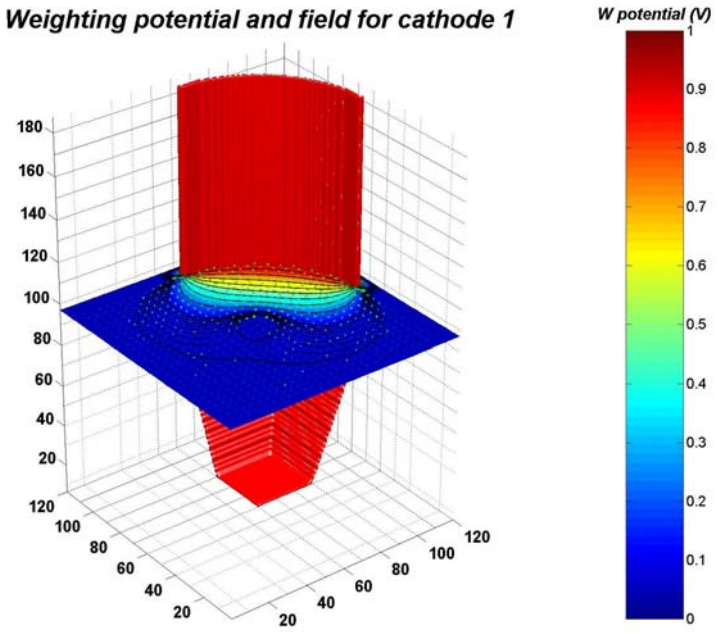

Figure IV.18: Weighting potential for cathode A1 in the X-Y plane for Z = 47 mm. The weighting potential has been calculated by solving Laplace equation $\nabla^2 u = 0$, for $u\ (x, y, z)_{A1} = 1$ V, and $u\ (x, y, z)_{electrodes} = 0$V, where the potential of all other electrodes (A2, A3, A4 and anode) is set to 0V.

2.3.4 Detector signals

At this stage, all the matrices needed to obtain the pulses resulting from a single interaction are available. Pulse shapes may then be generated by entering the position and energy of the interaction. It is possible to follow the time evolution of each parameter along the drift path: velocity, current, charge and electric field encountered in order to check the consistency of the data. The current induced on each electrode is calculated using Equation II.26

[23] The calculation of the weighting field is described in Chapter II, section 2.2.1.

$$i(t) = Q \cdot \vec{v}(t) \bullet \vec{E}_w \qquad \text{(IV.10)}$$

where Q is the total charge deposited by the γ-ray at the interaction[24] site; $v(t)$ is the time varying drift velocity vector, and $\vec{E}_w$ is the weighting field. The charge pulse is obtained by means of the integration of the current through a capacitance of (typically) 1pF. The three example pulses presented in Figure IV.2 were obtained at different radial interaction positions (R = 8, 17 and 26 mm), at an orientation of 45° relative to the X direction, for an energy of 662 keV deposited in the crystal.

2.4 Validation of simulation with experimental results

In order to compare the pulse shapes obtained with the simulation to the experimental pulses, it is necessary to simulate the operation of the charge sensitive preamplifier. The performance of the preamplifier has been measured and was presented in chapter III (section 2.4). The front end electronics was simulated using SIMULINK [MAT], a software package dedicated to the simulation of dynamic systems. The impulse response of the preamplifier is assumed to be of the form:

$$h(t) = \left[A\left(1 - \exp\frac{t}{T_r}\right)\right] \exp\left(\frac{t}{T_d}\right) \qquad \text{(IV.11)}$$

where A is the gain of the amplifier, T_r is the rising time constant and T_d is the decay constant. The values T_r and T_d have been calculated from the average of the preamplifier rise time measurements (Table III.1), and from fits to the decay part of anode pulses for crystal A.

The preamplifier is modelled by three transfer functions in series. The first function accounts for the rising part of the preamplifier impulse response. The second and third transfer functions account for the resistive feedback preamplifier, followed by the pole-zero cancellation stage (PZ). The final time constant of the system is very similar to the value measured on detector pulses. Figure IV.19 shows the schematic of the model. The noise from the fluctuations of the leakage current of the semiconductor diode was neglected.

[24] Q is equivalent to the number of electron/hole pairs generated times the electronic charge e.

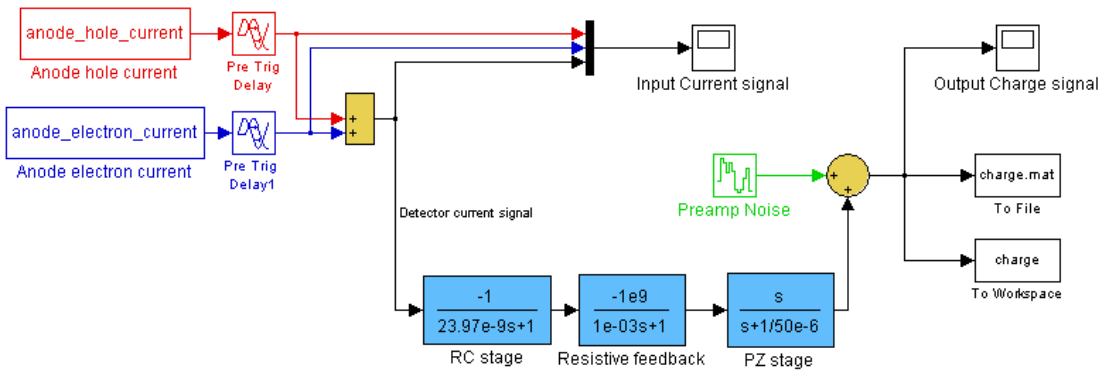

Simple model for EXOGAM Clover Front End

Figure IV.19: SIMULINK model of the preamplifier. The hole and electron currents calculated by MGS are loaded into the SIMULINK model. Both Pre Trig Delay boxes introduce a delay of 800 ns to the pulses. The detector (sum) current is then processed by the preamplifier transfer functions. The electronic noise is added to the final charge signal, before being sent back to the MATLAB functions for further analysis. The simulation runs for 12μs, using a "fixed-step" ODE solver (Ode5, Dormand Prince).

The noise added after the PZ transfer function represents the electronic noise within the preamplifier. The Power Density Spectrum (PDS) of the noise has been measured from the output of the GRT4 card[25], digitising the preamplifiers signals at a rate of 80MHz. The noise generator box generates a white noise distribution, of power P_N.

Figure IV.20 presents typical noise results from the detector. Figure IV.20 (a) presents a typical outer cathode noise signal digitised by the GRT4 card. The magnitude has been scaled to keV. Figure IV.20 (b) shows the PDS and integrated PDS from the cathode noise signal. Over the 125 MHz bandwidth of the preamplifier, the noise power has been estimated at P_N = 3.75 keV (6.01 $J.K^{-1}$). The gain of the preamplifier has been set to match the requirements for the EXOGAM Clover (200mV/MeV).

[25] The GRT4 Card is presented in Chapter V.

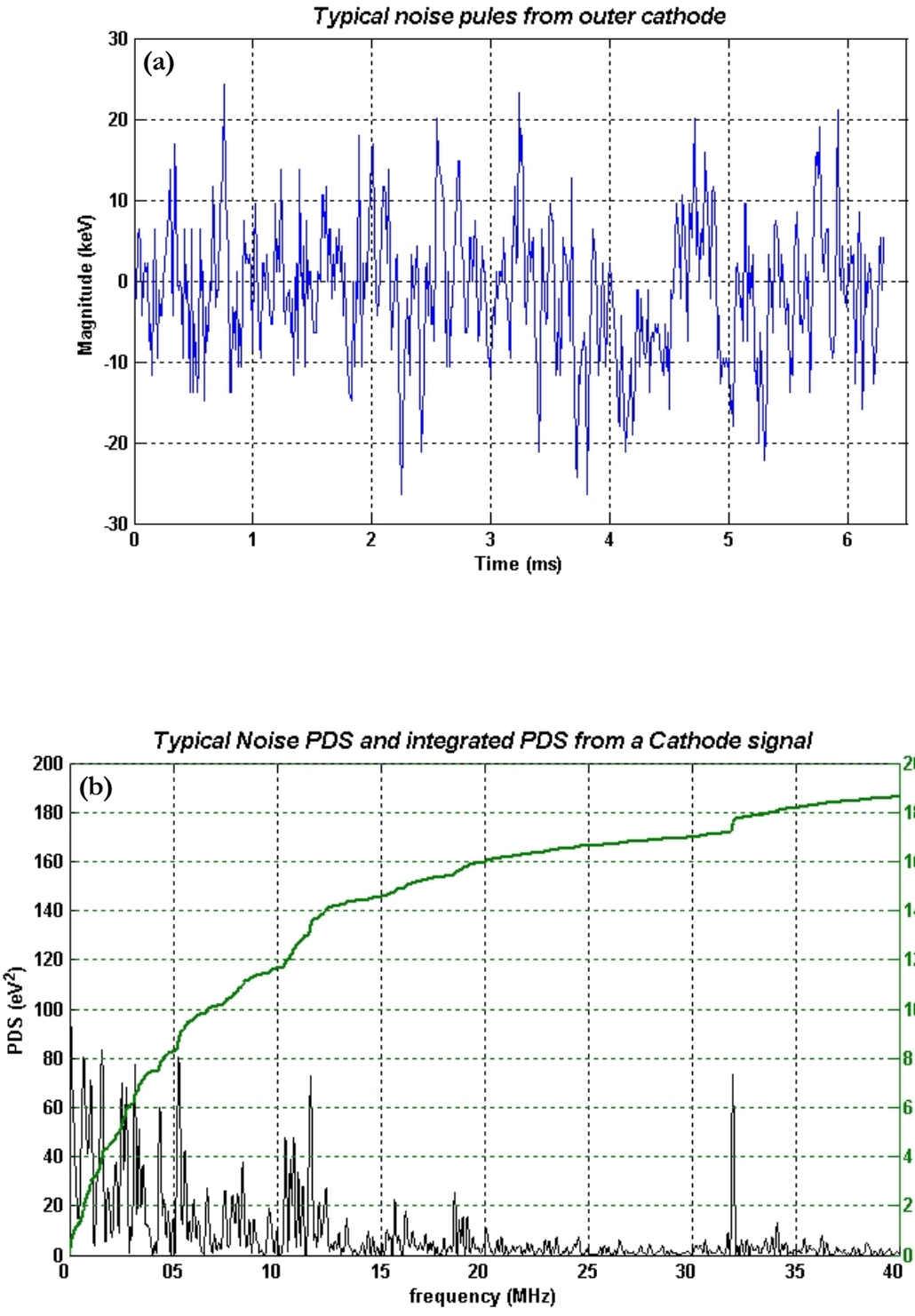

Figure IV.20: (a) Detector noise signal, the magnitude, given in (keV) has been scaled to 1.05 keV/channel; (b) Power Density Spectrum of a typical noise signal from the Clover detector. The green continuous curve represents the integrated PDS.

Examples of the final charge pulses, after processing by the simulation model are presented in Figure IV.21, Figure IV.22 and Figure IV.23. The initial current pulses presented in Figure IV.3were used as input to the model. The magnitude of the pulse actually corresponds to the experimentally observed magnitude. The resulting charge pulses present long rise times for both interaction located near the electrodes. At R = 8 mm, the rise time of the pulse is ~240 ns. Near the cathode, at R = 26 mm, the value of T90 is ~210 ns. At mid radius, where the drift time of the carriers is minimum, the rise time is ~140 ns. Qualitatively, this shows good agreement with the pulses presented in Figure IV.5. In the future, the MGS software will be used in conjunction with the AGATA prototype scan data.

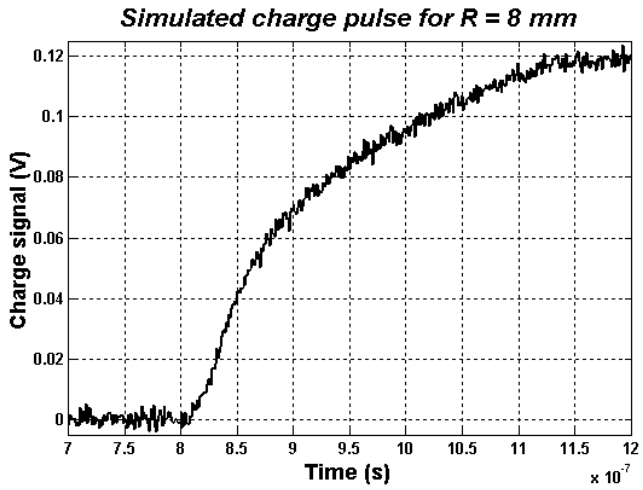

Figure IV.21: Simulated charge pulse for interaction at R = 8 mm. The corresponding T90 value is ~ 240 ns.

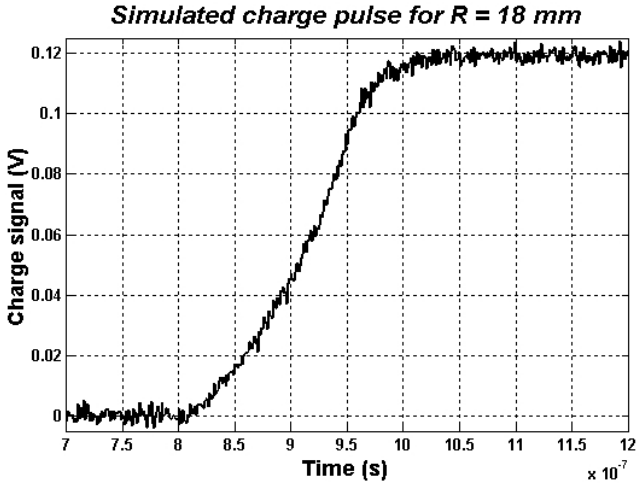

Figure IV.22: Simulated charge pulse for interaction at R = 18 mm. The corresponding T90 value is ~140 ns.

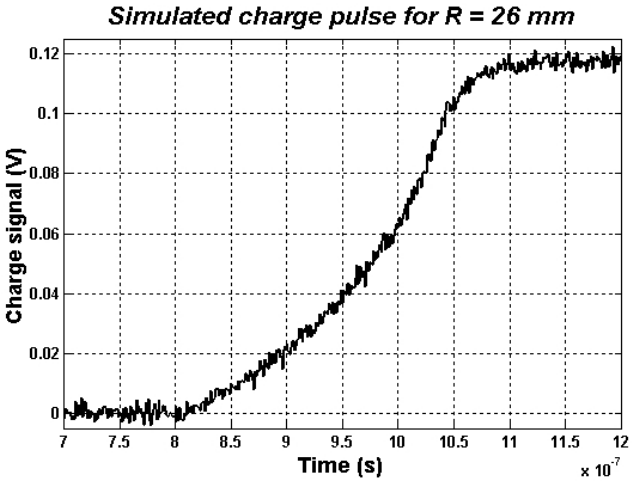

Figure IV.23: Simulated charge pulse for interaction at R = 26 mm. The corresponding T90 value is ~210 ns.

Chapter V

CHARACTERISATION MEASUREMENTS

Experimental details and detector scanning

After the description of the EXOGAM Clover detector and the introduction of the characterisation methods employed in this work, the following chapter is intended to give the reader a description of the experimental methods used to perform the characterisation of the EXOGAM Clover 06 detector. The first section considers the aims and motivation behind each measurement. The experimental set-up available is described, along with general results from each measurement.

1 Presentation of the characterisation measurements

1.1 Aims

1.1.1 Evaluation of the crystal design

The aim behind the experimental measurements is to evaluate the design of the EXOGAM Clover detector for use with digital PSA. The first step was to investigate the electrostatic properties of the crystals through measurements involving a precise knowledge of the location of gamma–ray interactions within the detector volume.

1.1.2 Improvement of the position determination

This work also details the performance of the detector as a function of interaction position of a gamma-ray photon. The segmentation of the EXOGAM Clover coupled with digital acquisition electronics enables the use of PSA methods (see Chapter IV) in order to improve the position location of gamma-ray interactions. Although the Clover detector has not been designed for such utilisation, this work investigates how well PSA techniques perform with a non cylindrical Ge crystal and gives some results on the possible improvement of the determination of the interaction site within a segment. However, the limits of this intra-segment detection need to be defined in terms of improved granularity, for each particular segment geometry.

Characterisation measurements are the first step towards the overall improvement of the energy resolution. Indeed, better information on the interaction position would lower the uncertainty on the emission angle of a γ-ray, and would therefore lead to a further reduction of Doppler broadening. The **S**egment **P**ulse **A**nalysis **C**ard for **E**XOGAM (SPACE) module [Fra04], dedicated to the PSA of the segment signals is under development at the IPN Orsay.

1.2 The experimental characterisation of the detector

1.2.1 Scan measurements

Several measurements were performed with the EXOGAM Clover 06 detector. The experimental procedure was identical for all measurements: a radioactive source was collimated and placed at different positions in front of the detector. The response signals were then recorded during a finite time and the source was moved to the next position. For each measurement, the whole set of data consisted of a *scan* of the detector.

A ^{137}Cs and a ^{57}Co source were chosen for the measurements. Both sources provide a well defined γ-ray energy line at 122 keV and 662 keV, respectively. The resulting energy spectrum can then be analysed in terms of "Full Energy Peak" (FEP) and "Compton Continuum" components, ideally reducing the background down to the number of random coincidences from environmental and cosmic radiations. The different penetration depths of the gamma-rays delivered by the sources are indicated in Table V.1. The mean free path of a 662 keV photon in Germanium is about 25 mm, which allows the probing of the detector over the whole thickness of the crystal. The mean free path of 122 keV γ-rays is about 5 mm, restricting most of interactions to occur within the first 10 mm of Germanium.

Several scan measurement were performed with the two sources:

- A singles front face (X-Y) scan at 662 keV. The objective of the scan was to investigate the general properties of the Germanium crystals. The data set was also used to perform a general position calibration.

- A singles X-Y scan at 122 keV. The ^{57}Co source was used to characterise the closed ended region of the germanium crystal and study the effects of the complex electric field configuration in this region.

- A single side (Z) scan at 122 keV. The ^{57}Co source was used to probe a single Clover crystal along a tapered segment. The drift properties of electrons along the full length of the segment were investigated. The rise times are expected to be uniform for interactions occurring along the coaxial region of the crystal, and then vary along the tapered side. Such a scan was also important to provide a direct understanding of the effect of the dead germanium layer at the back of the crystals on the electric field and on the generation of the detector signals.

Source	Activity (Bq)	Photon energy (keV)	Mean free path in Ge (mm)
^{57}Co	3.7×10^{9}	122	~5
^{137}Cs	12×10^{9}	662	~25

Table V.1: Properties of the ^{57}Co and ^{137}Cs sources used in this work.

2 Data acquisition system

2.1 The Liverpool detector scanning system

The scanning system used in conjunction with the EXOGAM Clover was built especially for the purpose of characterising HPGe detectors and was first described in detail in [Des02]. Several HPGe detectors of coaxial and planar geometries, comprising different segmentation patterns, have been scanned in the Nuclear Physics Laboratory at the University of Liverpool. Such a system has proved to be an essential device to understand the behaviour - and detect particular problems – of segmented HPGe detectors [Bos04, Gro03 and Nor03]. The scanning system consists of a computer controlled positioning table on which is placed a collimated radioactive source. The source is moved in the horizontal (X-Y) plane in order to record output signals arising from several interaction positions within a germanium detector.

The scanning set up is presented in Figure V.1 in the X-Y configuration. The detector is positioned vertically, facing down, in front of the collimated source placed on the top of the moving table. The source and the detector are separated by a 80 mm long by 20 cm diameter Lead cylinder, in which a Tungsten (high γ-ray attenuation power) collimator is inserted. The collimator dimensions were 80 mm long with 2 mm inner diameter (see Appendix B, Figures B1 and B2). An identical collimator with 1 mm inner diameter was also available but, in spite of the thinner beam spot provided by the finer collimation, the count rate was too small given the available source strengths and the improvement obtained was not significant compared to the 2 mm collimator.

2.2 Data acquisition

The detector was connected to a digital acquisition system, based on the newly developed **V**ERSA **M**odule **E**urocard (VME) **G**amma **R**ay **T**racking **4** channels (GRT4) cards [Laz04] designed to operate with highly segmented HPGe detectors. The output of the detector charge preamplifiers were fed into the GRT4 input channels, which digitised and pre-processed the pulses resulting from an event.

2.2.1 The GRT4 card

The GRT4 module was developed in the frame of the UK Gamma Ray Tracking project. Its design utilises **F**lash **A**nalogue to **D**igital **C**onverters (FADC) and **F**ield **P**rogrammable **G**ate **A**rrays (FPGA) to digitise and process the detector pulses.

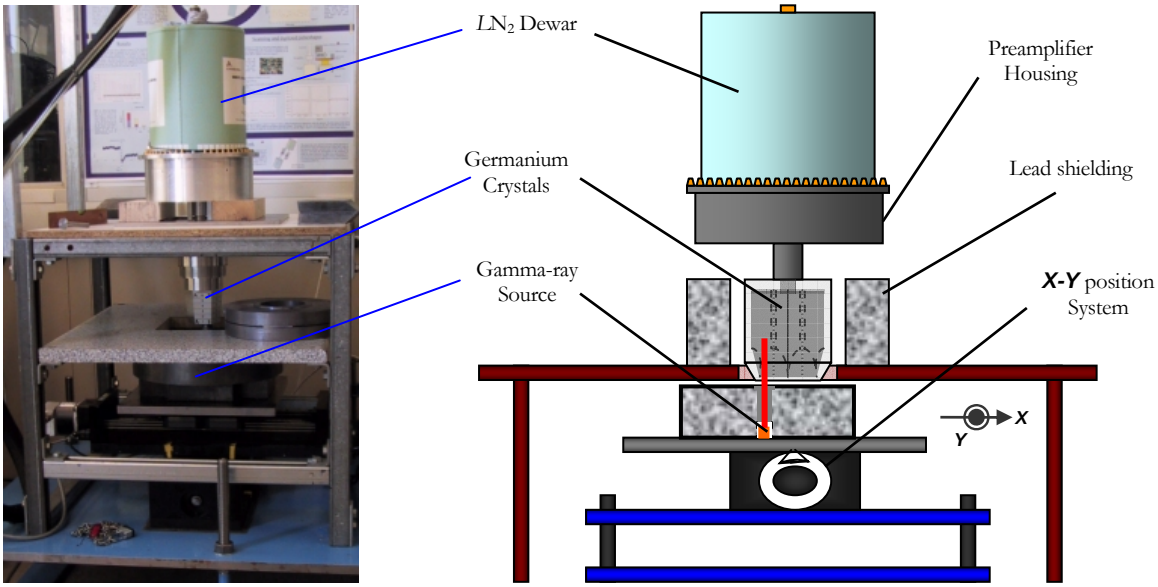

Figure V.1: Picture and schematic view of the scanning apparatus. The left picture presents a coaxial segmented HPGe detector on the scanning table; the lead cylinders located on the right side of the Ge crystal are used to shield the Germanium from environmental radiation. On the right, a schematic view presents the EXOGAM Clover on the scanning system set for the X-Y scan.

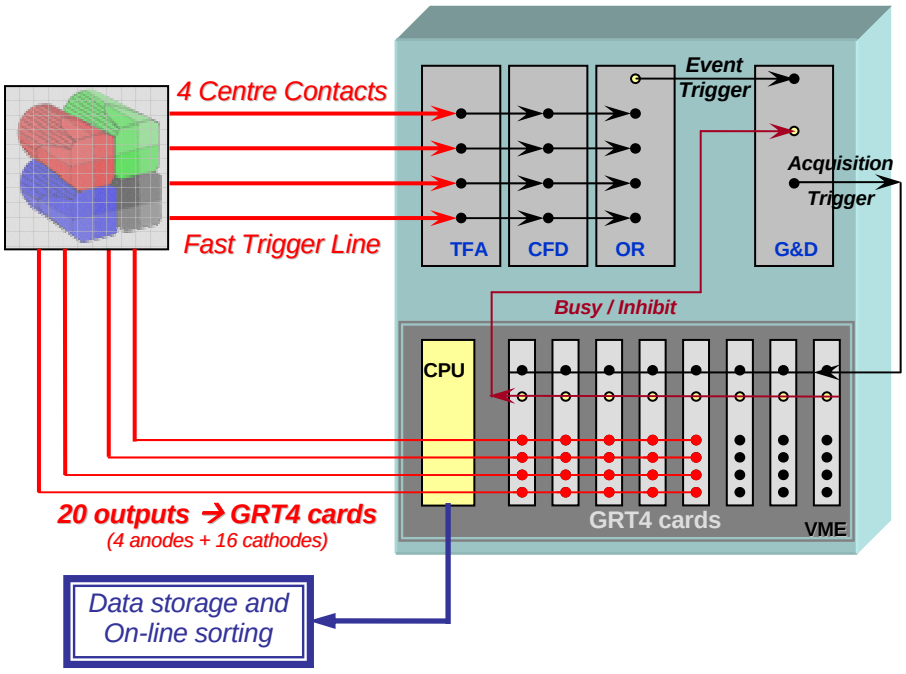

Figure V.2: Schematic illustration of the data acquisition system (DAQ). The *Event Trigger* is generated by the four centre contacts. The *Acquisition Trigger* signal is delivered to the GRT4 cards by the G&D module. Data are read by a fast VME processor and sent through an Ethernet link to the acquisition PC.

A GRT4 card consists of 4 input channels running in parallel, each including an ***AD6645*** FADC [AD03] and two ***Spartan Xilinx 2*** FPGA [Spa03]. The FADC provides a 14-bit dynamic range over 2.2V, with an internal clock at a frequency of 80 MHz. The first FPGA contains a circular buffer, a digital CFD, the internal trigger and energy measurement algorithms, while the second FPGA is dedicated to buffering and pulse pre-processing tasks. At the time of the measurements (May to August 2002), the GRT4 was used in "oscilloscope mode": the detector pulses were digitised by the FADCs and sent directly (without pre-processing) to the acquisition computer for storage and off-line analysis. The digital signal consisted then of an ID word, a 48 bit timestamp (three 16 bits words) and 508 samples corresponding to a 6.5 μs long pulse. The pre-trigger[26] point was set to the sample number 64. From this period, the FPGA programs were tested and regularly upgraded[27]. The GRT4 now delivers a shorter block of data consisting of an ID word, a 3 word timestamp, an *Energy* word, which is then followed by 250 samples centred on the leading edge of the pulse.

2.2.2 The Acquisition system

Five GRT4 modules were needed in order to process the 20 signals from the Clover detector; the full data acquisition (DAQ) system is presented in Figure V.2. The output line of each centre contact was split into two branches. The first branch was connected to the input of the first GRT4 module, while the outer contact signals were grouped by crystal, connecting the four channels from the same crystal into the same card. The second branch consisted of a fast triggering chain in which each core signal was processed by a Timing Filtering Amplifier (TFA) followed by a Constant Fraction Discriminator (CFD), delivering the fast triggering signals. The four fast trigger lines were connected to a logical OR and delivered the *Event Trigger* signal. The *Acquisition Trigger* signal was then generated from the *Event Trigger* by a Gate & Delay (G & D) box, duplicated by a logical Fan In / Fan Out module and fed into the TRIG IN front port of each GRT4 card. Once an event was validated, the *Acquisition Trigger* signal was sent to the GRT4 cards for the processing and storage of the detector pulses until the internal buffer of the cards was full. Data were finally read out sequentially from the card; inhibiting the *acquisition trigger* (G & D box) until the last GRT4 module was read out.

---

[26] The pre-trigger point corresponds to the sample with a value equal or closest to half of the maximum pulse value.

[27] After the last upgrade, the FPGA include the following algorithms: a Moving Window Deconvolution (MWD) algorithm [Geo94, Lau04] to calculate the energy; a digital CFD, an internal trigger, and a pile up rejection algorithm. In addition, the length of the digital signal is now truncated from 512 to 256 data words, thus reducing further the output data stream by delivering only the leading edge of the pulse, which contains the shape information.

The five GRT4 cards were placed in a VME crate and read out by a fast VME processor. The data were sent via an Ethernet link to a Linux PC running several programs for the acquisition, processing and online analysis of the data. A Tape Server merged the data before storage on magnetic tape, or made them available for online analysis. The data acquisition, the parameterisation of the GRT4 and the scanning table were controlled by the **M**ulti **I**nstance **D**ata **A**cquisition **S**ystem (MIDAS), developed at CCLRC Daresbury Laboratories [MIDAS] and some "in-house" software [Cre02]. The online analysis of the data was performed using the MTsort package from the University of Liverpool [MTsort].

3 Experimental measurements

The front face of the detector was scanned in singles mode by utilising both ^{137}Cs and ^{57}Co sources. Then, the detector was scanned along a tapered segment with the ^{57}Co source. The interaction length of 662 keV photons from the ^{137}Cs source allows the whole crystal depth to be probed. For this reason, the ^{137}Cs measurements form the major part of the results presented in the following sections.

3.1 Front face scan with ^{137}Cs

3.1.1 Scan configuration

The ^{137}Cs source was placed behind the 2 mm diameter collimator, facing the entrance surface of the detector. The distance between the collimator and the aluminium front case was measured to be 3 mm. The source was displaced over the detector front face in 2 mm steps in ***X*** and ***Y*** directions, producing a total of 3136 points. The collimator was held static for 3 minutes at each position, in order to ensure that enough statistics were available for the subsequent analysis. The scan lasted 8 days, producing ~1.2 TB of data which were stored on SDLT magnetic tapes.

The levels of the CFD thresholds were set just below the lower edge of the 662 keV photo peak (~ 650 keV) so that the *Event Trigger* was only delivered for events from photons that would deposit all their energy in a given crystal. It also reduced the amount of unwanted data collected in the Compton background (for data storage consideration), providing a maximum count rate of ~50Hz to the DAQ. Although our trigger suppressed the ability to detect scattered events between adjacent crystals, it was still possible to investigate Compton scattering between segments from the same crystal.

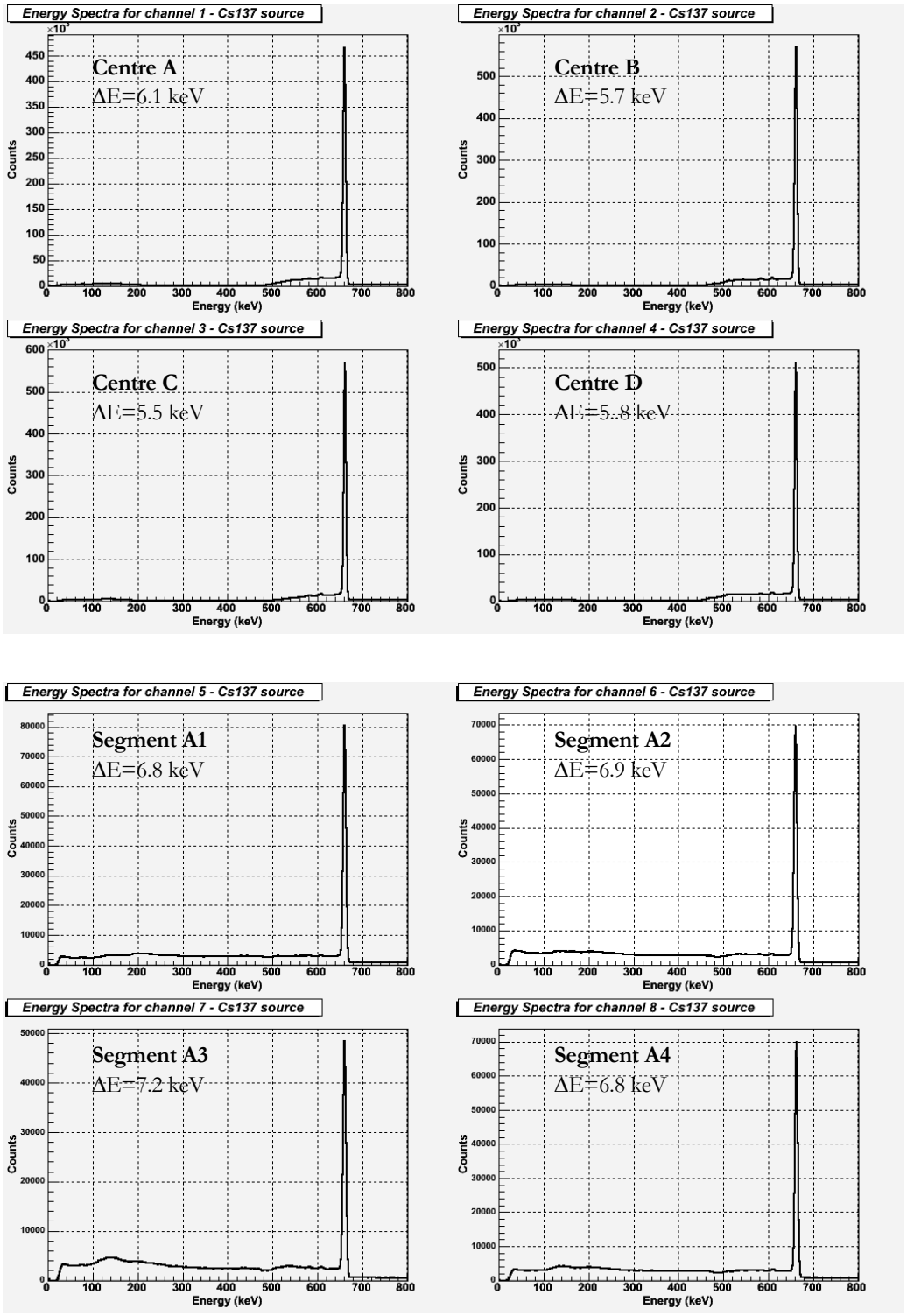

Figure V.3: Energy spectra from centre contacts A, B, C and D (top, channels 1, 2, 3 and 4). The spectra from the outer contacts of crystal A are presented at the bottom. Energy resolution values ΔE are indicated on the spectra. The large measured values are explained by the presence of a parasitic noise introduced by the GRT4 cards before the FADCs digitise the signals.

During the offline analysis, the 20 output signals from each event were split between real charge pulses, transient signals (image charge) and noise signals (zero). The energy was calculated using a simple baseline difference calculation. A first average value of the baseline was taken over 400 ns before the rise of the charge pulse and a second average was calculated from a 400 ns range located, after the rise of the pulse. The standard deviation of the random noise fluctuations was extracted from a range of 700 ns before the start of the pulse. A real charge pulse was observed if the difference between the two average values exceeded 3 times the standard deviation of the noise. If the condition was not fulfilled, the algorithm was looking for an image charge signal. The procedure consisted of looking for an absolute value for the pulse being greater than twice the standard deviation of the noise. The resulting energy resolution is not optimised compared to analogue or MWD results. However this method of energy calculation has no impact on the rise time analysis[28].

Each event was then filtered by a set of conditions on the energies, in order to ensure that only Full Energy Events (FEE) were considered:

1. The energy measured on the anode had to be included within a tight energy window (gate) centred on the **F**ull **E**nergy **P**eak (FEP) (655 – 666 keV);

2. The validation of an event required the sum of energies measured on the four segments to be equal to the energy measured on the central contact of the same crystal. In this way, Compton Scattered Events (CSE) between segments are also recorded.

Example energy spectra resulting from the scan are shown in Figure V.3. The four centre contact spectra are presented along with the four outer contact spectra of crystal A. The values of energy resolutions are much higher than expected, mainly due to the presence of a parasitic noise, induced inside the digitising cards.

3.1.2 Detector and segment Fold

The detector Fold (F) is defined as the total number of crystals or total number of segments that fire in coincidence, while the event Multiplicity (M_γ) refers to the actual number of γ-rays

[28] The MWD calculation method could have been used to calculate the energy, but the charge pulse needs to be at least 12μs long to obtain good energy resolutions from the algorithm. Anyway, the spread of rise time due to a larger FWHM of the photo peak is negligible compared to the spread induced by the geometry of the detector and CSE.

interactions within a detector[29]. Corresponding fold spectra obtained for 662 keV FEE are shown in Figure V.4 and Figure V.5. The fold spectra given for the four crystals are presented in Figure V.4. The centre contact spectrum was incremented for each event whose core signals magnitude were above the CFD thresholds. In parallel, the segment fold was incremented when the level of any cathode signal was above the electronic noise, and discriminated from an image charge pulse.

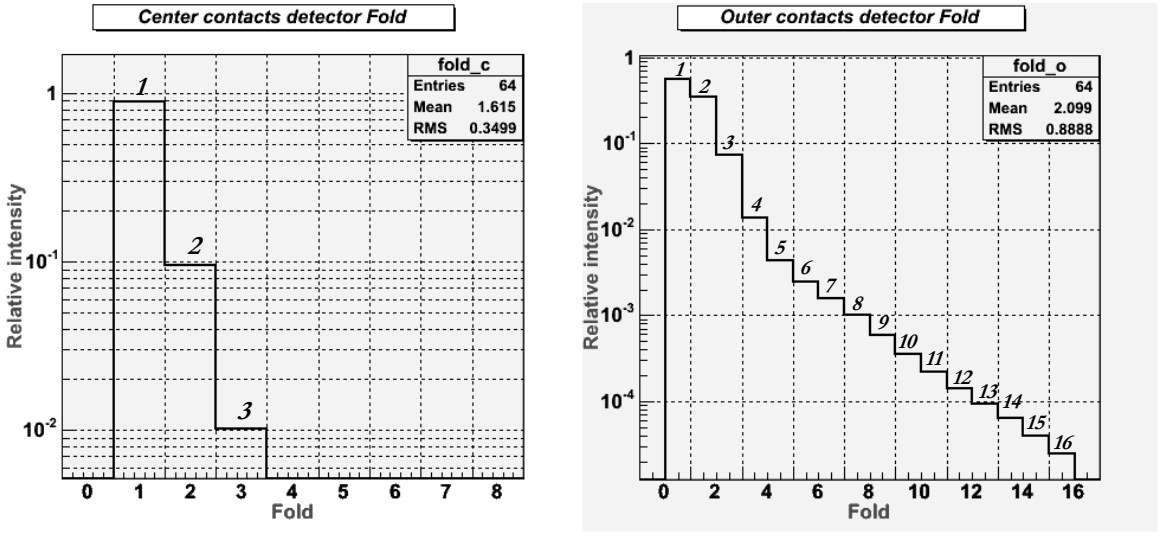

Figure V.4: Detector Fold spectra for centre contact and outer contacts. For clarity, the Fold F is indicated above each bin of the histogram. The intensity has been normalised to the total number of gated events recorded during the scan. On the left, the Centre contact fold spectrum represents the number of gated events detected in coincidence by the four crystals. Fold 1 (F1) events constitute 89.5% of the detected events, while Fold 2 (F2) and Fold 3 (F3) events accounts for 9.5% and 1% respectively. The proportion of Fold 4 events is quasi null (< 0.01%). The right spectrum represents the outer contact fold. The main contribution is coming from F1 to F3.

The majority of events were restricted to a single crystal, as shown by Figure V.4. The proportion of scattering between crystals constituted about 10% of the total events, shared between Fold 2 (F2) and Fold 3 (F3) events. Higher order Fold events were recorded by the segments. However, segment Fold greater than 4 were more likely to be caused by random coincidences from γ-rays absorbed in different parts of the detector, rather than multiple scattering between several crystals (the time overlap between the four CFDs was 200 ns). These high Fold events only accounted for ~ 1.1 % of the total intensity. Inter-crystal

[29] For instance, a Compton scattered event, where a gamma-ray interacts twice in a segment and one time in an adjacent segment will give a fold F = 2, while the multiplicity of the event is M = 3.

scattering was possible, provided that the scattered photon interacting in an adjacent crystal carried an energy larger than the level of the CFD threshold, which restricted considerably the range of scattering angles permitted. The absence of depth segmentation allowed the detection of inter-crystal scattering especially for source positions located near the boundary between two crystals. This explains the small fraction of 2–crystals scattering observed in Figure V.4, which accounts for 9.5% of the total intensity[30]. The probability to detect a CSE between three crystals was negligible (~1%) and quasi null between four crystals.

In Figure V.4, segment fold > 1 can also be attributed to events scattering within segments belonging to the same crystal. Therefore, an investigation of the fold within a crystal is necessary to separate and clarify the contribution of both scattering processes.

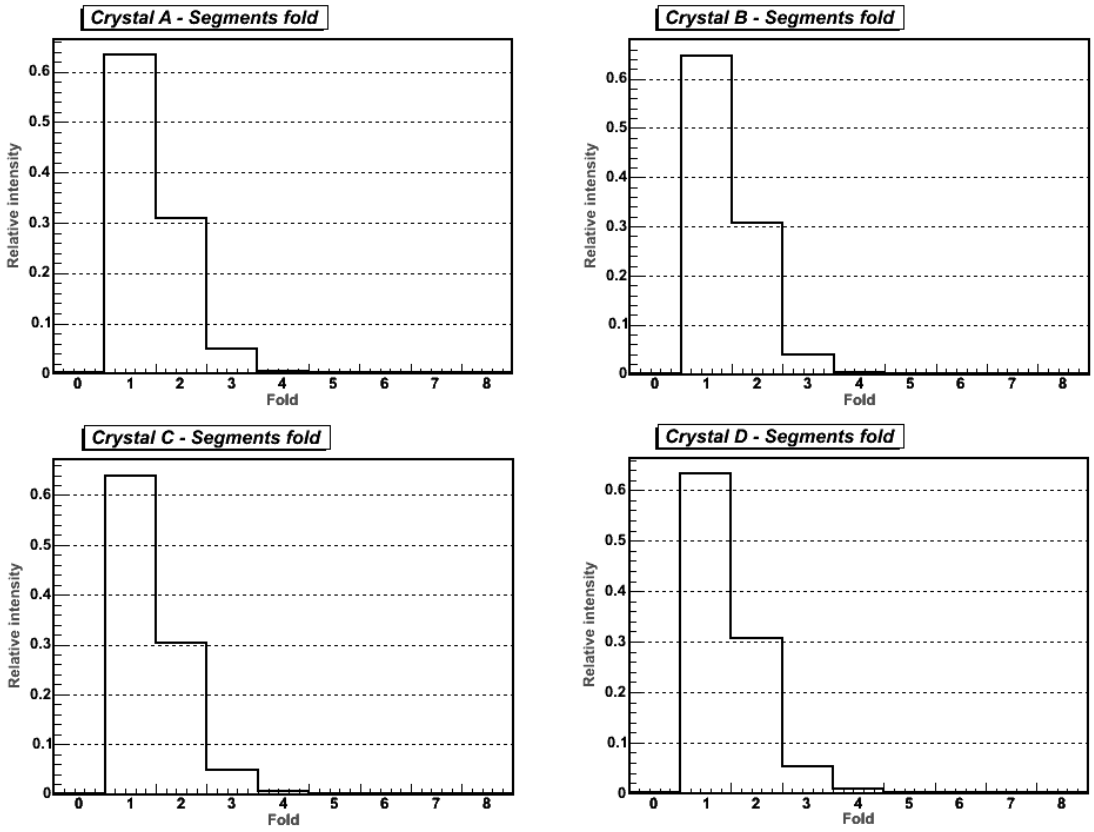

Figure V.5: Fold spectra for segments of each individual crystal. For each crystal, the majority of events are F1 and account for 63-65%, while F2 and F3 are ~30% and ~5% respectively. The reader should note the difference between Fold and Multiplicity: the Fold distributions do not correspond to the average number of interactions of a 662 keV photon in Germanium. The small proportion of F4 events is caused by random coincidences.

[30] One must be aware that a lower CFD threshold would have allowed the consideration of a larger fraction of scattered photon during the acquisition and increased the relative intensity measured for F2 and F3 events.

Each crystal behaved in a similar manner as illustrated in Figure V.5: the majority of events were due to the detection of a single interaction[31] and account for 63 – 65% of the data. Then two fold events accounted for 30 – 31% and a smaller fraction ~5% of intensity is attributed to 3 photons scattering. Finally the proportion of four photons scattering was below 0.1%, which is therefore negligible.

3.1.3 Detector sensitivity to 662 keV energy photons

Ungated Energies

The number of photo peak events recorded at each position, referred to as the intensity map of the detector, is shown in Figure V.6 (a). Each pixel corresponds to a particular source position and shows the number of validated events per source position[32]. Crystals A, B, C and D are identified in Figure V.6 (b), going clockwise from the top right hand corner. The active volume, with intensities > 12000 counts (with a maximum count rate of ~130 cps), is distinct from the background intensity[33] (from 9000 to 12000 counts or 50 to 66 cps). Such a large number cannot result solely from environmental radiations. The design of the collimator was not ideal and let some source γ-rays emitted at large divergence angles escape through the thin thickness of Tungsten. The γ-rays which were not blocked by the Lead were detected in the Germanium. The effect of the incomplete collimation appears clearly in the simulation of the collimator presented in Appendix B. In Figure B.3, the intensity of γ-rays detected at large radii in the front part of the germanium cannot be simply explained by back scattering. A relatively important part of γ-rays transmitted at large angle through the lead contributed to the large outer flux observed in the front of the crystal. During the scan, a large number of γ-rays were still hitting the detector for sources positions out of the detector front face, resulting in the large background intensity.

The four crystals are also well separated from each other, as shown by the lower sensitivity measured at the crystal boundaries. The larger intensity values are observed for the inner detector region where the thicker amount of germanium material is available. The intensity then decreases while moving towards the edges of the detector, where the active Germanium

[31] The large volume of the segments allows a large proportion of multi scattered events to be treated as single interactions. The only way to detect these particular events is to use digital PSA techniques.

[32] The corresponding intensity will also be referred to as count per second (cps).

[33] The detector was not ideally shielded; so the background has a large contribution from environmental radiations (e.g. ^{40}K…), as well as cosmic rays interacting within the germanium crystals. In this case, the ratio of 'good event' to 'background counts' is ~ 1:3.

volume reduces due to the tapering of the crystals. Also, the energy cut imposed by the CFD threshold suppresses events which deposit an energy lower than 650 keV; this especially applies to Compton scattered events (CSE) near the outer boundary of the detector, where the scattered γ-ray escapes from the Germanium and results in a lower intensity in the peripheral regions of the detector.

Although the four crystals are supposed to have similar performances, some differences are noticeable. The four central circles displaying a lower intensity are due to a small amount of material in front of the anode, where the minimum germanium thickness is ~8 mm.

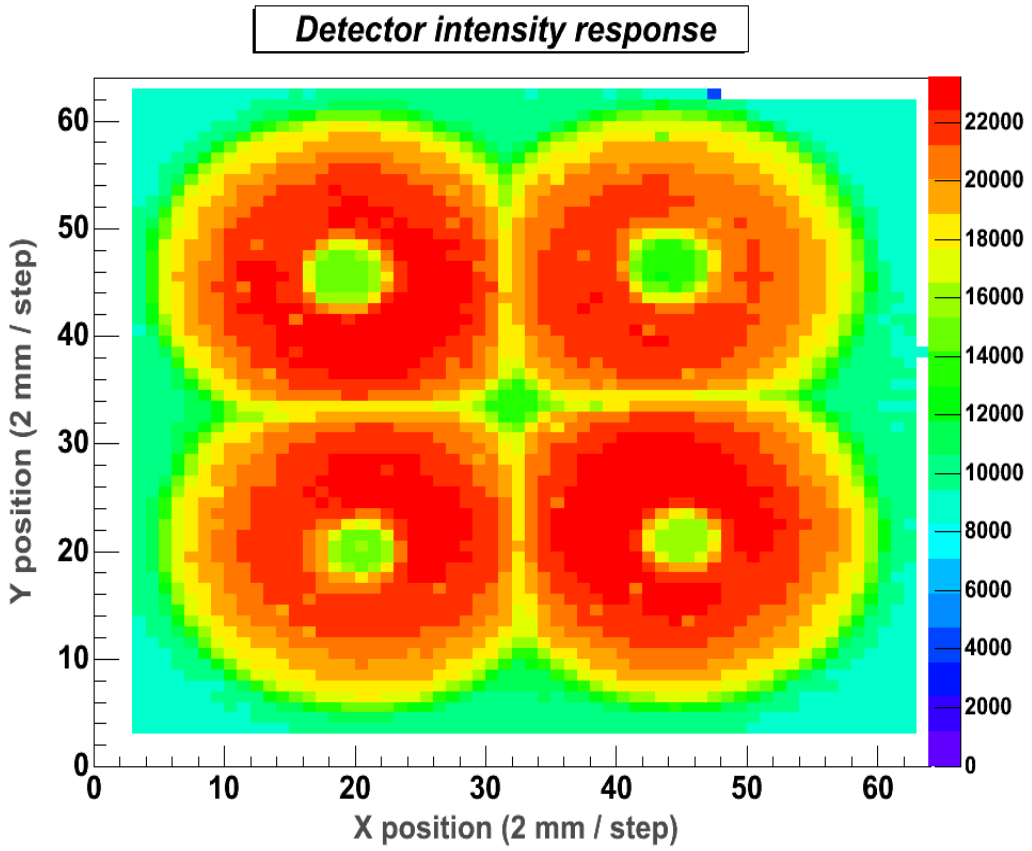

Figure V.6: (a) Intensity response of the Clover 06 detector. Each pixel corresponds to a collimated source position. The colour scale on the right indicates the number of events detected per position during 3 minutes. The active volume of Germanium (red) stands out from the background due to random events (blue). The position of the crystals is indicated in Figure V.6 (b).

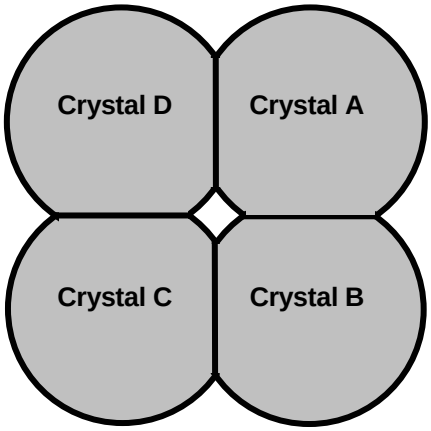

Figure V.6 (b) Position of the crystals. This labelling scheme will be adopted from now in the next parts of this thesis.

The four anodes have a specified diameter of 10 mm, crystal A and D seem to have a larger inner region of lower sensitivity. Two things could possibly cause such a difference: the diffusion of Lithium impurities could have been deeper than expected during the manufacturing of the central electrode, which creates a thicker dead layer around the anode with a very low sensitivity. Also, several reprocessing cycles of the central contact, by etching the surface of the inner hole could have removed some material and resulted in a larger diameter hole. Both effects, taken individually or in combination could explain such differences. However, the diameter of the inner hole of each crystal is indicated in Appendix A, and crystals A and D effectively have the larger inner diameter (respectively 10.7 mm and 10.1 mm). These values are consistent with the results shown in this section.

Gated Energies

The response of the four crystals to 662 keV energy photons has been produced by selecting events that fulfilled the set of conditions defined in section 3.1.1. Results for the anodes and cathodes are shown in Figure V.7 (a) and Figure V.7 (b) respectively. Due to the stringent condition on energy, a large portion of background is removed and CSE between crystals – and segments – are suppressed; the four crystals now clearly stand out of the background. The maximum count rate is ~72 cps, measured at the centre of the detector, compared to ~11 cps measured in the background, giving a 1:7 ratio between true events and background. Crystals A and D have the lowest sensitivity to 662 keV photons, relative to crystals B and C; this is illustrated in Figure V.7 (a). One can observe again the effect of the transmission of 662 keV gamma-rays through the collimator material, which results in a large background intensity.

These transmitted γ-rays appears clearly in Figure B.8 as the outer flux at the front of the germanium.

The segment response is presented in Figure V.7 (b). This plot shows the effective segmentation of the detector volume due to the electrical segmentation of the crystal. This is very important, since it shows the true response of the detector; rather than the ideal response as given by the geometrical segmentation (see Figures III.5 and III.6). It is therefore gratifying to see such good separation between the segments. The reader should also note the difference in physical size between the different segments. Again, crystals B and C present a larger sensitivity to 662 keV photons than crystals A and D.

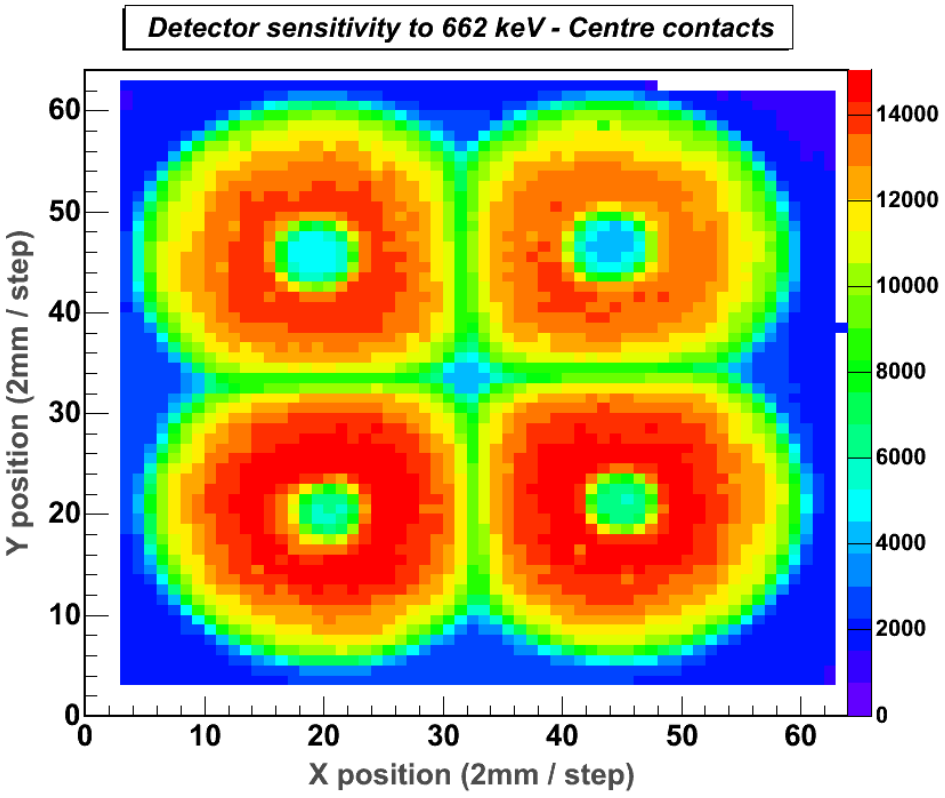

Figure V.7: (a) intensity map for 662 keV gamma-ray photons detected by the centre contacts. Compared to Figure V.6, the Germanium crystals stand clearly out from the background. The decrease in intensity observed in the periphery of the crystals results from the escape of Compton scattered gamma-rays, as well as from the reduction of Germanium volume in the tapered sides. Crystals A and D possess a lower sensitivity, this is consistent with the values of relative efficiency given in Appendix A.

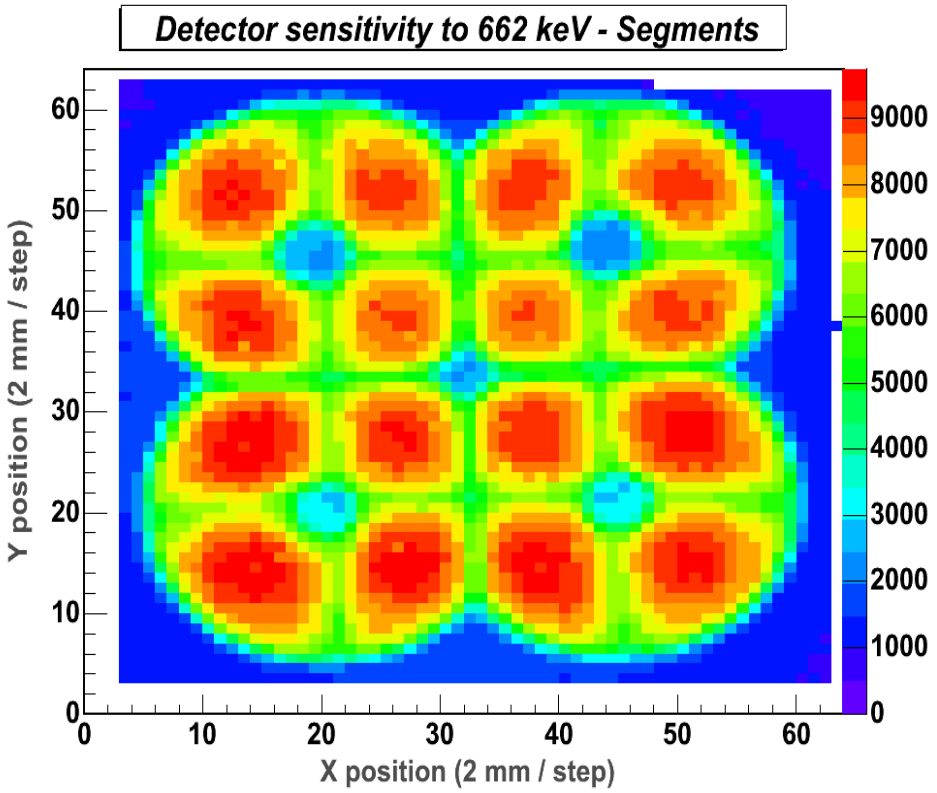

Figure V.7 (b) intensity map for 662 keV gamma-ray photons detected by the segments. The plot required the detection of 662 keV in coincidence between the anode and the cathode. The effective segmentation of the detector is observable: the decrease in intensity at the segment boundaries is due to Compton scattered events between the segments and crystals.

The drop in intensity observed at the segment boundaries within an individual crystal comes from the particular selection conditions used to produce the 2D matrix. The selected events correspond only to F1 events since all CSE between segments are suppressed. The probability of observing such Compton events is maximum at the boundary between segments, hence resulting in an artificial reduction of intensity in these regions. Thus the FEP includes single interactions and Compton within a single segment.

Due to the large amount of data produced, it was decided to focus the subsequent analysis on a single crystal. The similar geometry of the crystals should lead to conclusions that would apply to other crystals; however the full characterisation of the detector still requires the analysis of each individual crystal. Data inherent to crystal A will be analysed. Crystal A does not possess the best performance in terms of relative efficiency and detection sensitivity but this does not have a real impact on the analysis of the characterisation measurements.

3.1.4 Response of a single crystal to FEE

As discussed above, the use of the energy gate reduced the amount of background; the coincidence that was required between the anode and any one of the cathodes restricted the analysis to only F1 events, and filtered the data so that only FEE were considered. However, due to the large volume defined by the segmentation, there will inevitably be a proportion of events that will Compton scatter within a segment, and those will initially appear as F1 events. The intensity response of crystal A is presented for F1 events in Figure V.8 (a). The intensity response for F2 events, displayed in Figure V.8 (b), has been obtained by requiring a coincidence between the anode and two cathodes whose energy sums to a FEE. F3 and F4 events are discarded, since their contribution to the total intensity is insignificant relative to F1 and F2 events.

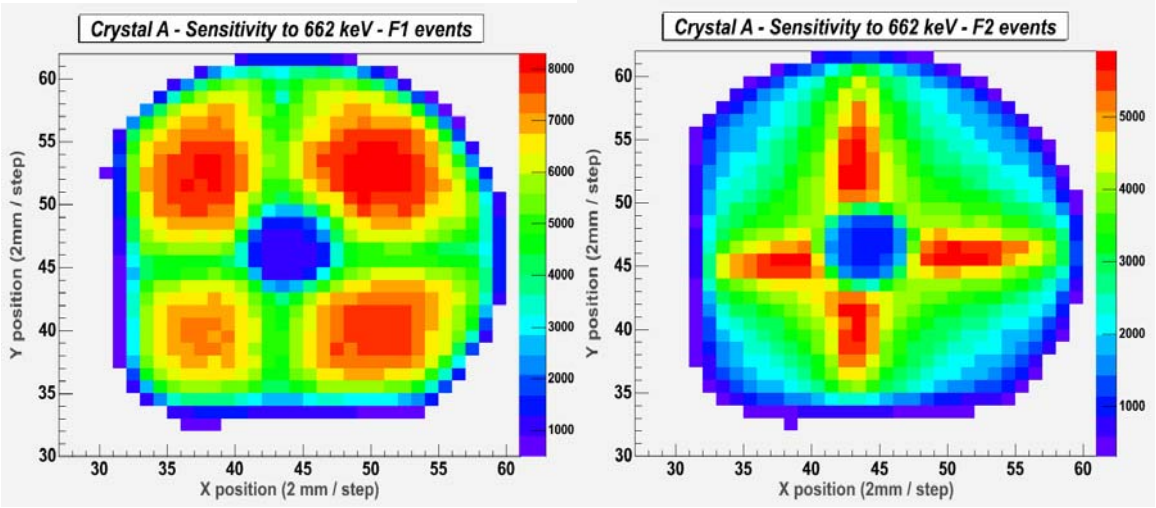

Figure V.8: Crystal A, sensitivity to 662 keV measured for F1 (left) and (F2) events (right). Both figures have been generated by requiring 662 keV on the anode and on a segment for F1 events, and requiring the sum of the energy from 2 segments equalling the energy measured on the anode for F2 events. Both pictures are complimentary: the probability to detect a FEE is maximum at the middle of a segment and minimum at the segment boundaries (left), while the probability of detecting a CSE is higher at the segments boundaries and lower at the centre of the segments. A minimum threshold of 550 counts was required to clarify both pictures.

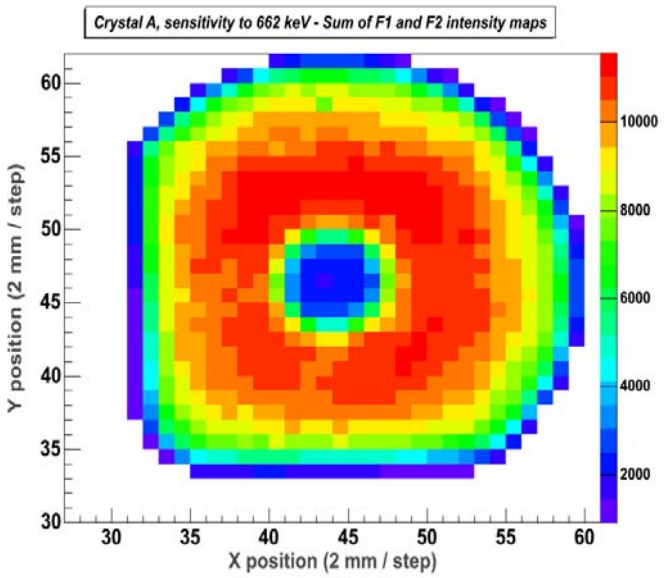

Figure V.9: Sum of F1 and F2 histograms (Figure V.8), which corresponds to 95 % of the intensity observed in crystal A. A minimum threshold of 500 counts was required to generate the picture.

The sum of both intensities, displayed in Figure V.9, corresponds to 95% of the intensity observed in crystal A. The information contained in Figure V.8 (a) and Figure V.8 (b) is complimentary:

- The intensity for F1 events is maximum at the centre of each segment and minimum at the segment boundaries. The probability of observing a F1 event is higher when the source is facing the middle of a segment since it is more likely to terminate a Compton scattering sequence within the segment volume. Consequently, the F1 intensity map also includes higher order multiplicity events that may only be detected by the means of PSA algorithms.

- The intensity for F2 events is maximum at the segment boundaries and minimum in the central zone of a segment and at the edge of the crystal. When the source is near the segment boundary, scattered photons are more likely to be absorbed in the neighbouring segment. Also, the divergence of the collimated gamma-ray beam causes some of the FEE to occur in the adjacent segment even though the source is still in front of a particular segment.

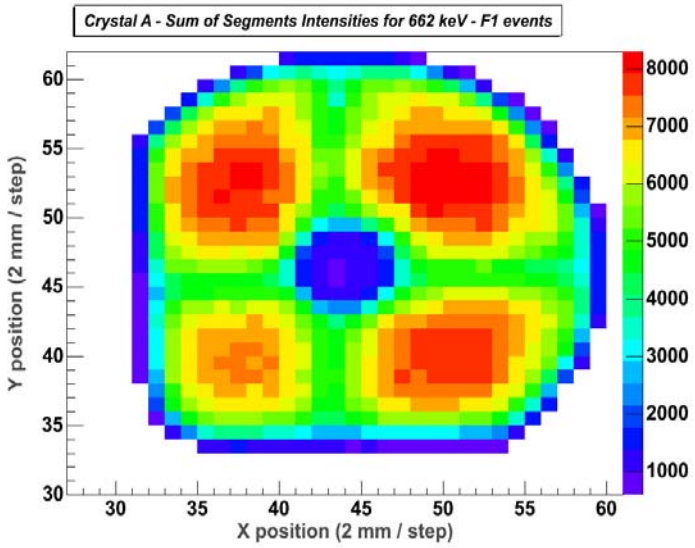

Figure V.10: Cathode response to FEE at 662 keV in crystal A. The intensity map has been obtained by summing the intensity of each individual segment, and appears identical to the intensity map presented in Figure V.7 (b) for the anode response.

The response of the segments to FEE is shown in Figure V.10. The coincidence between the anode and a segment was required, therefore only F1 events contribute to the intensity. The resulting map has been obtained by summing the intensity of each individual segment, and is identical to the map obtained for F1 events detected by the anode (Figure V.8).

3.2 Front face scan with ^{57}Co

The scan performed with the ^{57}Co source allows the investigation of the frontal region of the crystal. It takes advantage of the low penetration depth of the 122 keV gamma-rays in order to reduce the proportion of data coming from the coaxial region of the crystal. Thus, the particular electric field and charge carrier drift properties in the closed end volume of the crystal are directly studied with this measurement.

At the front of the detector, each of the 4 crystals sides are flat, and the anode contact starts at a depth of 8 mm relative to the front face. This particular geometry creates channels of stronger electric field along the directions perpendicular to the centre of each plane face, while leaving volumes of low field strength at the corners between adjacent perpendicular sides, as illustrated in Figure IV.12. Moreover, the tapering of two sides of the crystal will modify the field configuration as well as the drift properties of the charge carriers with depth. Their drift path increases with depth while going from a region of complex electric field in the closed end region towards a more uniform electric field region in the coaxial part of the crystal.

This measurement was initially thought of in order to compare the results of this scan with the analysis of the ^{137}Cs source scan. It would allow an interpolation of the drift properties of the charge carriers and rise time values in the coaxial region, enabling a possible separation of the crystal into two depth regions by PSA (this is discussed Chapter VI). Finally, the ^{57}Co source has the advantage that 122 keV interacts predominantly by photoelectric effect, reducing significantly scattering inside the detector.

3.2.1 Scan configuration

The experimental set-up is identical to the one described in the previous section. The ^{137}Cs source was replaced by the ^{57}Co source, and the CFD thresholds were lowered to the high edge of the 60 keV absorption peak of a ^{241}Am source. The X-Y scan was performed using 5 mm steps and staying 2 minutes per position, which provided enough statistics in the photo peak for analysis. The resulting number of points was 2304. Full energy events were selected by applying a narrow energy gate around the 122 keV photo peak. Figure V.11 presents two example energy spectra from crystal B. The large peak is the 122 keV photo peak from the ^{57}Co source. At 122 keV, the energy resolution measured with analogue systems is typically ~1 keV. However, not only the use of the simple baseline difference to calculate the energy, but the electronic noise is also responsible for the large values of energy resolutions observed in Figure V.11. The 122 keV photopeak sits on a large background due to the Compton continuum from the 1460 keV γ-ray line of ^{40}K. The relative background intensity could have been reduced by using a source of higher activity, or mounting the actual source in a different collimation system which would provide a higher count rate.

3.2.2 Detector sensitivity to 122 keV gamma-rays

The intensity response of the full detector to 122 keV FEE is presented in Figure V.12. Again, a tight energy gate was set around the 122 keV FEP and a coincidence was required between the anode and its corresponding cathodes. Compared to the scan with the ^{137}Cs source, the scan resolution obtained in this case is poor and the segmentation is hardly distinguishable. The difference in intensity observed between the front of the anodes and the rest of the crystals is now lower compared to the scan performed with the ^{137}Cs source. This is due to the smaller interaction length of 122 keV photons – as compared to 662 keV photons – which is of the order of the minimum distance between the two electrodes in this particular zone. The count rate observed in the background is B ≈ 1.7 cps, while the good events count rate is N ≈ 11.7 cps, giving a ration B /N ≈ 1/7.

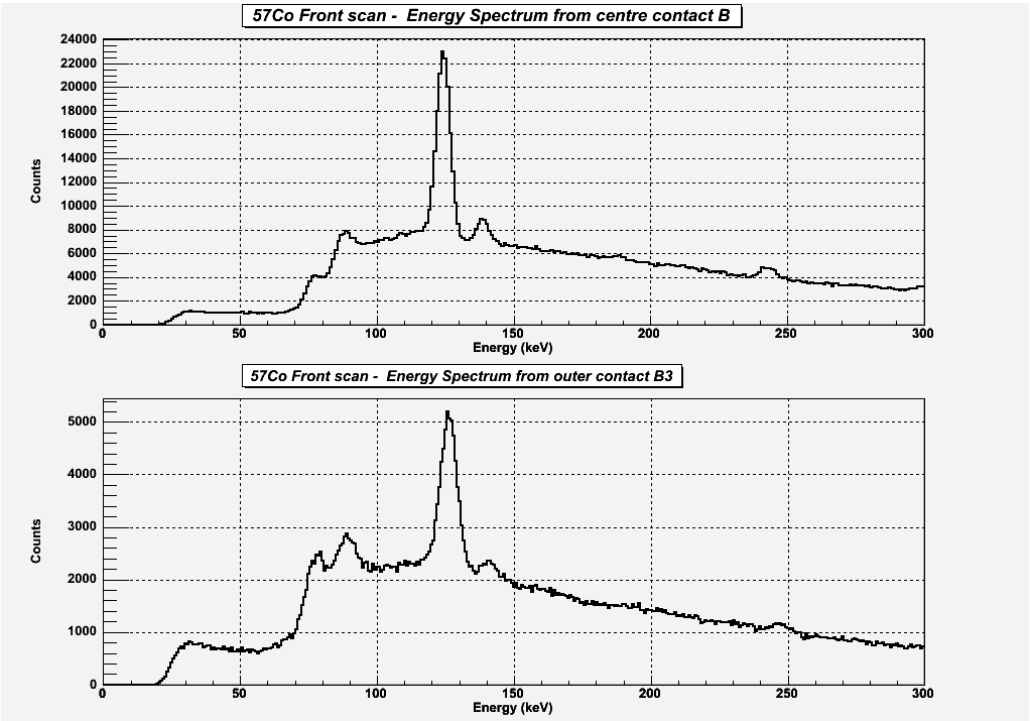

Figure V.11: Example energy spectrum from the ^{57}Co front scan. The top spectrum is the core energy spectrum of crystal B. The bottom spectrum is the spectrum collected on segment B3. The energy resolutions at 122 keV given by the baseline difference are $\Delta E_{B} \approx 5.85$ keV and $\Delta E_{B3} \approx 7.23$ keV. The 133 keV peak is present, as well as Lead X-rays on the left of the 122 keV FEP.

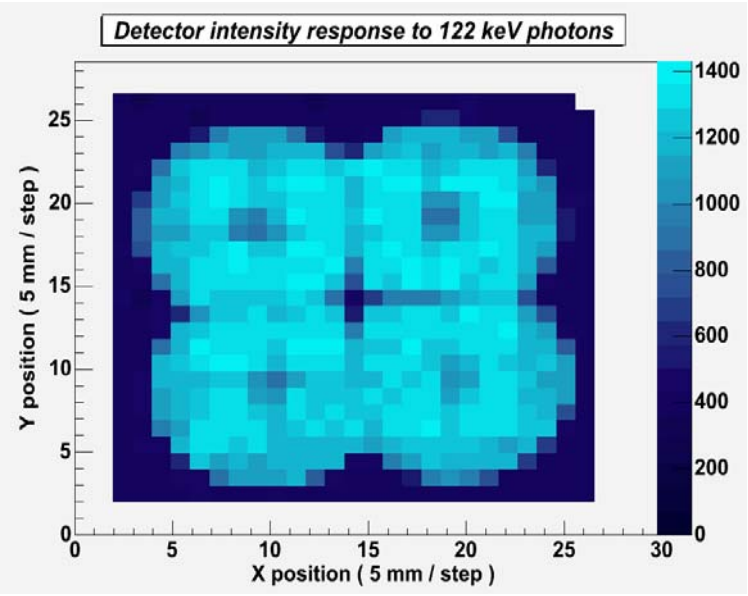

Figure V.12: intensity response of the detector to 122 keV gamma-rays. Despite a lower resolution compared to the ^{137}Cs scan; it is possible to separate individual crystals. The use of low 122 keV energy γ-rays allows one to probe the very front face of the detector.

3.3 Side Scan with ^{57}Co

The final measurements described in this section consisted of a linear scan along the full length of a tapered segment. In the frontal and tapered region, the inter-electrode distance and the drift path of the charge carriers varies the position of interaction, whereas the coaxial part of the segment is expected to exhibit uniform drift properties[34] since the distance between the anode and cathode is constant along the depth (Z axis). However, the dead Ge layer at the back of the crystal is known to induce some distortions in the electric field, which can cause a partial loss of charges as suggested by [Med04, San02] and by the results from MGS calculations (Chapter IV). The electric field configuration at the back of the crystal can be directly investigated through the intensity response of the detector to the side scan and by the study of the drift behaviour of the charge carriers. These measurements will also give an idea of the dimensions of the low strength field volume. In parallel, some information on the drift properties of electrons along the depth can be obtained for both the tapered and the coaxial regions.

3.3.1 Scan configuration

The detector was positioned sideways, and the collimated source was oriented horizontally and placed so that the beam of gamma-rays hit the detector on segment A1 as illustrated in Figure V.13. The height of the collimator was precisely adjusted, and the distance between the collimator and the aluminium case was 2 mm. Finally the collimator was placed so that the gamma-ray beam hit the segment A1: a comparison of rise time distributions[35] provided an approximate orientation of 15±5 degrees relative to the long axis of the crystal. The **X** range of the automated table was set to 150 mm, with 2 mm step size and pulses were acquired for 12 minutes at each position. The thresholds of the CFD were adjusted to 60 keV.

3.3.2 Results

The corresponding line of intensity response to 122 keV gamma-rays is presented in Figure V.14 both for the anode A and for the segment A1. The core intensity has been produced for gated FEE, while the segment intensity was obtained by applying a gate on both the core and the segment energies. The number of detected events is above the level of random background (B ≈ 1.11 cps for Segment A1 and B ≈ 2.8 for Centre contact A) between position indexes 22 and 69, which corresponds to a germanium depth of approximately 92 mm. Due to

[34] This is only true at a particular orientation.

[35] Refer to Chapter VI.

the low energy of the probing gamma-rays, the majority of events are F1 and no scattering of the 122 keV gamma-rays is observed between outer electrodes. Figure V.15 (a) and Figure V.15 (b) show the corresponding energy spectra for crystal A. The centre contact spectrum is displayed in Figure V.15 (a). Spectra observed for the segments A1 to A4 are shown in Figure V.15 (b). The large peak at low energy is the 122 keV peak from the ^{57}Co source.

Figure V.16(a) shows the anode – cathode coincidence energy matrix for the whole scan. The energy coincidence for the absorption of 122 keV and 133 keV are represented by the maximum intensity spots observed at the centre of the matrix. As expected, the energy coincidence follows a linear relationship, of linear coefficient = 1. However, the large number of counts observed below the coincidence line indicates a deficiency of charges collected on the cathode relative to the anode for a small fraction of events. The background intensity below the equal energies line appears to be the same for each collimator position, suggesting that these events are independent from the depth of interaction within the crystal. An investigation of the background events against the rise time distribution measured on both anode and cathode signals was carried out in order to look for a correlation between the events and the radial position of interaction (See Chapter IV). The results show no correlation between the background events and any particular rise time value from either the central or outer electrode. The background can possibly due to a small fraction of 122 keV γ-rays which interacts by Compton scattering in segment A1, and reaches the neighbouring segment A2. This process would prevent the measurement of the full photon energy in A1.

In Figure V.17, a minimum threshold of 15 counts was set in order to suppress the background counts, and revealed a second tendency that deviates from the expected linear behaviour. It appeared that such effect is only observable for positions located at the back of the crystal. The coincidence matrices from a set of positions located at the back of the crystal are presented in Figure V.18. The deviating effect appears at positions 24 to 31 (refer to Figure V.14), which correspond to a region of ~ 12 mm thick at the back of the crystal.

This deviation from the linear behaviour seen in Figure V.16, Figure V.17 and Figure V.18 is the evidence of a systematic loss of charge carriers before they are collected by the centre and outer contacts. A deficiency in charge collection on the cathode relative to the anode is suggested by the amount of coincidences recorded below the coincidence line (Figure V.16). Figure V.19 shows the holes drift velocities calculated by MGS for the back of the crystal.

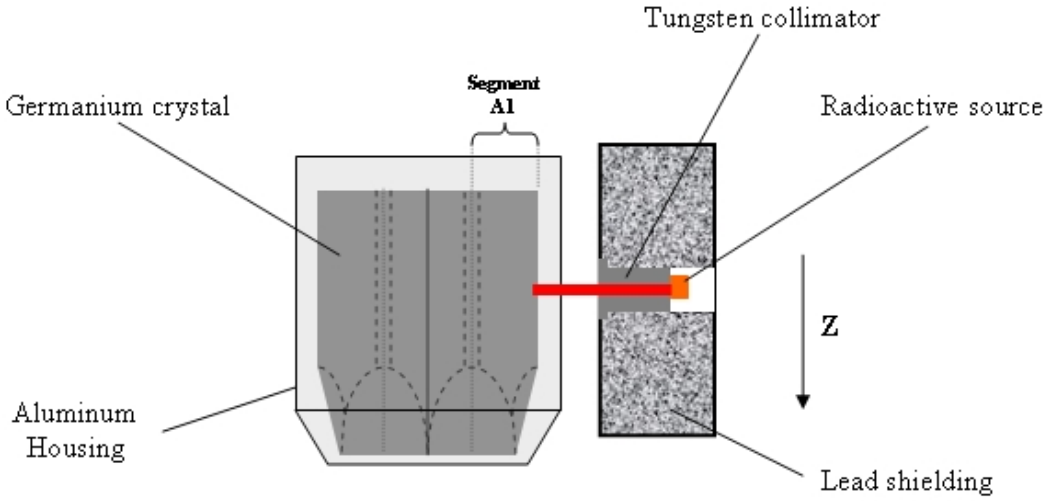

Figure V.13: Schematic illustration of the side scan set-up with the ^{57}Co source. The collimated source is firing gamma-rays towards segment A1, which is scanned along the whole crystal depth. The source was moved in 2 mm steps, staying 12 minutes per position.

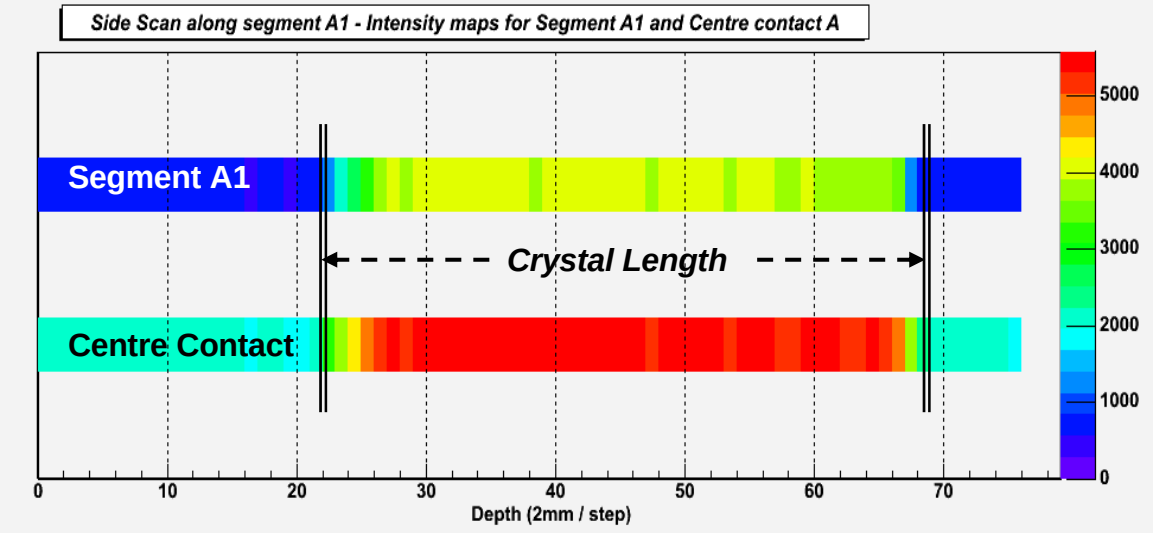

Figure V.14: Intensity lines obtained from the side scan along segment A1 for the Centre contact and Segment A1 as a function of depth. The plot represents the number of counts recorded on the core and outer electrodes for each position of the source during the side scan. The centre contact line was obtained by requiring 122 keV on the core. The segment intensity line was obtained requiring 122 keV on the core and in segment A1. The approximate position of the Germanium crystal is indicated.

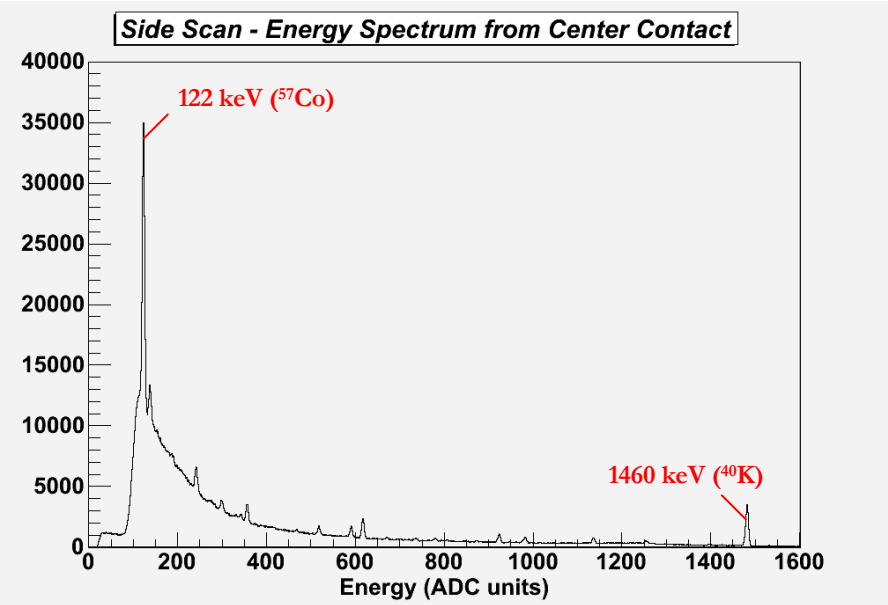

Figure V.15: (a) Centre contact energy spectrum. The 122 keV FEP is indicated. The detector was not shielded against environmental radiations, which explains the presence of parasitic peaks and large Compton background from ^{40}K.

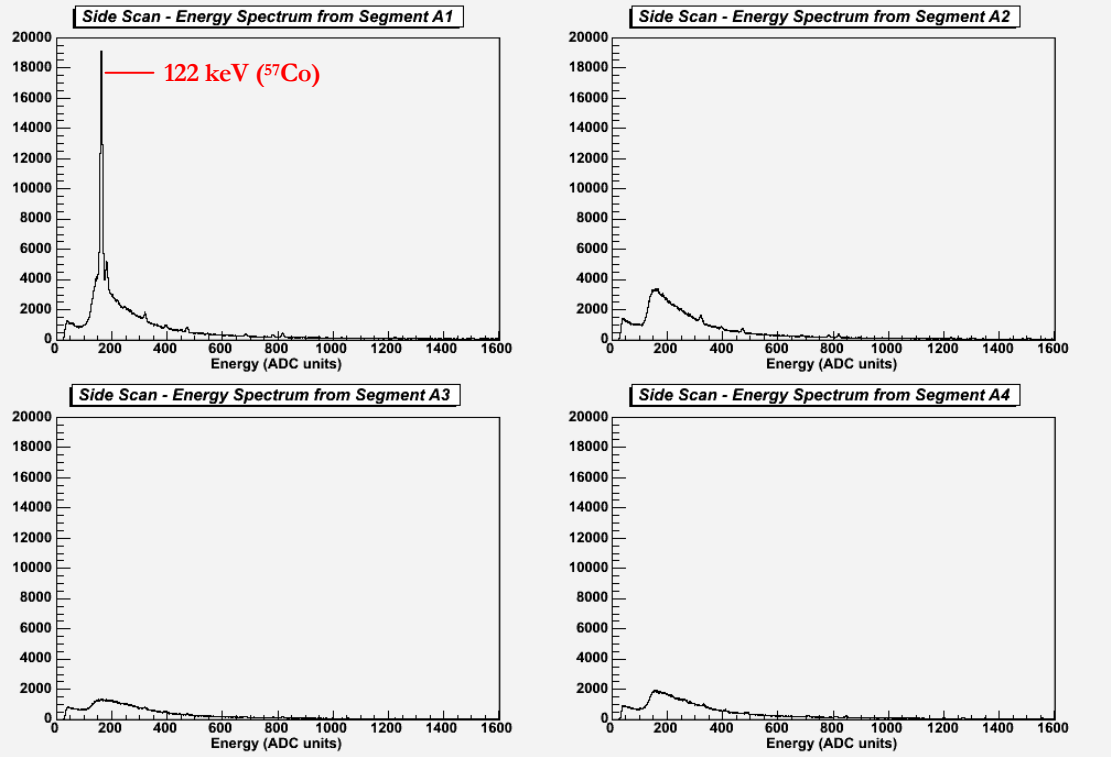

Figure V.15 (b) Energy spectra for segments A1 to A4. The 122 keV FEP only appears in segment A1 as expected.

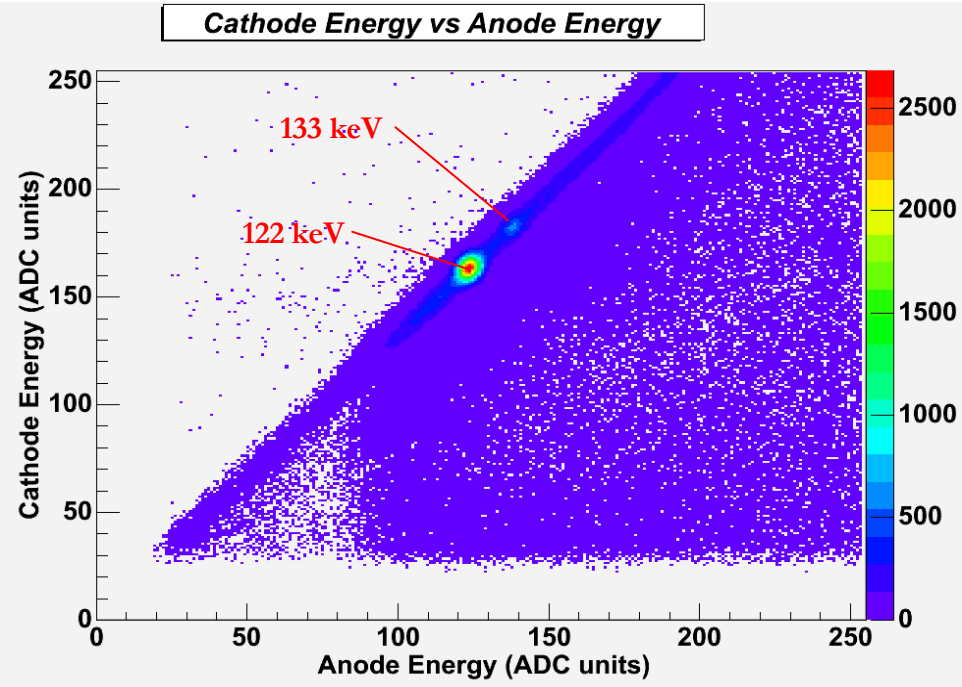

Figure V.16: Energy coincidence matrix between anode A and cathode A1. The 122 keV and 133 keV peaks are indicated. The coincidence ideally follows a linear relationship of coefficient 1. The large number of events observed below the coincidence line indicates a loss of charges at the cathode relative to the anode.

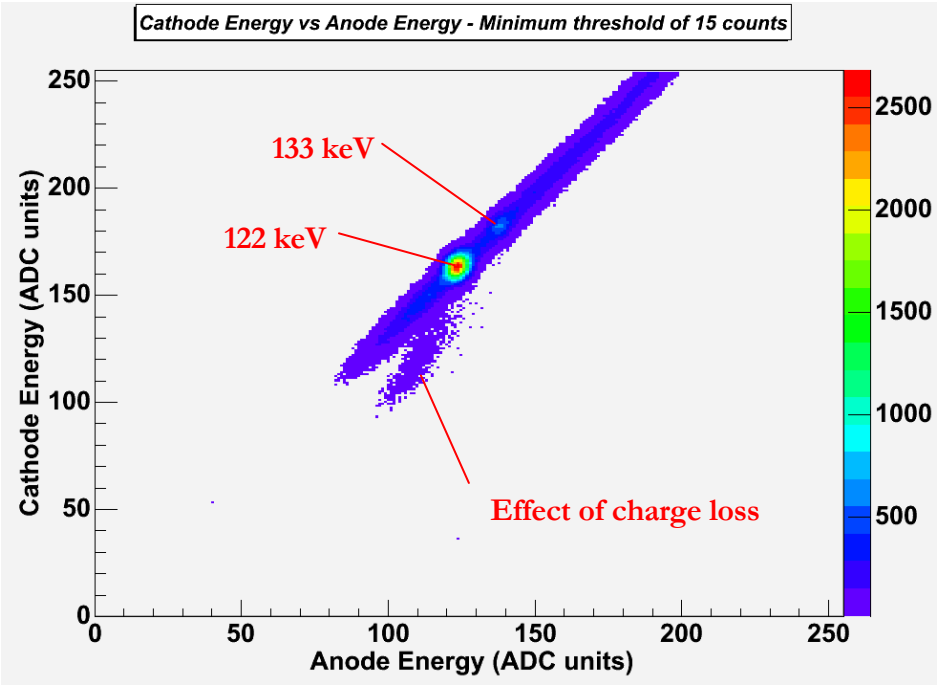

Figure V.17: Anode – cathode energy coincidence matrix. A minimum threshold of 15 counts has been applied in order to extract the deviation of 122 keV towards lower energy. This effect indicates incomplete charge collection of 122 keV energy in the crystal.

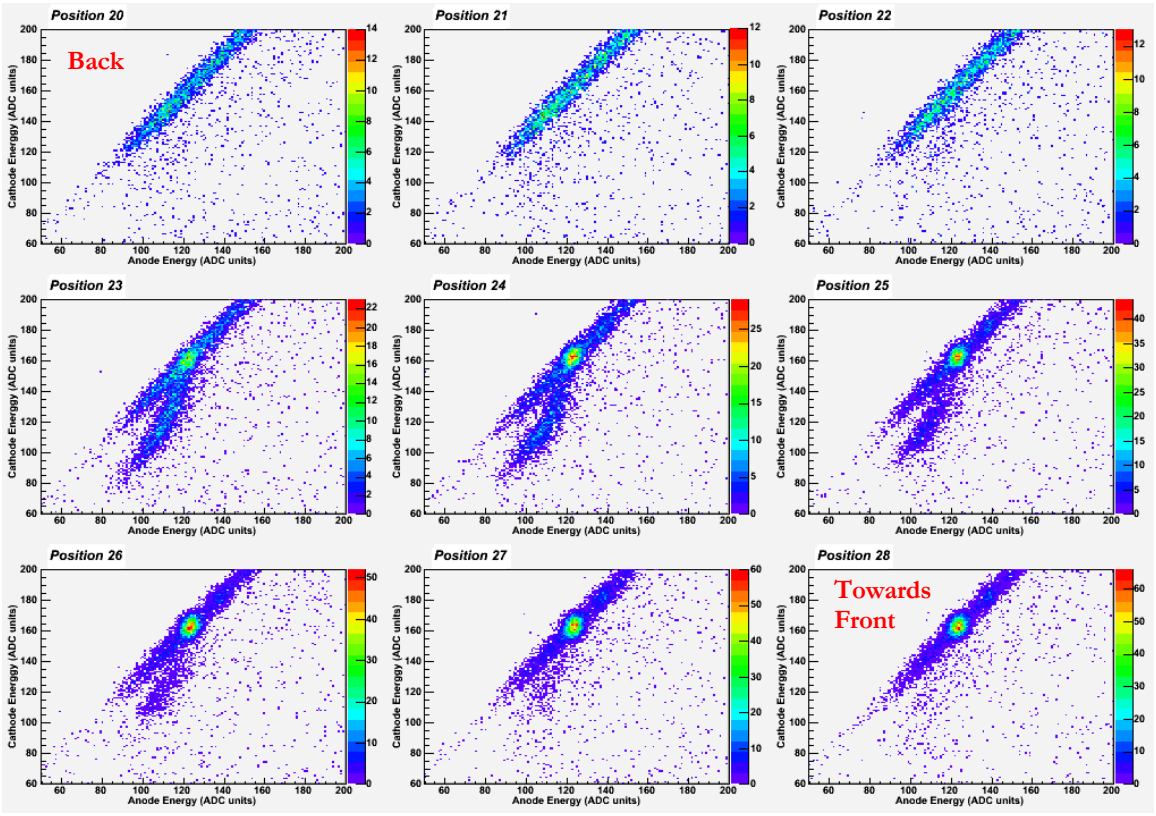

Figure V.18: Energy coincidence matrices for positions located at the back of the crystal. The increasing position number goes from the back to the front of the crystal. The 9 positions cover a range of ~20 mm. The Germanium crystal starts at position 22 (refer to Figure V.14). The 122 keV coincidence spot starts to appear at position 23, with a large effect due to charge loss. As the collimator moves towards the middle of the crystal the proportion of charge loss reduces and disappears after position 28. The corresponding range is ~16 mm deep.

The low field intensity expected in this region lowers the drift velocity below the saturated regime, and reduces the life time of the charge carriers to a point where they are subject to trapping. Furthermore, when considering the 122 keV γ-ray collimated beam moving towards the back of the crystal, for interactions occurring particularly near the cathode, the holes are directed towards the dead Ge layer at the back of the crystal whereas electrons are still collected by the anode. This is illustrated by the diagram in Figure V.20. The holes then recombine on the passivated layer, which must lead to the existence of a recombination current at the back of the detector. The z component of the hole drift velocity vector is represented. It shows clearly that the holes generated in the back region will terminate their trajectory in the dead Ge layer at the back.

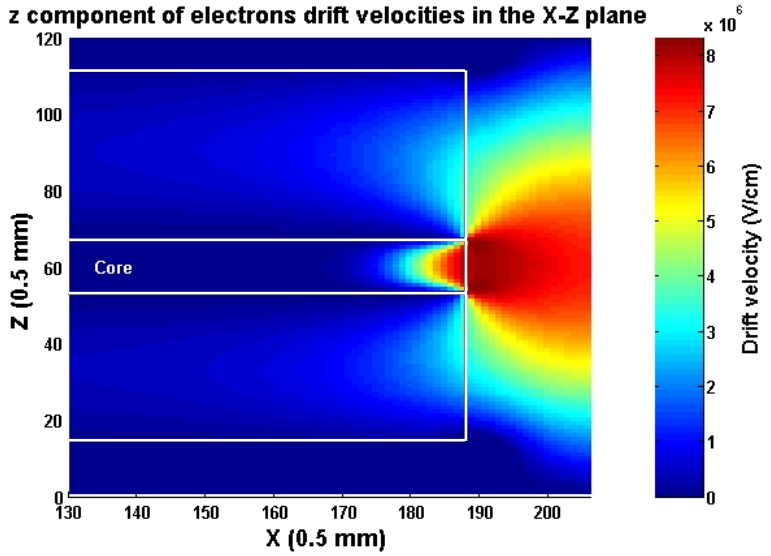

Figure V.19: MGS calculations for the z component of the hole drift velocity vector in the back 20 mm of the crystal. The results show an important magnitude of the z component of the drift velocity vector.

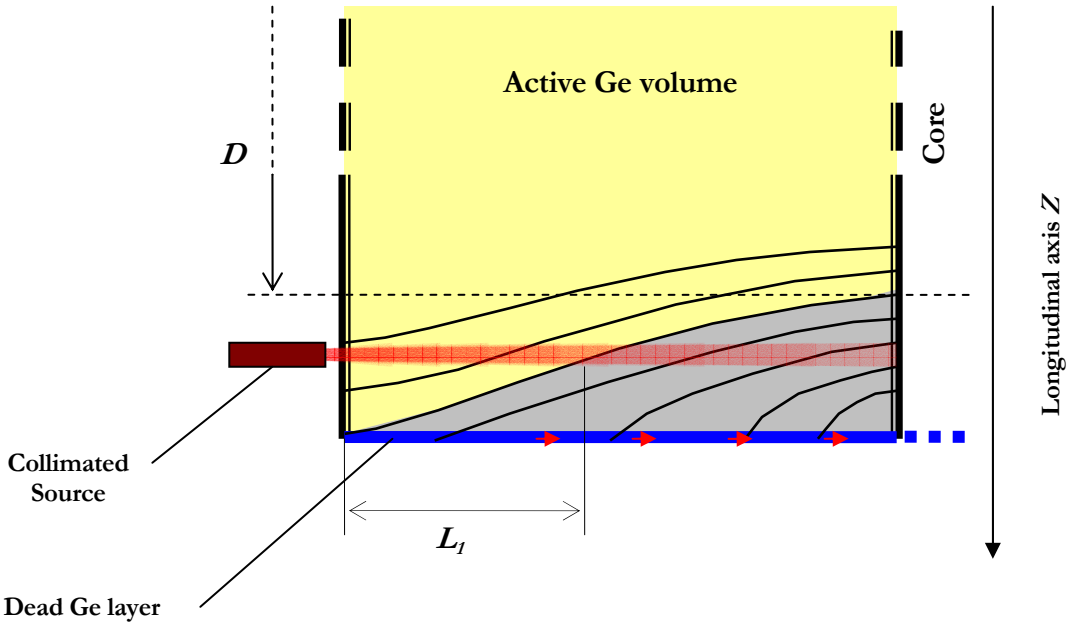

Figure V.20: Schematic illustration of the field configuration at the back of the crystal. For source positions further than *D*, the holes start to be directed towards the passivated layer, where they recombine and give existence to a recombination current. The zone where holes are lost is indicated in grey. Due to the attenuation of 122 keV gamma-rays in Ge, the holes will be lost only for a small proportion of interactions. As *Z* increases, the number of interactions occurring in the back zone, becomes more and important. The distances L_1 represent the interaction depth for which electrons and holes are collected. Beyond, only electrons are collected which gives rise in the second line observed in Figure V.17 and Figure V.18.

Chapter VI

ANALYSIS OF THE DETECTOR RESPONSE

Rise time analysis and position determination

The chapter describes the study of the detectors drift properties through the distributions of partial rise times described in the previous chapters. The variation of the signals with the collimated source position is position radial position is investigated. The experimental results are then compared to simulated sets of partial rise time data.

1 Rise time Analysis

The following sections present the rise time analysis of the data from the X-Y scan performed with the ^{137}Cs source described in the previous chapter. In order to facilitate a full analysis of the partial rise times[36] obtained for each event, the evolution of the distribution of the rise time values was investigated as a function of position. In the case of asymmetric distributions, the use of the mean to estimate the real rise time value yields, in most of the cases , a misleading result for a given position. In the following, complex rise time distributions are presented and different arguments are followed in order to justify the rise time parameterisation proposed.

1.1 Analysis procedure

The following analysis is based on the investigation of changes in the shape and characteristics of the partial rise time distributions measured from charge pulses with the position of interaction. Results obtained from a single crystal volume are presented, before comparing the behaviour of the results from the four different Clover crystals. For each position of the scan measurements described in Chapter V, the distributions of partial rise times were extracted for full energy events (FEE). The first step consisted in the filtering of events:

1. in energy: only FEE were selected by applying a tight energy gate (656 keV to 668 keV) on the ^{137}Cs photo peak;

2. by segment fold in each crystal: cathode signals were separated into net charge pulses, image charge pulses and zeros. The rise time distributions of anode signals resulting from segment Fold 1 and Fold 2 events are investigated.

In the second step, the net charge pulse was linearly interpolated, in order to determine the partial rise times with a precision of 1 ns. The interpolated pulse shape was then smoothed by a 3 points moving average filter. The contribution of the preamplifier response function was not removed from the signal, since it cannot easily be dissociated without a complete knowledge of the preamplifier's characteristics. Therefore, the quoted time values correspond to the signals measured from the detector in real experimental conditions.

The analysis of the data was mostly performed with the ROOT software package [ROOT], which consists of an object oriented framework providing an extensive list of C++ classes

[36] The partial rise times T30, T60 and T90 are introduced in Chapter IV, section 2.

dedicated to the acquisition and analysis of experimental data. For each source position and detector Fold, the rise time values were filled into histograms and stored in root files for the subsequent steps of the analysis.

1.2 Uncertainty on the location of γ-rays interaction

Two kinds of uncertainty need to be accounted for:

1 The uncertainty on the position of the source given by the scanning system. The precision of the stepper motors is ~100 μm. Therefore, the uncertainty in the (X-Y) position of the source, for the scan measurement, is given by the resolution of the data grid from the scan: 2 mm steps give a resolution of ±1 mm.

2 The uncertainty in the interaction position of a γ-ray is related to the profile of the γ-ray beam within the germanium (Ge) crystal. This value was estimated from a Monte Carlo simulation of the collimator assembly (Appendix B). The average position uncertainty was determined to be ± 2.04 mm, for scan positions where the crystal depth is 90 mm. In front of the tapered volume, the uncertainty increases from 2.04 mm to 2.61 mm. The largest value applies to the edge of the tapered electrode due to the increased of beam divergence.

1.3 Singles Scan with ^{137}Cs source

Following the discussion in Chapter V (section 3.1.2), the interaction of a 662 keV γ-ray can result in Compton scattered photons triggering one or more segments from a given crystal. Therefore, in the Clover detector, such events can result in a large variety of pulse shapes. In order to isolate the contribution of low multiplicity events, and hence facilitate the characterisation of the detector, pulses were separated by segment fold for each full energy events (FEE) in a crystal. The next sections describe the different shapes of partial rise time distributions observed on the core electrode of crystal A. Anode signals have the advantage of being simpler to analyse than cathode signals, as they do not contain any image charge contributions. However, they contain additional complexity when Compton scattered events occur within a segment, as demonstrated by the example in Figure IV.5.

During the ^{137}Cs scan, 795 source positions were located in front of crystal A. The corresponding position map is shown in Figure VI.1. Each position was numbered in order to allow easy access to the information during the analysis. The reader should refer to this plot in

order to identify the location of a position *n* (P*n*) in the following discussions. The intensity map of the crystal for full energy events is also represented. The partial rise time T30 and T90 values were calculated as described in Chapter IV, and a distribution of values was obtained for each source position. The positions were selected from an initial circle of 32 mm radius centred on the centre of the crystal. The coordinates of the centre (X_C, Y_C) were evaluated from the intensity map shown in Figure V.7.

$$\begin{aligned} X_C &= (87.3 \pm 0.5)\,\text{mm} \\ Y_C &= (92.0 \pm 0.5)\,\text{mm} \end{aligned} \tag{VI.1}$$

In the following discussion, the radius was calculated for all source positions relative to the centre point of the crystal, giving an average error in the radial position of interaction of ± 2.1 mm.

1.3.1 Random events

For every position of the source during the scan, there is a fraction of events that contribute from random coincidences detected in the crystal. The typical intensity of random counts is ~2.5 cps for Fold 1 events, this number is negligible in comparison to the contribution of true 662 keV events. However the importance of random events becomes significant at the front of the anode, where the thickness of germanium material is 8 mm: both intensities, random and true events, have comparable statistics, with a ratio of ~1:2 between good and random events for the worst case. Typical random event distributions for two source locations at a radii

R > 25 mm indicated by (P288) and (P16) in Figure VI.2, are presented in Figure VI.2 (a) and Figure VI.2 (b) for Fold 1 and Fold 2 events respectively. These two positions lie outside of the crystal volume. Both Fold 1 events distributions have a similar profile: as (P16) is located closer to the crystal; the divergence of the photon beam may allow a small fraction of source γ-rays to interact at large depth within the crystal. The Fold 2 random event distributions have a very low intensity, of about ½ of the intensity obtain for Fold 1 events.

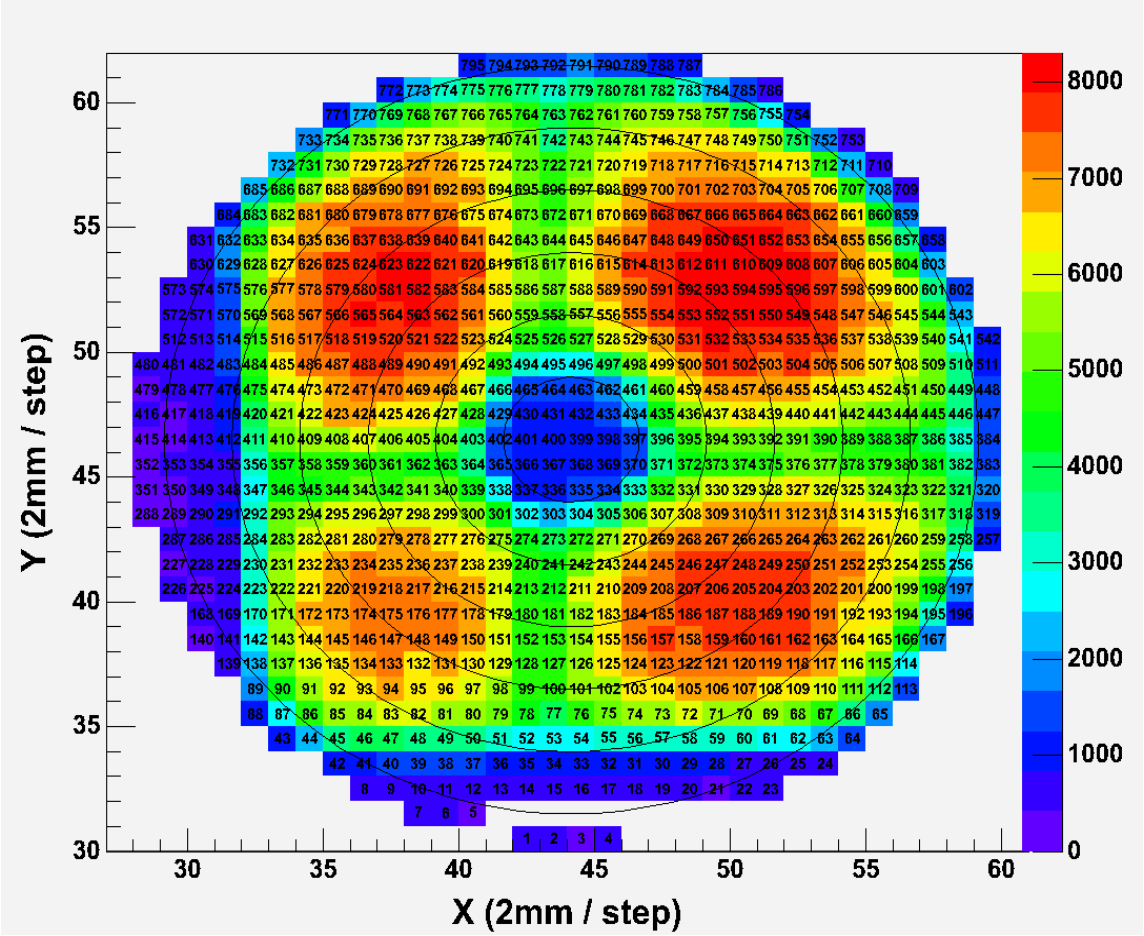

Figure VI.1: Position numbering scheme for the analysis of the rise time distributions. The intensity map for 622 keV FEE detected in coincidence with the core and outer electrodes is used to identify the position of the source relative to the crystal. Positions with a low intensity correspond to random coincidences. The concentric circles define different radial ranges relative to the position of the centre of the crystal: 0-5 mm, 5-10 mm, 10-15 mm, 15-20 mm, 20-25 mm and 25-30 mm.

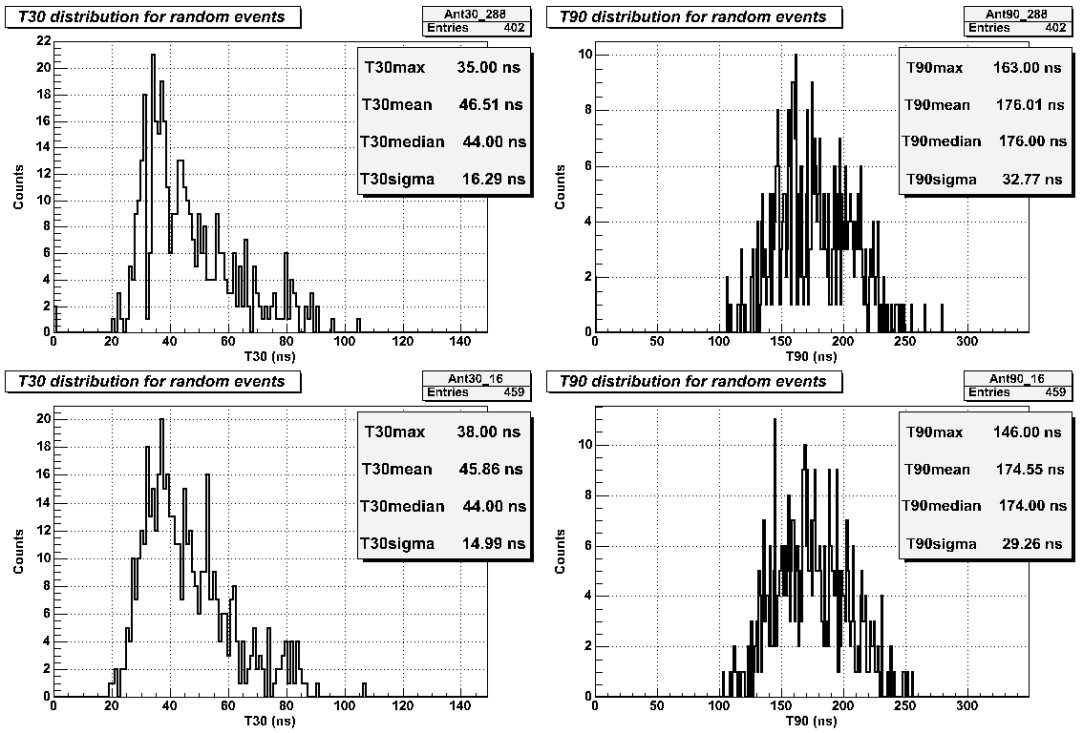

Figure VI.2 (a): Example of rise time distributions from Fold 1 random events detected by the core, recorded for source positions out of the crystal volume. The top two distributions are taken at a position located at R~32 mm along the short axis of the detector. The two bottom distributions are from a position located at R~28 mm. Both sets of distributions present the same profile.

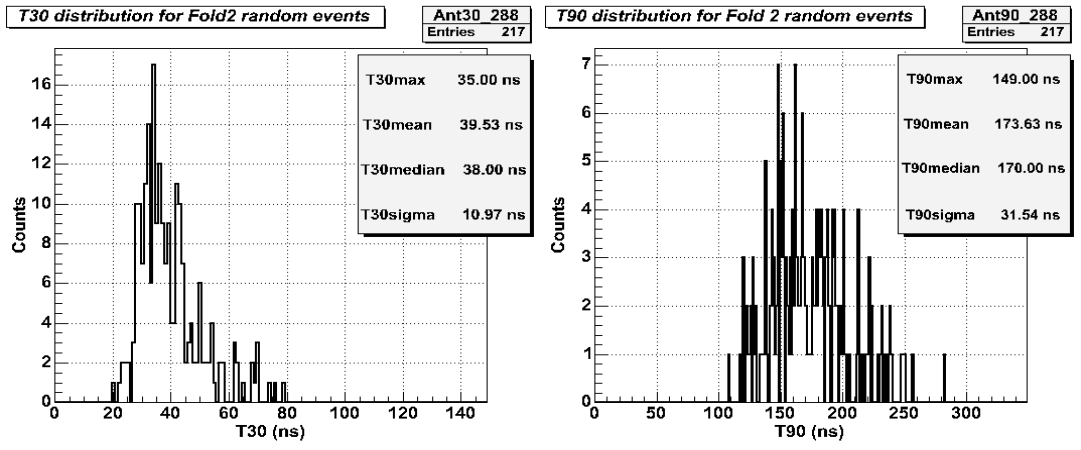

Figure VI.2 (b): Example of random T30 and T90 distributions for Fold 2 random events. The profile is similar to that observed for Fold 1 events, a significant reduction in statistics is observed.

1.3.2 Description of partial rise time distribution from anode signals

The complex geometry of the Clover crystal has an important effect on the shape of the rise time distribution observed. Depending on the distance between the electrodes and the shape of the cathode, the electron and hole collection time will vary, and the change in electric field configuration in the crystal – orientation and strength – will have an effect on the charge carrier drift direction and velocity. In Chapter IV, the electric field calculations showed that near the cathode, for depths located in the coaxial region (Z > 30mm), the electric field is stronger and the drift velocity of the charge carriers is larger along the short crystal[37] axes. This allows the division of the crystal into 4 different frontal zones as shown in Figure.VI.3:

1. The first zone (**A**) corresponds to the area directly at the front of the core electrode for radii R < 5.5 mm. As shown in Figure IV.12, the uniform configuration of the electric field is very similar to a planar configuration. This results in the fastest charge collection times measured in the crystal.

2. The second zone (**B**) includes all source positions where the holes are either collected on the taper or on the external rounded surface of the cathode. The difference in the drift direction relative to the orientation of the crystallographic axes should be noticed, as the charge carriers will either drift along the main <100> and <110> directions (respectively fast and slow axes) as indicated by the picture.

3. The third zone (**C**) is composed of two identical triangular shaped regions, and corresponds to source positions where the holes are collected on the flat edges of the cathode.

4. The fourth zone (**D**) corresponds to the source positions where the holes are directed towards the inner rounded corner of segment A3 (parallel to the <011> direction). The results from the electric field simulation predict a weak electric field magnitude and the drift velocity of the charges is expected to be slower compared to other orientations as shown in Figure IV.13 and Figure IV.15.

[37] The reader should refer to the discussion in Chapter IV, section 3.3.2 on the electric field simulation of the EXOGAM crystal.

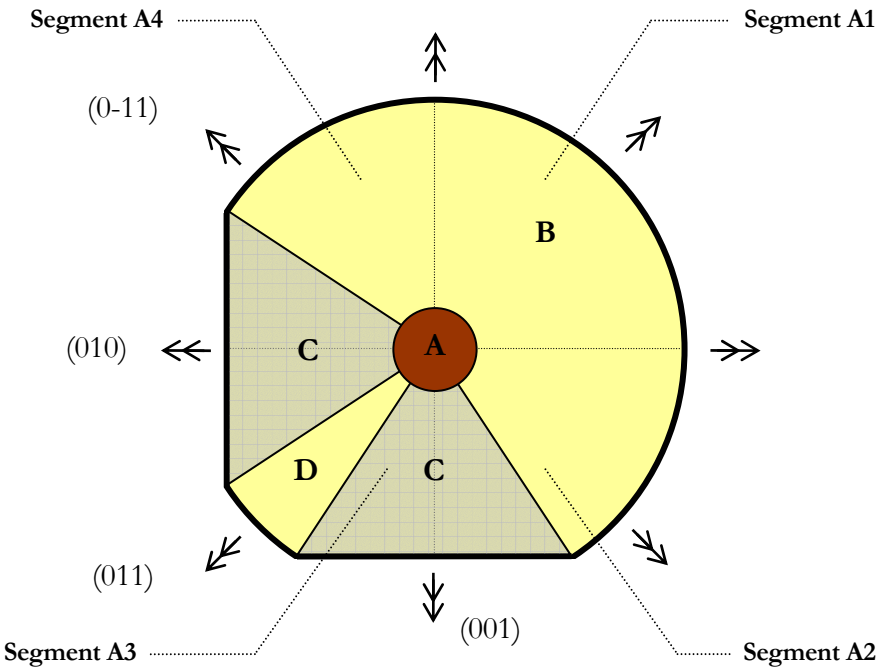

Figure.VI.3: Frontal separation of the Clover crystal. Zone A corresponds to the source locations where the holes are collected in front of the core electrode on the front face of the crystal. Zone B corresponds to interactions where the holes are either drifting towards the taper or the circular surface. Zone C corresponds to interactions where the holes are directed towards the flat sides. Zone D corresponds to volumes where the holes are drifting towards the corner. The crystallographic directions are indicated by the arrows on the diagram.

1.3.3 Zone A, central source locations

For the source positions in the central zone (A), both T30 and T90 distributions present a sharp peak located at fast rise time values, with a wider distribution at longer rise times. Figure VI.4 presents a set of distributions from an example source location (P400 in Figure VI.1). The top histogram shows the T30 and T90 rise time distributions for Fold 1 events, while the bottom histograms represents the T30 and T90 rise time distributions for Fold 2 events (FEE detected in coincidence between the core electrode and 2 segments).

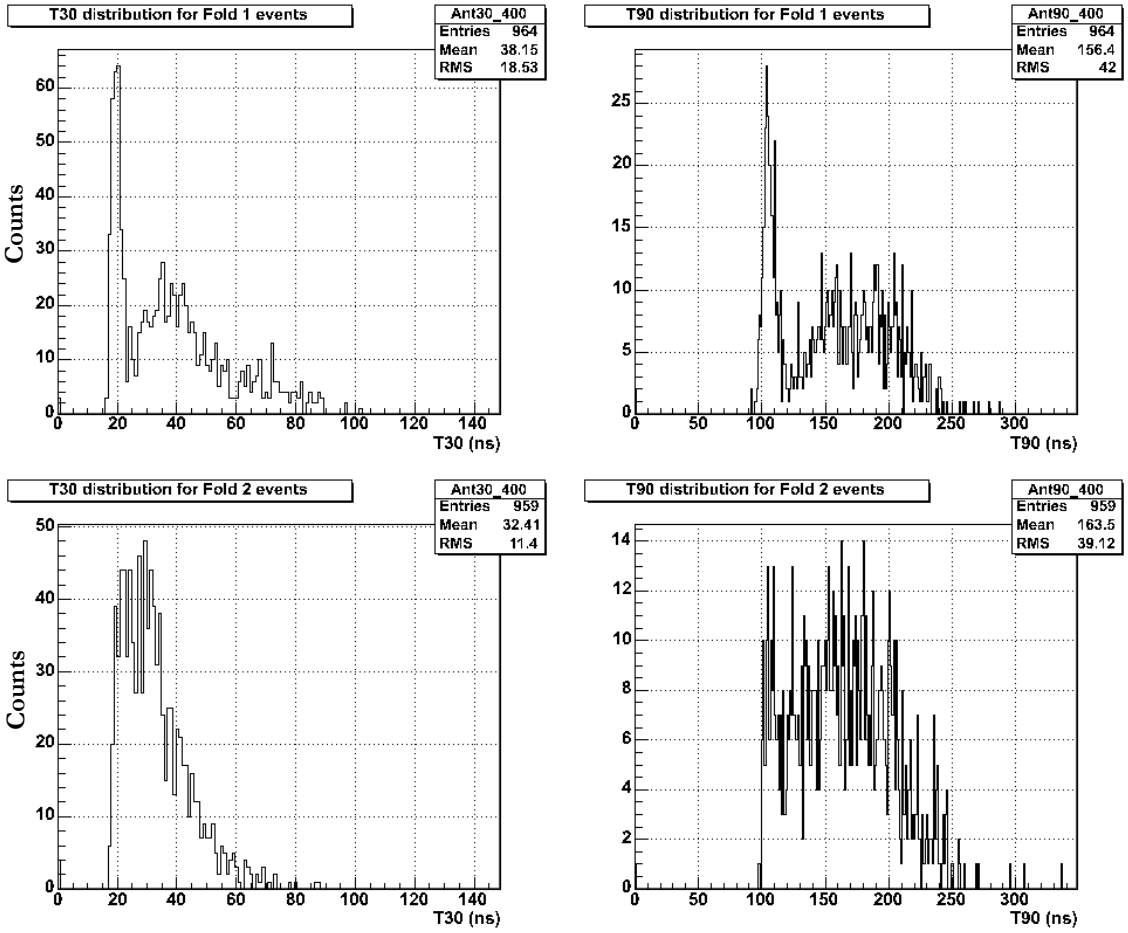

Figure VI.4: Example core rise time distributions for the central region of the crystal (R < 5.5 mm). The top distributions show anode pulse rise times for Fold 1 events. The bottom distributions present anode pulse rise times for Fold 2 events. In the window at the top right hand corner, the total number of events contributing to each distribution is referred as the number of "Entries". The mean value and standard deviation (RMS) are also indicated. The title of the window on the top right hand corner gives the type of distribution presented: "**Ant30_400**" signifies **An**ode signals, **t30** distribution from position P*n* = P**400**.

The intensities for Fold 1 and Fold 2 events are comparable. The sharp peak in both Fold 1 distributions results from interactions that deposit their full energy in the 8 mm of Germanium in front of the core electrode. The charge collection time is fast, as shown by the maximum T30 and T90 values of 36 ns and 105 ns respectively. The sharp peaks observed for Fold 1 events correspond to interactions where the full energy of the γ-ray is absorbed, due to the geometrical constraints these events are mainly single photoelectric interactions. The second broad distribution observed at longer time values are the sum of the two following contributions:

1. Random Fold 1 events in the crystal. The central region is the only region for the scan where the intensity of the random events is comparable to the intensity given by the collimated source.

2. Compton scattered events (CSE). In the 8 mm of germanium available, γ-rays can scatter towards deeper regions in the crystal where the collection time of the charge carriers is longer. At 662 keV, a large proportion of photons will preferentially undergo forward scattering[38]. Results from the Monte Carlo simulation of the collimator (Appendix C) show that the profile of the of the γ-ray beam through the germanium crystal diverges significantly after ~10 mm in the material. Therefore, the scattered γ-rays will mainly interact at relatively small radius, while the remaining collimated photons will continue their paths through the crystal core hole and not be detected.

Figure VI.5 shows both the Fold 1 and Fold 2 distributions overlapped on the same plot. Therefore, the distribution observed at long T90 values is clearly due to γ-rays that Compton scatter deeper in the germanium material. The large difference in intensity between Fold 1 and Fold 2 distributions for T30, within the range 25 ns to 35 ns, illustrates the importance of Compton scattering. This range of T30 values correspond typically to interactions occurring at small radii in the coaxial part of the crystal, as discussed later in section 2.2.

[38] From the Klein-Nishina formula, given in Equation II.17.

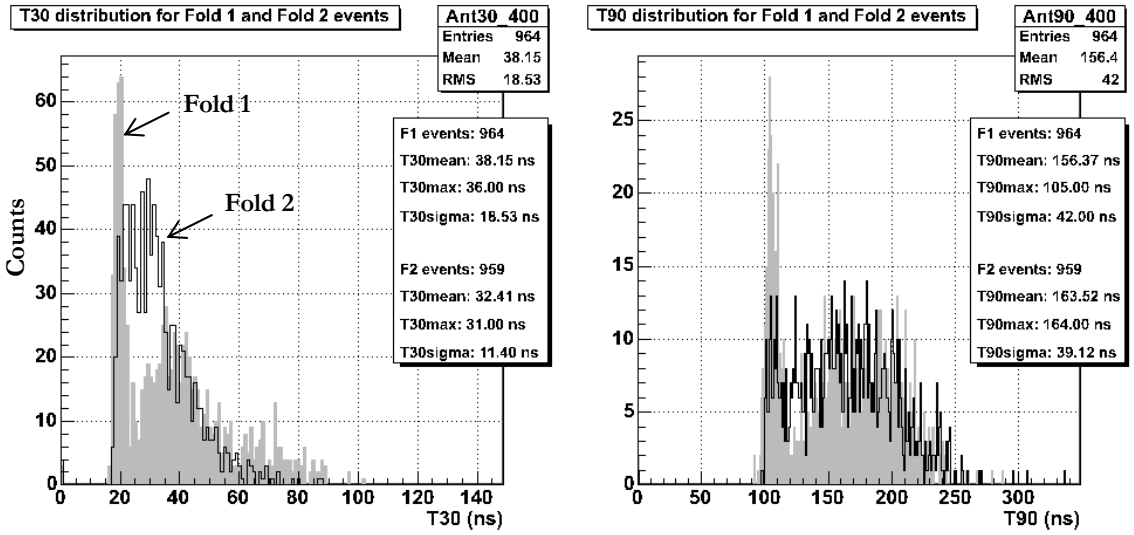

Figure VI.5: Comparison of Fold 1 and 2 rise time distributions. The filled histogram contains the data from Fold 1 events. The Fold 2 histogram is represented by the black line.

1.3.4 Zone B, source located in front of the taper

Two types of distributions are observed when the source is located in front of the taper. At small radii, the beam of γ-rays scans the full depth of the crystal and the holes are the main contributor to the development of the detector signals, as illustrated by Figure VI.6. As derived from the results of the electric field simulation (Figure IV.15 and Figure IV.17), the detector can be divided into three main depth regions along the taper, showing different rise time properties due to the different hole collection times:

(1) the front, where the holes are collected by the front face of the crystal;

(2) the taper, where the collection time of the holes increases with depth;

(3) the rounded surface of the cathode, where the crystal is considered to be coaxial.

Figure VI.7 (a) presents a typical example of rise time distributions encountered at a small radius R = 10.4 mm (P530). For Fold 1 events, the T30 distribution presents a single peak at 34 ns, with a small tail that extends towards longer values. T90 presents a fast maximum with ~125 ns rise time, and a broad distribution at ~219 ns.

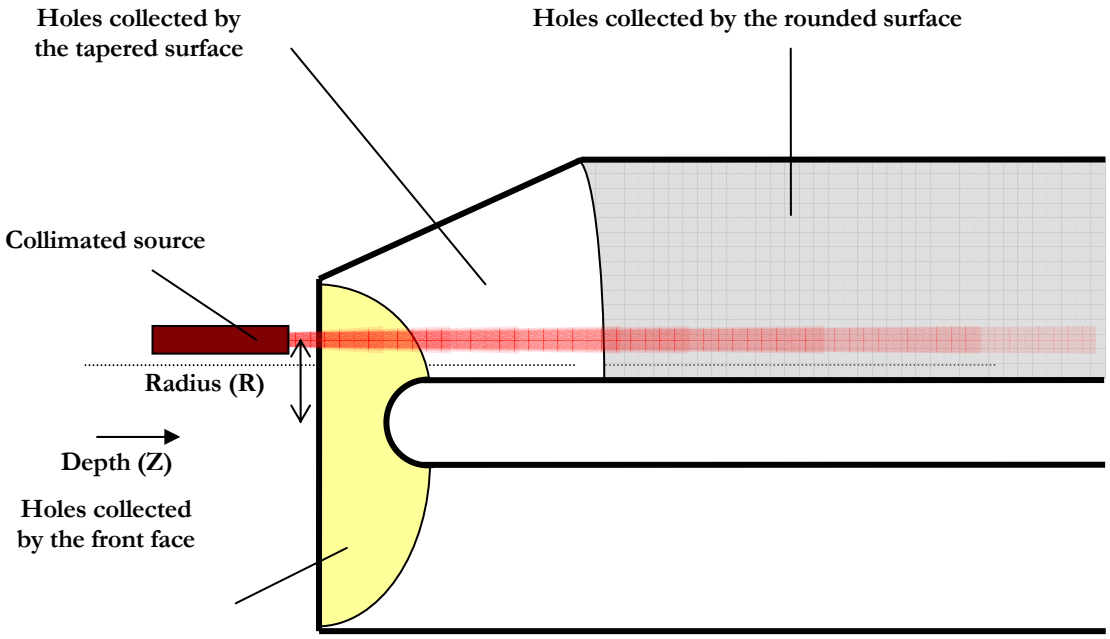

Figure VI.6: Schematic illustration showing the different regions of interactions where the holes will be collected either by the front face, the taper or the rounded surface of the cathode. Due to the attenuation of γ-rays a large fraction of pulse shapes will present the characteristics of interactions occurring at the front (fast T30 and T90). With increasing radius, this proportion will reduce. At large radius, pulse shapes exhibit the properties of a true coaxial response.

The presence of two maxima in the T90 distribution is a combination of effects due to the detector geometry and the segmentation. Figure IV.15 shows a maximum electrons drift velocity in frontal region of the crystal. Therefore the faster peak corresponds to interactions occurring at the front of the crystal where the holes are collected on the front face. There, the short inter-electrode distance and the strong electric field result in a fast pulse rise time. Deeper in the crystal, photoelectric and Compton scattering interactions occur at positions where the holes are collected by the cathode on the crystal sides. At small radii, the charge carrier drift time is the longest, thus inducing large rise time values and generating the distribution of longer values observed in the second maxima of the T90 distribution.

The 4-fold segmentation of the Clover crystal creates large segment volumes, where a large proportion of Compton scattered events are detected as Fold 1 events. Due to the preferential forward scattering cross section, the first interaction in a Compton scattering sequence will deposit a small amount of energy. Considering a 2-interactions Compton event, for which a 662 keV incident γ-ray scatters at 10°, where first interaction deposits an energy ~13 keV at small radius; the main interaction will deposit ~650 keV. Given a path of 2 cm in the crystal

for the scattered photon, the main interaction is more likely to occur at small radii, which also leads to a long rise time.

The rise time profile of a Compton scattered event (CSE) is dependent on the position of the source relative to the crystal geometry. Fold 2 events showing a long rise time must result from photons scattered at large angle in order to be detected in an adjacent segment. Therefore the main interaction must occur near the position of the source. Monte Carlo simulation carried with GEANT 4 predicted that for 662 keV in Germanium, the main interaction is the first interaction for ~60% of the FEE [Des02]. Therefore the distribution of rise time observed for CSE should be maximum at the peak value observed for Fold 1 events. The ratio of intensities between CSE from Fold 1 and CSE from Fold 2 events could be obtained by comparing the energies from the segment in front of the source with the energy from the adjacent segment. In this work they are assumed to be identical.

Therefore, the shape of the T90 distribution can be understood as the sum of contributions from single photoelectric and Compton scattered events. Figure VI.7 (a) and (b) present both Fold 1 and Fold 2 distributions along with the difference between Fold 1 and Fold 2 distributions. The comparison between both Fold 1 and Fold 2 histograms in Figure VI.7 (a) reveals the contribution of Compton scattered events to the tail of the T30 distribution: while T30 is fast at small radii, Compton scattered events increase the T30 value of the charge pulses. However, the value of the mean, calculated for the Fold 1 and for the difference distributions shown in Figure VI.7 (b) are similar. The remaining tail in observed in the difference spectrum is probably due to higher order multiplicity events ($M\gamma > 2$) within the segment. The difference between both T90 distributions displays two distinct peaks. The peak at fast rise time results from interactions occurring in the front region, demonstrated by the value $T90_{max}$ of ~122 ns. The second peak corresponds to interactions that occur deeper in the coaxial region of the crystal, where the holes are collected by the circular surface of the cathode.

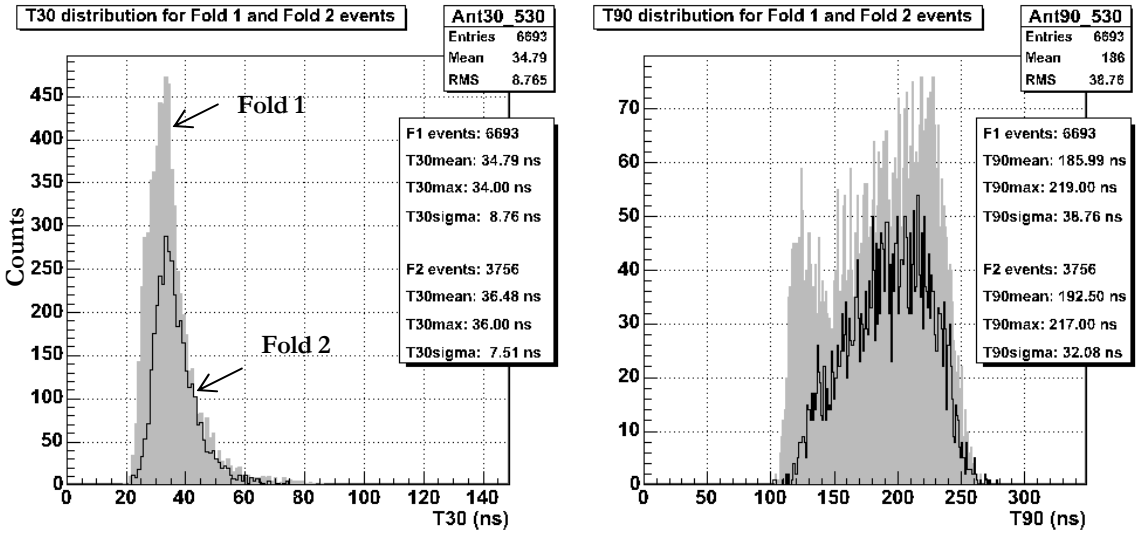

Figure VI.7: (a) Example Fold 1 and Fold 2 rise time distributions for T30 and T90. The source is located in front of the tapered region of the crystal at a small radius R = 10.4 mm (P530). The plain histograms present the data from Fold 1 events. The Fold 2 histograms are represented by the black line.

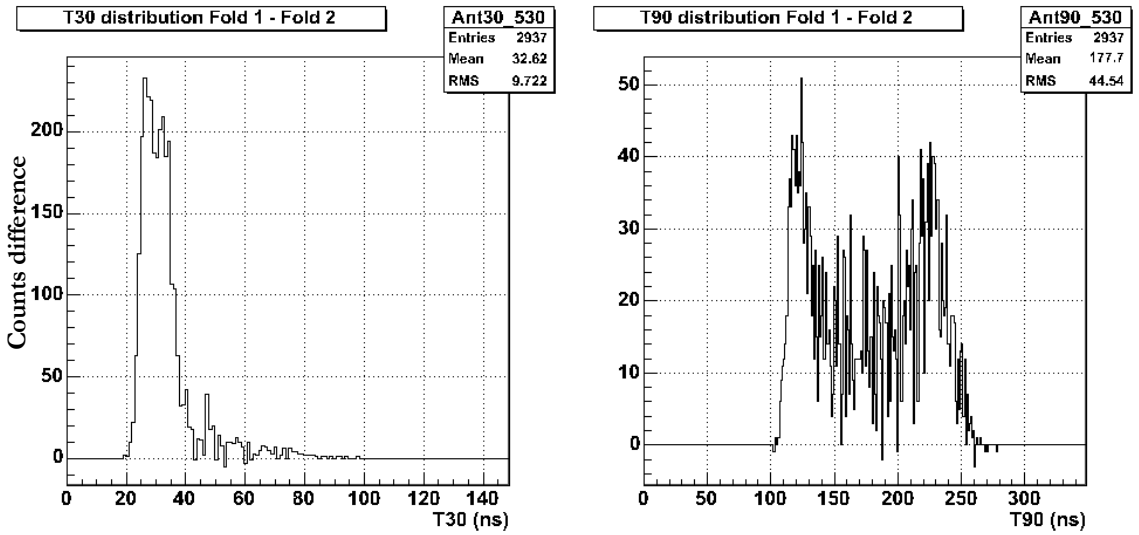

Figure VI.7: (b) Difference between Fold 1 - Fold 2 for T30 and T90 distributions for source position P530 et R = 10.4 mm. T90 shows two distinct peaks at ~123 ns and ~226 ns, while the maximum of the T30 distribution is 30.7 ns.

Figure VI.8 (a) presents the T30 and T90 distributions for a source position at mid radius (R = 17.8 mm, P550). The position of the T30 and T90 centroid is similar for both Fold 1 and Fold 2 distributions with a smaller intensity for Fold 2 events. The figure shows that Fold 1 events include some contributions from Fold 2 events. Indeed at mid radius, the proportion of Compton scattered events to the Fold 1 distribution is the largest: the probability for an event of multiplicity $M_\gamma \geq 2$ to contribute to FEE is the highest.

In Figure VI.8 (b) the large tail towards long T30 and T90 values is still present despites the subtraction of the distribution of Fold 2 Compton events, and may contribute from event of multiplicity $M_\gamma \geq 2$ that have deposited their full energy within the segment.

At maximum radius, the total number of events decreases due to the lower amount of material available for the detection of γ-rays. Figure VI.9 (a) shows an example Fold 1 and Fold 2 distributions for T30 and T90, observed for a source position close to the outer cathode (R = 27.8 mm, P656). The most remarkable is the different centroid observed for the T30 distribution: compared to the previous example in Figure VI.8, the centroid of the T30 distributions for Fold 1 and Fold 2 events are separated by ~20 ns.

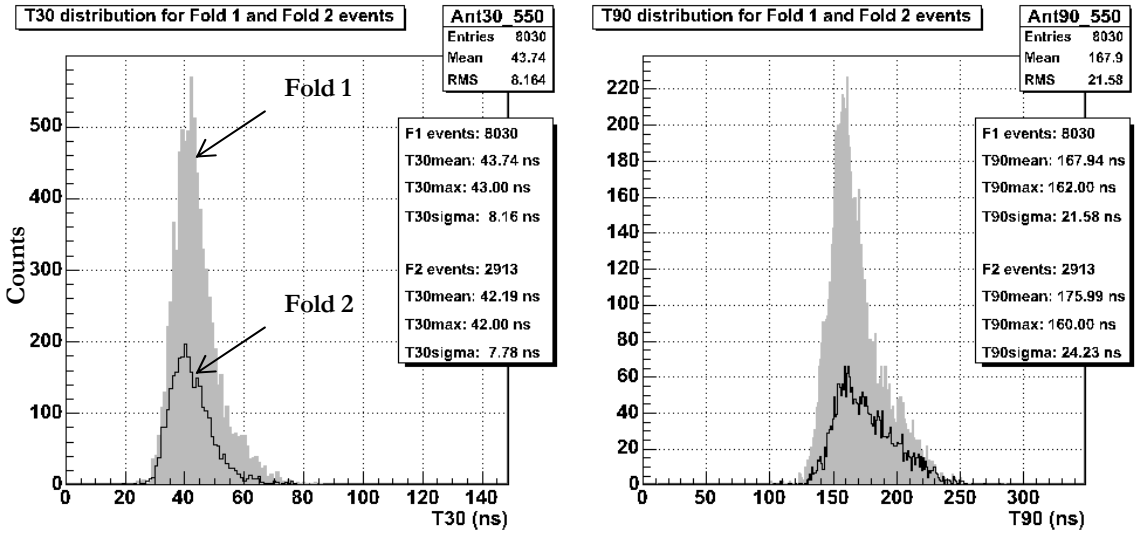

Figure VI.8: (a) Example rise time T30 and T90 distributions for the collimated source positioned at mid radius (R = 17.8 mm, P550). The picture shows both Fold 1 and Fold 2 rise time distributions.

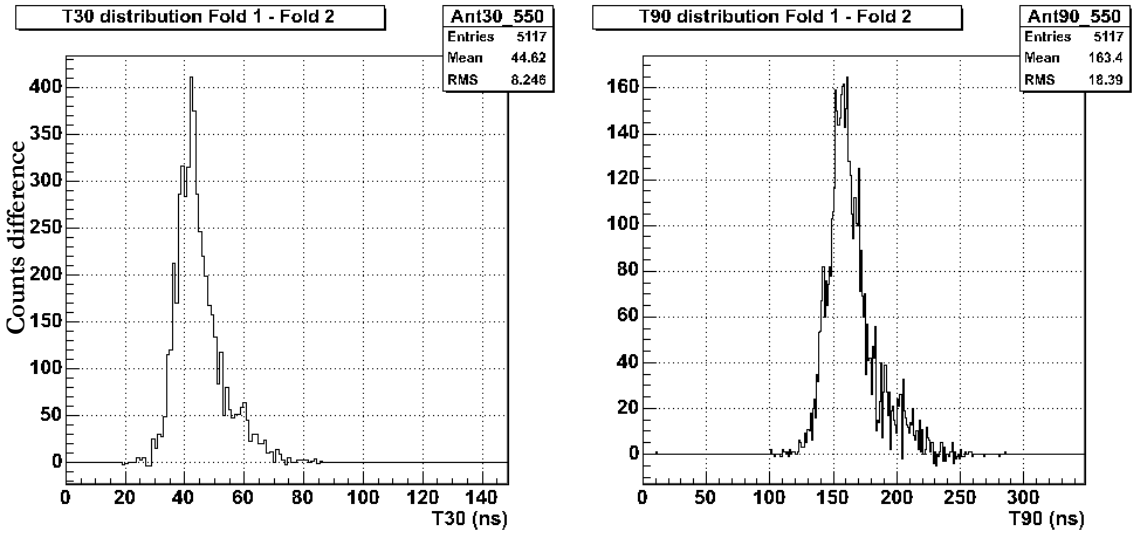

Figure VI.8 (b) Difference Fold 1 - Fold 2 for T30 and T90 distributions for source position P530. T90 shows a single distinct peak at ~158 ns, while the maximum of the T30 distribution is ~44 ns.

Figure VI.9 (b) presents the result of the difference between Fold 1 and Fold 2 events for T30 and T90 distributions at the position P656. A wide T30 difference distribution, with a large tail towards fast values, is observed. The position of the maximum is at the same value compared to the T30 distribution presented in Figure VI.8. The T90 difference distribution presents a profile similar to the distribution previously observed for Fold 1 events in Figure VI.8.

For both difference distributions, a fast T30 and T90 tail is still present. While the profile of Fold 2 events in Figure VI.9 (a) allows one to identify the contribution of Compton scattered events to T30 and T90 Fold 1 distributions, the presence of the large tail in the difference distributions may be explained by the following: at large radial positions, the γ-rays interact in a region of coaxial geometry. In such region, at depth $Z \geq 30$ mm, the electric field calculations presented in Figure IV.13 shows a low field value of ~800 V/cm. From the calculations presented in Figure IV.14, the electric field intensity is below the value that would ensure the saturation of the drift velocity of the charge carriers. In this hypothesis, the drift of the charges will vary with the strength of the electric field. The skew in the T30 distribution is believed to contribute from events interacting at radii $R < 28$ mm in the coaxial region where the electric field is stronger, thus inducing pulses with a faster T30 value. The tail observed in the T90 difference spectrum may result from the sum of scattered events with random background.

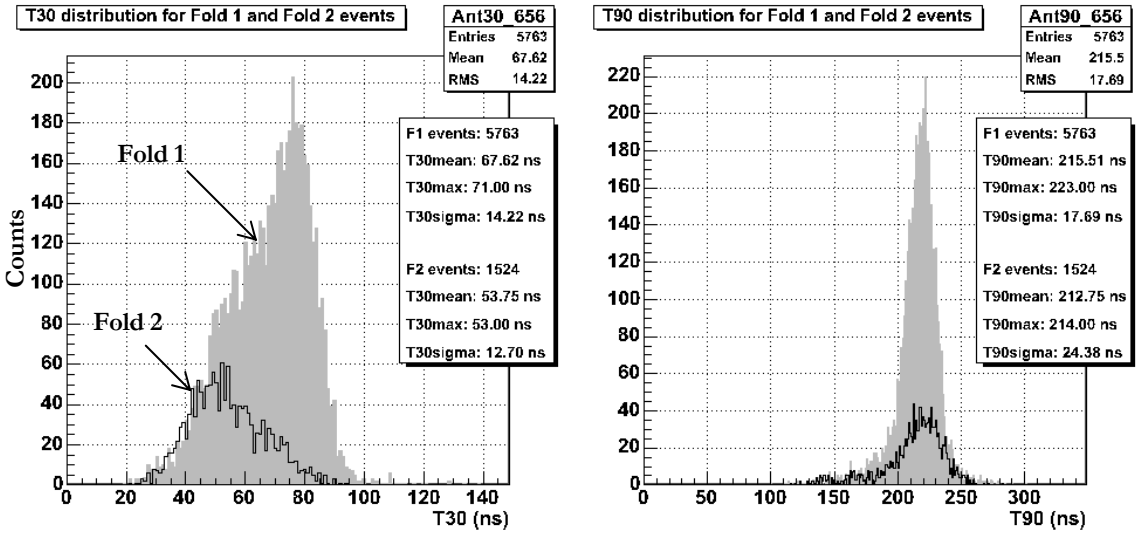

Figure VI.9: (a) Example rise time distributions for the collimated source positioned at a large radius (R = 27.8 mm, P656). The picture shows both Fold 1 and Fold 2 rise time distributions for T30 and T90.

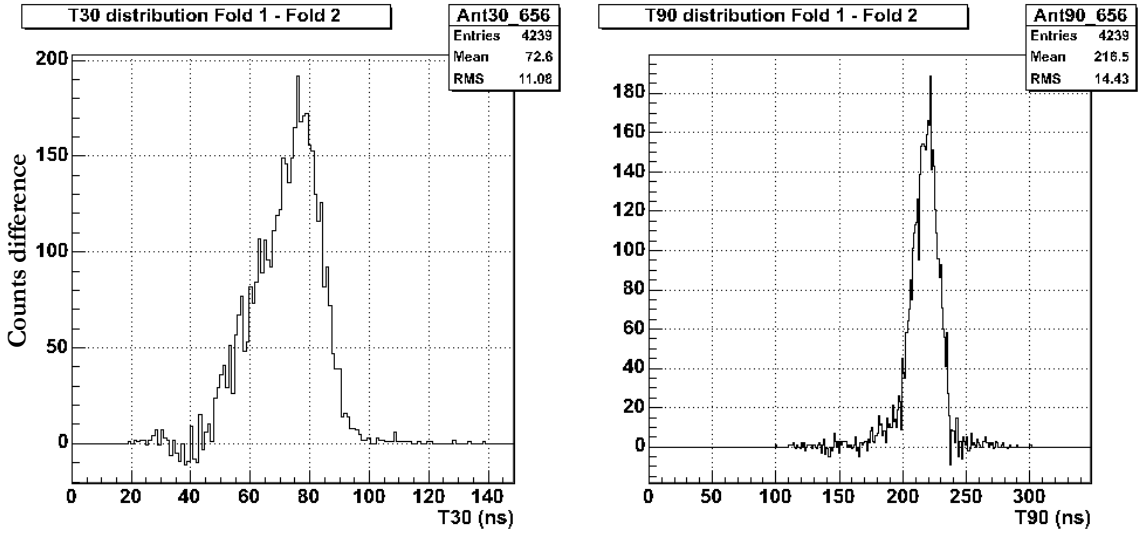

Figure VI.9: (b) Difference between Fold 1 and Fold 2 rise time distributions for large radius (R = 27.8 mm, P656) for T30 and T90. T30 is maximum at 75 ns, and T90 is maximum at 218.4 ns.

1.3.5 Zone C, Source located in front of the flat edge

For sources located at positions where the holes are directed towards the flat edge of the cathode, the collection time of the charge carriers is the fastest for the whole coaxial region. The distance between the core and outer electrodes is the shortest (24 mm) along the <001> direction. This induces a stronger electric field, and maximises the drift velocities of the charge carriers relative to other orientations.

Figure VI.10 (a) presents the rise time distributions obtained at a small radius (R = 9.3 mm, P404) along the <010> direction. The intensities of Fold 1 (5198) and Fold 2 (5186) distributions are almost identical. For such a position, at the segments boundary[39], the contribution of Fold 2 events is maximum and the contribution of Fold 1 is minimum, as seen in Figure V.8. Therefore, a Fold selection of events operated at positions along the segmentation line have the advantage of being able to isolate the contribution of Compton scattered events that would deposit their full energy within a single segment, and effectively maximise the number of Fold 1 events. In Figure VI.10 (a) the Fold 1 histogram contribution from single photoelectric events is maximum. Both Fold 1 and Fold 2 T30 distributions have similar shapes and characteristics. In the case of T90, two distinct peaks, of significantly different relative intensity, are observed with rise time values of 105 ns and 180 ns. The presence of two peaks in the Fold 1 distribution is due to photoelectric interactions occurring at the front (fast maximum) and in the coaxial region (wide distribution at long T90). This observation is consistent with the relative volume of germanium.

One must notice the difference between the maxima observed in the Figure VI.10 (a) and in the difference T90 distribution shown in Figure VI.7 (b). This difference is believed to result from the contribution of single photoelectric interaction along the tapered electrode: the broad maximum in Figure VI.10 (a) is located at a smaller T90 (~185 ns) compared to Figure VI.7 (a) (~225 ns). The absence of taper is responsible for the much sharper rise time profiles.

[39] The position considered was actually facing segment A4, close to the boundary with segment A3.

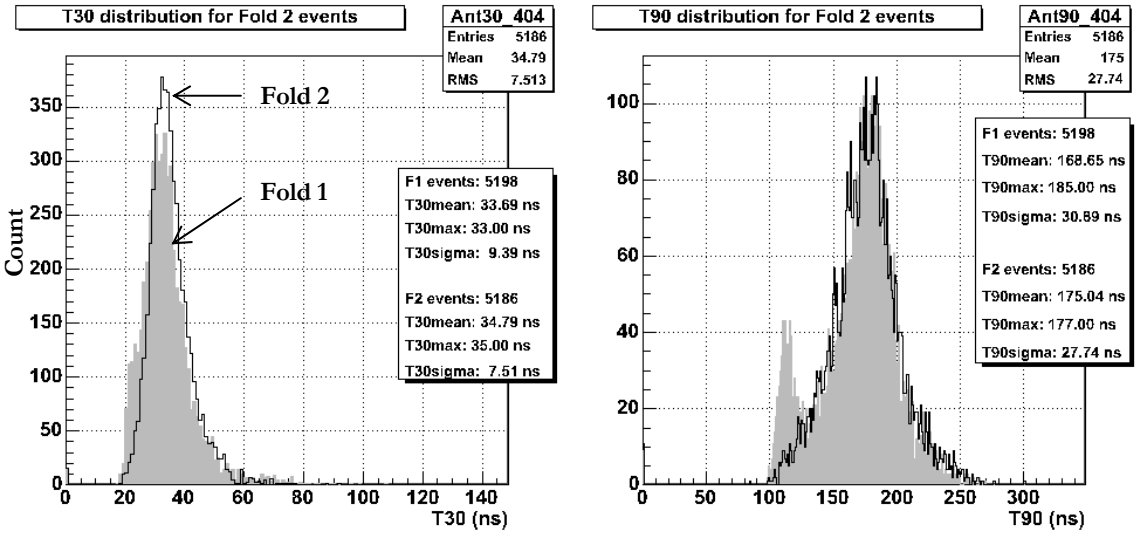

Figure VI.10: (a) Example T30 and T90 rise time distributions for Fold 1 and Fold 2 events. The collimated source was located at small radius (R = 9.3 mm, P404) along the <010> direction. The intensity of both Fold 1 and Fold 2 is identical. For such position, facing the segment boundary, the contribution from Compton scattering to Fold 1 events is minimised. The small peak observed at fast T90 corresponds to photoelectric interactions occurring at the front of the crystal. The large peak corresponds to interactions occurring in the coaxial region at the back of the crystal.

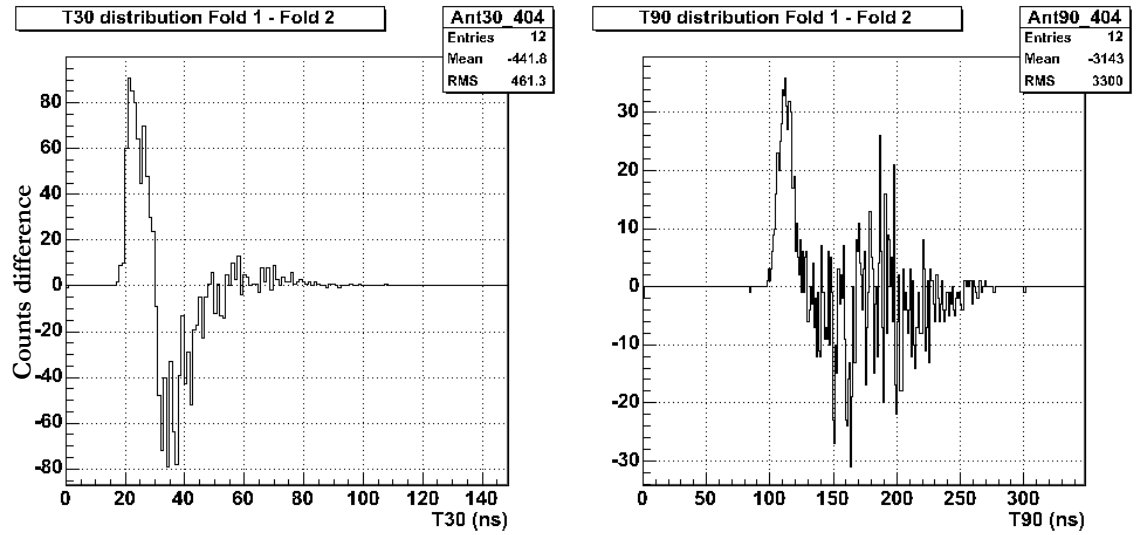

Figure VI.10 (b) Difference between Fold 1 and Fold 2 rise time distributions at small radius along the segmentation line (P404).

The Fold 2 distribution follows the long rise time peak of the Fold 1 distribution, demonstrating the predominance of forward scattering for 662 keV photons. One can then clearly identify two separate drift profiles from the difference between the Fold 1 and Fold 2 distributions for T30 and T90 shown in Figure VI.10 (b):

- For T30, the positive peak corresponds to the T30 value where the contribution of Fold 1 events is maximum compared to the contribution of Fold 2 events, while the negative peak presents the inverse behaviour. Therefore single photoelectric FEE have a shorter T30 than CSE, as shown by the positive peak centred at ~23 ns, and the negative peak centred at ~35 ns;

- For the T90 distribution of Fold 1 events, the pulse rise times are is centred around the fast maximum at ~125 ns rise time, which correspond to a typical rise time observed in the front of the crystal. The difference distribution shows no statistically significant difference for the long rise time values. This could be interpreted as Compton scattered event being detected as Fold 1 events either in segment A4 (indicated in Figure.VI.3) or in segment A3. Therefore, a large range of rise time values are observed for interactions occurring within the same segment.

The large range of rise times observed illustrates the necessity to segment germanium crystals not only azimuthally but also longitudinally, in order to separate the contribution of interactions from the front of the crystal (fast drift times) relative to the rest of the crystal with a coaxial configuration. This has been realised for the TRIUMF-ISAC Gamma Ray Escape-Suppressed Spectrometer (TIGRESS), composed of 36-fold segmented Clover detectors [Scr05, Sve05]. The Crystals are segmented azimuthally in quadrants as for the EXOGAM Clover detector, with an additional segmentation at 20 mm from the front face of the detector.

At mid radius and large radius, the rise time distributions are similar to those presented in Figure VI.7 and Figure VI.9, as shown by the examples in Figure VI.11 and Figure VI.12. The intensity of Fold 2 events reduces with increasing radius, due to γ-rays escaping through the side of the crystal.

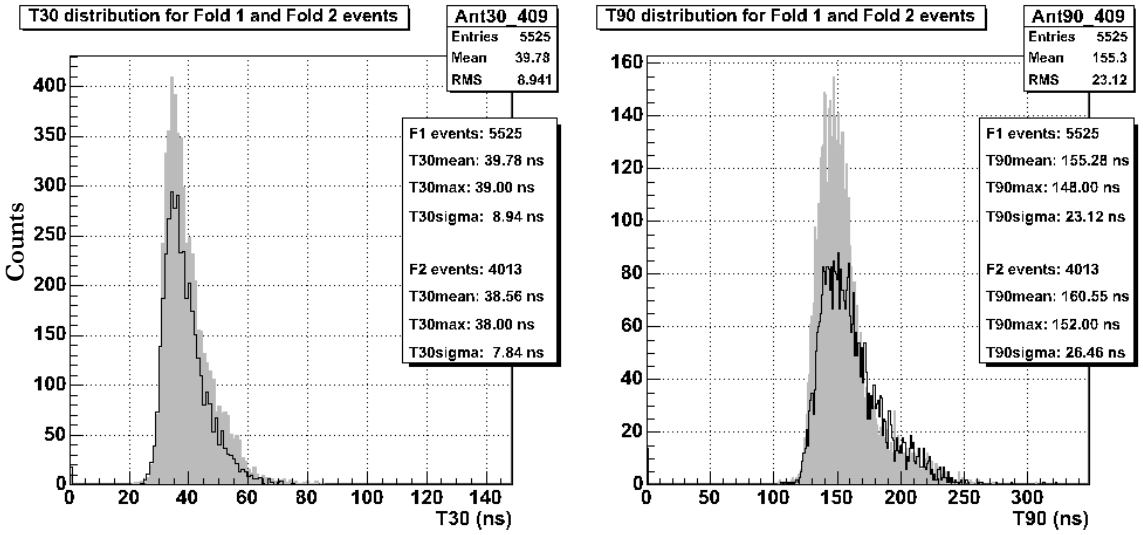

Figure VI.11: Example Fold 1 and Fold 2 distributions for T30 and T90. The collimated source was located at mid radius (R = 19.3 mm, P409) along the <010> direction.

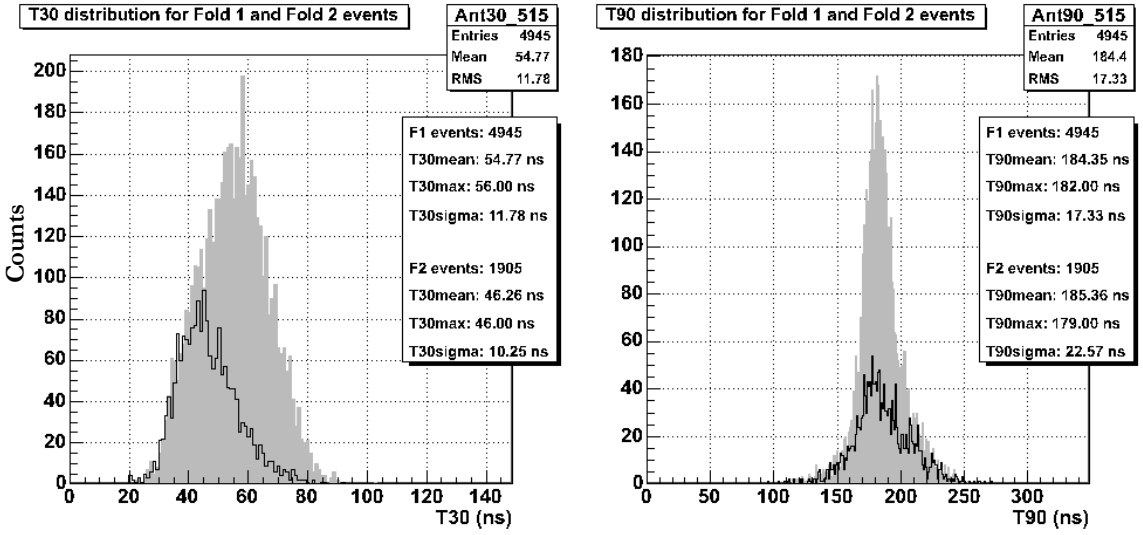

Figure VI.12: Example Fold 1 and Fold 2 distributions for T30 and T90. The collimated source was placed at large radius (R = 24.6 mm, P515).

1.3.6 Zone D, source position along the <110> direction

In the last region defined in Figure VI.6, the holes are directed towards the rounded corner. The rise time distributions observed at small and mid radii are similar to those observed in the previous regions; the holes are directed towards the front face or towards the rounded surface of the cathode. The characteristics of this region depend on the influence of the geometry on the electric field strength and direction. At this orientation, MGS calculations presented in Chapter IV predict a weak electric field and a low drift velocity for electrons and holes in the corner near the cathode as illustrated in Figure IV.16 representing the drift velocity of holes along the <011> axis. The results predict poor drift properties, due to the non saturation ($v_{drift} < 10^7$ cm/s) of the charge carriers drift velocity.

Figure VI.13 and Figure VI.14 present the rise time distributions from two source positions near (R = 26.4 mm, P92) and at the corner (R = 29.3 mm, P86) between the two adjacent faces. The contribution from Compton scattered events is similar to the previous examples seen in Figure VI.12, the centroid from Fold 1 and Fold 2 events are located at different T30 values. The main difference is the observation of the larger proportion of longer T30 values (T30 > 80 ns) observed for the distribution from Fold 1 events. Such feature is not observed at similar radial positions along the taper (Figure VI.9 (a)) where the edge of the T30 peak for

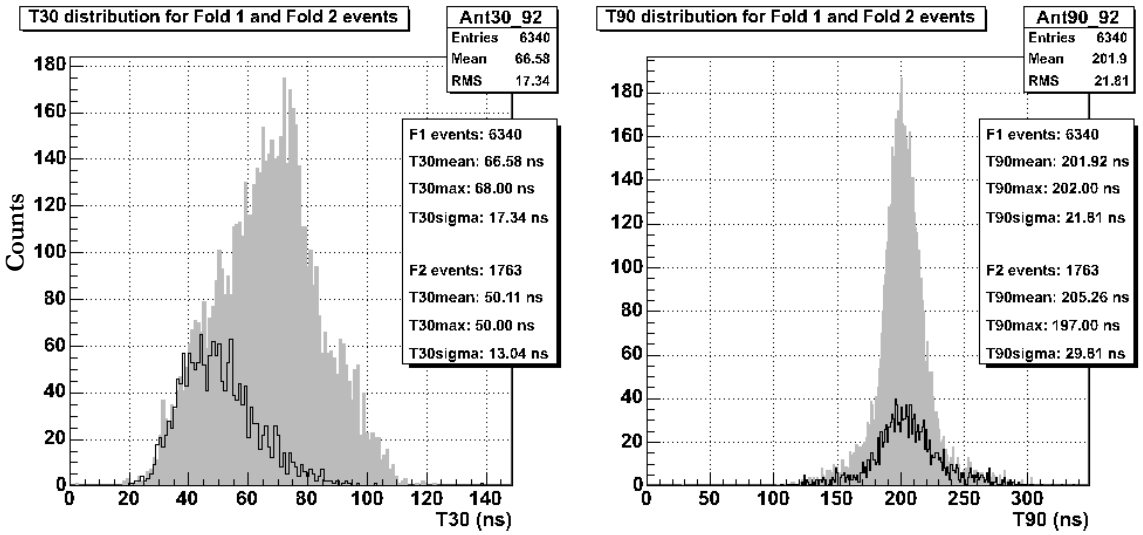

Figure VI.13: Rise time distributions observed for Fold 1 and Fold2 events in segment A3 near the corner between the two adjacent flat faces, for a radial source position of R = 26.4 mm.

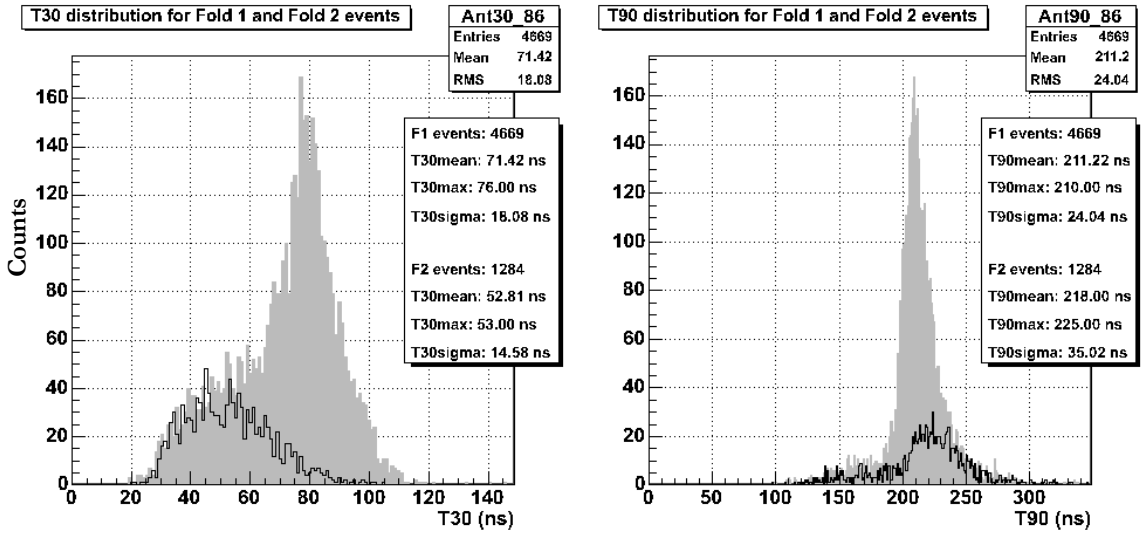

Figure VI.14: Rise time distributions observed for Fold 1 and Fold 2 events in segment A3, in the corner between the two adjacent flat faces, for a radial source position of R = 29.3 mm.

the Fold 1 distributions decreases sharply. Such long T30 values are attributed to interactions occurring in a low field region, where the drift velocity is unsaturated. The drift velocity of the electron cloud is therefore strongly dependent on the magnitude of the electric field. This effect is also observed at smaller radii along the flat edges of zone C (Figure.VI.3), for source positions near to the cathode.

1.3.7 Dispersion of the partial rise time values

The dispersion of the values given by the standard deviation is presented for each Fold 1 distribution in Figure VI.15. The average deviation gave very similar results and lead to identical conclusions, therefore its variation is not represented. The standard deviation has been calculated form the mean of each distribution. The dispersion of T30 is larger in the outer radial range R = [25-30] mm. As shown in Figure VI.9 and Figure VI.12 in the previous section, the larger dispersion of T30 is probably due to Compton scattered events. The larger values of dispersion observed at the corner in the region (X, Y) = (34, 36) is believed to arise from the low electric field, where the drift velocity of the carriers varies a lot with the electric field. This effect is also apparent in the whole outer ring between R = 25 mm and R = 30 mm. The dispersion observed for T90 at small radial range has been discussed earlier in section 1.2.2. Larger dispersion extends more along the directions where the taper extends to a maximum depth.

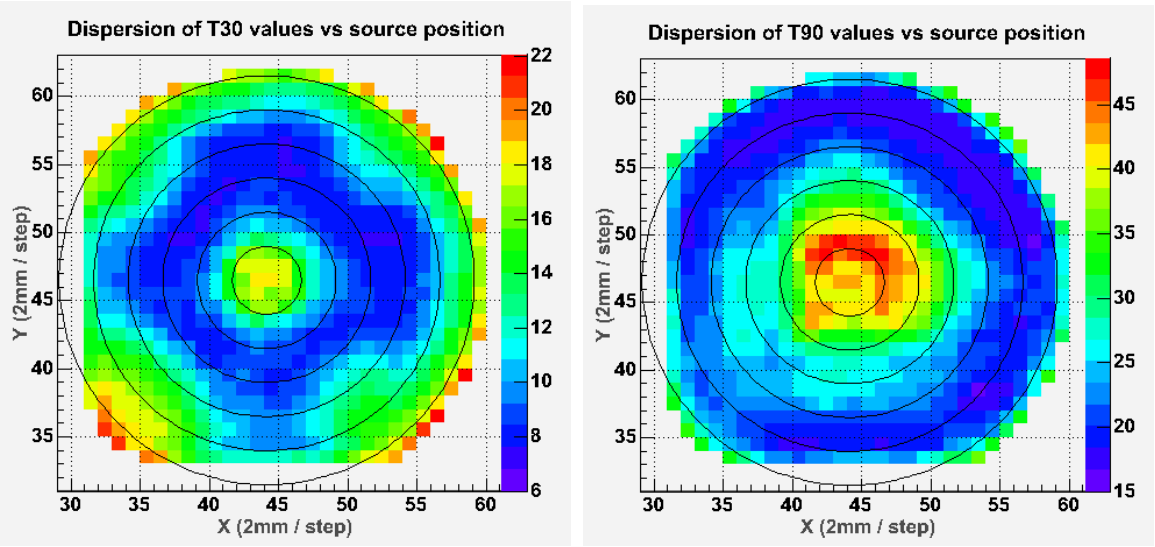

Figure VI.15: Variation of the standard deviation of T30 and T90 distributions with position of the source position.

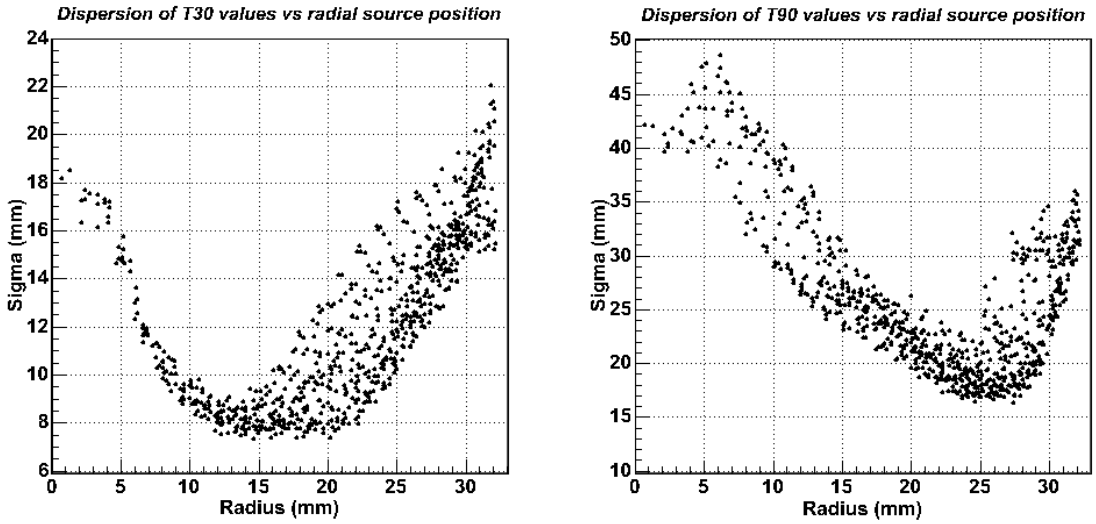

Figure VI.16: variation of the standard deviation of T30 and T90 distribution with radial source position.

For T30 distributions, the standard deviation decreases from ~18-20 ns at the front of the crystal to a minimum of ~8 ns at R < 14 mm. One observes then a broad range of values for larger radii, depending of the orientation: The value $\sigma_{(T30)}$ is generally wider along the <110> directions. The dispersion of the T30 values is maximum for a large outer ring.

T90 distributions present a different profile of dispersion. The value $\sigma_{(T90)}$ is maximum at the centre of the crystal and decreases with increasing radius up to R ~ 25 mm. The large range of dispersions observed is a direct effect of the geometry of the detector. The large volume of the segments causes Compton events to worsen the quality of the data.

2 Variation of rise time distributions with source position

2.1 Statistical estimators

To a first approximation, the rise time values will cluster around a central value which will correspond to the rise time observed at the particular position of interaction. The dispersion of the values is then caused by the combination of single photoelectric events (PE) and Compton scattered events (CSE), as seen in the previous section, along with the contribution from interactions occurring at different depths. The approach described here tries to characterise the partial rise time distributions with a restricted number of estimators. For each distribution of N values, the parameters listed below were determined and their variation with position was investigated in order to find the best statistical estimator of the distribution.

2.1.1 Estimators for the central value

The *mean*, or first central moment of the distributions. The mean is defined as

$$\overline{Tn} = \frac{1}{N}\sum_{j=1}^{N} Tn_j \qquad \text{(VI.2)}$$

where $\overline{Tn}$ is the mean of the partial rise time Tn distribution (where n = 30% and 90%), and N is the number of elements in the distribution.

The *mode*. The mode Tn_{mode} (also referred to as Tn_{max}) represents the peak or maximum value of the distribution. If the distribution of interest has a strong central tendency, the mean and the mode are almost similar. Otherwise, this will indicate an asymmetry in the rise time distribution, as observed in Figure VI.14. The mode is particularly useful for the description of bimodal distributions, in order to study the variation of both maxima.

The third candidate estimator is the *median* of the distributions. The median of a distribution is the value Tn_{med} for which

$$\sum_{j=1}^{n_{med}} Tn_j = \sum_{j=n_{med}}^{N} Tn_j \tag{VI.3}$$

The median defines the partial rise time value for which the number of larger recorded Tn values ($Tn > Tn_{med}$) and the smaller number of recorded Tn ($Tn < Tn_{med}$) values are equal. The median is a good estimator for central distributions where most of the data is under a single peak. The median is estimated as:

$$\begin{aligned} Tn_{med} &= Tn_{\left(\frac{N+1}{2}\right)} && \text{for N even} \\ Tn_{med} &= \frac{1}{2}\left(Tn_{\left(\frac{N}{2}\right)} + Tn_{\left(\frac{N}{2}+1\right)} \right) && \text{for N odd} \end{aligned} \tag{VI.4}$$

For a perfectly symmetric distributions, one gets

$$\overline{Tn} = Tn_{\max} = Tn_{med} \tag{VI.5}$$

2.1.2 Estimators for the dispersion of values

Once the central value (mean, median or mode) is defined, the dispersion of the values can be measured by the standard deviation σ and the average deviation A_{dev}. The standard deviation is defined as

$$\sigma_{(Tn)} = \sqrt{\sigma^2} \tag{VI.6}$$

Where σ^2, the variance of the distribution is defined as

$$\sigma^2 = \frac{1}{N-1}\sum_{j=1}^{N}\left(Tn_j - \overline{T}\right)^2 \tag{VI.7}$$

The average deviation is calculated as

$$A_{dev} = \frac{1}{N}\sum_{j=1}^{N}\left|Tn_j - \overline{T}\right| \tag{VI.8}$$

The average deviation gave similar results and lead to the same conclusions as the use of the standard deviation. Although both variance and average deviation are defined relatively to the

mean in Equations VI.7 and VI.8, the dispersion estimators must be calculated from the most appropriate central value in order to be meaningful.

2.1.3 Asymmetry and Skewness

The degree of asymmetry in a distribution can be evaluated by calculating the asymmetry A between the mean and the mode:

$$A = \frac{\overline{Tn} - Tn_{\max}}{\overline{Tn} + Tn_{\max}} \tag{VI.9}$$

The skewness, related to the third moment about the central value:

$$Skew(Tn) = \frac{1}{N\sigma^3} \sum_{j=1}^{N} \left[Tn_j - \overline{Tn} \right]^3 \tag{VI.10}$$

A positive skew indicates a distribution with an asymmetric tail extending towards longer rise time values, while a negative skew indicates a tail extending towards faster rise time values.

2.2 Variation of the distributions estimators

2.2.1 Overview in the X-Y plane

As discussed previously, the shape of the rise time distributions varies significantly with the position of the source relative to the front face of the crystal. Due to the large number of positions involved, it is impossible to study each of then as done in the previous section. The use of the statistical estimators described above provides a robust method for investigating the characteristics of the rise time distributions with the position of the source, and provides an insight towards the possible improvement of the radial position of interaction. Figure VI.17 shows the variation of the mean, median and mode of the T30 and T90 distributions measured on anode signals for Fold 1 events, as a function of the γ-ray source position. The partial rise time central estimators generally present similar patterns though some differences are apparent between the mode, mean and median:

- The mean T30 generally decreases from ~37 ns at the centre of the crystal[40] to a minimum of ~30 ns near mid radius, before increasing towards the outer electrode where the maximum value of ~70 ns is attained. The mode increases from ~20 ns at

[40] Remembering that for R < 5 mm, the active material is only located in the first front ~8 mm of the crystal.

central radius the front to a maximum of ~80 ns at the cathode. The variation of the median is similar to the variation of the mean with a slight difference between the values at each position. Some visible differences exist between the mode and the mean of T30 distributions and are related to the contribution of Compton scattered events to the rise time distributions for locations at the front of the crystal.

- The mean T90 is fast at the front of the anode (~150 ns). In the coaxial part of the crystal, the value decreases from ~180 ns to a minimum in the range 149-170 ns[41] before increasing to a maximum of 205 ns to 220 ns near the outer electrode. The variations of $T90_{mode}$ follow an identical behaviour, but one observes faster values measured at the front of the crystal. However at small radii (R ~10 mm), the presence of two maxima in the rise time distributions induce the emergence of a few positions with slower $T90_{mode}$ values near adjacent positions of fast rise times. This illustrates the limitation in the use of the mode as a statistical estimator. The example in Figure VI.7 shows a difference of ~100 ns between the fast and slow maxima. The variation of $T90_{med}$ is similar to the variation of the mean T90; with a larger range between the minimum and maximum values (from ~130 ns to ~225 ns).

The three estimators show the effect of the anisotropic drift properties of the charge carriers. At identical radii, the central values are faster along the <010> and <001> directions relative to the <011> directions (refer to Figure.VI.3 for crystal orientation). A variation of approximately 9% is observed between <010> and <011> orientations for a radius $R \approx 20$ mm in the largest segment of the crystal.

The results from Figure VI.17 demonstrate the possibility to calibrate the Crystal of an EXOGAM Clover detector for radial position of interaction. The mode of the distributions would be the ideal estimator to investigate due to the superior range of values available both for T30 and T90 distributions. However, it is not a robust estimator in the case of T90 due to the presence of two maxima observed in T90 distributions in the small radial range.

[41] The fastest mean T90 value of 149 ns is measured along the short axis, parallel to the <010> direction.

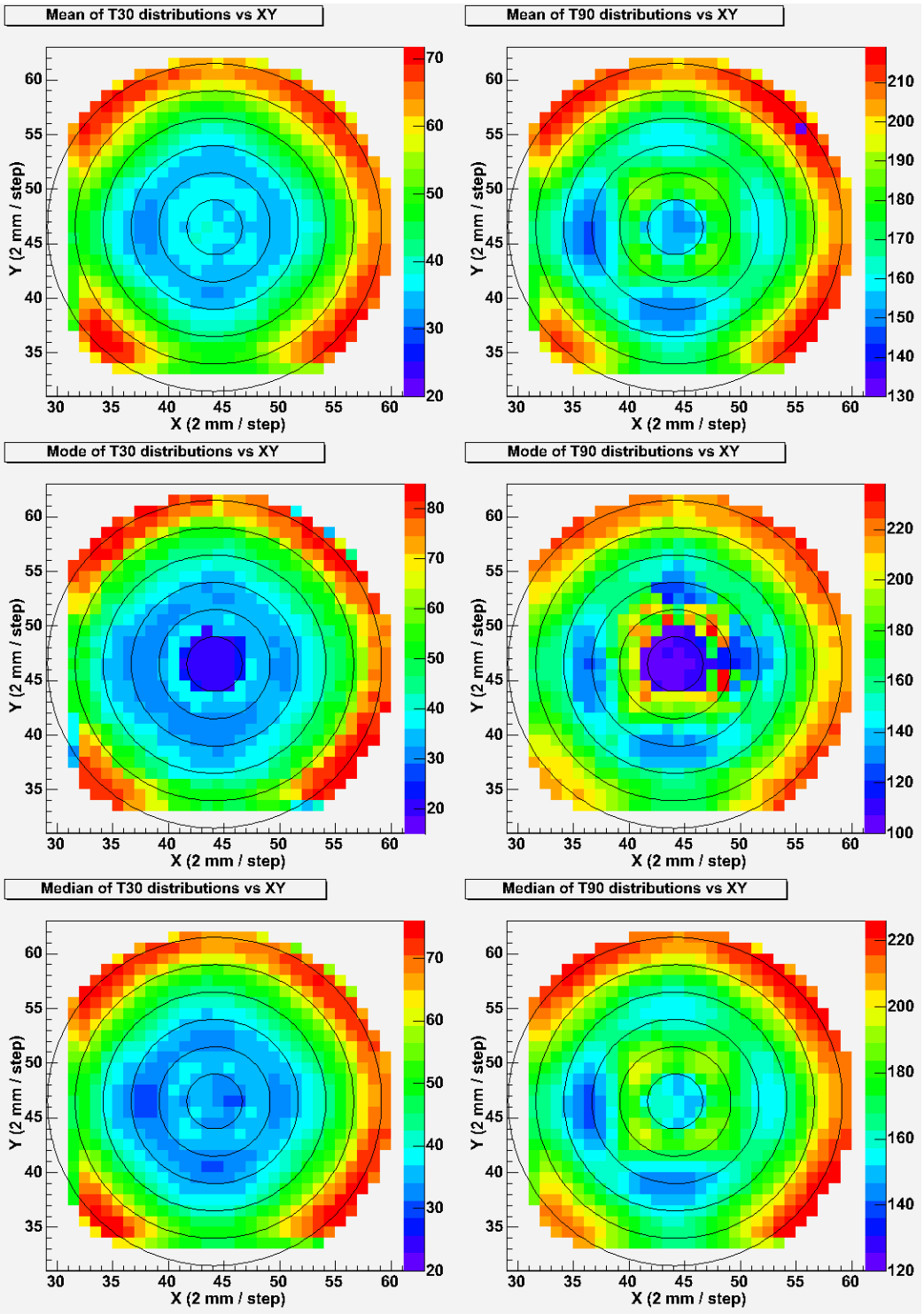

Figure VI.17: Mean, mode and median values of the T30, and T90 distributions measured for the different source positions in front of crystal A for Fold 1 events. The colour scale indicates the value of mean, mode and median value of the rise time distributions for each source position. the concentric circles indicate different radial ranges, from the centre of the crystal towards the outer radius by increment of 5 mm.

2.3 Variation of the distribution estimators with radius

2.3.1 Overview of radial variation

The variation of the three estimators with radial position gives an insight on the possibility to use the T30 and T90 values for radial position determination. For each source position, the cylindrical coordinates (R,θ) were calculated relative to the central position of the crystal; the average error in radial position is 2.1 mm (section1.3). The radial variation of each of the T30 and T90 distribution estimators was then plotted for all source position. Results for Fold 1 distributions shown in Figure VI.18 presents the following similar features:

- Different radial ranges, with identical variation: T30 is constant at low radius followed by a decrease down to a minimum value at small radius. T30 then increases up to maximum radius. T90 increases at low radius up to a maximum, then decreases to a minimum value at mid radius. It finally increases and appears to saturate at maximum radius. The particular variation observed for the mode of T90 distributions is discussed further in the section.

A large dispersion of the T30 and T90 values observed for a particular radius. The dispersion is due to the anisotropic drift properties of the charges. As a result, the range of rise times varies with orientation in the crystal. The maximum partial rise times are measured along the <010> directions, while the slower values are observed along the <110> directions. Another important effect adding to the dispersion of values is the particular geometry of the crystal: the distance between the core and the outer electrode – which changes with orientation (as illustrated in Figure.VI.3) and changes the strength of the electric field – induces different drift times observed at a same radius for different orientation. This is illustrated by the data points observed below the main tendency at radii R > 25 mm in Figure VI.18. This point is developed in the next section (Figure VI.21).

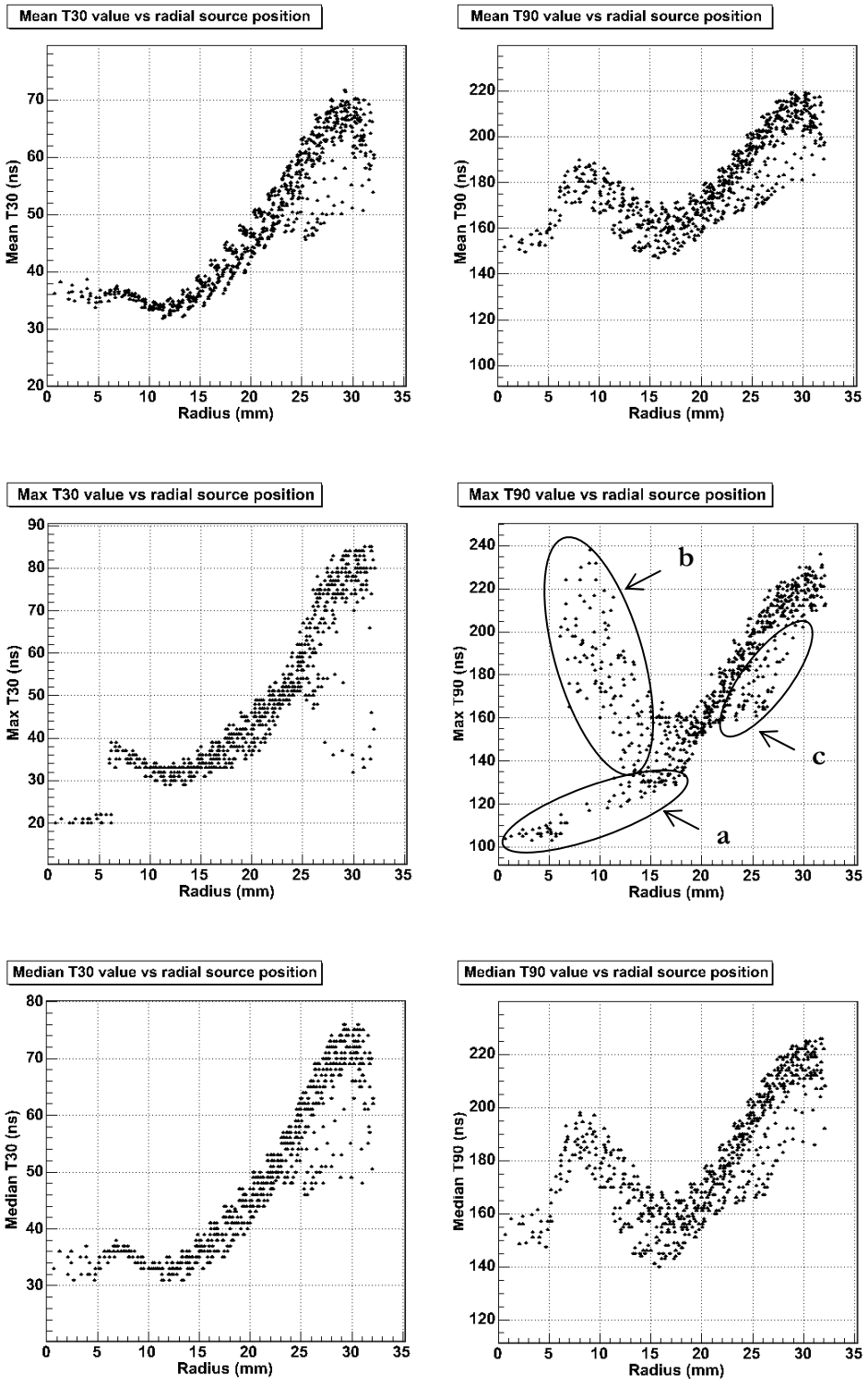

Figure VI.18: Variation of mean, mode and median of the T30 and T90 rise time distributions with radial position of the source in front of crystal A. The average error in radius is 2.1 mm. The zones indicted for the radial variation of the mode shows the contribution of interactions occurring at (a) the front of the detector, (b) along the taper and (c) along the flat edge of the cathode.

2.3.2 Radial variation of T30

The profile of the mean, mode and median T30 variations allows the division of the radius in 3 ranges. In the first range, the behaviour of the median and the mean are similar: the variation of the mean is constant around an average value of 36 ns. A similar value is observed for the median (~34 ns), whilst the value of the mode is constant about an average value of 22 ns. In the second range, the T30 value decreases linearly with the increase in radius. Both the mean and the median show a small variation from 33 to 31.5 ns. The variation of the mode shows an abrupt change in the distribution: the T30 maximum value decreases from 37 ns down to 32 ns. Finally, in the last range, the values of the three estimators increases up to a maximum of 70 ns for the mean, 85 ns for the mode and 76 ns for the median.

The physical implication of the different radial ranges becomes clear when illustrated on the side view of the crystal in Figure VI.19:

- The first range corresponds to R = [0, 6.5] mm;
- the second radial range corresponds to R = [6.5, 12] mm;
- the third radial range corresponds to R =12 mm to maximum radius.

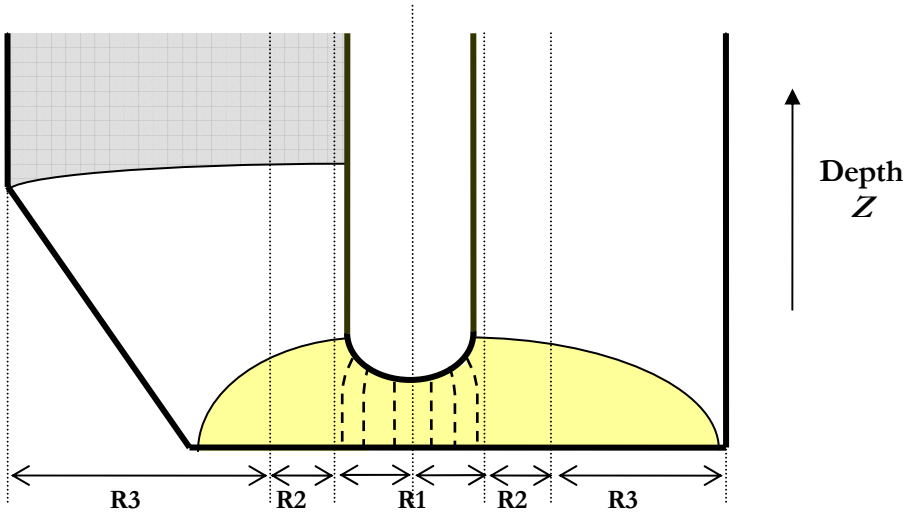

Figure VI.19: radial ranges derived from the radial variation of the T30 estimators. R1 corresponds to R = [0, 6.5] mm, R2 is defined by R = [6.5, 12] mm and R3 = [12, 30] mm. The drift direction of the charge carriers in front of the anode is illustrated by the dashed lines.

First radial range

In the first radial range (R < 6.5 mm), the fast value of T30 observed for the three estimators does not show a strong variation with radius. This radial range corresponds to the front of the core electrode (Figure VI.19) where the configuration of the electric field is nearly uniform and approaches a planar configuration. The electric field simulation (Figure IV.12 and IV.13, for Z = 5 mm) shows a strong electric field intensity, resulting in the only region in the detector where the drift velocity of the charges is saturated (v_d ~1.2×10^7 cm/s) over the whole distance between the core electrode and the outer cathode. Therefore the drift time of the charges only depends on the distance between the two electrodes. However in this region, with an increasing radius, one does not observe an increase of T30 as expected[42] but a dispersion of the data points around a mean value up to ~ 5 mm for the mean and the median. This difference is probably due to the difficult determination of the central position of the crystal (from the resolution in the position of interaction (at different interaction depths) given by the diameter of the collimator and from the 2mm steps used during the scan). Due to their central properties, the mean and median values observe a smooth increase towards the T30 value observed in the case of interactions along the anode in the coaxial region; following the increase in intensity in the coaxial region of the crystal. The mode is related to the most probable drift time, thus a more linear behaviour is observed. One may even suspect a linear increase from 20 ns to 22 ns in the first radial range. The variation shows then an abrupt change, where most of interactions occur at small radius in the coaxial region.

Second radial range

In the second range, T30 decreases for the three estimators. The source moves into a region of transition for the charge carriers drift directions: in front of the anode, the rise time value will vary as a function of the interaction depth of the photon, between the anode and the cathode (0 to 8 mm). As the source is moving away from the front of the anode, a larger number of Compton events contribute to the T30 distribution.

Third radial range

In the third range, the three estimators increase with radius. With reference to the mode, the rate of increase with radius can be divided into two linear functions. The two different slopes join at R ~ 23 mm. A geometrical explanation may arise from the maximum drift distance to

[42] With a supposed rounded anode of 5 mm radius, the minimum front distance is 8 mm at the centre and 13 mm at the edge. Also, the bending of the drift directions increases further the drift distance, which should result in a longer carrier drift time.

the cathode along the short axis of the crystal, in zone C (as indicated in Figure.VI.3), relative to the maximum drift distance in the opposite side of the crystal (long axis in zone A). Figure IV.13 illustrates the electric field configuration in the coaxial region at Z = 30 mm and 60 mm. The electric field is stronger in front of the flat edge of the cathode compared to the rounded edge of the cathode. As a result, the electrons drift velocity is near saturation in the first region, while the field intensity drop in the second region lowers the carriers velocity below saturation. This difference in drift velocities may result in a longer T30 for radii larger than 25 mm.

The T30 value decreases to a minimum at R = 12 mm radius. A similar effect has been observed with a coaxial detector [Des02]. This minimum corresponds to the shortest collection time for electrons in the coaxial part of the detector. At this stage, the causes for the increase in electrons drift time when approaching the anode, and for the occurrence of the minimum collection time at 12 mm radius, are unknown. This may be explained by the configuration of the electric field in the coaxial region of the detector. In theory, with a coaxial configuration, the electric field magnitude varies as 1/R (refer to Equation II.9). As R$\rightarrow$0, the magnitude of the electric field tends to large values. Past a certain electric field threshold, the carrier drift velocity does not saturate, and one observes a region of *negative differential conductivity* (NDC) where the drift velocity of the carriers decreases with increasing field strength [Mos82]. Thus for interactions near the anode, the electrons may enter a drift velocity regime where the saturation plateau is followed by a NDC region. In the second range (defined above), the increase of electric field strength would results in charge carriers drift velocity to be in the NDC region. Due to the 1/R decrease, the electric field would then reach a range of values for which the drift velocity saturates; as observed by the minimum at R ~ 12 mm. Then, following the decrease in electric field, the drift velocity of the charge carriers decreases as the regime is below the saturation value up to maximum radius. Finally, the decrease observed for T30 in the range R = [6.5, 12] mm results in a potential ambiguity in the value of T30 at small radii.

The dependence of each of the estimators has been fitted with three straight lines, each of which fits the variation of the parameter within one of the following radial ranges:

1. Range 2, for R2 = [6.5, 12] mm;

2. Range 3a, for R3a = [12, 23] mm;

3. Range 3b, for R3b = [23, 30] mm.

The third radial range was split in order to account for the different rate of increase observed in the radial variation of $T30_{mode}$.

The fitting parameters *a* and *b*, from the linear relation

$$T30 = a \cdot R + b \tag{VI.11}$$

and their error, σ_a and σ_b, were determined from a least squares fit, using the MINUIT routines implemented in ROOT. The values of parameters for each range are given in Table VI.1. The error on the median and the mode were calculated as:

$$\Delta Tn_{(\mathrm{mod},med)} = \frac{w_{(\mathrm{mod}.med)}}{\sum_i w_i} Tn_{(\mathrm{mod},med)} \tag{VI.12}$$

Where w is the value of the bin containing the variable $Tn_{(mod)}$ or $Tn_{(mean)}$, and with the sum of the weights on the denominator. The error on the mean of the distribution is taken as the standard deviation of the distribution.

The different slopes give the sensitivity (in mm/ns) for the determination of the radius of interaction from the linear relations presented above. In range 2, the best sensitivity is observed for the mode: $a_{(range\ 2)}$ = (-1.19±0.07) mm/ns. The largest sensitivities observed for ranges 3a and 3b are both observed for the median, $a_{(range\ 3a)}$ = (2.12±0.05) mm/ns and $a_{(range\ 3b)}$ = (5.63±0.04) mm/ns, respectively.

T30 estimator	**Range 2**			**Range 3a**			**Range 3b**		
	a (mm/ns)	*b (mm)*	χ^2	*a (mm/ns)*	*b (mm)*	χ^2	*a (mm/ns)*	*b (mm)*	χ^2
Mean	-0.71 (0.03)	41.52 (3.64)	0.02	1.81 (0.09)	9.61 (1.67)	0.17	2.47 (0.23)	-6.69 (6.20)	0.43
Mode	-1.19 (0.07)	44.79 (0.69)	1.74	2.10 (0.07)	2.10 (1.3)	0.43	4.30 (0.04)	-48.01 (1.06)	0.75
median	-0.92 (0.07)	43.04 (0.69)	0.68	2.12 (0.05)	3.91 (1.03)	0.46	5.63 (0.04)	-87.84 (10.83)	0.8

Table VI.1: Fitting parameters for the fit of radial variation of the mean, median and mode of the T30 distributions. The values of sensitivities obtained from the variation of each estimator are highlighted for each of the radial ranges.

For a T30 measured at (65 ±0.5) ns, one would obtain a radius:

- R = (27.1±3.9) mm with the median (best sensitivity);
- R = (26.3±6.5) mm, with the mode (large sensitivity);
- R = (29±7.2) mm, with the mean (smallest sensitivity);

With relative errors of 19% for the median and 25% for both the mode and the mean.

2.3.3 Radial variation of T90

The radial variation of the three T90 distributions estimators is shown in Figure VI.19. The profile of the mean, mode and median T90 variation allows the division of the radius in 3 radial ranges:

- the first range corresponds to R1 = [0, 6.5] mm;
- the second radial range corresponds to R2 = [6.5, 17] mm;
- the third radial range corresponds to R3 =17 mm to maximum radius.

in the first radial range, both the mean and the median present similar characteristics. The T90 mean value increases with a small rate and a large dispersion of values between 150 ns and 160 ns. The median of the distributions shows a large dispersion around T90 ~150 ns. The sharper increase then observed for the mean and the median from R = 5 mm to 8 mm, is related to the change in source radial position from the region of fast collection time (front of the crystal) to a region of slow collection time (coaxial region). The mode presents a clear continuous increase, from ~ 105 ns to ~110 ns.

In the second range, the mean and the median values decrease down to the radial point where both charge carriers have an equal drift time, at R~17 mm. The variation of the mode presents two different varying tendencies:

1. a region of decrease (similar to the one observed for the mode and for the median), with a large dispersion of values, reaching a minimum for R ~17 mm;
2. a continuation of the increase of the values observed in the first radial range.

This double varying behaviour is induced by the two maxima present in the rise time distributions at small radii, discussed and presented in Figure VI.7 (a) and Figure VI.10 (a). The two tendencies showing the evolution of both maxima allows one to deduce the variation of rise time for interaction where the holes are collected on the front face, and also for interactions where the holes are collected on the sides of the crystal (refer to schematic illustration in Figure VI.6).

The larger spread observed in the decreasing region is due to the wide possible range of rise time along the tapered electrode. Another factor adding spread is the algorithm used to deduce the value of the mode for each distribution. The mode was searched in each histogram as the bin with the larger number of counts. Therefore, this estimator is very sensitive to statistical fluctuations. From the variation of the mode, three regions can be identified (indicated as a, b and c in Figure VI.19), depending on the source position and where the interaction is believed to occur:

- Interactions occurring near the front face of the crystal: where the holes are collected on the front face (a).

- Interactions at small radius, where the holes are collected on the taper and on the rounded electrode (b).

- Interactions occurring at large radius, in zone C (defined in Figure.VI.3): the further the source position is form the short axes, the longer the measured rise time. The main increasing tendency corresponds to source positions in zone B as defined earlier (c).

In the third radial range (R > 17 mm), following the increase of the three parameters, one observes an increase in the spread of T90. The potential reason is that the geometry of the crystal produces a large range of rise times, where the fastest values are measured along the short axes of the crystal, and the slowest values in the coaxial region. The orientation of the crystal lattice relative to the segmentation boundaries maximises these differences.

The variations of the three estimators have been fitted in the three following radial ranges: R = [5-8] mm, R = [8-17] mm and R > 17 mm. The results from the fits are presented in Table VI.2. The median gives the best sensitivity results for the three radial ranges. In the third range, given a measured T90 of (190 ± 0.5) ns, one would obtain a radius:

- R = (24.7±1.9) mm with the median (best sensitivity);

- R = (24.9±.3.6) mm, with the mean (smaller sensitivity).

The relative errors given for the determined radii are 8% for the median and 14% for the mean.

T90 estimator	Range R1			Range R2			Range R3		
	a (mm/ns)	*b (mm)*	χ^2	*a (mm/ns)*	*b (mm)*	χ^2	*a (mm/ns)*	*b (mm)*	χ^2
Mean	9.02 (5.57)	114.22 (36.50)	0.05	-2.90 (0.50)	204.4 (6.91)	0.23	4.70 (0.17)	73.14 (4.12)	0.36
Median	13.89 (4.21)	87.74 27.38	0.13	-3.66 (0.02)	215 (0.33)	0.83	6.289 (0.16)	34.5 (3.83)	0.72

Table VI.2: Fitting parameters for the fit of radial variation of the mean, median and mode of the T90 distributions.

2.4 Azimuthal variation of T30 and T90

The azimuthal variation of the partial rise times gives information on the directions of the maximum and minimum collection times in the coaxial region of crystal. The behaviour of the T30 and T90 estimators with azimuthal source positions was investigated. Figure VI.21 presents results for the mode, mean and median of T30 and T90 distribution. In each plot, the azimuthal 0° orientation corresponds to the long axis, parallel to the <010> crystallographic axis. The range of values at each angle is delimited by: a maximum time value obtained for source positions near the electrodes; and a minimum value obtained for the radius at which T30 or T90 is minimum, which provides the full radial range observed at a given radius. Both T30 and T90 estimator values vary periodically with azimuthal angle, being minimum along the <010> directions and maximum along the <011> directions. The structure observed in all pictures contains 2 deep wells centred on the $\theta = 180°$ and $\theta = 270°$.

Two following main contributions can be identified:

- Maximum available radius $D(\theta)$. The radius of maximum drift time gives the maximum value of the range of drift times observed at a particular orientation. Due to the geometry of the crystal, the maximum available drift distance varies with the

orientation and the depth z along the tapered electrode. In the coaxial region, its contribution can be modelled as the magnitude of the vector $\vec{r}$:

$$D(\theta)_{z>30} = \|\vec{r}(\theta)\| = \|\vec{r}_2(\theta) - \vec{r}(\theta)_1\| \quad \text{(VI.13)}$$

r_1 being the radius of the anode (5 mm), r_2 being the distance from the cathode to the central point of the crystal. In the coaxial region, the variation of *r* with azimuthal direction is represented in Figure VI.20. The flat edges on the cathode are responsible for the large "wells" observed at 180° and 270° orientations (also 0° and 90° to a lesser extent). Each zone defined in Figure.VI.3 is clearly identified and labelled in Figure VI.20.

- Anisotropic drift velocity. As the drift direction changes, the different crystallographic orientation will be encountered. As the directions <010> and <001> are equivalent, as well as <011> and <0-11>, one encounters a periodical variation of the drift collection time, which is reproduced on the measured pulse rime times. However, due to the increase in anisotropy with the electric field magnitude (the difference between the drift velocity along the <010> and <100>direction increases with field magnitude up to the saturation value; this is shown in Figure IV.14), one must keep in mind that this effect should also vary with radius of interaction. In the coaxial region, the anisotropy is more important at small radius, where the field is stronger, than at large radius, where the field is the weakest.

The variation of the mode for T30 and T90 distributions presents interesting features. The line of points centred on T30 = 20 ns corresponds to the source positions located in front of the core electrode. A distribution of points is observed for T90 between 112 ns and 115 ns. The cloud of points observed on the same plot, between T90 = 120 ns and 140 ns, and centred on 0° and 90° are the response of interactions occurring in the front of the crystal at mid radius, as presented in Figure VI.18, for the plot presenting the radial variation of the mode.

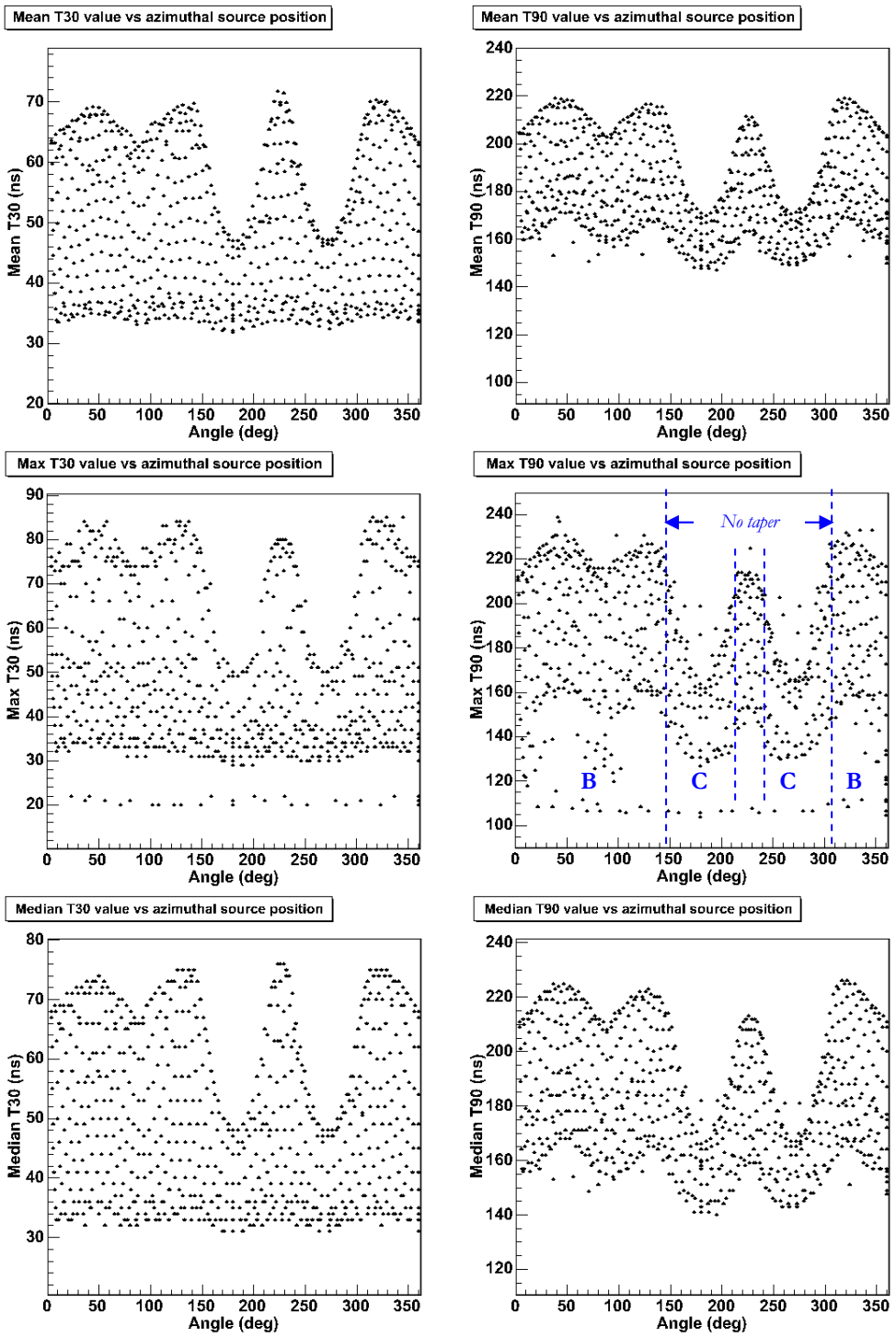

Figure VI.20: variation of T30 and T90 estimators represented for all azimuthal source positions. Since all radial positions are included, on observe for each angle a range of values between a minimum and a maximum respectively corresponding to small and maximum radii. The causes of the wave-like shape of the distributions are the geometry of the crystal and the drift velocity anisotropy of the charge carriers, where the maximum and minimum respectively correspond to the slow and fast crystal axes.

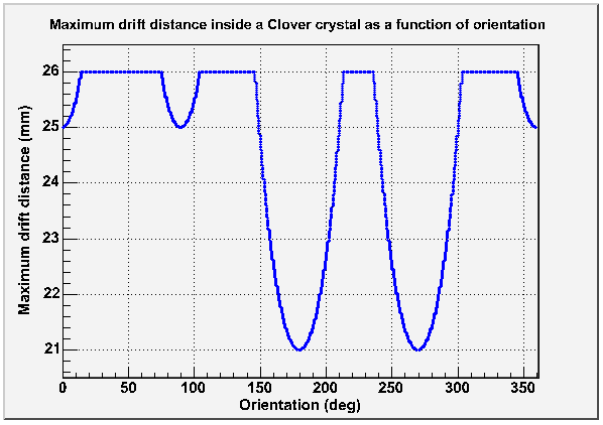

Figure VI.21: Variation of the maximum drift distance with orientation in an EXOGAM Clover crystal. The drift distance is minimum along the short axes at 180° and 270°.

Referring to the above observations, a precise measurement of the radius in the EXOGAM Clover crystal cannot be separated from the determination of the azimuthal angle. Therefore the use of the segments to locate primarily an interaction within the crystal is compulsory. The investigation of the variation of each T30 and T90 distributions parameters within each segment would indicate whether it is possible to improve the determination of the radius by linear fits to the radial variation of the partial rise time distributions. More complex fitting functions could be used instead of the simple linear approximation to model the radial variation of the partial rise time distributions parameters. This could also lead to some improvements in the determination of radius.

2.5 Test of the radial position determination with linear fit

In order to estimate the accuracy provided by the linear fits, T30 and T90 data from several known positions, located at different radii, were analysed in order to calculate the corresponding radius of interaction. Figure VI.22 shows the distribution of calculated radii given by T30 and T90 using the linear fits deduced for the respective ranges R3b and R3 for a collimator position of 25.7 mm located on front of segment A4 (P728 in Figure VI.1). The radii were calculated on an event by event basis. The error for each radius was calculated from the values given in Figure VI.1 and Figure VI.2 using the propagation of errors, with an uncertainty of 0.5 ns for each partial rise time value.

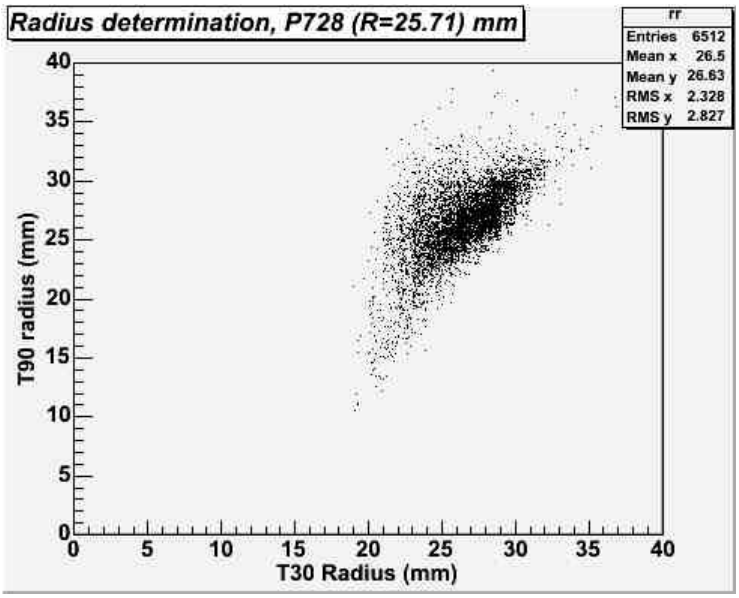

Figure VI.22: Calculated radii obtained from 6512 events in P728. The radii were estimated for each event using the linear fits in the larger radial ranges described in section 2.3. The mean radius values are indicated on the figure for T30 and T90 as *Mean x* (R=26.5 mm) and *Mean y* (R=26.63 mm).

For a total of 6512 events, the average radii given by T30 and T90 are respectively 26.5±3.9 mm and 26.63±1.8 mm, which shows good agreement with the known value of 25.7 mm, with relative errors of 14.7% for T30 and 6.8% for T90. The large dispersion of radii observed in Figure VI.22 is due to the following effects: the absence of depth segmentation, the transmission of source γ-rays through the collimator material, both of which are superimposed on the spread caused by the divergence of the collimated beam. Without the knowledge of the radius of interaction, the lack of depth information does not allow a clear distinction between rise times measured for interactions occurring at the front and in the coaxial part of the crystal, therefore leading to false calculated radial positions. In addition, due to the transmission of γ-rays at large angles by the source shielding, a large number of interactions can occur at radii other than the small range defined by the collimator dimensions. As a result, calculated rise time values which do not correspond to the real source position must be considered. Furthermore, at smaller radial source positions, it becomes less evident to determine the radius of interaction accurately. The rise time values depend strongly on the depth location of the γ-ray impact, owing to the increasing number of photons interacting in the strong electric field region and to the effects of the varying distance between the anode and the cathode. It becomes then impossible to obtain an accurate estimation of the radial position for radii smaller than 20 mm.

3 Radial position determination with T90 – T30 correlations

3.1 T90 – T30 correlations

The determination of the radial position of interaction is possible for the EXOGAM Clover detector. As seen in previous sections, the particular geometry of the crystal combined with the 4-fold segmentation is not ideal for the PSA method using T90-T30, as applied in [Des02]. However, such a method can provide a better position sensitivity relative to the existing segmentation pattern, by looking at the 2D distributions of T90 – T30 correlations.

3.1.1 Example distribution

T90 – T30 correlation matrices have the advantage of displaying both distributions at the same time. Instead of looking for a particular value from each independent T90 and T30 variation with radius, the correlation of both values allows one to look for the displacement of the centroid corresponding to the maximum of both distributions.

Two example correlation matrices, taken from a central position within a segment are presented in Figure VI.23. The correlation from a Fold 1 event distribution and Fold 2 events distribution are shown in Figure VI.23 (a) and . Figure VI.23 (b) respectively. The radial and azimuthal coordinates are indicated in both figures; one must refer to Figure VI.1 in order to identify the position in the scanning grid. Both plots show a centroid located at (T30, T90) = (42 ns, 158 ns), proving that Fold 2 and Fold 1 events present similar rise time contributions: given the forward scatter, the radius is constrained. Although both distributions show a triangular 2D profile, the Fold 2 matrix in Figure VI.23 (b) does not show a strong correlation, as seen for the Fold 1 events distribution (Figure VI.23 (a)).

3.1.2 Random events distributions

A 2D distribution measured for a position out of the detector crystal (P288 in Figure VI.1) is presented in Figure VI.24 in order to illustrate a typical random background contribution. The triangular profile appearing in the matrix is similar to the pattern observed in Figure VI.23; therefore the low number of correlations may be attributed to random background events.

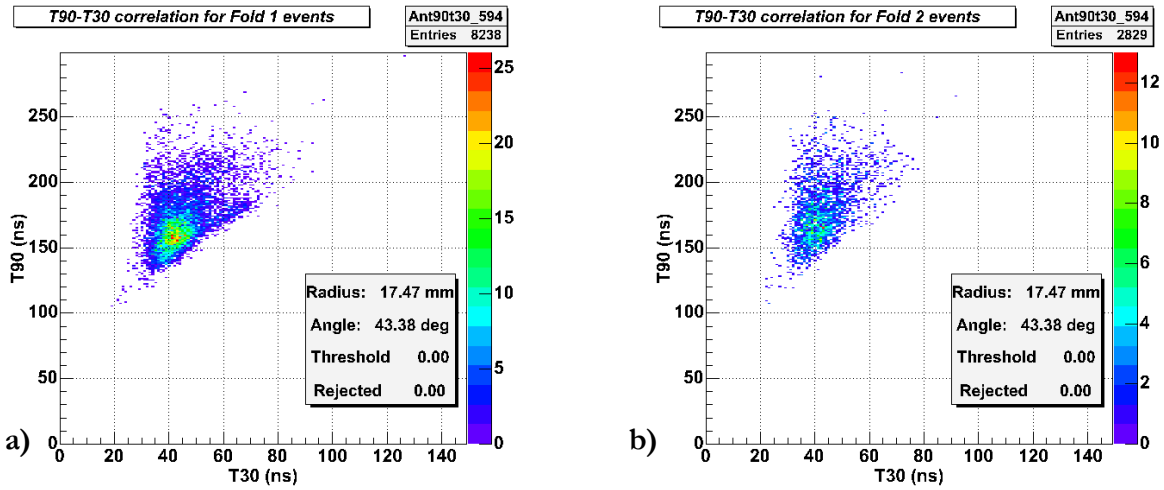

Figure VI.23: T90 – T30 correlation from a central position P594 for (a) Fold 1 and (b) Fold 2 full energy events. The centroid represents the most frequent correlations obtained at a particular source position. For both distributions, the centroid is located at (T30, T90) ~ (45 ns, 160 ns). The radius and the azimuthal position of the source are indicated.

In order to remove the background contribution, a minimum threshold was applied to the matrix. This method has the advantage of selecting the information arising from the source distribution by suppressing unwanted data with a low impact on good T90 – T30 coincidences. The effect of a minimum counts threshold of 2 and 3 are presented in Figure VI.25 (a) and Figure VI.25 (b) respectively. As shown on Figure VI.25 (b), a threshold of 3 counts removes 98% of the random correlations.

The same threshold value was applied to the correlation histograms from P594 initially shown in Figure VI.23. The effect of the threshold is presented in Figure VI.26. The Fold 1 correlation matrix presents a clearer definition of the centroid, with a proportion of rejected data points of 23 %. For an identical threshold, 52% of the data are suppressed from the Fold 2 events distribution. Finally, the position of both centroids appears to be clearly identical. It is then possible to use the T90 – T30 correlation with a minimum threshold of 3 counts in order to investigate the variation of the centroid with radial position of interaction in a particular segment. The evolution of the number of rejected data versus threshold is presented in Figure VI.27. A threshold of 3 is a good compromise when the numbers of rejected Fold 1 events of 22%, which consists mainly of scatter photons within a single segment, is compared to the rejection of more than 50 % of events for the Fold 2 events distribution.

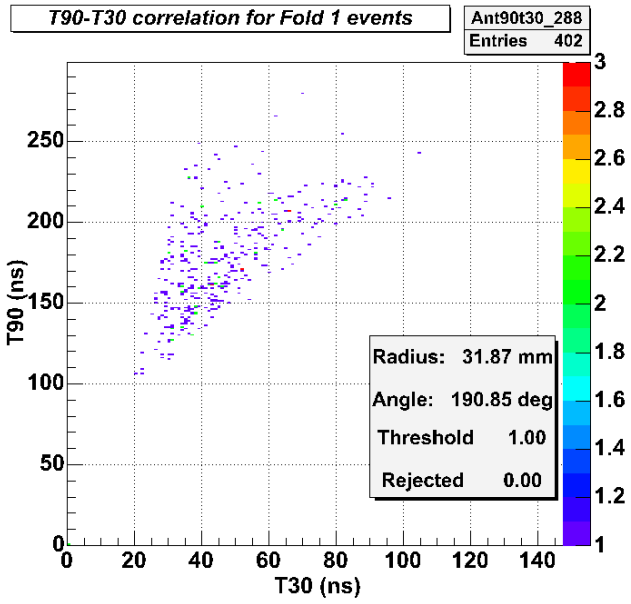

Figure VI.24: T90 – T30 correlation for random background events. The number of random counts is reduced by the application of a minimum threshold of 3 counts at the position (P288, in Figure VI.1). The cylindrical coordinates relative to the centre of the crystal (radius and angle) are indicated. The threshold value gives the minimum number of counts to consider the correlation. The rejected value indicates the fraction of events suppressed by the threshold procedure for the actual position.

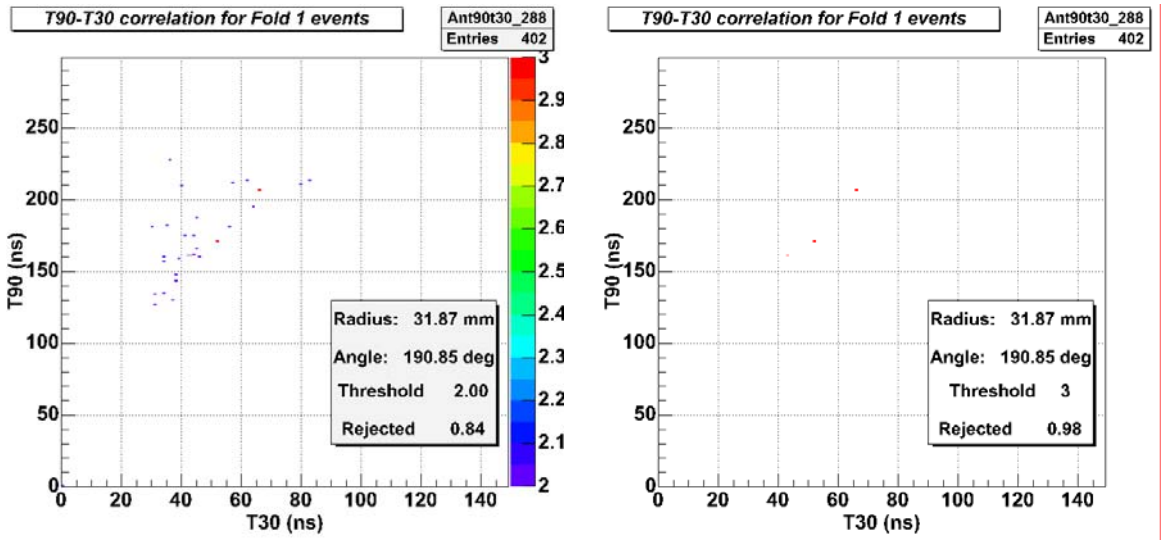

Figure VI.25: Effect of threshold on random background correlation. (a) The application of a limit of 2 rejects 84% of the background, while a threshold of 3 (b) removes 98% of the counts.

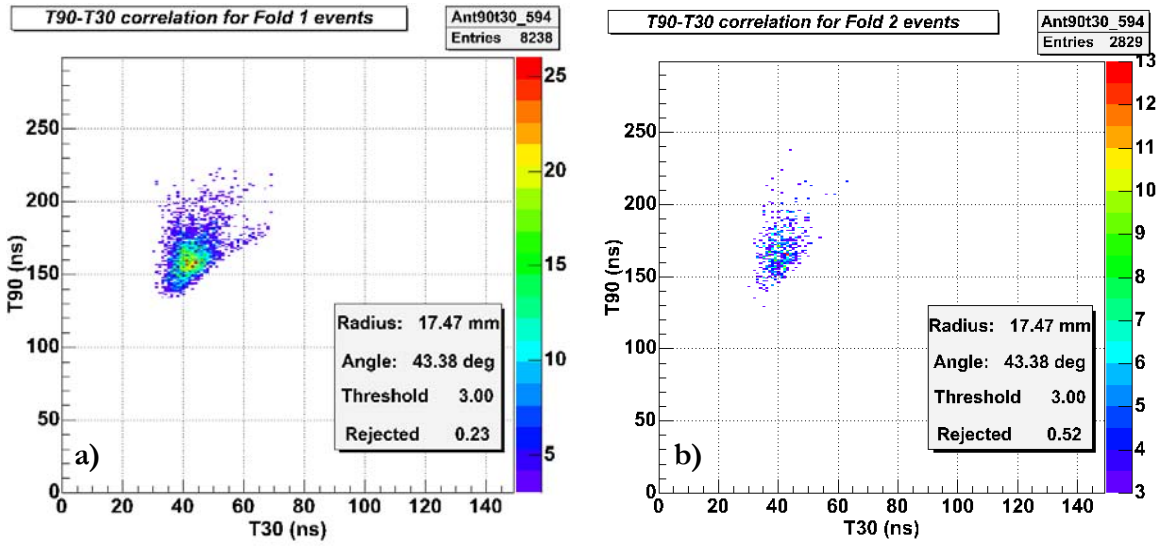

Figure VI.26: T90 – T30 correlation matrices for Fold1 and Fold 2 events, taken for a source position P594, with an applied minimum counts threshold of 3. Both centroids are located at the same position (T30, T90) = (42 ns, 158 ns).

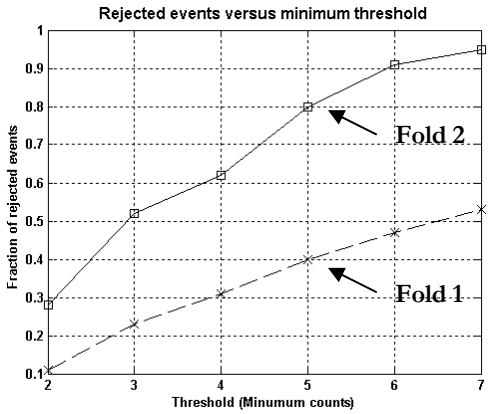

Figure VI.27: Evolution of the fraction of rejected events for Fold 1 (dashed line) and Fold 2 (plain line) correlation matrices with minimum counts threshold value.

3.2 Evolution of the T90 – T30 correlation distribution as a function of position

Using the threshold argument with the T90 – T30 correlation matrix, it is possible to define several radial ranges within a particular segment of the EXOGAM Clover crystal. As demonstrated in the previous sections, the different sizes and shapes of the segments do not allow an optimised use of the T90 – T30 method. However, it is still possible to improve the determination of the position of interaction within a crystal segment Figure VI.28 and Figure VI.29 present a set of T90 – T30 correlations taken from 12 positions along a radial line in front of segment A1. The orientation was chosen in order to align the radial line with the

<011> direction. Segment A1 has the advantage of providing the same available radius over a large azimuthal range of the segmentation, therefore minimising the effect of the function D(θ) defined in the previous section. However, one must keep in mind that the influence of the taper on the charge pulse rise time will inevitably broadens the correlation response in the small radial range.

A second set of distributions is presented in Figure VI.30 and Figure VI.31 for comparison purposes. The distributions have been taken from a radial line at an orientation close to the <010> direction, in front of segment A4, where the maximum radius available in this range is 25 mm and no taper can affect the detector response.

3.2.1 Evolution of the T90 – T30 distribution for segment A1

With reference to Figure VI.28, the evolution of the centroid is remarkable as the radius increases. One observes a general evolution of the centroid from a well defined point at small T30 and T90 values, with low statistics (due to the central position of the source, facing the anode); to a location at large T30 and T90 value. The path observed by the centroid of the distribution with increasing radius is not linear, as expected from the complex variation of T90 with radius (see Figure VI.19). Also, the shape of the distribution changes as the position of the source changes.

At small radius, when the moves away from the front of the core electrode and faces the coaxial region of the crystal, (P462, P499 and P531 in Figure VI.28), an elongated distribution which extends from fast to slow T90, is observed. Such broad T90 distribution is caused by the contributions from interactions occurring at the front of the detector, and in the deeper coaxial region at small radius. This was discussed in details in the previous sections, where a typical example T90 distribution encountered at small radius was presented in Figure VI.7 (a).

From position P594, located at mid radius, the distribution of data becomes centred, and the centroid more defined, as the source moves towards the edge of the crystal. The displacement of the centroid evolves towards the maximum values for T30 and T90, observed at large radius for position P707.

The centroid values for the different radial positions in segment A1 are given in Table VI.3. For most of the source positions, an approximate range of T30 and T90 values is given, in order to account for the broad distribution observed. The radial ranges are defined as follows:

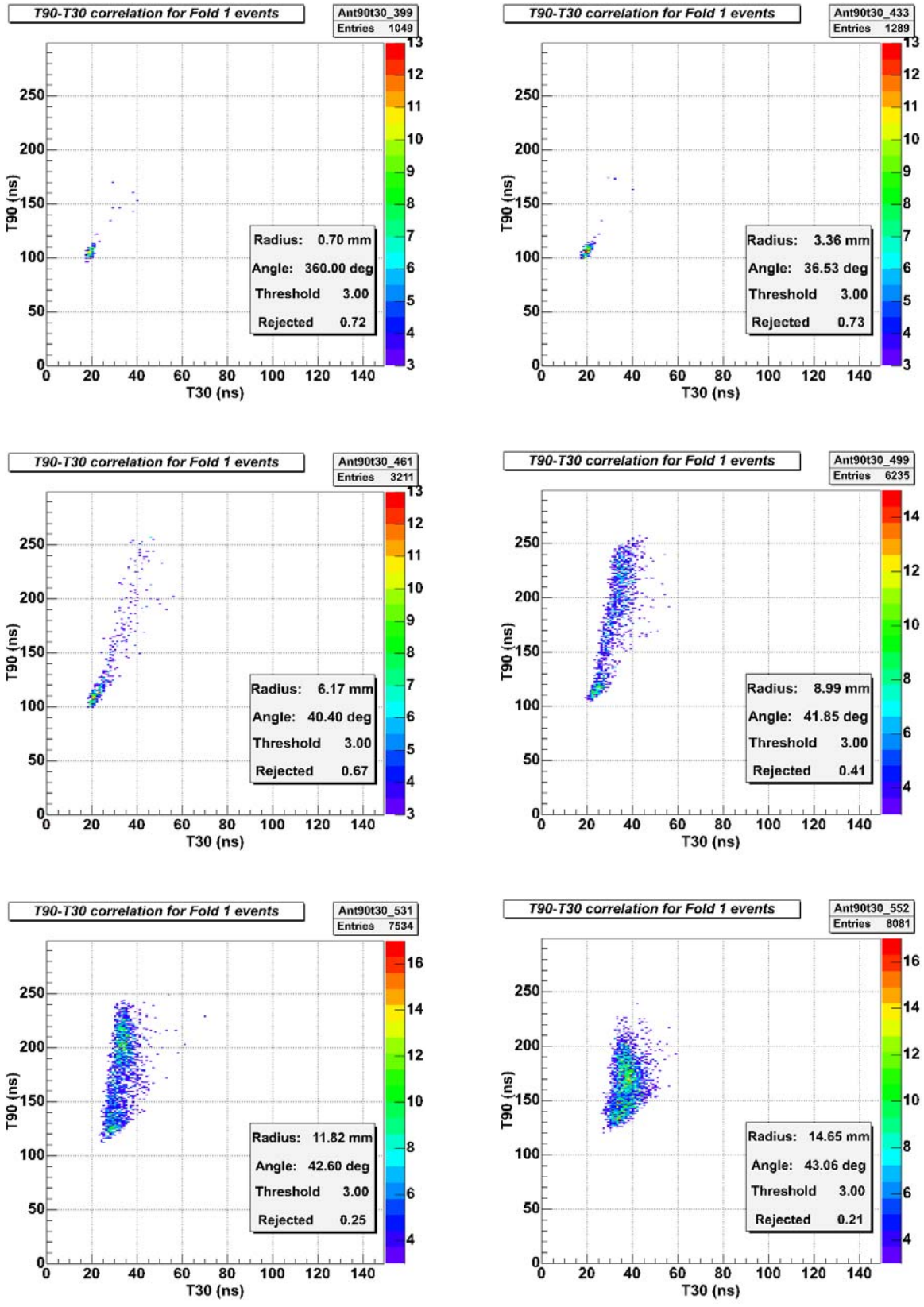

Figure VI.28: Variation of the T90 – T30 correlation along the <011> direction in segment A1. The source positions evolved from P399 located at the centre of the crystal at R = 0.7 mm towards a mid radial position P552 at R = 14.65 mm.

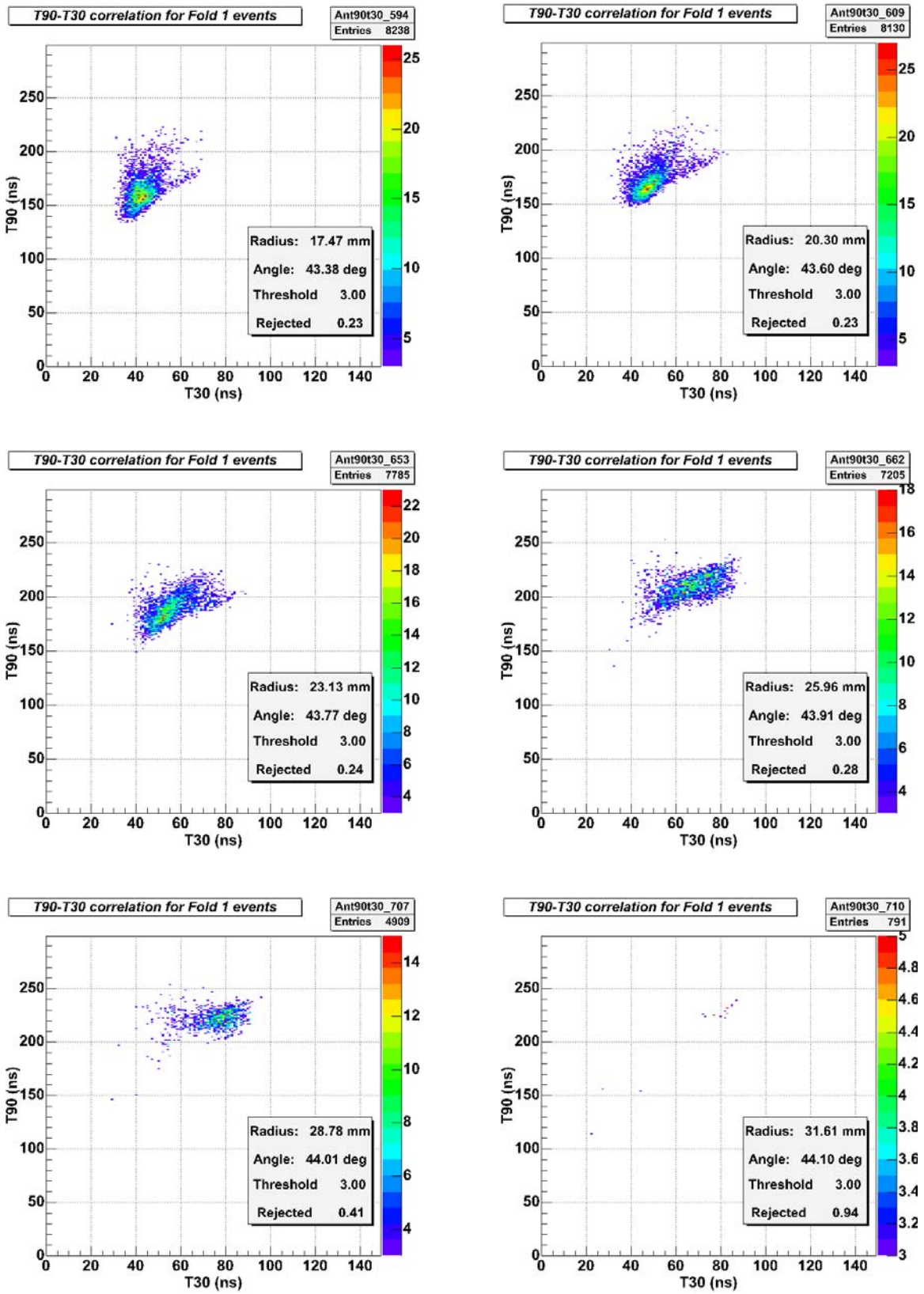

Figure VI.29: Variation of the T90 – T30 correlation close to the <011> direction in segment A1. The source positions evolved from P594 located at mid radius R = 17.47 mm, towards the maximum position P710 at R = 31.61mm, where the source is out of the detector volume.

- R1 = [0, ~6] mm: a set of very close T30 and T90 values are observed, due to the configuration of the electric field in front of the core electrode. A change in the centroid location is nearly distinguishable.

- R2 = [~6, ~17] mm, may define a second radial range, which would include the stretched T90 distributions observed at small radius.

- R3 = [~17, 25] mm, the third radial range includes the region of the matrix where both T30 and T90 values increase with radius.

- R4 = [25, 30] mm defines the fourth radial range, from R = 25 mm to the edge of the crystal.

In order to obtain an estimate of the radial position, such a radial separation requires the application of elliptical or polygonal gates defining the different radial regions in the T90 – T30 matrix. Logically the next step would be to test the accuracy of the defined radial separation with a set of data from a known source position, and measure the proportion of events falling in the right radial range. It would also be interesting to compare the number of rejected data points by the minimum counts threshold with the proportion of data that does not fall into the radial range.

3.2.2 Evolution of the T90 – T30 distribution for segment A4

The evolution of T90 – T30 distributions from the radial line oriented along the <010> direction (segment A4) is shown for 12 source positions in Figure VI.30 and Figure VI.31. The results show a response similar to the variation observed for the line in front of segment A1. For positions facing the anode (P400, P401 and P402), one observes a well defines centroid; however, the location of the centroid is constrained to a smaller range of values, as indicated in Table VI.3.

At small radii, the emergence of a second centroid at larger T90 values (P403, P404 and P405 in Figure VI.30) shows a clear difference between the contributions from interactions occurring in the two separate frontal and coaxial regions of the crystal defined in the previous sections. The position of the fast centroid (located at fast T30 and fast T90) does not vary significantly with radius, until the transition between P404 and P405 (from R = 9.3 mm to R = 11. 3 mm). In contrast, the large centroid, attributed to the detector response from

interactions in the coaxial region, moves down from T90 ~ 190 ns to an approximate T90 value centred on 150 ns. Both centroids merge completely at R = 13.3 mm (P406). Following the radial increase, the unique centroid then follows a path from (T30, T90) = (30 ns, 120 ns) to the largest T30 and T90 values of (T30, T90) = (50 ns, 160 ns).

The smaller range of drift time available along this radial line hinders the definition of clear radial ranges, apart from the separation of the radius in an inner range from R = 0 mm to R ~20 mm and an outer range from R ~ 20 mm to R = 25 mm. The geometry of the crystal is, in this case, responsible for preventing a more accurate determination of the position of interaction. The attempt to separate the Clover crystal in different radial ranges from the investigation of the T90 – T30 correlation matrices led to the following conclusions:

- The possibility to determine the radial coordinate of a γ-ray impact depends on its relative location in the crystal volume. Interactions occurring within the larger segment A1, where the maximum radial distance available does not vary with orientation[43], lead to a determination of the position within 4 radial ranges as illustrated by Figure VI.32. In regions where the maximum drift distance is shorter (along the short axes), the range of T30 and T90 values is restricted. The determination of the interaction position can be performed from the separation of the radius into 2 ranges.

- At small radius, front and back regions of the crystal could be separated owing to their different contributions. Both centroids (positions P404, P404 and P405 in Figure VI.29) have significantly different paths with increasing radius, up to the position where they merge. Therefore, a T90 – T30 correlation giving a fast T90 and a fast T30 would result from an interaction occurring at the front of the crystal, contrarily to an interaction occurring in the back coaxial region with a T90 – T30 correlation showing a fast T30 with a slow T90. However the depth delimitation between both regions is arbitrary. It is proposed to use the starting point of the taper as a limit (Z = 30 mm): the response from interactions occurring below this limit (fast T90 observed for fast T30) is assigned to the frontal region.

[43] When the influence of the taper is not considered.

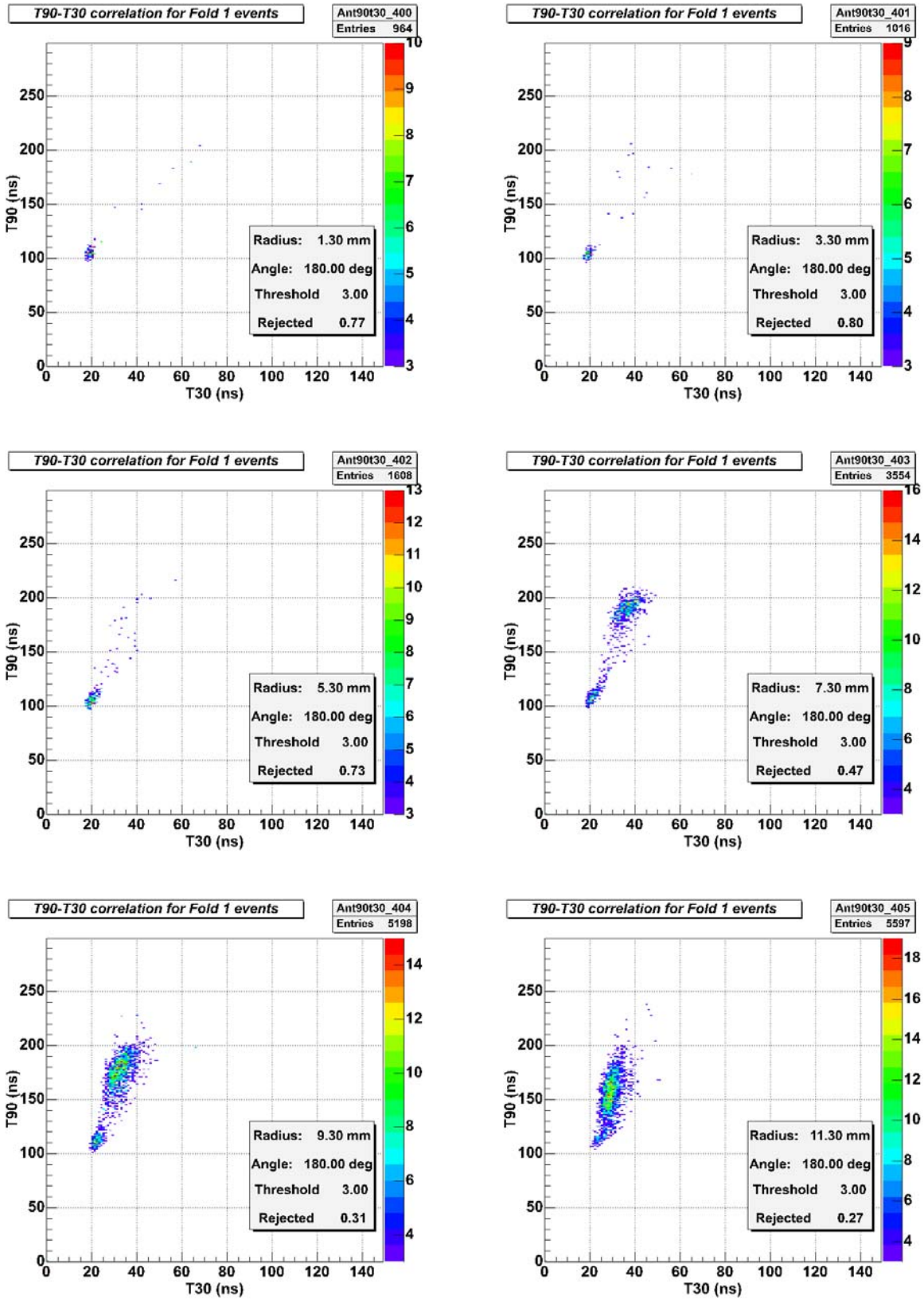

Figure VI.30: Variation of the T90 – T30 correlation close to the <010> direction in segment A4. The source positions evolved from P400 located at the centre of the crystal at R = 1.3 mm towards a mid radial position P405 at R = 11.65 mm.

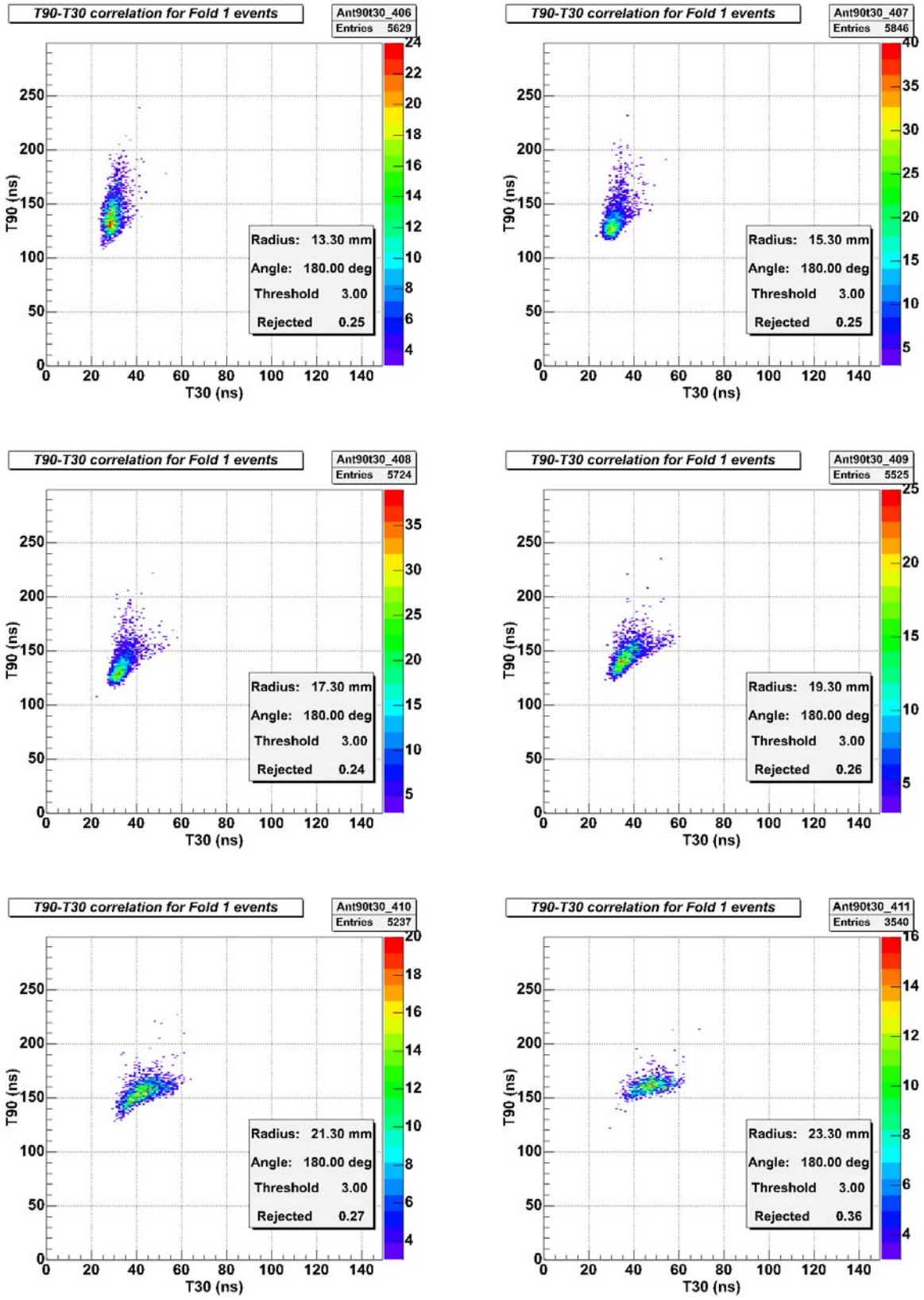

Figure VI.31: Variation of the T90 – T30 correlation along the <010> direction in segment A4. The source positions evolved from P406, located at mid radius R = 13.3 mm towards a large radial position P411 at R = 23.30 mm.

Segment A1			Segment A4		
Radius (mm)	**T30 (ns)**	**T90 (ns)**	**Radius (mm)**	**T30 (ns)**	**T90 (ns)**
0.70	20	105	1.30	15-20	100-110
3.36	20	105	3.30	15-20	10-110
6.17	20-25	100-120	5.30	15-25	110-115
8.99	20-30	110-250	7.30	20-45	100-210
11.82	25-40	110-240	9.30	20-40	100-200
14.65	30-45	120-210	11.30	20-40	110-200
17.47	30-50	130-190	13.30	20-40	100-200
20.30	35-60	150-200	15.30	25-35	110-170
23.13	40-65	160-220	17.30	25-40	115-160
25.69	50-85	145-230	19.30	25-45	115-160
28.78	60-85	210-240	21.30	30-55	120-170
31.61	Position out of crystal		23.30	35-60	150-170

Table VI.3: Position of the centroids for T90 – T30 correlations matrices.

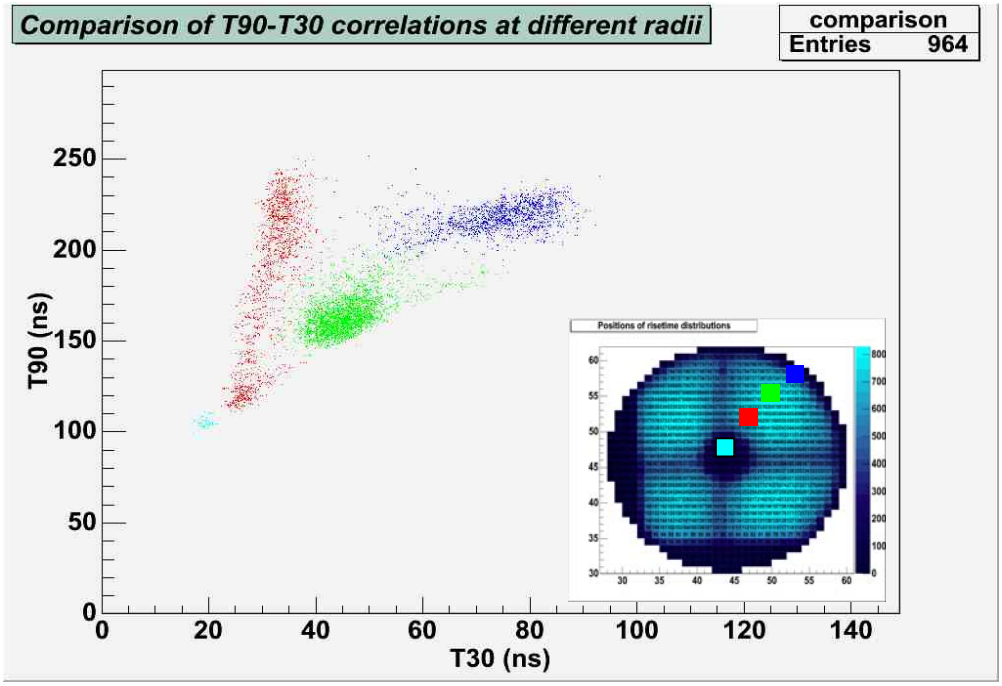

Figure VI.32: Illustration of the different radial ranges available in the largest segment of the EXOGAM Clover crystal. The T90 – T30 correlation regions corresponding to each radial range are represented on the figure. The different colours represent the distribution of points obtained for each of the position indicated on the intensity map. Due to the threshold of 3 minimum counts applied, the different distributions do not overlap, making possible the separation of the radius into four distinct ranges.

4 Electric field simulations

4.1 Radial variation of T30 and T90 from anode signals

The MGS simulation package presented in Chapter IV was used to generate current pulses from a set of interaction positions within the Clover crystal. The comparison between simulated and experimental results is presented in the following section. The interaction of mono energetic 662 keV photons was simulated for several positions in segment A1. The data presented in this section were selected according to the following conditions:

- The interactions occurred in the coaxial region at two different depths, Z = 50 mm and Z = 52 mm, along the <010> orientation;

- The interactions occurred at the front of the crystal, at Z = 2 mm, along the <010> orientation.

The current pulses were processed by the model of charge preamplifier described in Chapter IV (section 3.4) and the rise time values were calculated with the same algorithm used to extract the experimental values of partial rise times.

The radial variation of both simulated T30 and T90 variables are compared to the experimental radial variation of the mode of T30 and T90 distributions. The mode was chosen since it represents the most probable value of partial rise time in the distribution, as compared to the mean or the median, which the determination inevitably contributes from interactions occurring in a range of several radii.

4.1.1 T30 variation

Figure VI.33 presents the comparison between the simulated radial variation of T30 in the coaxial region (a) and the radial experimental variation of the mode from T30 distributions (b). The results show a general good agreement between the simulated and experimental values of T30. The main tendencies, small decrease at small radius and increase from mid to maximum radius are observed in both cases. Two distinct radial ranges can be defined from the simulated T30 values:

1. From R = 4 mm to R = 7 mm, the simulated T30 decrease from T30 = 36 ns to a minimum value of 18 ns.

2. At larger radii, an increase from the minimum value of 18 ns up to a maximum of 76 ns is observed.

3. no data are present below 5 mm, due to the presence of the core of the crystal.

Despites the qualitative agreements between experimental and simulated results, several differences are noticed:

1. The position of the minimum simulated T30 at R = 7 mm, occurs at a smaller radius compared to the value R ~ 12 mm obtained from the experimental data;

2. The value of the minimum T30 measured from the simulated pulse shapes is smaller (T3 = 18 ns) than minimum T30 deduced from the experimental measurements (T30 = 30 ns).

As seen in Figure VI.33, the increase from the minimum 18 ns at R = 6 mm to 76 ns at R ~ 26 mm is not linear, but shows a spread in the data. The spread may result from the estimation of the radial position on a grid, or could be introduced by the contribution of the preamplifier noise. In the last case, the simulated T30 radial dependence may indicate that in reality, the calculation of T30 is not independent from the noise contribution, which may induce some spread in the experimental T30 data.

4.1.2 T90 variation

The comparison between simulated T90 values and the experimental variation of the mode of the T90 distributions is presented in Figure VI.34. The "+" refers to data points simulated in the coaxial region at Z = 50 mm and Z = 52 mm. The "o" corresponds to simulated data obtained for Z = 2 mm at the front of the crystal.

Again, a good qualitative agreement is observed between experimental and simulated data. The simulated results show a variation within two radial ranges in the coaxial region:

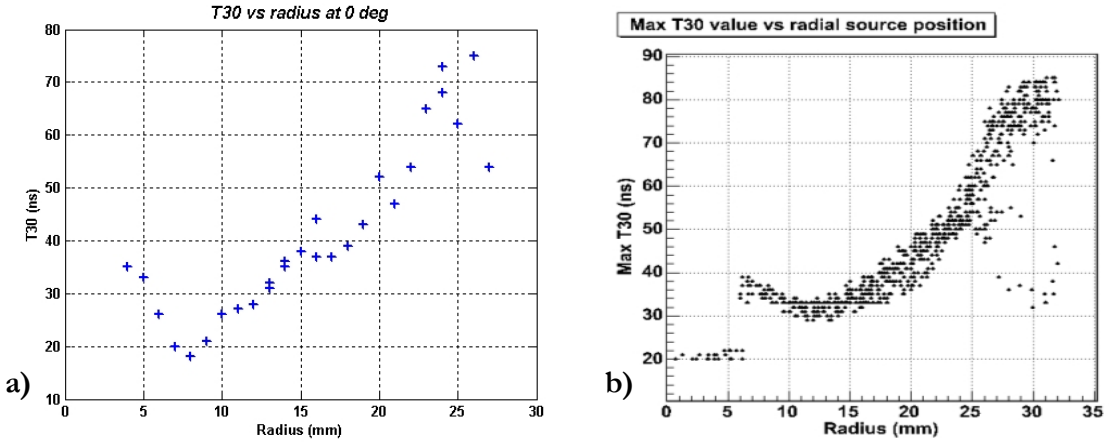

Figure VI.33: (a) simulated variation of T30 with radial position of interaction for depth Z = 50 mm and Z = 52 mm at 0° orientation; along the <100> direction; (b) experimental variation of the mode of the T30 distribution.

1. a linear decrease from T90 = 284 ns observed at small radius to a minimum value observed for T90 = 115 ns at a radius R = 17 mm;

2. an increase from the minimum value up to a saturation at 170 ns, observed for R = 23 mm to maximum radius.

The T90 simulated for interactions occurring at the front of the crystal increases, from small radius (70 ns) up to the value given by the minimum observed in the coaxial region at 130 ns, which correspond to the edge of the taper for the data generated at Z = 2 mm.

Both experimental and simulated values are qualitatively consistent in the range of decreasing values between R = 6 mm and R = 16 mm The simulated T90 rise time varies from 250 ns at 6 mm radius down to ~120 ns at R = 16 mm, corresponding to an approximate gradient of - 2.7.mm/ns. For comparison, in section 2.3.3, the sensitivity calculated from the variation of the mean experimental T90 gave a gradient a = (2.90±0.5) mm/ns.

The radial position for the minimum T90, located at R = 16.5 mm is also consistent with the range of values seen experimentally (16-18 mm). This shows a good quantitative agreement between the experimental and simulated values. The ratio between the drift velocities of electrons and holes can be calculated from the radius to minimum drift time. The simulated values present a minimum of 110 ns at ~16.5 mm, which corresponds to a drift velocities ratio

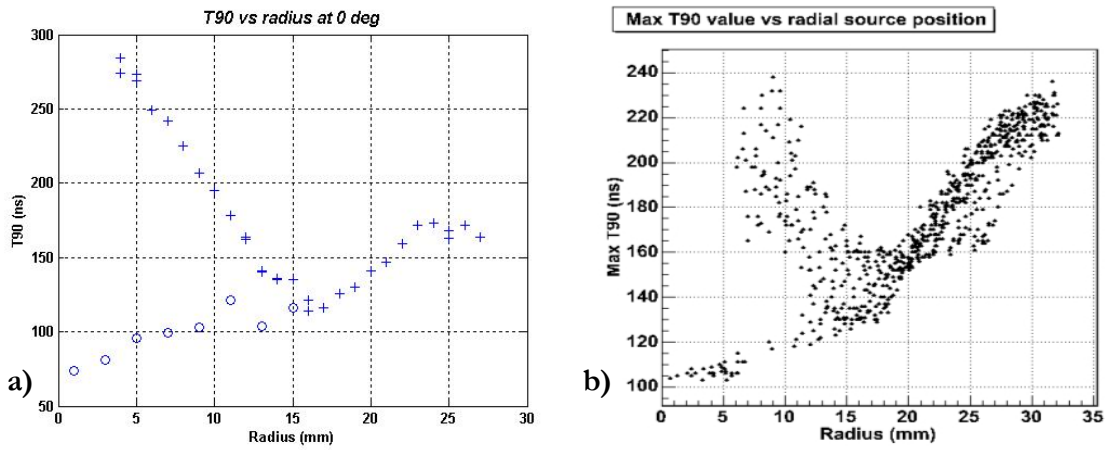

Figure VI.34: (a) Simulated variation of T90 with radial position of interaction at depths Z = 50 mm and Z = 52 mm at 0° orientation, along the <010> direction; (b) experimental variation of the mode of the T90 distributions.

of v_e/v_h of ~0.85%. For the experimental data, the minimum T90 value of 140 ns is observed for R ~ 16.5 mm, which corresponds to an identical ratio. Both results are close to the effective masses ratio value of m^*_e/m^*_h = 0.857 at 77 KeV given in [Kno00]. However, a number of differences are observed between the simulated and experimental T90 values:

- in the second radial range, R = [16, 30] mm, the saturation observed at large radius does not correspond to the values observed experimentally at such orientation (see variation of the mode in Figure VI.18). From the electric field calculations presented in Chapter IV, one can extrapolate the information given in Figure IV.13 for Z = 40 mm and Z = 60 mm to a depth of 50 mm. The electric field increases inside a large circular region in the vicinity of the cathode. This is an effect of the size of the grid used to generate the geometry of the crystal. The squares of the grid are approximated as a succession of flat surfaces, leading to a wrong approximation for the configuration of the electric field near the cathode instead of the known radial configuration. The solution would be to reduce the grid size.

- The increasing tendency observed for simulated data at the front of the crystal is actually lower than for the measured data. This could also be an effect of the size of the grid used to simulate the detector.

5 Comparison of the different crystals

Despites the identical crystal geometry imposed by the design of the EXOGAM Clover, the responses of the four crystals can be different. The impurity concentration values inherent to each crystal, as well as the various positions and diameters of the inner holes (Appendix A), and to a lesser extent the operating temperature are examples of parameters which affect the drift of charges in HPGe crystals. The existence of different depletion voltages for each crystal is directly related to the difference in active germanium volume and to the different impurity concentrations of the crystals; both of which have an influence on the charge carriers drift times. In order to obtain a relative comparison of the crystals responses, the mean value of the partial rise times T30 and T90 distributions were compared for similar source positions taken from the ^{137}Cs front scan.

Due to the 2 mm step size used to move the collimator, it was easier to find similar positions at larger radii rather than smaller radii. The results are reported for two sets of positions located in front of the large segment and placed along the (011) direction (45° from the long axis). The first set was chosen so that the four different positions were located within a circle of 2 mm diameter centred on the radius R = 20 mm, while the second set was centred on the radius R = 25.5 mm, as illustrated in Figure VI.35. Results for the four crystals are shown in Figure VI.36 and Figure VI.37.

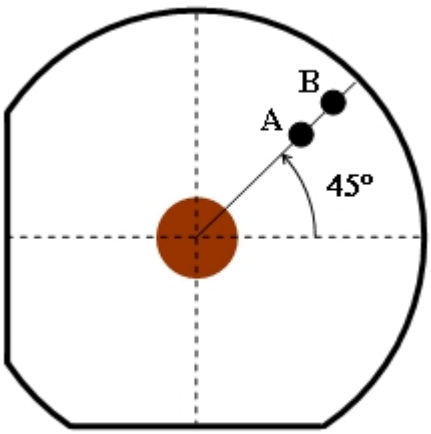

Figure VI.35: positions used to compare the responses of the different crystals.

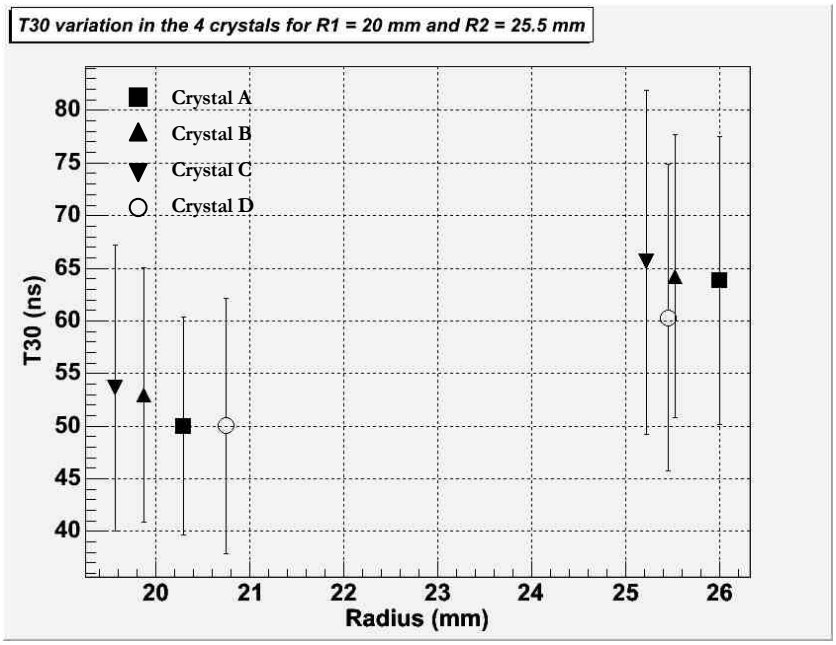

Figure VI.36: Mean T30 values measured in front of the 4 crystals of the EXOGAM Clover at R1~20 mm and R2~25.5 mm. The vertical bars represent the dispersion of the T30 values for each distribution, taken as the standard deviation of the distribution.

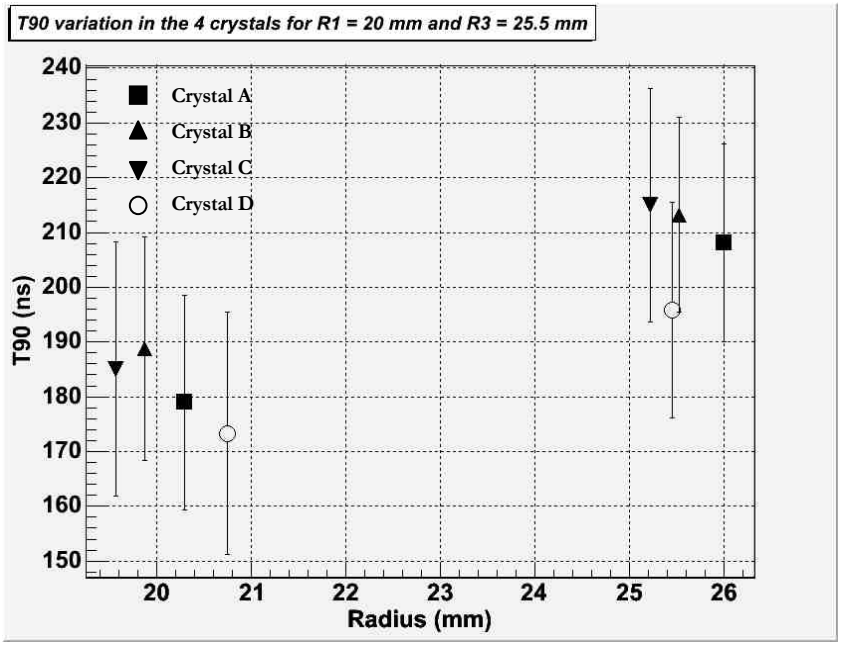

Figure VI.37: Mean T90 values measured in front of the 4 crystals of the EXOGAM Clover at R1~20 mm and R2~25.5 mm. The vertical bars represent the dispersion of the T30 values for each distribution, taken as the standard deviation of the distribution.

The first set of positions, where the average radius at R1 = 20.08 mm, present T30 values ranging respectively from 50 ns to 54 ns and T90 values from 173 ns and 189 ns. For the second set of positions, the average radius is R2 = 25.81 mm; the T30 values ranges from 60 ns to 66 ns and T90 from 195 ns to 214 ns. The average T30 and T90 values are given in Table VI.4 for both radii. For all crystal, the mean T30 and T90 are consistent with each other, both sets of rise times are longer at larger radius, which follows the increasing trend observed in crystal A (Section 2.3 of this chapter) at large radial source positions. However, due to the large step size used to displace the collimator, and due to the absence of segmentation depth, it is difficult to make a quantitative comparison of the crystals responses. A measurement dedicated to the comparison of each of the Clover crystal would consist in a collimated coincidence set-up as described in [Vet00]. Such a set-up would have many advantages over choosing similar positions from a front face scan, the most relevant being the constraint of the interaction locations into a small volume of a crystal (of the order of 10 mm^3). Detector responses from precise radial and azimuthal interaction locations could then be obtained, with the possibility to compare the crystal responses for different depth of interaction.

Average radius (mm)	**Average T30 (ns)**	**Average T90 (ns)**
R1 = 20.08 mm	51.8 ± 12.0	181.5 ± 21.37
R2 = 25.81 mm	63.5 ± 14.6	208.0 ± 19.3

Table VI.4: Average T30 and T90 values calculated from the data measured on the four different crystals of the EXOGAM Clover, at the two radial positions R1 and R2.

Chapter VII

CONCLUSIONS

1 Conclusions

The EXOGAM array, commissioned at GANIL, is a high efficiency γ-ray spectrometer dedicated to the study of exotic nuclei. The array consists of up to 16 escape suppressed Clover detectors. The EXOGAM Clover comprises four HPGe crystals, and each crystal is four-fold segmented in order to increase the granularity of the detector. The improvement of the resolving power of the array can be achieved by the reduction of the energy resolution. Locating the interaction of a γ-ray within a segment will enhance the Doppler correction performances, and improve the energy resolution of the Clover detectors. This sub-segment position measurement can be attained with digital pulse shape analysis (PSA) techniques and dedicated pulse processing electronics. However, the complex geometry of the Clover crystals and the absence of depth segmentation restrict the possibility to obtain good results and lead to non uniform detector responses depending on the position of interaction in a crystal. It was therefore necessary to evaluate the design of the EXOGAM Clover for pulse shape analysis. This work presents the investigation of the properties of the EXOGAM Clover detector for position determination. The characterisation of a detector manufactured by ORTEC was performed in order to understand the response of the crystals for different γ-ray interactions positions, focusing on the effects of the crystal geometry, and the implication of the large segments sizes on the position determination. An estimate of the performances for sub-segment position determination was deduced for the radial position of interaction.

The approach chosen for the characterisation consisted of experimental scan measurements, completed by the use of MGS, a new software package dedicated to simulate the operations of HPGe detectors. The experimental measurements provided different set of pulses taken at various positions, from which the response of the detector was investigated. A new digital acquisition electronics module was used in order to obtain high quality signals for pulse shape analysis. In addition, a scan made along the depth of the crystal presented the effect of poor charge collection and charge loss at the back of the crystal. The PSA method measured the values of the T30 and T90 partial rise times from the detector charge pulses. The shape of the partial rise time distributions were studied for each singles scan position, which allowed the identification of weak electric field regions, with poor electrons and holes drift properties, arising from the complex geometry of the crystals. The resulting non uniformity of the detector response leads to the division of the crystal into 5 frontal regions, where the drift characteristics of the charge carrier are similar. The particular shapes of the partial rise time

distributions observed both for photoelectric and scattered events revealed the importance of Compton scattering in detectors with large segments and exposed the contributions from interaction occurring at different interaction depths.

The second part of the analysis consisted in the application of PSA methods to improve the position determination in the Clover detector, and indicate whether the Clover detectors would perform well with PSA algorithms. The investigation of the radial variation of the partial rise time distributions gave an insight into the possibility to improve the granularity of the detector through radial position determination. The direct study of the radial variation of T30 and T90 inside a crystal lead to the comprehension of the effect of the crystal design on the performances: the best results are obtained for interaction occurring at large radius. The method, which was tested against experimental measurements, provided a minimum relative error of 14.7% in the determination of the radial position from T30 and 6.8% from T90 at R = 25.7 mm. However, the method fails to provide an accurate estimation of the interaction radius for smaller interaction radii, and the ambiguity discovered in the radial variation of both partial rise times cannot be resolved. A second method involved the investigation of the radial variation of the correlation between T30 and T90. The radial evolution of such correlation led to the division of the largest segment into four radial ranges at R1 = 6 mm, R2 = 17 mm and R3 = 25 mm. In the worst case, the crystal radius was divided into two unequal ranges along the short axes at R = 20 mm. Both methods are well suited for coaxial configurations, but do not perform well for the complex geometry encountered at the front of the crystal. The addition of a depth segmentation line below the beginning of the taper (Z = 30 mm) could improve the performances for sub-segment position location: the responses from the front and the back of the crystal would be separated, allowing a specific analysis of the complex front detector response. Additionally, a large number of Compton events would be isolated; the immediate effect would be the reduction of the data dispersion in the partial rise time distribution, and bring significant improvement to the separation of the crystal radius with T90 – T30 correlations.

Finally, the simulation of the electric field, and drift velocities of the charge carriers in the crystal volume allowed the direct confirmation of speculations regarding the poor drift properties of the crystals, and provided a means of predicting qualitatively the drift properties of the charge carriers in the crystal. The comparison between experimental and simulated rise time values at the front of the crystal and at half-depth in the coaxial region, demonstrated

good qualitative agreement. An improvement of the simulation results could be possible by using a smaller grid size for the calculation of the electric potential. The development of a model to estimate the holes drift velocity, similar to the parameterised model described in [Mih00], would be necessary in the perspective of using the pulses generated by MGS to predict precisely the response of HPGe crystals of known dimensions, impurity concentrations and bias voltages.

2 Future work

2.1 Determination of the azimuthal position of interaction

The next step in the determination of the interaction position is the calibration of the crystal for azimuthal position. Due to the large segment volume, the magnitude of most image charge signals are at the level, or below the level, of the random noise encountered on every pulse. A preliminary analysis compared the image charge magnitude with the maximum value of the random noise for each event. The distributions of noise and image charges could not be simply resolved for most of the positions. Unfortunately, at the time of the measurements, the prototype GRT4 cards were suffering from a parasitic oscillating noise of frequency 7~8 MHz, probably due to capacitive effects between internal components of the cards. The additional noise was centred on the pulse region where the presence of image charge signal was searched for, and therefore had a strong impact on the measurement of the image charge magnitude. The study of the image charges would have required the use of specific noise filtering and the analysis of the signal in the frequency domain. However, the preliminary analysis showed that the sensitivity of the crystal to image charge variation with azimuthal position is expected to be large enough near the boundaries between segments. The area of regions with measurable sensitivity still needs to be determined. Once these regions are identified, the segment could then be divided in different zones defined by the radial ranges deduced in Chapter VI, and azimuthally delimited by the regions of measurable image charge magnitude.

2.2 The T90 – T30 method

A suggested method of using the radial ranges defined in the Chapter VI (Section 3) consists in the definition of four areas or 2D polygonal gates in the T90 – T30 matrix, where each defined region would correspond to a particular radial range. The partial rise times (T30, T90) measured from a charge pulse would then fall in one of the 2D gates and the corresponding event would be assigned the radial value of the centre of the range.

3 Differences between ORTEC and CANBERRA designs

An EXOGAM Clover detector (EXOGAM Clover 03) manufactured by CANBERRA EURYSIS was scanned in 2004 with the same scanning system described in Chapter V. The online analysis of the data monitored the intensity of 662 keV γ-rays measured at each position and the energy measured at each contact. Figure VII.1 presents the intensity responses from both CANBERRA EURYSIS and ORTEC manufactured detectors, for 662 keV γ-rays measured in coincidence on the core and outer electrode. The two detectors appear to have different crystal geometries.

Compared to the ORTEC manufactured detector, the frontal cross section of the CANBERRA EURYSIS crystals is more "symmetric". The position of the anode is centred, and the flat edges located at the boundaries between adjacent crystals are shorter, resulting in a larger empty space at the centre of the detector. Also, the diameter of the central holes seems to be identical for the four detector crystals. Such design appears to be very similar to the geometry of the EUROBALL segmented Clover detector [The98]. In comparison, the ORTEC module presents an off centred crystal geometry (although it follows the specifications on Figure III.5 and Figure III.6): the flat edges are larger, resulting in a more compact configuration with less void space at the centre of the detector. In addition, the central holes have different diameters, and their positions are closer to the centre of the detector, causing the inner segment to be smaller.

Both geometrical designs are different. As mentioned in Chapter III, the distance between the front face of the crystal and the central anode is about 8 mm for Clover detectors delivered by ORTEC; whereas the specification sheet provided with the EXOGAM Clover 03 indicates a value of 12 mm for the same distance. Although the crystals meet the specifications in terms of relative efficiency and energy resolutions, there will be considerable differences between the sensitivities of the detectors, especially to low energy gamma-rays, which are being absorbed in the first centimetre of material at the front of the crystals. Indeed, the configuration of the electric field in the frontal region differs due to the distinct anode positions: the radial configuration typically encountered in the coaxial part is expected to occupy a smaller volume further back from the front of the crystal in the case of the CANBERRA EURYSIS design. It is then suspected that different responses will be obtained when PSA techniques are applied to such crystals, since the region of complex electric field occupies a larger volume of the crystal. The off line analysis of the scan data is currently being carried out at GANIL.

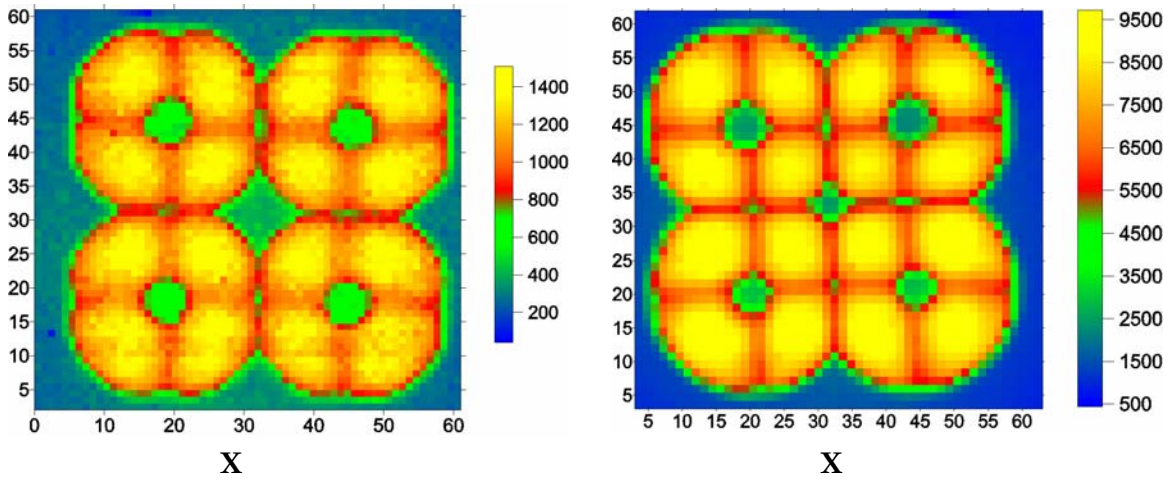

Figure VII.1: (Left) Intensity map from an EXOGAM Clover manufactured by CANBERRA EURYSIS (Clover 03). The intensity map corresponds to the segment response. The intensity map obtained for the EXOGAM Clover 06, characterised in this work is shown on the right. The difference in the shape of the crystals is remarkable.

EXOGAM 06 DATA SHEET

ORTEC EXOGAM DETECTOR OPERATOR'S MANUAL

QUALITY ASSURANCE DATA SHEET

MODEL NUMBER: EXOGAM **SERIAL NUMBER: EXOGAM-06**

CHARACTERISTICS	Detector - A	Detector - B	Detector - C	Detector - D
Crystal Serial Number:	N21687A	N21697A	N21744A	N21706A
Outer Diameter (mm)	61.1	62.0	62.0	61.5
Outer Length (mm)	90.8	92.6	92.8	91.0
Hole diameter (mm)	10.7	9.5	9.2	10.1
Hole depth (mm)	83.8	84.3	84.2	83.0
Imp. Concentration Open-end (Imp./cc)	~ 5 X 10^{+8} N-type	~ 5 X 10^{+8} N-type	~ 5 X 10^{+8} N-type	~ 5 X 10^{+8} N-type
Imp. Concentration. Closed-end (Imp./cc)	1.2 X 10^{+10} N-type	1.9 X 10^{+10} N-type	1.9 X 10^{+10} N-type	1.8 X 10^{+10} N-type
Depletion Voltage (V)	2000	2300	2300	2000
Operating Voltage (V)	2500	3000	2800	2500
Relative Efficiency (%)	39.8	41.7	41.3	39.8

RESOLUTION PERFORMANCE (See FIGURES 1 and 2 on pages 15 and 16 for orientation):

Channel	For 1.33 MeV				For 122 keV			
	@ 6 usec		@ 3 usec		@ 6 usec		@ 3 usec	
	FWHM (keV)	FWTM (keV)	FWHM (keV)	FWTM (keV)	FWHM (keV)	FWTM (keV)	FWHM (keV)	FWTM (keV)
Center – A	2.28	4.15	2.39	4.58	1.29	2.45	1.58	2.84
Center – B	2.30	4.31	2.40	4.59	1.30	2.40	1.51	2.84
Center – C	2.25	4.18	2.39	4.48	1.27	2.27	1.47	2.64
Center – D	2.24	4.12	2.38	4.51	1.29	2.32	1.56	2.84
Outer – A 1	2.46	4.69	2.72	5.11	1.69	3.04	1.91	3.57
Outer – A 2	2.50	4.62	2.84	5.24	1.91	3.69	1.95	3.59
Outer – A 3	2.60	4.85	2.90	5.58	1.72	3.16	2.03	3.68
Outer – A 4	2.43	4.51	2.86	5.09	1.74	3.05	1.98	3.57
Outer – B 5	2.42	4.48	2.87	5.25	1.70	3.17	2.03	3.56
Outer – B 6	2.48	4.66	2.80	5.27	2.00	3.83	2.21	3.89
Outer – B 7	2.47	4.63	2.86	5.34	1.70	3.28	2.17	3.81
Outer – B 8	2.58	4.58	2.74	5.16	1.76	3.18	2.01	3.72
Outer – C 9	2.48	4.70	2.82	5.05	1.90	3.52	2.04	3.71
Outer – C 10	2.50	4.60	2.77	5.21	1.72	3.15	2.01	3.68
Outer – C 11	2.65	4.88	2.85	5.19	2.02	3.83	2.24	3.96
Outer – C 12	2.41	4.64	2.69	5.08	1.72	3.19	2.06	3.74
Outer – D 13	2.55	4.71	2.79	5.02	1.80	3.30	2.02	3.73
Outer – D 14	2.60	4.70	2.84	5.33	1.77	3.23	2.05	3.76
Outer – D 15	2.62	4.87	2.88	5.58	2.00	3.81	2.22	3.95

2

For technical and customer service support, contact: pat.sangsingkeow@ortec-online.com

Appendix B

MONTE CARLO SIMULATION OF THE COLLIMATOR ASSEMBLY

1 Investigation of the photon beam profile

The beam of gamma-rays exiting the collimator is not rectilinear because the collimator is of finite length. This is shown in Figure.B.1. The divergence of the beam is defined by the geometry of the collimator. The spot size, *s*, can easily be calculated as a function of the penetration depth in the detector by equation (B.1)

$$s = A\left(1+\frac{2D}{L}\right) \tag{B.1}$$

Where *A* is the size of the inner hole, *D* is the distance between the collimator and the plane at which the spot size is considered, and *L* is the length of the collimator. The spot diameter varies linearly with depth; this is referred to as the ***geometric divergence***.

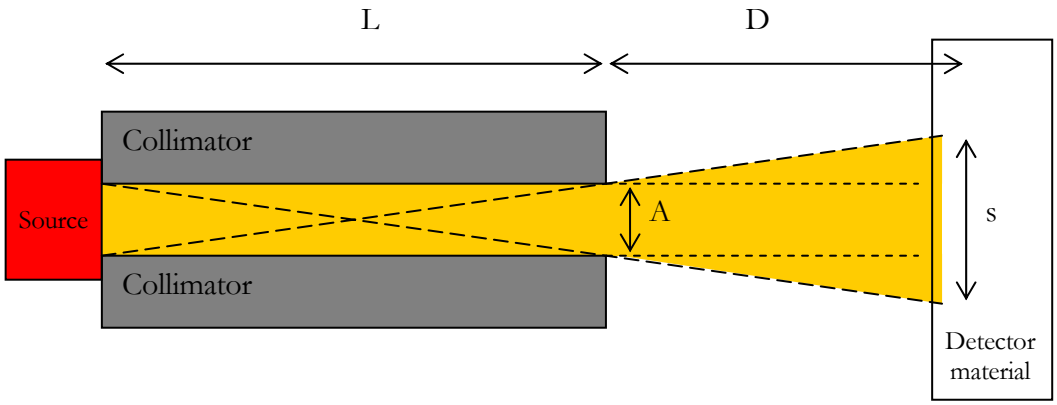

Figure.B.1: Geometry of the beam profile from collimation.

For the front face scan of the Clover detector with the ^{137}Cs source[44], *A* was 2 mm, *L* was 80 mm, and *D* was composed of the sum of three distances: the spacing between the detector and the collimator (measured to be 3 mm), the inner gap between the aluminium housing and the germanium crystal (8 mm), and the depth considered in the crystal *z*.

[44] See chapter 5, section 3.3.1.

Equation (B.1) can be rewritten as:

$$s(z) = 2\left(1 + \frac{(8+3+z)}{40}\right) \tag{B.2a}$$

The variation of the spot size diameter is described by the linear relation

$$s(z) = 2.55 + 0.05z \tag{B.2b}$$

which involves only the depth of interaction in the germanium crystal. Several values of the geometric beam spot diameter have been calculated for different depths in Table B.1:

Depth (mm)	0	10	20	30	40	50	60	70	80	90
Spot size (mm)	2.55	3.05	3.55	4.05	4.55	5.05	5.55	6.05	6.55	7.05

Table B.1: Calculated values for beam spot diameter.

For the configuration described in Figure.B.1, the spot size of the gamma-ray beam at the entrance of the detector (depth z = 0 mm) has a diameter s = 2.55 mm, which almost triples (s = 7.05 mm at z = 90 mm) on the back surface of the germanium crystal. A degradation in knowledge of interaction position arises from such divergence as the considered depth of interaction increases.

On the top of the geometric divergence, one must take into consideration the effect of scattering. At 662 keV, the Compton scattering cross section is larger than the single photoelectric absorption cross section. Consequently, the possibility to observe a Compton scattering sequence that results in the detection of a **F**ull **E**nergy **E**vent (FEE) in a single segment is far from being negligible. The last factor to account for is the scattering of gamma-rays from the front part of the collimator; however these photons carry a fraction of the full energy and mainly contribute to the low part of the energy spectra, which is dismissed by the high CFD threshold (Chapter V, section 3.1).

2 Monte Carlo simulation of the collimator

2.1 Aims

For each position of the scan, there exists an uncertainty associated with the interaction position of the gamma-rays. This uncertainty is caused by the design of the crystals, which are not segmented along the depth (Z axis), and from the collimator dimensions: at a particular depth, interactions are restricted to occur within a specific diameter defined by the geometric divergence. An interaction can occur at any depth between the front and back face of the germanium crystal within the limits defined by the geometric divergence.

As well as the intensity of radiation decreases due to attenuation of the gamma-rays flux with depth in Germanium material, the Compton scattering process also contributes to the variation of the flux in the detector. Photons scattering at large angles reduces the central flux and increases the outer flux. Consequently, inside a germanium crystal, the gamma-ray flux profile observed in the *X-Y* plane should look similar to a circular Gaussian distribution with a flattened top. The characteristics of this 2-dimensional distribution (centroid, FWHM, FWTM) will vary with depth[45].The magnitude of the outer flux should follow the variation of a Compton scattering profile in Germanium.

The absence of knowledge in interaction depth makes necessary the definition of an average value for the uncertainty of interaction position. It should account for the divergence of the photon beam with depth and the effect of Compton scattering, which affect the uncertainty on the position of interaction, as well as for the attenuation of radiation in the crystal. Previous work [Des02] calculated that the spread of radiation from an identical collimator was 5 mm FWHM, for a collimator–detector distance of 10 cm. The contribution of the factors listed above to the value of uncertainty has never been systematically studied, and no real understanding of the collimated photon beam inside the detector exists. The use of a simulation of the collimator with the code **M**onte **C**arlo **N**-**P**articles **4c** (MCNP4c) [MCNP: *Los Alamos National Laboratory*] provided information on the variation of the photon beam profile with depth in germanium material, as well as on the relative importance of Compton Scattering in the uncertainty of the gamma-ray interaction position.

[45]The value of the centroid should be kept constant providing that the collimator is set parallel to the longitudinal axis of the crystal.

The following sections cover the study of the profile of the collimated photon beam in the situation of the front face scan performed with the ^{137}Cs source, aiming to describe and understand the variation of the beam profile inside the detector as a function of depth. After a brief description of the problem, the results regarding the flux from the collimator (*intrinsic flux*)[46] are compared to the gated energies flux[47]. Finally, the values of uncertainty obtained from the simulation will be discussed.

2.2 Details of the Simulation

Geometry

The elements considered in the simulation were the geometry and distribution of the ^{137}Cs source, the collimation block, and the germanium crystal. The source was modelled by an isotropic distributed source emitting 662 keV energy photons. The collimation block consisted of a 80 mm long Tungsten collimator with a circular hole of 2mm diameter (Figure B.2), surrounded by a Lead cylinder of dimensions 80 mm long by 200 mm diameter. The detector was modelled as a 60 mm by 90 mm long germanium cylinder. The dimensions of the Clover crystal could have been exactly defined in the problem, but one of the aims of the simulation was to obtain general results from which the uncertainty could be easily deduced.

As the uncertainty on the position of the interaction is related to the profile of the gamma-ray beam through the crystal, such a profile was determined by sampling the value of the radiation flux on surfaces perpendicular to the orientation of the collimator, located on 10 planes, each separated by 10 mm along the depth of the cylinder. The profile of the flux on each plane is measured by dividing each surface into 30 sub-surfaces made of concentric rings of 1 mm width; this assumes a cylindrical symmetry. The value of the flux is thus sampled every millimetre, from the centre to the outer surface of the cylinder. The geometry of the problem is illustrated by the schematic diagram in Figure B.2.

[46] Intrinsic flux: correspond to all energies between 0-662 keV.

[47] Gated energies flux: correspond to the gamma-rays whose energy passes the gate used to filter FEE depositing 662 keV (described in Chapter V).

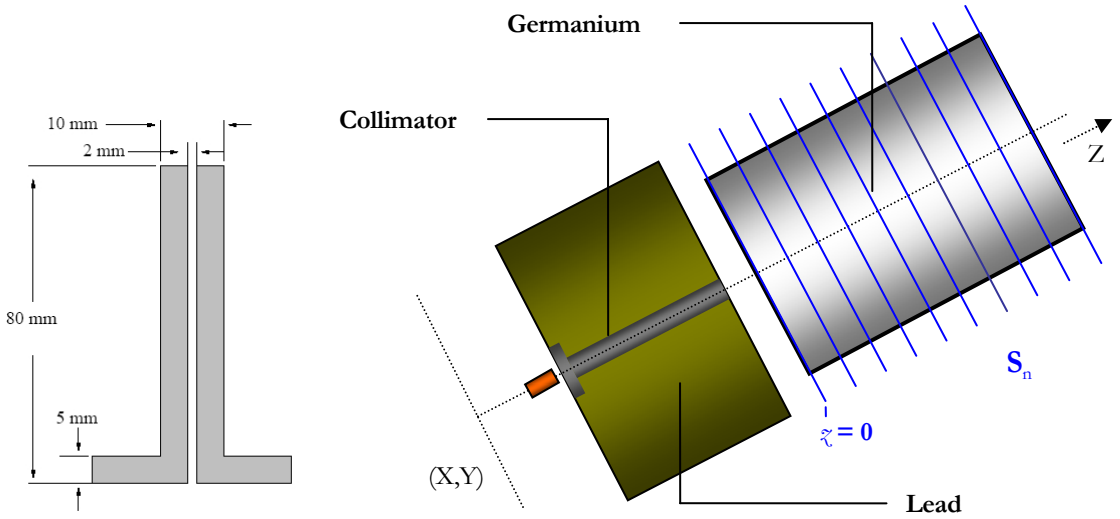

Figure B.2: geometry of the simulation. The gamma-ray source is placed at 5 mm from the Tungsten collimator. The Flux profile is measured in the Germanium cylinder on 10 surfaces S_n as indicated in the figure. The first surface starts at z=0. The dimensions of the Tungsten collimator are indicated on the left.

2.3 Evolution of the beam profile with Depth

The evolution of the intrinsic flux profile with depth, from z = 0 mm (surface S_0, at the entrance face) to z = 90 mm (surface S_{10}, at the detector end) is presented in Figure B.3 (a) to (d). For all surfaces, the distribution of the flux is maximum at the centre of each plane then decreases sharply with increasing radius. The variation of the central flux with depth follows the expected intensity attenuation for 662 keV photons with germanium thickness.

In order to calculate the average uncertainty of an interaction position, such variation is needed because it relates the value of the uncertainty with the relative contribution of the depth of interactions. Figure B.5 shows the extracted information from an exponential fit of the flux variation with depth in the central ring given by equation (B.3):

$$N(z) = \exp(e_0 + e_1 \cdot z) \tag{B.3}$$

The outer flux, defined for radii > 6 mm, shows a significantly different profile as a function of depth . The flux increases until z = 40 mm and then decreases. Such variation can be explained by the superposition of three effects:

1. the spread of the beam out of the collimator

2. the presence of scattered photons due to Compton Scattering inside the detector

3. the increasing photon absorption probability, with decreasing photon energy.

The geometric divergence of the beam is constant, and therefore the flux attributed to initial gamma-rays emitted at large angles is small and is attenuated. The increase of outer flux is probably due to scattered photons generated by Compton events. At 662 keV, forward scattering is more probable than back scattering[48] causing the net value of the Compton scattered profile to increase from the entrance surface up to a depth of 40 mm. At larger depths, the attenuation of radiation plays a double role: the absorption of initial gamma-rays reduces the number of scattered photons, which are also being absorbed. This finally results in a decrease of the magnitude of the outer flux.

2.4 Fitting method

The profiles obtained for each surface can be fitted by a sum of four individual Gaussian functions. The peak observed for the central flux can be modelled by the sum of a positive and a negative Gaussian, accounting for the sharp edges delimiting the central and outer fluxes and for the flattened maximum observed for the central flux. The outer flux is modelled by two other Gaussians functions, and accounts for the outer distribution of flux attributed to photons that Compton scatter forward or backward at large angles. Another source of outer flux are photons coming from the scattering of primary gamma-rays by the collimator towards the detector material.

[48] Klein – Nishina formula, see Chapter II, section 2

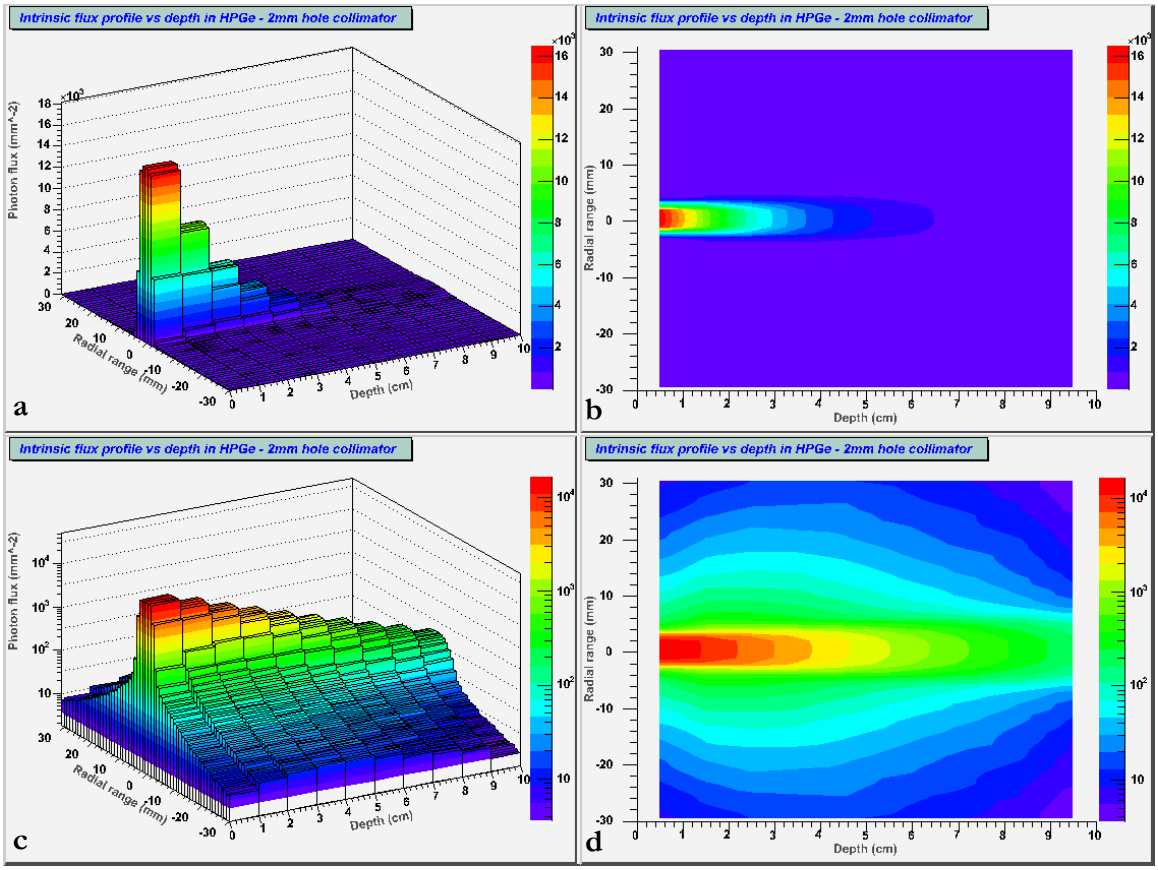

Figure B.3: variation of intrinsic flux inside the Ge cylinder. (a) and (b) represents the depth variation of the flux in linear scale. (c) and (d) present the same plots in a logarithmic scale. The right figures allows one to appreciate the depth profile of the gamma-ray beam within the Ge cylinder. (c) shows that most of the flux is concentrated within the central region, and that most of interactions occur at the front of the Germanium. (d) presents the variation of the outer flux with depth, which increases up to 4 cm depth, then decreases.

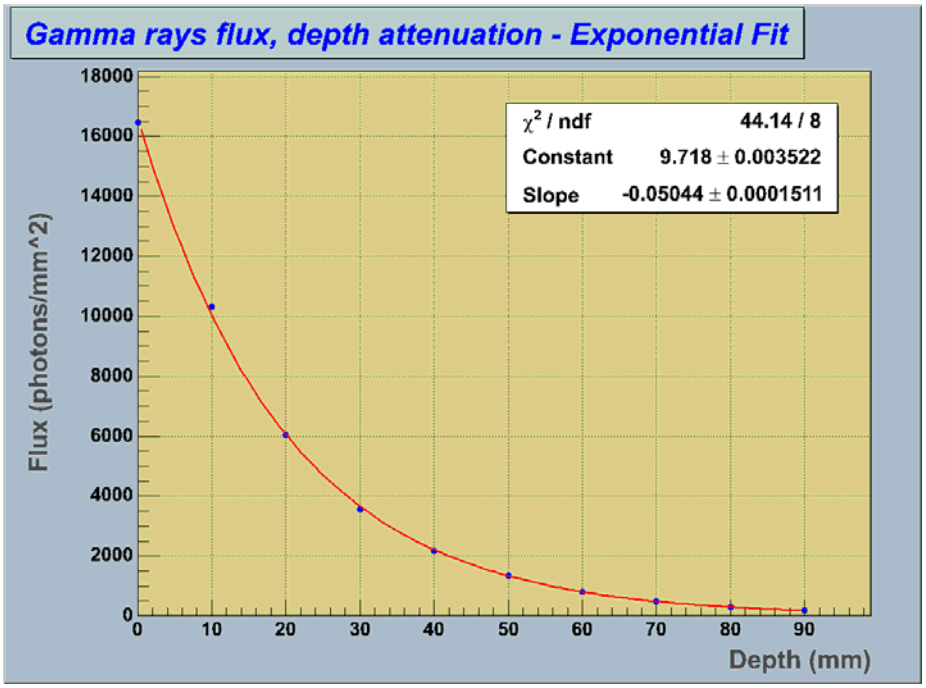

Figure B.4: Exponential fit of central flux attenuation. The points are values derived by MCNP (the uncertainties ranges from 0.3% at 0 mm to 3.3% at 90 mm). The fit shows excellent agreement with the exponential attenuation law.

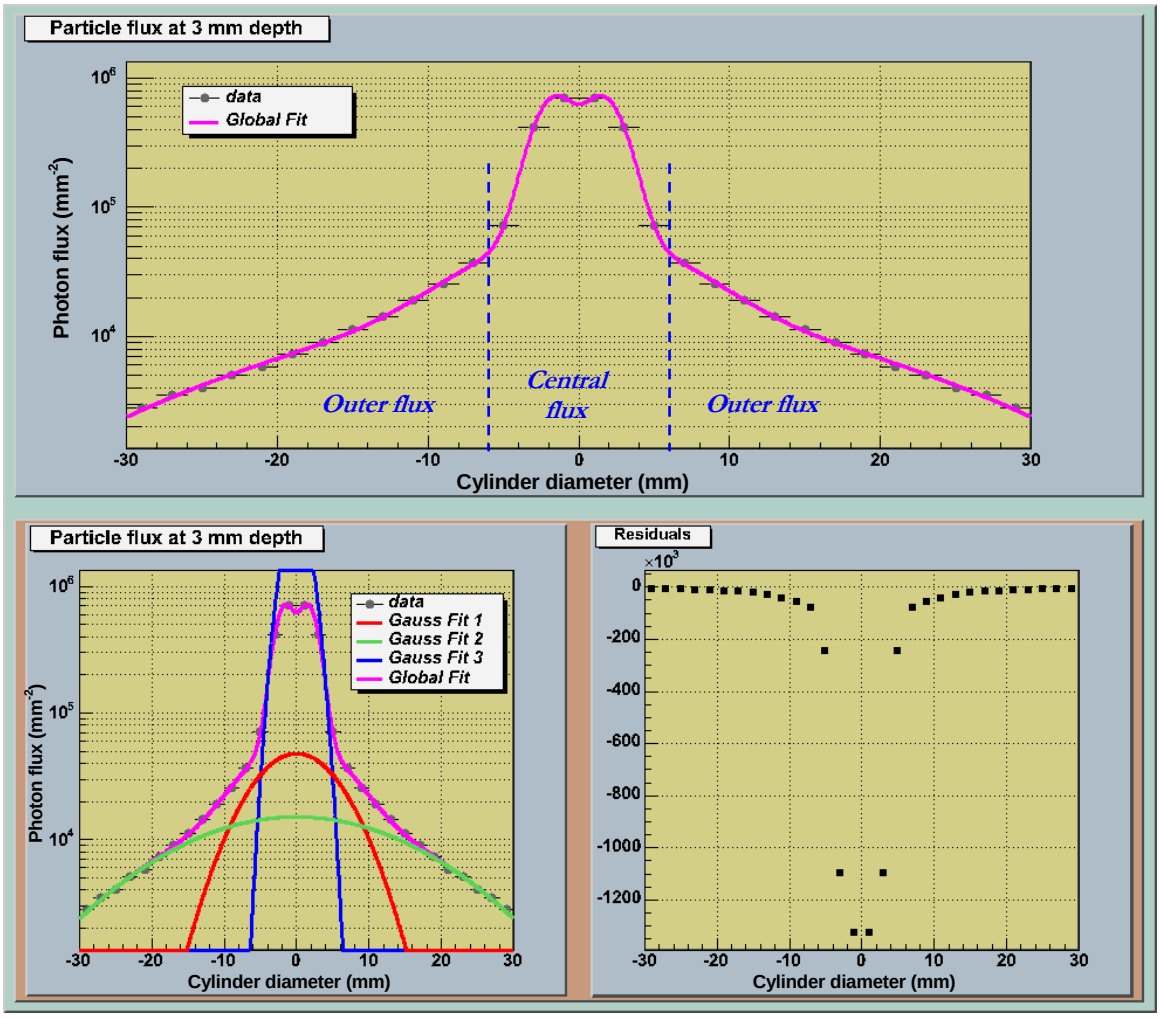

Figure B.5: Example fit of a flux profile with a sum of 4 Gaussian functions. The top plot contains the original data (data points with error bars), with the fit function superimposed. Below on the left is represented the top graph along with the 3 positive Gaussian fitting functions; the value of the residuals between the data and the global fit is displayed on the right graph. There is good agreement between the fit and the data for r = [2, 6] mm and r = [6, 30] mm (variation of outer flux, attributed to scattered photons). However, the values of residuals are getting very large for the fit of the central values of flux.

2.5 Characterisation of the profile distributions with depth

To characterise each distribution and investigate the variation of the flux profile with depth, the standard FWHM and FWTM parameters are used. However, these two parameters do not provide sufficient information to describe the shape of the flux on each plane and other parameters have been introduced to complete the description. The secondary parameters chosen for this study are the values of radius *a*, defined in Equation (B.4a) and (B.4b)

$$\boldsymbol{F}_a = q \cdot \boldsymbol{F}_{TOT} \tag{B.4a}$$

Where $\boldsymbol{F}_a$ is the integral of the flux for which the radius *a* is solution of equation (B.4b), *q* is a fraction factor chosen to be 0.7, 0.9 and 0.95, and $\boldsymbol{F}_{\mathrm{TOT}}$ represents the integral of the flux profile over the full diameter. Equation (B.4b)

$$\int_0^a F_S(r)dr = q \cdot \int_0^{30} F_S(r)dr \tag{B.4b}$$

gives then the solutions for the radius or diameter ($D_q = 2\times a_q$) defining the areas (centred on r = 0 mm) that enclose respectively 70%, 90%, and 95% of the total flux for a surface *S*.

The set of five parameters chosen to characterize each distribution is:

1) The Full Width at Half Maximum value: ***FWHM***
2) The Full Width at a Tenth of the Maximum value: ***FWTM***
3) The diameter $\boldsymbol{D_{70}}$ for which $q = 0.7$
4) The diameter $\boldsymbol{D_{90}}$ for which $q = 0.9$
5) The diameter $\boldsymbol{D_{95}}$ for which $q = 0.95$

The depth variation of the FWHM and FWTM of the flux distributions are presented in Figure B.6, and the variations of D_{70}, D_{90} andBD_{95} is displayed in Figure B.7. The geometric divergence derived in Equation (B.2b) is represented for comparison purposes. The geometric divergence is referred to as "Collimation beam".

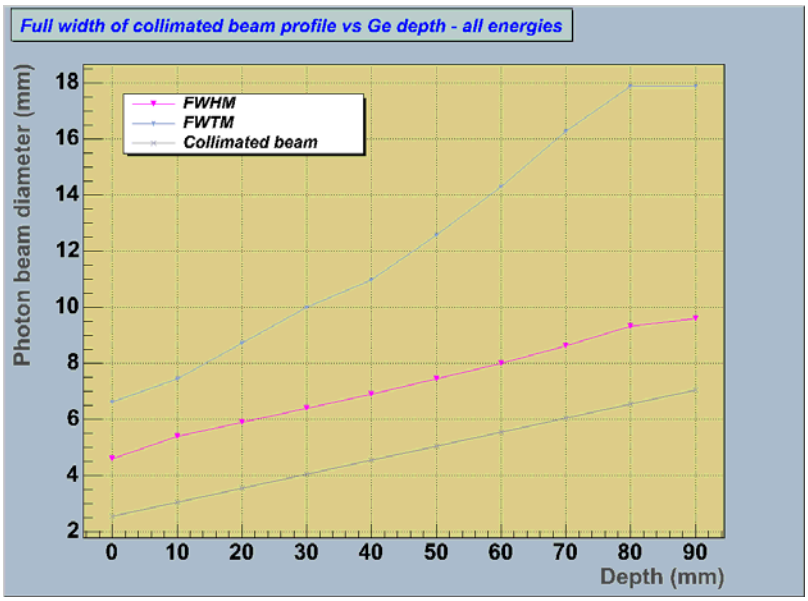

Figure B.6: Variation of FWHM and FWTM of intrinsic flux profile with depth. The FWHM increases linearly; the absence of back and forward scattered g-rays is observable at the front and back surfaces. The divergence of the FWTH follows the increasing number of scattered γ rays at larger diameter.

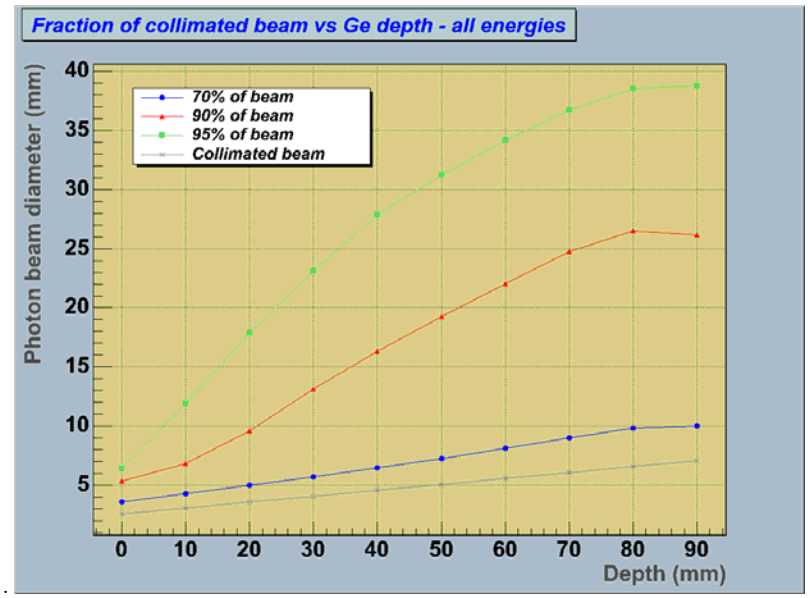

Figure B.7: variation of D_{70}, D_{90} and D_{95} with depth. The three parameters increase with depth. The larger diameters at the front surface are due to γ rays that scatter from the collimator, and from the Germanium. D_{70} increases linearly, while D_{90} and D_{95} follow the profile of scattered photons with depth. The negative curvature is due to the absorption of scattered γ rays with increasing depth.

In a simple interpretation, the variation of the FWHM shows a linear increase which follows the geometric divergence. The FWHM includes the flux from a large proportion of scattered photons, which explains the systematically large value of this parameter. The rates of increase for the beam and FWHM divergence are very similar, 5×10^{-3} and 5.5×10^{-3} respectively. The only deviations are observed on the first and last surfaces, where the intensity of radiation inherent to scattered photons is lower due to the relative absence of forward and backward scattering components compared to the middle region of the Germanium cylinder. The variation of the FWTM gets larger with depth, since the maximum flux at the centre decreases exponentially with depth, while the outer flux generally changes smoothly.

Considering the variation with depth of the diameters D_{70}, D_{90} and D_{95}, three different behaviours are noticed: D_{70} shows a linear increase, which then reduces at the back of the detector. D_{90} starts from a larger entrance diameter (due to scatters from the collimator) with a linear increase, followed by a small negative curvature and a reduction of the diameter at the exit surface. D_{95} starts from a linear increase, followed then by an earlier negative curvature (at z = 10 mm). The increase of negative curvature between D_{70}, D_{90} and D_{95} is a consequence of the decrease of the outer flux; caused by the absorption of gamma rays with energy $E_\gamma < 662$ keV, which increases with the thickness of absorbing medium.

The characterisation of the central flux is made through the variation of the FWHM and D_{70}. A similar evolution is noticeable for both parameters, although their linear rate of increase is different. The value of D_{70} is smaller than the FWHM until a depth of ~55 mm. Also, the FWHM follows closely the evolution of the geometric divergence of the beam. The other parameters allow the characterisation of the beam profile in larger radial zones, where the information then corresponds to the profile of scattering inside the detector as a function of depth. For all of the parameters, different behaviours are observed at the front of the Germanium crystal - between 0 - 10 mm depth; and at the back, for depths greater than 80 mm. These effects are caused by the absence of forward scattered photons at the front and absence of backward scattering combined with linear attenuation at the back of the detector.

Finally, the main goal of this study is to derive a suitable value of uncertainty for the position of interaction of gamma-ray photons. The use of D_{70} versus depth is the appropriate estimator for the size of the collimated beam, from which the uncertainty will be determined. Indeed, D_{70} is related to the total flux profile over a constant surface along the whole depth as shown

in Equation B.4b, compared to the FWHM which relates the variation of the flux to the central flux value at each surface.

2.6 Uncertainty on position of interaction

The Clover crystal is only segmented azimuthally, therefore it is impossible to locate the interaction position along the depth. Consequently the experimental data will consist of contributions from absorptions occurring at any depth. The average the size of the beam $\overline{D_{70}}$ over the whole length of the crystal is given by Equation B.5

$$\overline{D_{70}} = \frac{1}{Z_{tot}} \cdot \int_0^{Z_{tot}} D_{70}(z)\,dz \tag{B.5}$$

where Z_{tot} represents the full germanium thickness.

Also, the absorption cross section for photons in the germanium crystal depends on the depth of interaction, and decreases exponentially as illustrated in Figure B.4. Therefore more data will contribute from the front part of the crystal than from the back. Practically, the uncertainty in the beam diameter σ_d is chosen to be the average of $D_{70}(z)$ over the whole depth, weighted and normalised accordingly to the depth attenuation profile $N(z)$ defined previously in Equation B.3. The determination of σ_d is given by Equation B.6:

$$\sigma_d = \frac{\frac{1}{Z_{tot}} \cdot \int_0^{Z_{tot}} N(z) \cdot D_{70}(z)\,dz}{\frac{1}{Z_{tot}} \cdot \int_0^{Z_{tot}} N(z)\,dz} \tag{B.6}$$

The variation of $D_{70}(z)$ has been fitted by a 5th order polynomial (providing the best χ^2 value) in the range 0-90 mm:

$$\begin{aligned} D_{70}(z) = 3.566 + 0.06475\,z + 1.001\times10^{-3}\,z^2 - 4.595\times10^{-5}\,z^3 \\ + 8.228\times10^{-7}\,z^4 - 4.744\times10^{-9}\,z^5 \end{aligned} \tag{B.7}$$

The coefficients of the function N(z) have been defined in Figure B.6

$$N(z) = \exp(9.718 - 0.05044z) \tag{B.8}$$

Finally, substituting Equations B.7 and B.8 into Equation B.6, the value for σ_d is finally obtained:

$$\sigma_d = 4.95\,\text{mm} \tag{B.9}$$

For a germanium depth Z_{tot} = 90 mm, the average uncertainty in the position of a gamma-ray interaction is 4.95 mm, which is comparable to the value D_{70} (χ=20) = 4.98 mm.

Due to the specific geometry of the Clover crystal, when the source is located in front of the taper, the thickness of material available to the gamma-ray beam is smaller than 90 mm. The distance between the collimator and the detector is also larger, therefore a wider beam must be considered. In this case, Equation B.6 is no longer valid, and an analytic formula relating the value of uncertainty σ_d with the distance ΔZ between the collimator and the entry point of the beam in the detector, has been derived for the value of uncertainty

$$\sigma_d(\Delta z) = \frac{\int_0^{Ztot-\Delta Z}\left[N(z)\cdot D_{70}(z+\Delta Z)\right]dz}{\int_0^{Ztot-\Delta Z} N(z)dz} \tag{B.10}$$

The range of uncertainty obtained from Equation B.10 is σ_d = [4.95, 7.00] mm, with the maximum value occurring at the outer limit of the taper on the edge of the crystal.

3 Results for the 662 keV energy gate

In order to facilitate comparisons with experimental data, the same work needed to be done for gamma-rays whose energy entered the energy window used to select the data for pulse shape analysis. The previous program was modified by the addition of the energy window which was set to include photon energies between 658 keV and 666 keV. The present situation is different to the case that considered the intrinsic flux, because only photons with energy E_γ = [658 – 666] keV are taken onto account, therefore most of scattered photons disappeared from the data. As a result, the arguments for the fitting method with a sum of 4 Gaussians was no longer valid. Instead of looking for a function to model the flux profile at each surface, the data were linearly interpolated, and the parameters used to characterise the distributions were deduced by the means of discrete algorithms.

3.1 Evolution of the beam profile with depth

The general variation of the flux profile with depth illustrated in Figure B.8 is very similar to the profile observed in the study of intrinsic flux. The central flux is at its maximum at the entrance plane, and then decreases exponentially with depth. The use of an energy window suppresses all flux inherent to scattered photons, which results in an outer flux quasi null at radii larger than 6 mm. Thus, the present data are almost free of scattering, except for forward scattered photons with energies between 662 and 658 keV, emitted with a divergence of 5.5° (calculated from the Compton scattering formula[49]).

Compared to the variation of the intrinsic flux, the absence of scattering is clear. Figure B.8(a) and (c) present a much sharper profile than shown in Figure B.3(a) and (c). As the edges of the beam are sharper, the photon flux is more concentrated towards the centre; which will reduce the uncertainty on the interaction position. The use of an energy gate not only restricts the analysis to full energy events, but also artificially lowers the divergence of the radiation beam to interactions with 5.5° divergence. The energy gate restricts trigger events to full energy events, while the full energy detected in anode-cathode coincidences selects only events with full energy inside a segment. These Fold 1 events include single photoelectric absorption and Compton scatter sequences within a same segment that also deposits the full (662 keV) energy. They could be either:

1. Single photoelectric absorption (multiplicity $M_\gamma = 1$);

2. Compton scattering followed by photoelectric absorption (multiplicity $M_\gamma = 2$);

3. A sequence of two Compton scatter followed then by photoelectric absorption (multiplicity $M_\gamma = 3$).

Multiplicities greater than 3 are possible, but negligible compared to the ones listed above. According to [She99], the main contribution comes from $M_\gamma = 2$, followed by $M_\gamma = 1$, then $M_\gamma = 3$.

[49] See Chapter II, section 2.

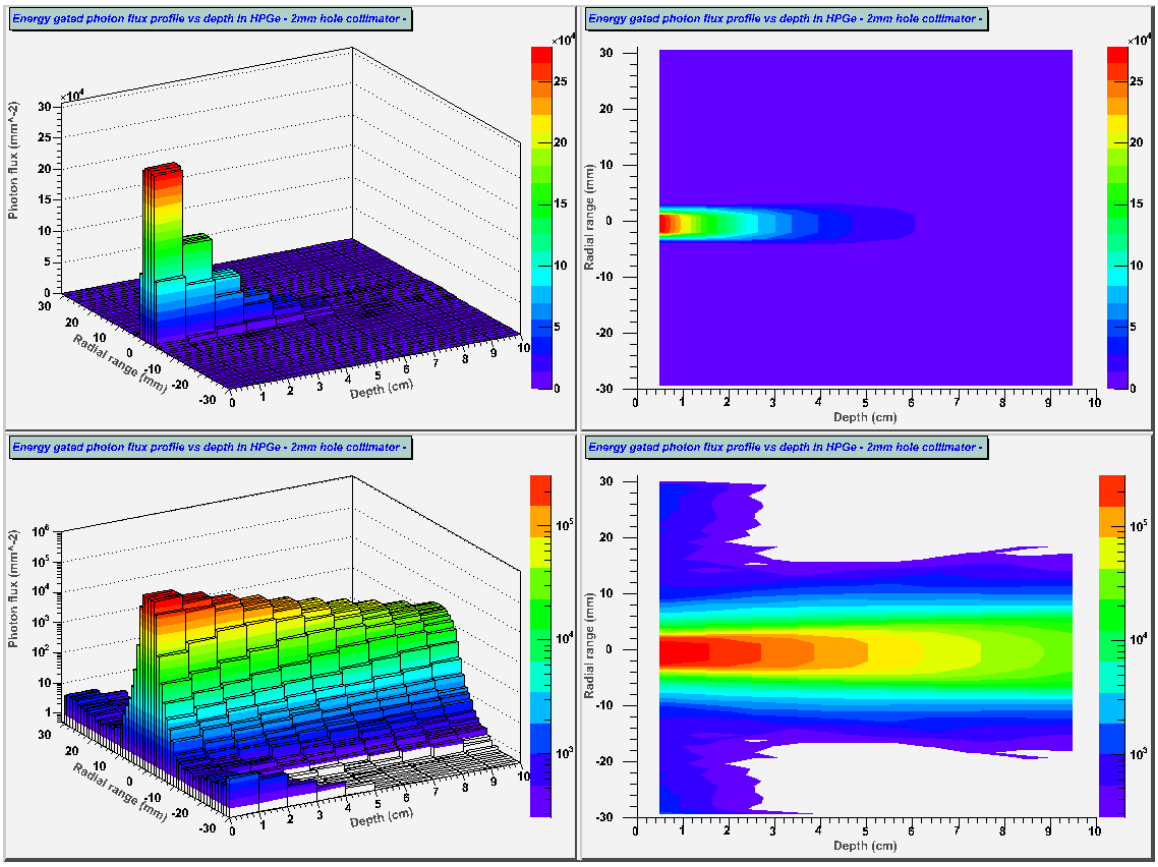

Figure B.8: Variation of 662 keV energy photons flux profile in the Ge cylinder. (a) and (b) represents the depth variation of the flux in linear scale. (c) and (d) present the same plots in a logarithmic scale. Compared to Figure B.3, the flux profile is now more linear, and the outer flux is quasi null after z =4 cm.

3.2 Characterisation of the profile distributions with depth

The attenuation has been fitted by an exponential function giving the following relation:

$$N(z) = \exp(12.52 - 0.05468\ z) \tag{B.11}$$

The variation of FWHM and FWTM are presented in Figure B.9, and the results for D_{70}, D_{90} and D_{95} are shown in Figure B.10.

The FWHM follows the geometrical divergence as observed in section B.2.5, where it increases at a rate of 49.6×10^{-3}, similarly the FWTM increases at a larger rate. However, when considering the influence of scattered photons, the use of an energy gate reduces considerably the range of scattering angles allowed for secondary photons and restricts the divergence of the beam within limits defined by the Compton scattering formula defined in Equation II.9.

The increase of the three diameters D_{70}, D_{90} and D_{95} has been respectively fitted with a 2nd order polynomial and two 3rd order polynomials. The positive curvature observed for D_{70}, D_{90} and D_{95} is due to the presence of a small proportion of scattered photons, and is discussed in section B4.

3.3 Determination of the uncertainty

The variation of D_{70} with depth z in the germanium crystal can be described

$$D_{70}(z) = 3.386 + 3.893\times10^{-2}\, z + 2.045\times10^{-5}\, z^2 \tag{B.12}$$

Substituting equations B.10 and B.11 into Equations B.7 and B.10 gives the following range of values for σ_d:

$$\sigma_d = [\,4.08, 5.22]\,\text{mm} \tag{B.13}$$

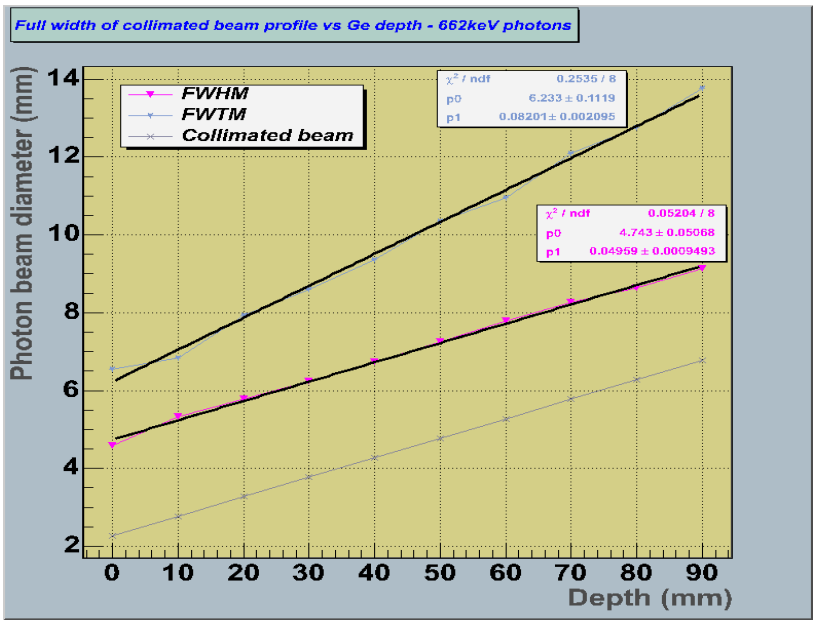

Figure B.9: Variation of FWHM and FWTM for 662 keV photons. A linear fit has been applied to both variations, the parameters are indicated in the Figure.

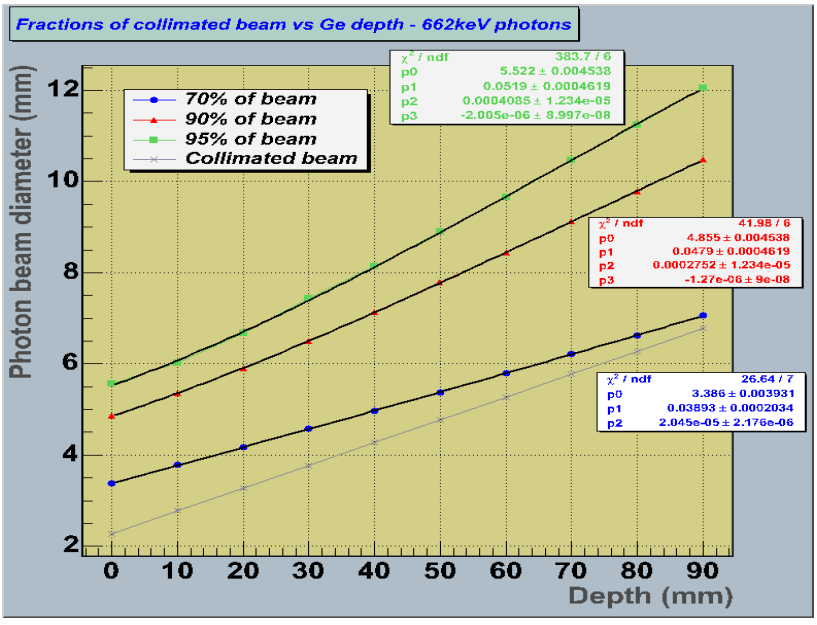

Figure B.10: variation of D_{70}, D_{90} and D_{95} for the 662 keV photon beam. The absence of low energy γ-rays is noticed by the increase of the three parameters from the entrance surface to the end surface of the Germanium. A fit has been applied to the variation of each parameter. The variation of D_{70} is modelled by a second order polynomial, while D_{90} and D_{95} are modelled by a 3rd order polynomial.

4 The beam profile within the germanium crystal

Comparing the results obtained for D_{70}, D_{90} and D_{95} from the intrinsic flux with the values calculated for the flux of 662 keV photons allows the full understanding of the properties of the collimated photon beam inside the Germanium crystal. The difference between each parameter, deduced from the intrinsic and energy gated fluxes will indicate the behaviour of low energy (< 656 keV) scattered γ rays. Figure B.11, B.12 and B.13 show the variation of the difference between both data sets for the D_{70}, D_{90} and D_{95} parameters with depth.

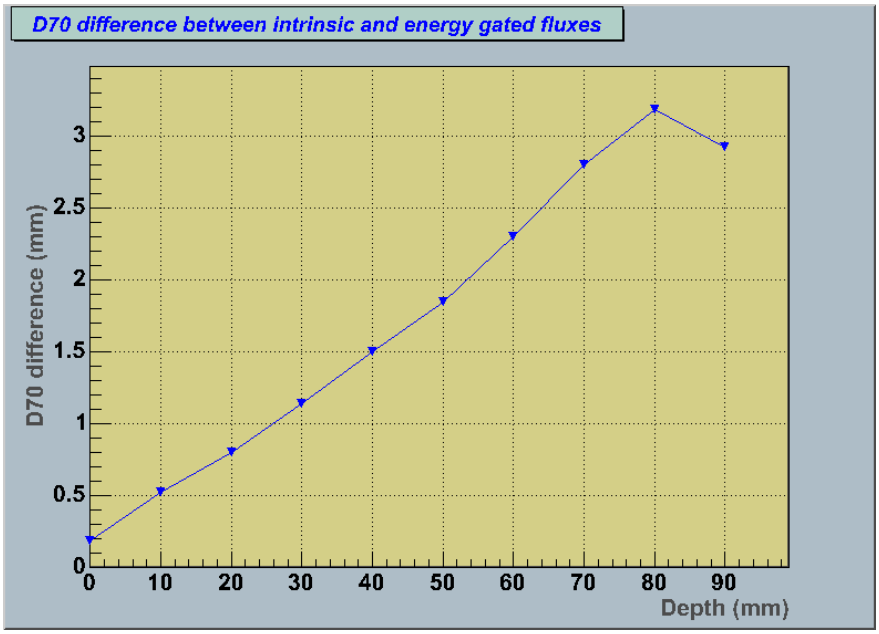

Figure B.11: Depth variation of the difference in D70 between intrinsic and energy gated fluxes.

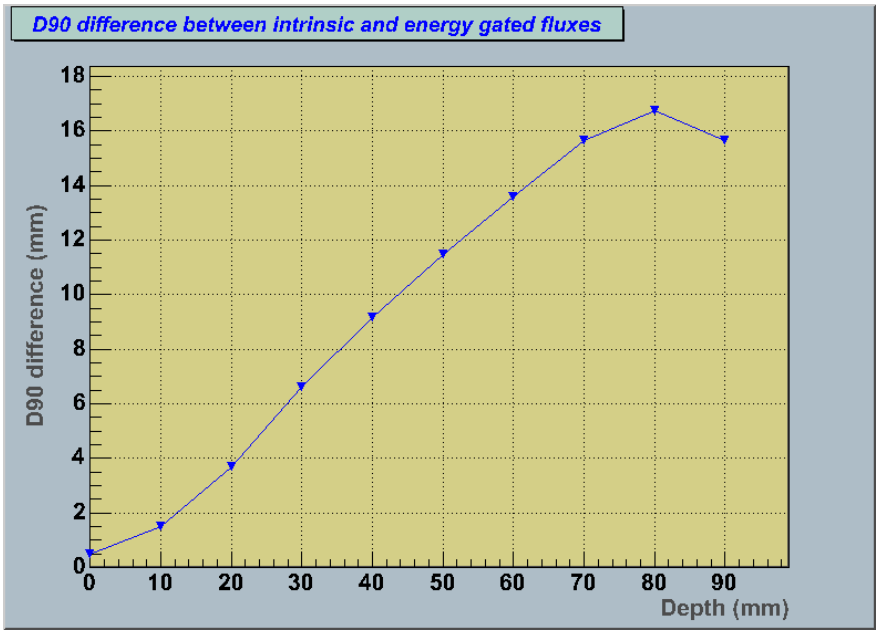

Figure B.12: Depth variation of the difference in D90 between intrinsic and energy gated fluxes.

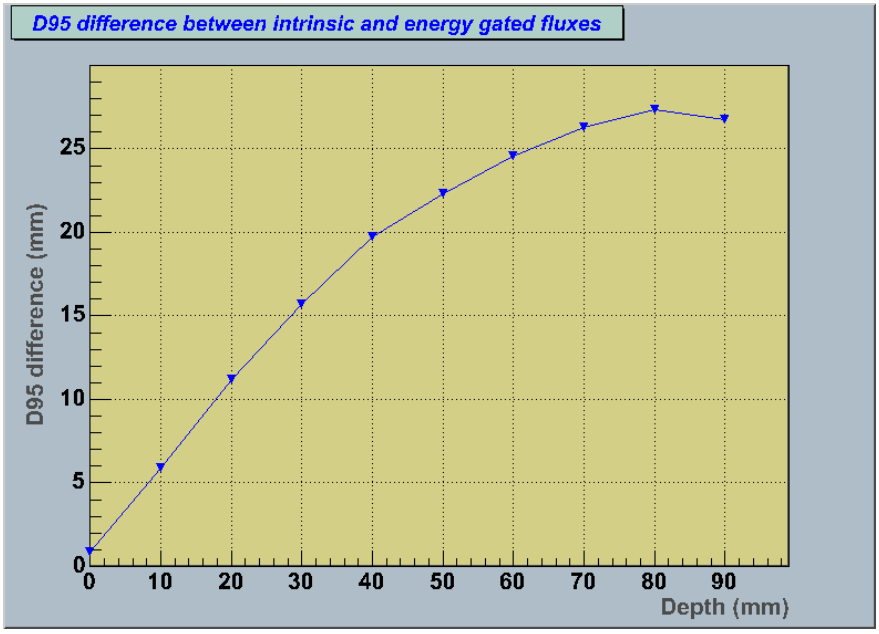

Figure B.13: Depth variation of the difference in D95 between intrinsic and energy gated fluxes.

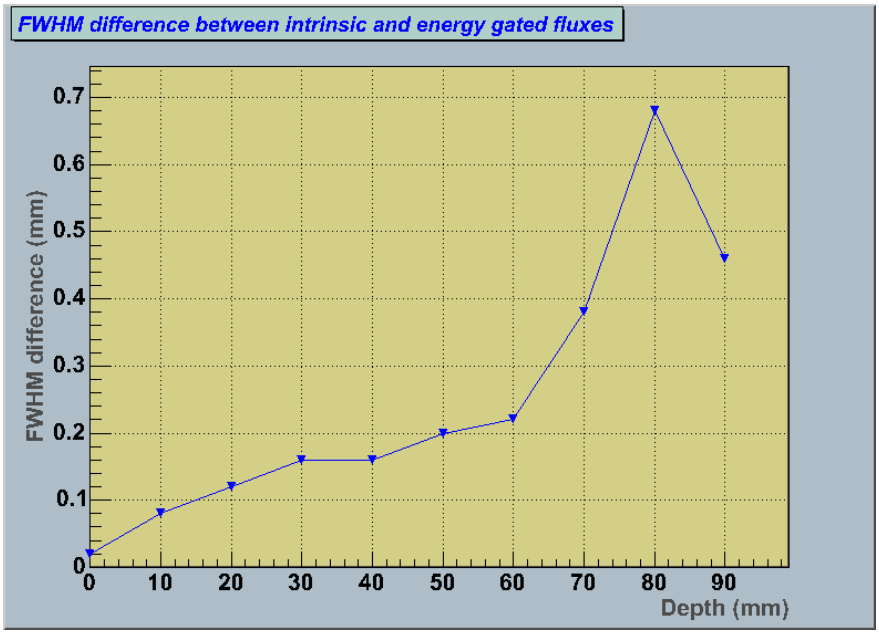

Figure B.14: Depth variation of the difference in FWHM between intrinsic and energy gated fluxes.

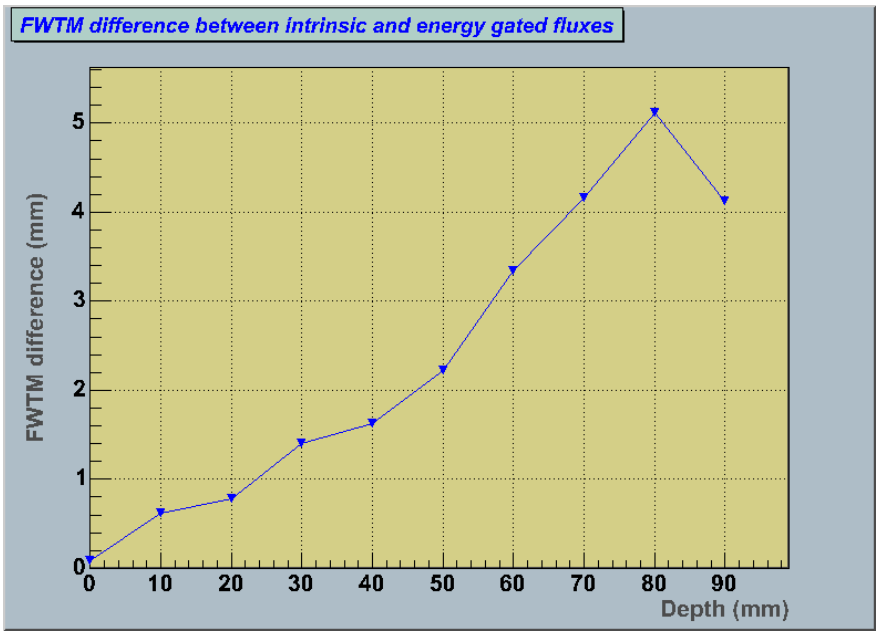

Figure B.15: Depth variation of the difference in FWTM between intrinsic and energy gated fluxes.

The variation of the parameters deduced from the gated energy tally presents a more linear increase than the variations of the intrinsic flux parameters. The difference between both sets of parameters reveals the history of scattered gamma-rays in the detector. The outer flux increases strongly with depth as illustrated in Figures B.11 to B.15, as initial 662 keV photons undergo scattering in the Germanium crystal. This is shown by a large rate of increase for D_{90} and D_{95}. At the back of the detector, the outer flux diminishes due to the radial attenuation of gamma rays in germanium, causing the smooth negative curvatures observed for D_{90} and D_{95}. Another factor contributing towards a sharper reduction in outer flux is the absence of back scattered photons, as shown by the break in the beam profile diameters D_{70}, D_{90} and D_{95} between z = 80-90 mm.

Such features are absent from the flux of gated photons, presented in Figure B.10. The energy window ensures that only forward scatters, with a reduced scattering angle are studied. Indeed, photons with energy below 658 keV, who scatter through an angle larger than 5.53°, are suppressed from the tally of interest, and therefore provide a more linear beam.

Another important factor is the scattering of source photons from the collimator towards the detector material. At the entrance surface of the detector, the majority of the initial photon flux is concentrated within the geometric divergence. Therefore the majority of the remaining flux can only be attributed to photons that have been forward scattered by the collimator. These photons have to carry an energy value within the energy window, which implies that they also scatter through an angle lower than 5.53°. In the limiting case where radiation scatters on the inner corner of the exit side of the collimator, this results in a 4.69 mm diameter beam spot on the entrance surface of the crystal. This value is comparable to the diameter enclosing 90% of the flux on the entrance surface $D_{90}(0)$ = 4.86 mm. Of course, 662 keV gamma-rays also penetrate the collimator material, and scatter out hitting the front face at a larger radius than defined by the limiting case above. This explains the behaviour of $D_{90}(z)$ and $D_{95}(z)$, both of which incorporate the majority of photons that scatter from the collimator, resulting in a larger diameter than expected in the front with a positive curvature rather than a linear divergence expected in the ideal case where the detector would be completely shielded against any radiation other than from the initial radiation beam.

5 Conclusions

For the purpose of determining an uncertainty value for the interaction position of gamma rays, a Monte Carlo simulation of the collimator used in the detector scanning has been performed. A study of the beam profile through a 90 mm germanium cylinder revealed the importance of scattered gamma rays in the determination of the uncertainty. Due to the complex geometry of the Clover crystal, an analytic formula that accounted for the geometry of the Clover crystal was derived. The beam profile was studied in two cases:

- The intrinsic flux included photons of all energies. In this case, the uncertainty calculated ranges between [4.95, 7.00] mm. The smaller value applies to detector front where the length of the crystal is 90 mm. The large value applies to the edge of the tapered crystal side, where the Germanium thickness is 60 mm.

- The flux of energy gated γ rays. In order to facilitate the comparison with experimental data, the same energy gate used in the off-line analysis of the ^{137}Cs scan data was included. The corresponding range of uncertainty was [4.08, 5.22] mm.

The range calculated in the second case is ~0.9 mm smaller for 90 mm thickness and 1.8 mm at the edge of the taper, compared to the intrinsic flux. The difference illustrates the effect of Compton scattered photons on the profile of the collimated beam in the Germanium crystal.

REFERENCES

[AD03] AD6645 Flash Analogue-to-Digital Converter Data Sheet, Analog Device, http://www.analog.com

[Baz04] D. Bazzacco, Nucl. Phys. A746 (2004) 248c

[Bea96] C. W. Beausang and J. Simpson, J. Phys. G 22 (1996) 527

[Bec92] F.A. Beck, Prog. Part. Nucl. Phys. 28 (1992) 443

[Bos04] A.J. Boston, *Gamma Spectroscopy in the Digital Era*, Talk given at the IOP Nuclear Physics Conference, April 2004, Edinburgh, Scotland

[Can74] C. Canali, et al., Solid State Comm. 15 (1974) 1213

[Cre02] Programs written by J.R. Cresswell

[Des02] M. Descovich, Improving the position resolution of Highly Segmented HPGe Detectors using Pulse Shape Analysis Methods, Ph.D. Thesis, University of Liverpool (2002)

[Dob03] J.J. Valiente-Dobon et al., Nucl. Instr. Meth. A505 (2003) 174

[Duc99] G. Duchêne et al., Nucl. Instr. Meth. A432 (1990) 90

[Ebe01] J. Eberth et al., Prog. Part. Nucl. Phys. 46 (2001) 389

[Ebe96] J. Eberth et al., Nucl. Instr. Meth. A369 (1996) 135

[Fra04] G. De France, Private communications

[Gatt82] E. Gatti et al., Nucl. Instr. Meth. 193, (1982) 661

[Gör03] A. Görgen, *Position sensitivity of the AGATA prototype crystal analysed using a database of calculated pulse shapes*, DAPNIA/SPhn - CEA Saclay (2003)

[Gro03] S. Gros et al., Conference records of the IEEE Nuclear Sciences Symposium, October 2003, Portland, Oregon

[Gun00] Christoph Gund, *The 6-Fold Segmented MINIBALL Module Simulation and Experiment*, Ph.D. Thesis, Ruprecht-Karls Universität Heidelberg, 2000

[Jon95] P.M. Jones et al., *Calibration of the new composite 'Clover' detector as a Compton polarimeter for the EUROGAM array*, unpublished and private communication

[Kno00] G.F. Knoll, *Radiation Detection and Measurement*, Third Edition, John Wiley and Sons, (2000)

[Kro01] Nucl. Instr. Meth. A463 (2001) 227

[Kro95] Nucl. Instr. Meth. A371 (1996) 489

[Lau04] M. Lauer, *Digital Signal Processing for Segmented HPGe Detectors Preprocessing Algorithms and Pulse Shape Analysis*, Ruperto-Carola University of Heidelberg, 2004

[Laz04] I. Lazarus et al., IEEE Trans. Nucl. Sci. NS-51, 4 (2004) 1353

[Lee04] I-Y. Lee, Nucl. Phys. A756 (2004) 245c

[Lee90] I-Y. Lee, Nucl. Phys. A520 (1990) 641c

[Leo94a] R. Leo, *Techniques for Nuclear and Particle Physics Experiments*, Second Edition, Springer Verlag, (1994), p 35

[MAT] http://www.mathworks.com

[Mat03] A.R. Mather, Monte Carlo simulation of HPGe crystal, Private communications

[Med03] P. Medina, private communications

[MIDAS] MIDAS package web page, http://nnsa.dl.ac.uk/MIDAS/base.html

[Mih00] L. Mihailescu et al, Nucl. Instr. Meth. A447, (2000) 350

[Mos82a] T. Moss et al, *Handbook on semiconductors*, North-Holland Publish. Co., (1982) 4B

[Mos82b] T. Moss et al, *Handbook on semiconductors*, North-Holland Publish. Co., (1982) 11A

[MTSort] MTSort package web page, http://ns.ph.liv.ac.uk/

[Nat63] M. I. Nathan, Phys. Rev. 130-6, (1963) 2201

[ND05] L. Nelson & M. Dimmock, 2005 IOP Nuclear Physics Conference, Poster presentation

[Nol94] P.J. Nolan et al., Ann. Rev. Nucl. Part. Sci. 45 (1994)

[Nor03] J. Norman et al., *The GREAT planar detector*, Talk given at the Position Sensitive Detectors Conference, June 2003, Stockholm, Sweden

[Oma87] M. Omar and L. Reggiani, Solid-State Electron. 30-12, (1987) 1351

[Oma87] M.A. Omar, L. Reggiani, Solid State Electron. 30 (1987) 1351

[Ott75] G. Ottavianni et al., IEEE Trans. Nucl. Sci., NS-22, (1975) 192

[Pal97] L. Palafox, *A New Method for the Determination of the Entry Position of g-Ray in High Purity Germanium Detectors by Current Pulse Analysis*, Ph.D. Thesis, College of Aeronautics, Cranfied University, 1997

[Pea02] C.J. Pearson et al., Trans. Nucl. Sci. NS-49, 3 (2002) 1209

[Pre99] W.H. Press, *Numerical Recipes in C*, Cambridge University Press, 1990

[Rad88] V. Radeka, Ann, Rev. Nucl. Part. Sci. 38 (1988) 224

[Reg77] L. Reggiani et al., Phys. Rev. B 16-6, (1977) 2781

[Rei02] P. Reiter et al., Nucl. Phys. A701 (2002) 209c

[Rei62] H.G. Reik and H. Risken, Phys. Rev. 126-5, (1962) 1737

[Ram39] Ramo, P.I.R.E 27 (1939) 584

[ROOT] http://root.cern.ch

[SM02] C. Santos & P. Medina, presentation at the 2002 AGATA workshop

[San03] P. Sangsingkeow et al., Nucl. Instr. Meth. A505 (2003) 183

[San99] P. Sangsingkeow et al., Proc. SPIE on Hard X-ray, Gamma-ray and Neutron detector physics 3768 (1999) 204.

[SB00] B.G. Streetman & S. Banerjee, *Solid State Elecrtonic Devices*, Fifth Edition, Prentice Hall, (2000)

[Scr05] H.C. Scraggs et al,. Nucl. Instr. Meth. , In Press

[She99] S.L. Shepherd et al., Nucl. Instr. Meth. A434 (1999) 373

[Shm98] G.J. Schmid et al., Nucl. Instr. Meth. A417 (1998) 95

[Sim00] J. Simpson et al., APH N.S., Heavy Ion Physics 11 (2000) 159

[Spa03] Spartan II FPGA Data Sheet, Xilinx, http://www.xilinx.com

[Sve05] C.E. Svensson et al, Nucl. Instr. Meth. A540 (2005) 348

[Sze02] S.M. Sze, *Semiconductor Devices*, Physics and Technology, 3rd edition, 2002

[The98] Ch. Theisen et al., *Tests of the Segmented Clover Detector 'Cloclo'*, Version 1 (1998), unpublished

[Trum] TRUMP PCI card, product information sheet, www.ortec-online.com

[VAM] VAMOS at GANIL: http://www.ganil.fr/vamos

[Vet00] K. Vetter et al., Nucl. Instr. Meth. A452 (2000) 105

[Vil01] A.C.C. Villari, Nuclear Physics A693, (2001) 465

[Wil96] M. Wilhelm et al., Nucl. Instr. Meth. A381 (1996) 462